UNIVERSITI TEKNOLOGI MARA

THE ROLE OF METAL OXIDES SUPPORTED ON EXTRACTED ALUMINIUM CATALYSTS IN THE CO-PYROLYSIS OF COTTON FABRIC AND POLYPROPYLENE WASTES FOR BIO-OIL PRODUCTION

NUR ALWANI BINTI ALI BASHAH

PhD

June 2026

UNIVERSITI TEKNOLOGI MARA

THE ROLE OF METAL OXIDES SUPPORTED ON EXTRACTED ALUMINIUM CATALYSTS IN THE CO-PYROLYSIS OF COTTON FABRIC AND POLYPROPYLENE WASTES FOR BIO-OIL PRODUCTION

NUR ALWANI BINTI ALI BASHAH

Thesis submitted in fulfilment
of the requirements for the degree of
Doctor of Philosophy
(Chemical Engineering)

Faculty of Chemical Engineering

June 2026

CONFIRMATION BY PANEL OF EXAMINERS

I certify that a Panel of Examiners has met on 10th March 2026 to conduct the final examination of Nur Alwani Binti Ali Bashah on her Doctor of Philosophy thesis entitled "The Role of Metal Oxides Supported on Extracted Aluminium Catalysts in the Co-Pyrolysis of Cotton Fabric and Polypropylene Wastes for Bio-oil Production" in accordance with Universiti Teknologi MARA Act 1976 (Akta 173). The Panel of Examiners recommends that the student be awarded the relevant degree. The Panel of Examiners was as follows:

Tan Huey Ling, PhD
Associate Professor
Faculty of Chemical Engineering
Universiti Teknologi MARA
(Chairman)

Mohd Azlan Mohd Ishak, PhD
Professor
Faculty of Applied Sciences
Universiti Teknologi MARA
(Internal Examiner)

Azam Taufik Mohd Din, PhD
Associate Professor
School of Chemical Engineering
Universiti Sains Malaysia
(External Examiner)

PROF DR HJH ZURAEDA IBRAHIM
Dean
Institute of Postgraduates Studies
Universiti Teknologi MARA

Date: 25 June 2026

AUTHOR'S DECLARATION

I declare that the work in this thesis was carried out in accordance with the regulations of Universiti Teknologi MARA. It is original and is the results of my own work, unless otherwise indicated or acknowledged as referenced work. This thesis has not been submitted to any other academic institution or non-academic institution for any degree or qualification.

I, hereby, acknowledge that I have been supplied with the Academic Rules and Regulations for Postgraduate, Universiti Teknologi MARA, regulating the conduct of my study and research.

Name of Student	:	Nur Alwani Binti Ali Bashah
Student ID. No.	:	2021330881
Programme	:	Doctor of Philosophy (Chemical Engineering) – EH950
Faculty	:	Chemical Engineering
Thesis Title	:	The Role of Metal Oxides Supported on Extracted Aluminium Catalysts in the Co-Pyrolysis of Cotton Fabric and Polypropylene Wastes for Bio-oil Production
Signature of Student	:	
Date	:	June 2026

ABSTRACT

Biomass is an alternative renewable energy source that can reduce dependency on fossil fuels. Biomass can be converted into carbon-based liquid fuel or bio-oil, which is environmentally friendly via heterogeneous catalytic process. The management of textile and plastic waste remains a critical environmental challenge, as conventional disposal methods generate greenhouse gases, toxic emissions, and persistent pollutants. Although pyrolysis offers a promising solution, its large-scale application is limited by poor product quality from individual feedstocks, low catalyst efficiency and stability, and the underutilization of industrial waste as a sustainable catalyst source. This study aims to investigate on the synthesized metal oxides supported on extracted aluminium (EA) derived from industrial sludge as catalyst in the reaction to produce bio-oil via co-pyrolysis of cotton fabric waste (CFW) and polypropylene plastic waste (PPW). The catalysts were developed as chromium-extracted aluminium (CE) and chromium/titanium-extracted aluminium (CTE). The catalyst was prepared via wet impregnation method at various metal loadings (5-20 wt.%) and heat treated at calcination temperatures between 400 °C to 800 °C and calcination time of 2 h to 6 h. Several characterization techniques were carried out including N_2 adsorption desorption, scanning electron microscopy-energy dispersive x-ray (SEM-EDX), x-ray diffraction (XRD), ammonia temperature-programmed desorption (NH_3-TPD), x-ray fluorescence (XRF), gas chromatography-mass spectrometry (GC-MS), and Fourier Transformed Infra-Red (FTIR). The catalysts activities were evaluated in a fixed bed reactor at different operating conditions including temperature (450 °C to 650 °C), time (15 min to 75 min), CFW/PPW ratio (80:20, 60:40, 50:50, 40:60, 20:80) and feedstock to-catalyst (F/C) ratio (2:1, 1:1, 1:1.5, 1:2). The results have revealed good catalytic activities, where 15CE-600-5 and CTE21-700-5 achieved highest bio-oil yield of 74.6% and 87.6%, respectively in co-pyrolysis of CFW and PPW. The reusability study shows that these catalysts can be regenerated for two cycles, where CTE21-700-5 could maintain better activity at 70.2% and 59.5% of bio-oil yield, compared to 15CE-600-6 that could be attributed to its higher surface areas. The best catalyst CTE21-700-5 achieved highest bio-oil yield of 87.6% at best operating conditions of 550 °C, 60 min, 50:50 CFW/PPW ratio, 1:1 F/C ratio and reusability for two cycles. The kinetic study revealed the co-pyrolysis of CFW/PPW with CTE21-700-5 catalyst was describe by 0.5 order with activation energy of 47.25 kJ/mol and pre-exponential factor of $1.19\times10^{3}s^{-1}$. The study concludes that the reusability heterogeneous catalyst synthesized via affordable and environmentally friendly method could effectively catalysed reaction to produce bio-oil from co-pyrolysis of CFW and PPW at moderate operating conditions.

ACKNOWLEDGEMENT

First, I would like to express my deepest appreciation to my main supervisor, Ir. Dr. Wan Zuraida Wan Kamis, for her continuous guidance, invaluable advice, and endless support throughout my PhD journey. Her patience, encouragement, and constructive feedback have been instrumental in shaping this research and my academic growth. My sincere gratitude also extends to Dr. Muhammad Zahiruddin Ramli, AP Ir. Dr. Siti Shawalliah Idris, and AP Dr. Mohamad Anuar Kamaruddin for their valuable technical support, insights, guidance, and motivation that greatly contributed to the completion of this thesis.

I would also like to acknowledge Universiti Teknologi MARA (UiTM) and the Ministry of Higher Education (KPT) for providing financial assistance through the SLAB scholarship. I am also grateful for the research funding received under the FRGS grant (FRGS/1/2022/TK0/UITM/02/95) and MYRA grant (600-RMC5/3/GPM (046/2022). Special thanks go to the Faculty of Chemical Engineering, Universiti Teknologi MARA Cawangan Pulau Pinang, the postgraduate studies committee, my colleagues, and the laboratory staff for their cooperation, assistance, and technical support. My heartfelt appreciation is also extended to Dr. Mohamad Khairul Nizam Zainan Nazri and his team for their mentorship in the Ph. D strategies and management program, as well as to Dr. Fakhrony Sholahudin Rohman, AP. Dr. Wan Izhan Wan Nawawi and his team for their valuable academic and research guidance.

I am sincerely grateful to all friends of the PhD circles, for their encouragement, discussions, and friendship that made this journey more meaningful. My warmest thanks also go to my dearest best friends for their unwavering support, laughter, and motivation through the difficulties of this journey. I would also like to thank all individuals who have contributed directly or indirectly to this research. Finally, my deepest love and gratitude go to my beloved family, my husband Muhammed Aswadde Abdul Stek, my daughter Adyra Nur Auleya Muhammed Aswadde, my mother and my extended family members, for their endless prayers, patience, and unconditional love. This accomplishment would not have been possible without their constant support and understanding.

TABLE OF CONTENTS

LIST OF TABLES

LIST OF FIGURES

LIST OF SYMBOLS

Symbols

A	Pre-Exponential Factor
E	Activation Energy
k	Reaction Rate
n	Reaction Order
R	Ideal Gas Constant
R^2	Coefficient of Determination
T	Temperature
t	Time
W_o	Initial Weight
W_f	Final Weight
W_t	Weight at time
α	Conversion Rate
β	Heating Rate
$\bar{\alpha}_{exp}$	Mean of Experimental Conversion Rates
∈	Set Membership
$\alpha_{exp,i}$	Experimental Conversion Rates
$\alpha_{sim,i}$	Simulation Conversion Rates

LIST OF ABBREVIATIONS

Abbreviations

AD	Aluminium Dross
BG	Bagasse
B-LDPE	Biomass-Low Density Polyethylene
B-HDPE	Biomass-High Density Polyethylene
BP	Biomass-to-Plastic
Ca/CB	Calcium/Carbon Beads
CB	Carbon Beads
CE	Chromium-Extracted Aluminium
CFW	Cotton Fabric Waste
CG	Coffee Ground
CHNOS	Carbon, Hydrogen, Nitrogen, Oxygen, And Sulphur
CHNS	Carbon, Hydrogen, Nitrogen, And Sulphur
CNS	Coconut Shell
COD	Chemical Oxygen Demand
CR	Coats-Redfern
CS	Corn Stover
CTE	Chromium/Titanium-Extracted Aluminium
CV	Chlorella Vulgaris
DFT	Density Functional Theory
DTG	Derivative Thermogravimetry
EA	Extracted Aluminium
EAFS	Electric Arc Furnace Slag
EDX	Energy Dispersive X-ray
EFB	Empty Fruit Bunch
EGA	Extracted Gamma Aluminium
F/C	Feedstock-to-Catalyst
FCC	Fluid Catalytic Cracking
FM	Friedman
GDP	Gross Domestic Product

GHG	Greenhouse Gas
H/C_{eff}	Hydrogen-to-Carbon Effective
HAP-ZE	Hydroxyapatite-Zeolite
HC	Aliphatic Hydrocarbon
HDO	Hydrodeoxygenation
HDPE	High Density Polyethylene
HHV	Higher Heating Value
HS-HZSM-5	Hollow Hierarchical Zeolite
HT	Hydrothermal
HTL	Hydrothermal Liquefaction
HZSM-5	H-Zeolite Socony Mobil-5
IPCC	Intergovernmental Panel on Climate Change
IRENA	International Renewable Energy Agency
ISW	Industrial Solid Waste
ISWA	International Solid Waste Association
KAS	Kissinger-Akahira-Sunose
KSi	Potassium-Silica
KSi-RG	Potassium-Silica Regeneration
LDPE	Low-Density Polyethylene
LG	Lignin
LLDPE	Linear Low-Density Polyethylene
MAH	Monoaromatic Hydrocarbon
MIDF	Malaysian Industrial Development Finance
MS	Molten Slag
MSCI	Morgan Stanley Capital International
MSW	Municipal Solid Waste
NETR	National Energy Transition Roadmap
NH_3-TPD	Ammonia-Temperatured Programmed Desorption
NLP	Non-Linear Programming
NPs	Nano Particles
NS	Neem Sawdust
ODE	Ordinary Differential Equation
OFAT	One Factor at Time

OFW	Ozawa-Flynn-Wall
OL	Organosolv Lignin
PAHs	Polycyclic Aromatic Hydrocarbons
PE	Polyethylene
PID	Proportional, Integral, Derivatives
PP	Polypropylene
PPW	Polypropylene Plastic Waste
PS	Polystyrene
PSD	Pore Size Distribution
PVC	Polyvinyl Chloride
RHA-T	Treated Rice Husk Ash
RM	Red Mud
SB	Sugarcane Bagasse
SCL	Sugarcane Leaves
SDG	Sustainable Development Goals
SEM-EDX	Scanning Electron Microscope-Energy Dispersive X-Ray
SFW	Surgical Face Mask Waste
SLO	Spent Lubricating Oil
SS	Sewage Sludge
SSE	Sum Square Error
ST	Starink
TEM	Transmission Electron Microscopy
TGA	Thermogravimetric Analysis
Ti3H5	Titanium Modified Hzsm-5
TiAH5	Titanium Anatase Modified Hzsm-5
TiO_2 Nps	Titanium Dioxide Nanoparticles
UNEP	United Nations Environment Programme
USY	Ultra-stable Y Zeolite
WCO	Waste Cooking Oil
WMAM	Waste Management Association of Malaysia
WtE	Waste-To-Energy
XRD	X-Ray Diffractometer
XRF	X-Ray Fluorescence

ZSM-5	Aluminosilicate Zeolite (Zeolite Socony Mobil-5)
ZSM-5@SBA15	Core Shell hierarchical Zeolite

LIST OF NOMENCLATURES

Nomenclatures

Al_2O_3	Aluminium Oxide
CaO	Calcium Oxide
Ce	Ceria
Ce/Al_2O_3	Cerium-Alumina
CeZrAl	Cerium-Zirconia-Aluminum
CH_4	Methane
Cl	Chlorin
CO	Carbon Monoxide
Co	Cobalt
Co-ZSM5	Cobalt- Zeolite Socony Mobil-5
CO_2	Carbon Dioxide
Co_3O_4	Cobalt (IV) Oxide
Cr	Chromium
Cr_2O_3	Chromium (III) Oxide
Cu	Copper
Cu-ZSM5	Copper- Zeolite Socony Mobil-5
Fe_2O_3	Iron (III) Oxide
Fe-ZSM5	Iron- Zeolite Socony Mobil-5
Ga	Gallium
H	Hydrogen
H_2O	Water
H_2SO_4	Sulphuric Acid
K_2O	Potassium Oxide
La	Lanthanum
MgAl	Magnesium-Aluminium
MgCr	Magnesium-Chromium
MgFe	Magnesium-Iron
MgO	Magnesium Oxide
$Mn\text{-}Al_2O_3$	Manganese-Aluminium Oxide

MnO_2	Manganese (II) Oxide
Mo	Molybdenum
Ni	Nickel
$Ni\text{-}Al_2O_4$	Nickel aluminate
$Ni\text{-}CaO\text{-}Al_2O_3$	Nickel - calcium oxide - Aluminium Oxide
Ni-MgO	Nickel- Magnesium Oxide
Ni-ZSM5	Nickel - Zeolite Socony Mobil-5
NiO	Nickel Oxide
Ni-SiO	Nickel-Silica
Pd	Palladium
Pd/Al_2O_3	Palladium-Alumina
Ru	Ruthenium
SiO_2	Silica
Ti	Titanium
TiO_2	Titanium Dioxide
V	Vanadium
Zn	Zinc
ZnO	Zinc Oxide
ZrO_2	Zirconium Oxide

CHAPTER 1
INTRODUCTION

1.1 Overview

This section describes an overview on current state of global energy and waste management, bio-oil as a renewable energy, pyrolysis technology for municipal solid waste (MSW) conversion, and the heterogeneous catalysts to produce bio-oil. This chapter also discusses the problem statement, research objectives, research scope and significant of study.

1.2 Research Background

The increasing global energy demand, driven by societal and economic development, has resulted in greater fossil fuel consumption, leading to increase carbon emissions and resource depletion. According to the MSCI Sustainability Institute, (2023), global energy consumption increased by nearly 2 % in 2023 over the year earlier, with fossil fuels such as coal, oil, and natural gas still relying for approximately 81 % of global energy supply. This heavy reliance on non-renewable resources has resulted in severe environmental challenges, including greenhouse gas (GHG) emissions, air pollution, and climate change. The Intergovernmental Panel on Climate Change (IPCC, 2022) highlights that without significant mitigation strategies, the world is on track to exceed 1.5 °C warming by 2030, leading to more extreme weather, biodiversity loss, and economic instability.

Recently, there has been a concern raised on the growing of municipal solid waste (MSW) generation due to socio-economic development. The worldwide production of plastic stood at 367 million tons in 2020 with only low recycling rate of plastic waste of merely 10 % and 14 % incinerated globally, 76 % of which ends up in landfills or the natural environment (Geyer, 2020). The durability of plastics causes them to accumulate in landfills and oceans, threatening ecosystems, and human life. Similarly, the textile industry generates approximately 92 million tons of waste per year globally, with cotton fabrics constituting a huge portion (Abtew et al., 2025). In Malaysia alone, the fabric waste accounted for 432.9 metric tons of the country's total

waste (Waste Management Association of Malaysia, 2025), while plastic waste accounts for approximately 1.1 million tons annually (Greenpeace, 2025). Most of this waste is disposed of in landfills, which are already nearing capacity, causing additional environmental burdens.

One promising strategy to address these challenges is thermochemical conversion of waste through pyrolysis, particularly co-pyrolysis, which involves the simultaneous thermal decomposition of two or more feedstocks. Co-pyrolysis of waste cotton fabric (biomass-derived cellulose) and plastics (hydrocarbon-rich polymers) has attracted growing attention due to its good interaction in enhancing bio-oil yield and quality. Cotton fabric provides oxygenated species that promote plastic degradation, while plastics contribute hydrogen, improving deoxygenation and increasing hydrocarbon selectivity. The resulting liquid product, bio-oil, can serve as a renewable alternative to fossil fuels or as a platform chemical feedstock for downstream industries.

However, bio-oil from pyrolysis often produces undesirable properties such as high oxygen content, low heating value, instability, and corrosiveness (Qiu et al., 2022). To overcome these limitations, catalytic pyrolysis has been widely investigated. Catalysts promote deoxygenation, cracking, and aromatization, thereby enhancing the yield of hydrocarbons and reducing oxygenated by-products (Sun et al., 2021). Metal oxides such as chromium (Cr), titanium (Ti), and aluminium (Al) based catalysts have shown significant potential due to their acidity, redox properties, and ability to stabilize active intermediates.

A contributing aspect of this research is the utilization of extracted aluminium (EA) from industrial sludge as the catalyst support. This approach utilizing industrial waste not only reduces dependency on commercial aluminium but also valorises another industrial waste stream, aligning with circular economic principles. Supporting metal oxides on EA enhances catalytic activity, recyclability, and environmental impacts associated with virgin material extraction. Moreover, incorporating kinetic modelling into the catalytic co-pyrolysis study provides quantitative insights activation energy, and pre-exponential factors. Such modelling is critical for scaling up the process from laboratory to industrial applications, ensuring efficiency and feasibility.

Thus, the present study integrates waste management, renewable energy production, and sustainable catalysis to support the Sustainable Development Goals, particularly affordable and clean energy (SDG 7), responsible consumption and production (SDG 12), and climate action (SDG 13). The catalytic co-pyrolysis of textile

and plastic waste into value-added bio-oil, coupled with the use of waste-derived catalysts, promotes cleaner energy generation, waste valorisation, and reduced greenhouse gas emissions, offering a practical approach to address energy, environmental, and sustainability challenges.

1.3 Motivation for This Work

The motivation of this work is to put forward one of solutions to the problem in producing bio-oil from catalytic pyrolysis. The solution requires the development of a heterogeneous catalyst that can meet several criteria including active catalyst with enhanced selectivity towards less reactive oxygenates as well as stable for repeated use. The aim of this research is to address these gaps by developing a heterogeneous catalyst comprising Cr and Ti oxides supported on EA derived from industrial sludge. Chromium oxide (Cr_2O_3) offers superior thermal stability and resistance to catalyst deactivation, while titanium dioxide (TiO_2) is highly active in cleaving C–O bonds and exhibits robust metal-support interactions. Aluminum oxide (Al_2O_3), with its strong acidity, large surface area, and excellent porosity, serves as an ideal support material. The unique combination of these components is expected to address critical limitations in existing catalytic systems.

The study further investigates the catalytic co-pyrolysis of cotton fabric waste (CFW) and polypropylene plastic waste (PPW), for in-depth understanding of the interactions of biomass and plastics. The effects of catalyst preparation for chromium-extracted aluminium (CE) and chromium/titanium-extracted aluminium (CTE) include metal loading, calcination temperature and calcination time, were studied. Moreover, the process conditions such as pyrolysis temperature, pyrolysis time, biomass-to-plastic (BP) ratio and feedstock-to-catalyst (F/C) ratio, are crucial to enhance the yield and quality of bio-oil. Additionally, the reusability study of newly developed catalysts is important for efficient activity in heterogeneous system. Furthermore, kinetic modelling of catalytic co-pyrolysis processes is still unexploited, most lack a comprehensive understanding on newly developed catalyst.

1.4 Problem Statement

Nowadays, the management of textile and plastic waste presents one of the most urgent environmental challenges. The textile waste, especially cotton fabric waste is biodegradable material, which generates carbon dioxide (CO_2) and methane (CH_4) emission during landfill decomposition. The alternative use of incineration for disposal method releases toxic gases such as carbon monoxide, nitrogen oxides, and volatile organic compounds (Tang et al., 2023). In contrast, plastics are highly resistant to degradation and have persisted in the environment for hundreds of years. The improper management and accumulation of waste contribute to land and marine pollution, leachate formation, and greenhouse gas (GHG) emissions. Moreover, conventional disposal methods such as landfilling and incineration pose significant drawbacks due to their high operational costs, lack of resource recovery, and the release of toxic emissions and microplastic contaminants that endanger public health (Ma et al., 2024).

Pyrolysis has been proposed as a promising waste-to-energy (WtE) technology, but its commercialization faces several limitations. Biomass, with its high oxygen and low hydrogen content, produces oxygen-rich pyrolysis products that reduce selectivity towards hydrocarbon. In contrast, hydrogen-rich plastics have poor thermal conductivity and high viscosity, leading to heavy liquid formation during individual pyrolysis (Sun et al., 2025). Although catalytic pyrolysis improves product quality, the high cost of commercial catalysts, and limited reusability restrict large-scale application. Thus, co-pyrolyzed of biomass with plastic and addition of catalyst emerging as an attractive alternative due to the interaction of biomass and plastic and utilizing catalyst can improve the characteristic of bio-oil (Luo et al., 2022).

The production of high-quality bio-oil through catalytic pyrolysis faces significant challenges, including limited catalyst efficiency, poor selectivity toward desirable compounds, and under-utilization of industrial waste as a resource for catalyst development. Existing catalysts are still facing challenges to meet the required performance standards, with issues such as low stability during repeated use, inadequate acidity for oxygenate reduction, and insufficient activity for bio-oil upgrading. Moreover, the potential of industrial sludge which is rich in valuable metal such as aluminium remains largely unexploited in catalyst synthesis, representing a missed opportunity for sustainable waste valorisation.

There is a notable research gap in the catalytic co-pyrolysis of CFW and PPW using metal oxides supported on EA catalysts. Only a few studies have investigated the simultaneous valorisation of CFW and PPW waste through catalytic co-pyrolysis, while limited work has examined the use of waste-derived aluminium as a catalyst support. In addition, the investigation of reusability and regeneration of the catalyst are scarce and kinetic modelling of catalytic co-pyrolysis remains underdeveloped, even though it plays a crucial role in reactor design, process optimization, and scale-up. Therefore, there is an urgent need for research that focuses on developing waste-derived catalysts, assessing their performance in co-pyrolysis, and incorporating kinetic modelling to promote efficient and sustainable waste-to-energy conversion.

Hence, the contribution of the study can be summarized as: (1) newly developed metal oxides (Cr and Ti) supported on aluminum derived from industrial solid waste catalyst with application in catalytic co-pyrolysis of CFW and PPW; (2) contribution to knowledge regarding to properties and behaviors of Cr/Ti and EA catalyst in terms of its characteristic, catalytic activity, catalyst reusability and regeneration and kinetic model. To the best of knowledge, the heterogeneous catalysts CE and CTE in the co-pyrolysis of CFW and PPW have not been reported.

1.5 Research Objectives

The objectives of this study are:

a) To synthesize and characterize heterogeneous metal oxides catalyst comprises of Cr, Ti and supported on EA from industrial sludge which are CE and CTE by variation in synthesis conditions (metal loading, calcination temperature, and calcination time).
b) To evaluate catalytic activities of the as-synthesized catalysts in the co-pyrolysis of CFW and PPW to produce bio-oil through investigation on variation in process operating conditions (pyrolysis temperature, CFW/PPW ratio, F/C ratio, and pyrolysis time).
c) To study the reusability and regeneration of the as-synthesized catalyst during co-pyrolysis of CFW and PPW.
d) To obtain reaction kinetics model for the catalytic co-pyrolysis of CFW and PPW using model fitting technique.

1.6 Significance of Study

Through this study, a reusable heterogeneous (solid) acid catalyst is developed for use in the synthesis of bio-oil through co-pyrolysis of CFW and PPW. The solid catalyst is expected to overcome drawbacks associated with low quality bio-oil due to high oxygen content biomass during catalytic process. The heterogeneous catalyst synthesis from industrial solid waste could alleviate the accumulation of industrial solid waste in landfill via resource utilization, thus reducing the damage caused by this waste to environment and providing significant amount of resources such as metal. The catalyst can be used to upgrade the bio-oil quality by deoxygenation to promote selective products such as hydrocarbon. Furthermore, this study has accomplished one of Malaysian government's goal in addressing renewable energy and sustainability development outline in Malaysia 2030 agenda for sustainability development goal (SDG 2030) and Malaysia shared prosperity vision 2030 (SPV 2030).

1.7 Research Scope

The present research scope includes the development, characterization, and the catalytic activity of the synthesized heterogeneous catalysts in the co-pyrolysis of CFW and PPW. This study focuses primarily on catalytic activity based on bio-oil yield in co-pyrolysis. The EA was prepared from industrial sludge using sulphuric acid (H_2SO_4) acid leaching method and precipitated with ammonium solution. Then it was dried, calcined, ground into powder form and used as support. The specific amount of Cr or/and Ti precursor was impregnated onto EA via wet impregnation method. The catalysts were synthesized at different metal loading (5 wt.% to 20 wt.%), different calcination temperatures (400 ºC to 800 ºC), and calcination time (2 h to 6 h) to obtain the best preparation conditions to maximize the yield of bio-oil based on one factor at time approach (OFAT). The range of calcination temperature was chosen based on the recommended temperature to produce active Al_2O_3 from industrial solid waste. The properties of the catalyst were characterized in terms of surface area and porosity using nitrogen adsorption-desorption, acidity using ammonia-temperatured programmed desorption (NH_3-TPD), surface morphology using scanning electron microscope-energy dispersive x-ray (SEM-EDX) and catalyst crystallinity using x-ray

diffractometer (XRD) and the composition of the catalyst is using x-ray fluorescence (XRF).

The feedstock of CFW and PPW were characterized in terms of its proximate and ultimate analysis. These characterizations were conducted using thermogravimetric analysis (TGA) and carbon, hydrogen, nitrogen, and sulphur (CHNS) elemental analyser, respectively. The thermochemical reaction was conducted in a fixed bed microreactor. Two stages in series reaction (ex-situ) configuration were performed in same column, where the first stage involves thermal cracking of feedstock and subsequently by catalytic cracking of pyrolytic vapours at second stage. The variables in the process parameter were investigated at: pyrolysis temperature (450 ºC to 650 ºC), CFW/PPW ratio (80:20, 60:40, 50:50, 40:60, 20:80), F/C ratio range from 2:1, 1:1, 1:1.5, 1:2), and pyrolysis time (15 min to 75 min). These ranges of process parameters are based on the values reported in literatures involves biomass and plastic co-pyrolysis. The catalytic performances of the synthesized catalysts in the co-pyrolysis reaction were evaluated using OFAT approach based on the maximum production of bio-oil yield. The product yield, i.e., char, bio-oil were determined using by weight, while remaining of total yield was non-condensable gases.

The catalyst reusability was investigated up to 3 reaction cycles based on the best conditions of catalytic co-pyrolysis of CFW and PPW. The catalyst was regenerated by calcination with air in muffle furnace at 600 °C and 5 h to remove deposited material on catalyst. The kinetic model bio-oil production via co-pyrolysis of CFW and PPW using CTE catalyst was estimated by Coats-Redfern model. The activation energy (E) and pre-exponential factor (A) parameters and reaction kinetic order were obtained.

1.8 Summary

This chapter provides an overview of bio-oil as a renewable energy source derived from biomass and plastic waste. It also discusses the valorisation of CFW and PPW from MSW through the co-pyrolysis technique for bio-oil upgrading. The use of catalysts in co-pyrolysis has been shown to enhance bio-oil yield and improve product selectivity through catalytic cracking and deoxygenation reactions. Nevertheless, several challenges are also addressed, including catalyst deactivation and the decline in stability during repeated use. Furthermore, this chapter emphasizes the potential of

extracting aluminium from industrial sludge for use as a sustainable catalyst, thereby promoting waste minimization and resource recovery.

In line with the principles of sustainable development, this work contributes to SDG 7 (affordable and clean energy) by producing renewable bio-oil as an alternative to fossil fuels, SDG 12 (responsible consumption and production) by transforming waste materials such as CFW, PPW, and industrial sludge into valuable resources, and SDG 13 (climate action) by reducing greenhouse gas emissions associated with waste disposal and fossil fuel dependence. Accordingly, the CE and CTE catalysts developed in this study aim to enhance the efficiency and sustainability of the co-pyrolysis process, leading to higher bio-oil production.

CHAPTER 2
LITERATURE REVIEW

2.1 Introduction

This chapter presents an overview on thermochemical conversion of solid waste material into valuable energy products (bio-oil), with a focus on pyrolysis technology. In this study, the term waste is used in a broad context to refer to discarded materials, including industrial residues. The waste valorisation of biomass and plastic in catalytic co-pyrolysis has emerged as promising approach for sustainable energy production. The presence of catalysts not only improves product yield and quality of bio-oil but also support waste valorisation and circular economy. Firstly, the worldwide waste production and potential for energy recovery are presented. Next, biomass as renewable energy and the pyrolysis process to produce bio-oil are discussed. The textile waste and plastic waste characteristics along with catalytic pyrolysis reaction are also discussed. Next, the various heterogeneous catalysts used in pyrolysis are reviewed. The basis for metal selection and catalyst synthesis method is also discussed. Furthermore, the effect of catalyst synthesis condition and effect of pyrolysis process conditions are presented. Finally, the reviewed catalyst reusability and kinetic model study are discussed.

2.2 Worldwide Waste Production and Potential for Energy Recovery

The rapid increase in global population and urbanization drives higher volumes of waste generation, making solid waste management increasing difficult. In 2016, municipal solid waste (MSW) generation reached 392 million tons in Central Asia and Europe, 289 million tons in North America, and 174 million tons in Sub-Saharan Africa. By 2030, these values are expected to rise to 440 million tons in Central Asia and Europe (11% increase), 350 million tons in North America (21% increase), and 269 million tons in Sub-Saharan Africa (55% increase) (Kaza et al., 2018). It was reported that in 2020, the MSW generation has reached 2.1 billion tons per year and will gradually increase to 3.782 billion tons per year in 2050. The increase of 1.152 % of gross domestic product (GDP) and 0.504 % of population growth, could be major contribution in increment of global MSW in 2050. It is observed, the MSW is predicted

to raise 80% in 2050 compared to 2020 by considering the GDP and population growth (UNEP & ISWA, 2024). Figure 2.1 shows the prediction of MSW generation, GDP growth, and population growth in 2050. Poor solid waste management threatens public health and accelerates environmental degradation, highlighting the urgent need for efficient waste treatment systems.

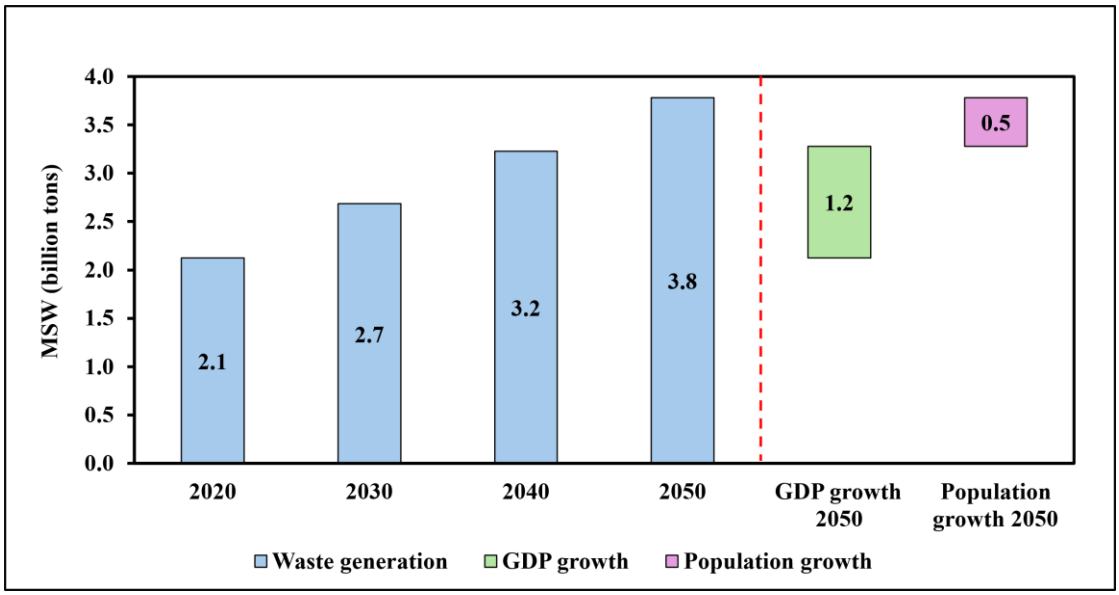

Figure 2.1 Prediction of MSW Generation by Year From 2020 to 2050, GDP Growth and Population Growth in 2050

Conventional methods such as landfilling remain dominant. However, the landfilling of MSW can lead to water, land and air pollution, including the GHG emission, leachate generation and long-term pollution of freshwater sources by pathogens and heavy metals (Kuchelar & Sudarsan, 2022). Alternatively, some of the useful resources in MSW can be reproduced into energy and value-added products using waste-to-resource technology such as via thermochemical processes. Biomass and plastics, which represent a major fraction of MSW, are often incinerated or landfilled despite their potential as feedstocks for energy recovery (Kaza et al., 2018).

The rising demand for renewable energy has further emphasized the potential of upcycling MSW specifically biomass and plastic. Biomass and plastic contain significant amounts of organic matter that can be converted into bioenergy and chemicals. Moreover, a long degradation times, limited space and environmental pollution in landfill, cause the thermochemical route to become significant to overcome the problem (Ndou & Rampedi, 2022). Pyrolysis has emerged as a promising thermochemical conversion process for managing MSW, particularly biomass and

plastic. Unlike incineration, pyrolysis operates in the absence of oxygen, decomposing organic materials into bio-oil, syngas, and char (Miandad et al., 2019). This approach not only reduces waste volume but also recovers valuable resources in the form of renewable fuels and chemicals. The process offers several advantages, including lower emissions of harmful gases, and higher energy recovery efficiency.

In pyrolysis studies, biomass and plastic wastes have typically been processed individually for bio-oil production. However, the resulting bio-oils are often of low quality and thermally unstable. Biomass-derived oils usually contain prominent levels of oxygenated compounds due to hydrogen deficiency. Conversely, plastic-derived oils frequently contain harmful compounds, including polycyclic aromatic hydrocarbons (PAHs) (Wee et al., 2023). Plastic contains high carbon and hydrogen content can supple hydrogen during pyrolysis, thereby complementing the drawbacks of biomass and improving overall bio-oil quality. Hence, co-pyrolysis has gained attention for producing higher-quality bio-oil by reducing oxygenates, enhancing stability, and increasing hydrocarbon yield. Consequently, co-pyrolysis represents a viable alternative for sustainable waste-to-energy (WtE) conversion and supports circular economy principles by transforming waste into valuable resources.

2.3 Biomass as Renewable Energy

Biomass is a promising resource used to reduce the utilization and reliance of fossil fuel such as crude oil, coal, and natural gas. Currently the biomass conversion to bioenergy has gained researchers attention in many countries especially those with biomass potential (Shrivastava et al., 2021). There are many researchers also reported on the negative impact on fossil fuel to environment such as increment of GHG emission that could cause global warming and climate change (Johnsson et al., 2019; Kumar et al., 2015; Shrivastava et al., 2021).

The advantages of utilizing biomass as bioenergy include easy handling and management of biomass solid, lesser carbon emission, and the availability of resources. Approximately there are 220 billion tons of dry biomass that is produced worldwide annually, making biomass as sustainable energy source (Abnisa & Daud, 2014). Currently, the trend of world energy development also observed to be shifted to energy with the characteristic of low-carbon emission, clean and environmental-friendly. (Rashidi et al., 2022). The global renewable energy generation capacity in 2023 was

reported to produced 3865 giga watt (GW) which represent about 43 % with growth about 23.43 % over 2022 (IRENA, 2024). Malaysia also put forward plans to address the net-zero emission target through National Energy Transition Roadmap (NETR) 2023, which highlight the sustainable energy pathways towards sustainable development. Under National Biomass Action Plan 2023–2030, Malaysia has potential to develop and deploy bioenergy on the strength of abundant biomass feedstock (MIDF, 2024). This is aligned with sustainable development goal 7 (SDG 7), which aims for affordable and cleaner energy.

Bioenergy from biomass sources can be produced via traditional (direct combustion) and modern approaches (liquid biofuel production, biogas generation by anaerobic digestion, or bio-refineries). Among all processes, the fast pyrolysis has shown emerging technology that suitable to produce bio-oil. The products produce includes char, oil, and gases which all of them can be transformed into value added products. Through fast pyrolysis process with optimum condition the bio-oil product could suppress char and gas production, hence make fast pyrolysis as potential technology to be employed in oil production for transportation. Figure 2.2 illustrates the bioenergy roadmap in various technologies.

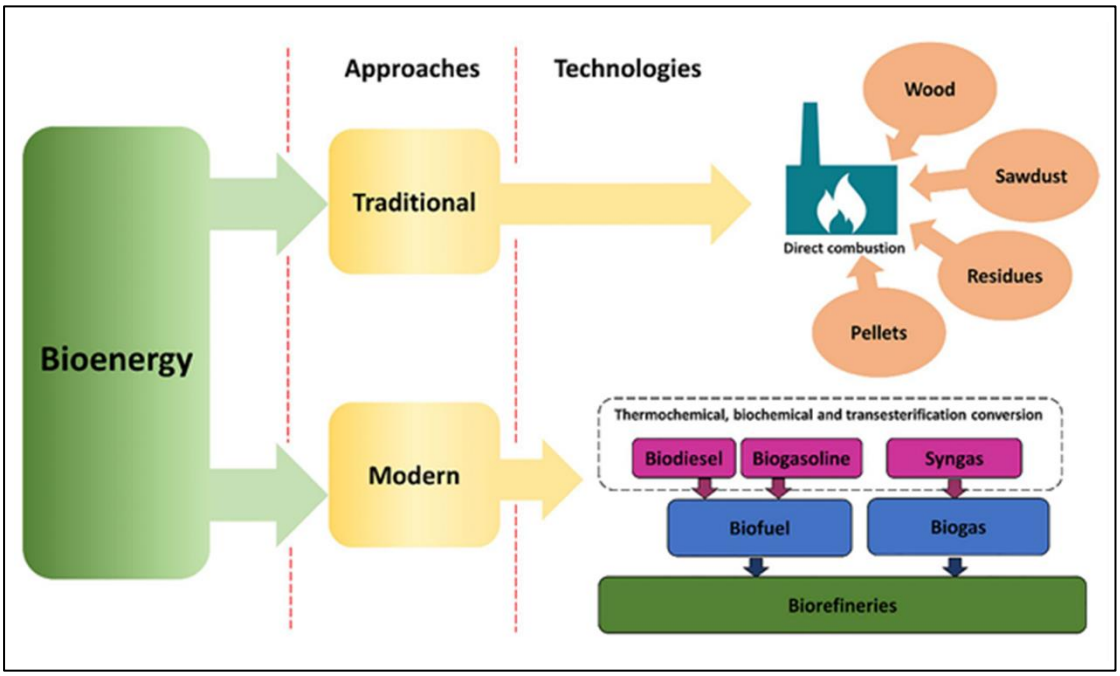

Figure 2.2 Bioenergy Roadmap from Typical Technologies

Source: (Rashidi et al., 2022)

2.4 Biomass Thermochemical Conversion for Bio-oil Production

Bioenergy from biomass is targeted to be utilized as transportation fuel and petrochemical feedstock such as aromatic and hydrocarbon (HC), via thermochemical conversion (Kim et al., 2016). Thermochemical conversion includes gasification, pyrolysis, liquefaction, and hydrothermal carbonization (Cho et al., 2018; Uzi et al., 2019). Among all the thermochemical processes, pyrolysis is more flexible for producing biofuels due to it is easy, functional, and low-cost process that can be applied to a wide variety of feedstock (Escalante et al., 2022).

2.4.1 Pyrolysis Process

Pyrolysis is a highly effective process that yields high energy density solid char, bio-oil, and gases in the absence of oxygen. Based on operating parameters such as pyrolysis temperature, heating rate, and residence time, the process can be classified into several types, including slow, intermediate, fast, flash, torrefaction, and microwave pyrolysis. Each type exhibits distinct product distribution profiles and selectivity. The key characteristics and product distributions associated with each pyrolysis type are summarized in Table 2.1.

Table 2.1
Key Characteristics of Pyrolysis and Product Selectivity

Pyrolysis	Operating parameter	Product selectivity	References
Slow	Low [a] (0.1–0.8 °C/min) Low-moderate [b] 300–550 °C Long [c] (hours-day)	Maximize biochar	(Roy & Dias, 2017)
Intermediate	Fast [a] (10–100 °C/s) Low-moderate [b] 450–550 °C Moderate [c] (10–30 s)	High bio-oil	(Bianasari et al., 2024)
Fast	Fast [a] (10–1000 °C/s) Moderate [b] 450–550 °C Short [c] (0.5–2 s)	High bio-oil	(Roy & Dias, 2017)
Flash	Rapid [a] (>1000 °C/s) High [b] 800–1000 °C Quick [c] (0.5 s)	Maximize bio-oil	(Bhaskar & Pandey, 2015)

Pyrolysis	Operating parameter	Product selectivity	References
Microwave	Quick [a] Low-high [b] 400–800 °C Quick [c]	Maximize bio-oil	(Li et al., 2016)
Torrefection	Low [a] (10 – 100 °C/s) Low [b] 200 – 300 °C Long [c] (<2h)	Torrified char	(Daful & Chandraratne, 2020)

Bio-oil is a dark brown liquid contains mainly organic matters such as hydrocarbons, acid, ketone, aldehyde, ester, phenols, sugar, and furans with 15–35 % of water (Bianasari et al., 2024). Most of the compound are oxygenates which resulting in high thermal instability, and low heating value (Hassan et al., 2020). The comparison of bio-oil properties between bio-oil derived biomass, plastic, biomass/plastic, and fuel is tabulated in Table 2.2.

Table 2.2
Physical Properties and Characteristic of Bio-oil from Various Sources in Catalytic Upgrading using HZSM–5 Catalyst.

Properties of bio-oil	Baggase (BG) (Suriapparao et al., 2020)	Polypropylene (PP) (Suriapparao et al., 2020)	BG: PP (Suriapparao et al., 2020)	Heavy fuel oil (Lehto et al., 2014)
Density (g/cm^3)	0.855 ± 0.04	0.853 ± 0.04	0.853 ± 0.04	0.990
HHV (MJ/kg)	34.5 ± 0.5	43.6 ± 0.6	42.9 ± 0.7	40.6
Viscosity (cP)	20.4 ± 1.0	5.1 ± 0.6	1.1 ± 0.2	180–420
Flash point (°C)	106.4 ± 1.0	77.2 ± 1.0	69.5 ± 1.0	>65

2.4.2 Feedstock for Pyrolysis Process

The source of biomass to produce biofuel is progress from its first generation until current fourth generation (Asadullah, 2014). First generation biofuels are produced from edible resources, such as sugars, starch, or vegetable oils; however, the main shortcoming of first generation biofuels is risking food security. These limitations gave rise to second generation biofuels, mainly from non-food crops such as lignocellulosic biomass and residues (Ocreto et al., 2021). Third generation biofuels are obtained from microorganisms such as microalgal and microbial biomass (Leong et al., 2021; Wang et al., 2021). Lastly, fourth generation biofuels involve genetically modified micro-

organisms to enhance biofuel production (Aron et al., 2020). Figure 2.3 shows the shift of feedstock in bio-fuel generations.

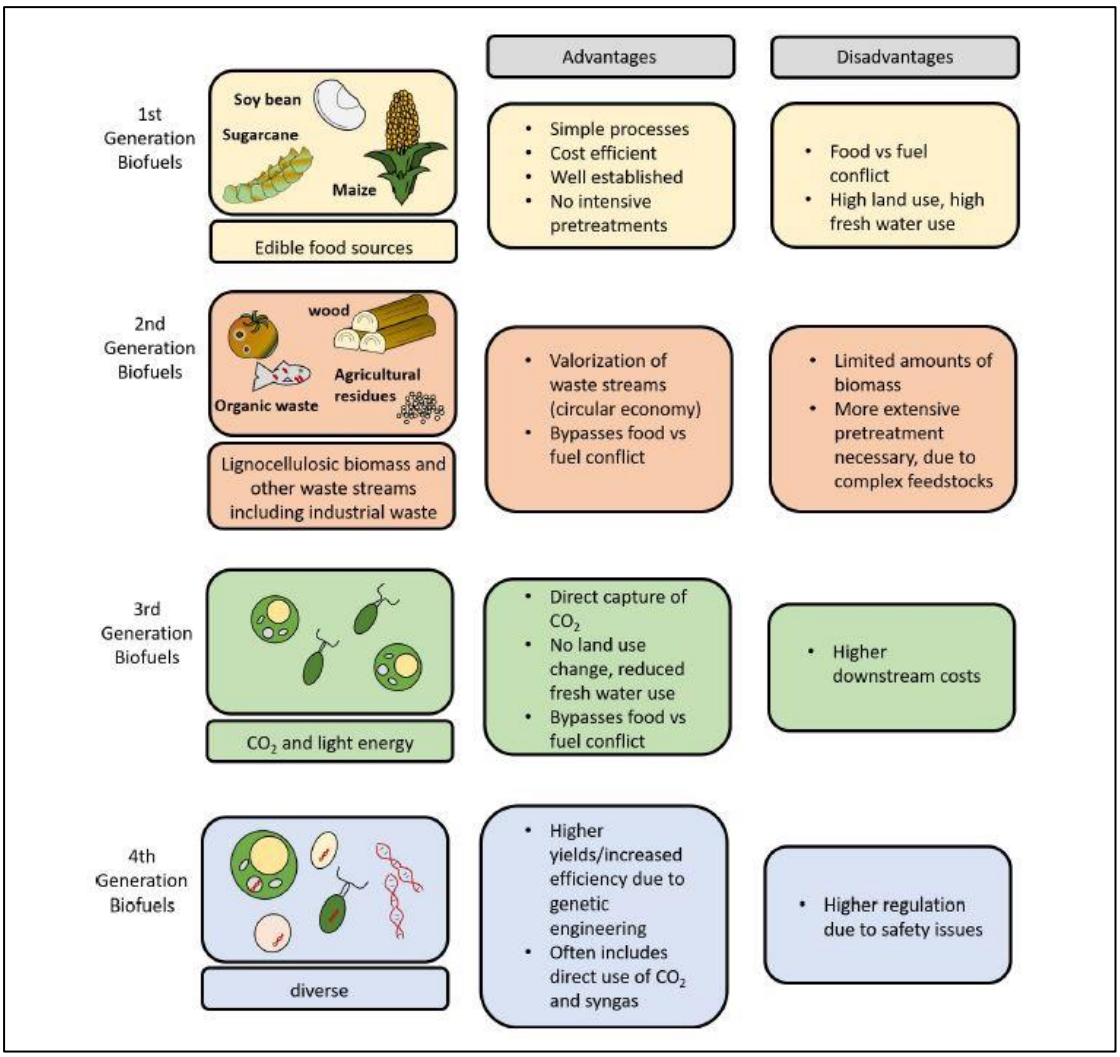

Figure 2.3 Biofuel Generations

Source: (Cavelius et al., 2023)

Among them, lignocellulosic biomass is widely used as feedstock in biomass energy conversion. Lignocellulosic sources contain of cellulose (40–50 wt.%), hemicellulose (15–30 wt.%), lignin (10–30 wt.%), extractives (0–15 wt.%) and small portion of inorganic mineral substances (Zhong et al., 2022). The composition of lignocellulosic biomass highly depends on its source whether it is derived from hardwood, softwood, or grasses. Among the components in biomass, holocellulose which includes cellulose and hemicellulose, contained most of glucose and various type of monosaccharides, respectively (Shao et al., 2024). Figure 2.4 shows the main component in lignocellulosic biomass.

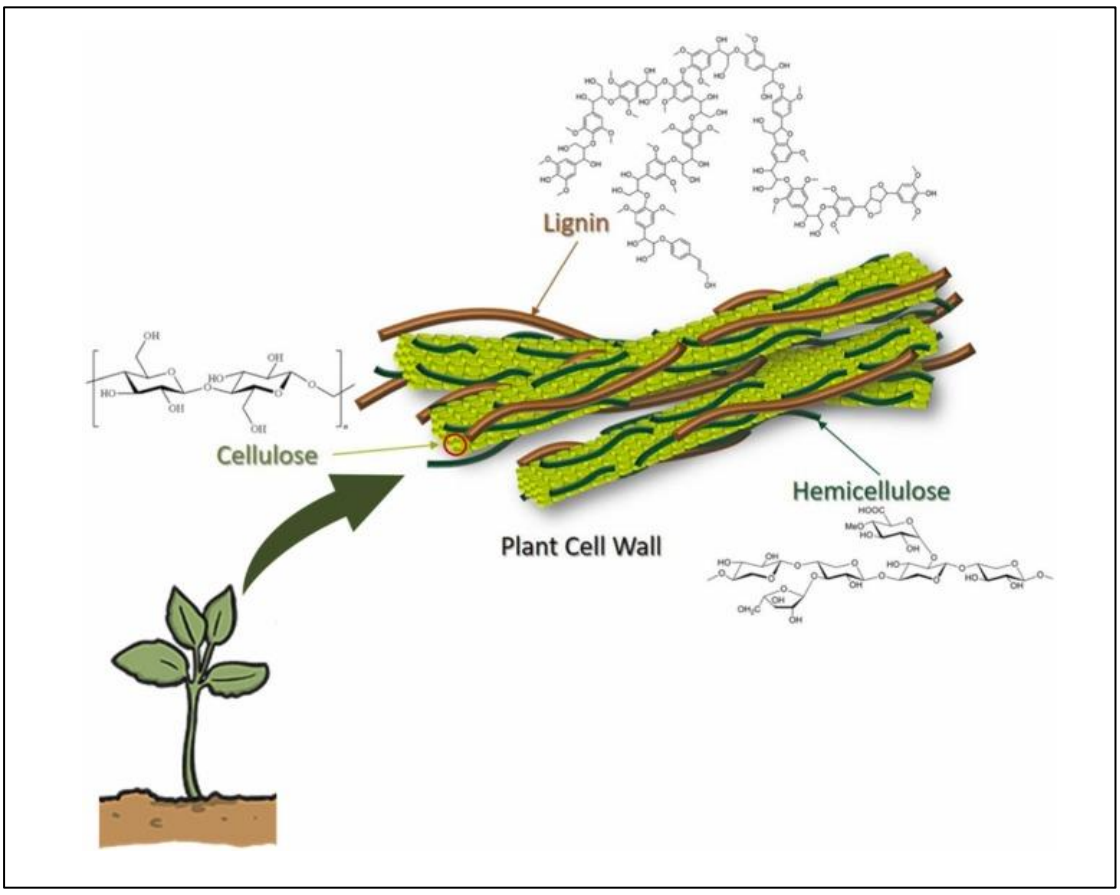

Figure 2.4 Main Component in Lignocellulosic Biomass
Source: (Vilas-Boas et al., 2025)

In recent years, the circular economy concept has gained significant attention, encouraging the utilization of MSW through thermochemical energy conversion processes (Alfè et al., 2022). Plastics, which dominate landfills and require hundreds of years to degrade, represent a major target for such approaches (Geyer et al., 2017). Similarly, the recycling of textile waste has become a global concern due to the rapid turnover of fashion trends and the short lifespan of clothing (Niinimäki et al., 2020). Natural textiles such as cotton, jute, and hemp remain in demand, even though synthetic textiles are increasingly popular (Filho et al., 2024). During pyrolysis, holocellulose in natural fibres releases enormous amounts of volatiles that are rich in oxygenated compounds. These volatiles can interact with plastics, promoting polymer decomposition, while the radicals released from holocellulose can remove hydrogen from plastics, further enhancing the co-pyrolysis process (Nardella et al., 2022).

2.5 Feedstock Characteristics: Textile Waste and Plastic Waste

Municipal solid waste from household consists of plastic, paper, metal, textile, organic waste and many more. The variation of the compositions depends on the regions, lifestyle, and culture of the area. Figure 2.5 shows the composition of MSW reported in East Asia and Pacific, Europe and Central Asia, and North America.

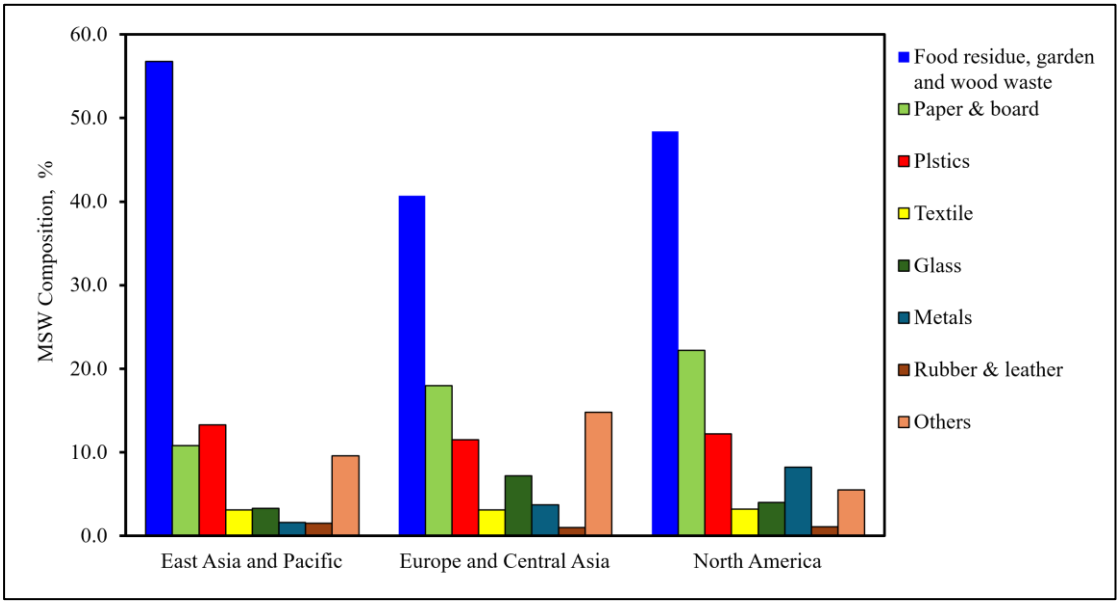

Figure 2.5 Composition of MSW in East Asia and Pacific, Europe and Central Asia, and North America

Source: (Cook et al., 2026)

The food residue, garden and wood waste are the most significant component in all three regions, with East Asia and Pacific having the highest (56.8 %) and the Europe and Central Asia the lowest (40.7 %). Paper and board are also major components, with Europe and Central Asia having the highest percentage (18 %). Plastics are present in all regions, with the East Asia and Pacific (13.3 %) having the highest share, while glass, metals, rubber, and leather are a substantial part of the waste stream only in all regions. The textile waste shows low percentage in MSW. However, the global per capita textile consumption has increased 7 to 13 kg, and 134 million tons of textile waste is expected to be produced by 2030. From the numbers, only 15–16 % of the textile waste generated each year is recycled (Singhal et al., 2023).

2.5.1 Textile Waste

Textile waste is considered as one of the potential feedstocks to be used as fuel. It is estimated about 2,000 tons of textile waste and other wearable has been discarded daily in Malaysia and about 5 % are dumped in landfilled (Kloth Care, 2019). Landfilling poses several drawbacks, including inefficient land use, leachate contamination (Huang et al., 2024) greenhouse gas emissions such as carbon dioxide (CO_2) and methane (CH_4) from the biodegradation of natural textiles, and limited effectiveness in managing non-biodegradable synthetic textiles (Mazibuko et al., 2019).

There are three types of material used to produce fabric which divided into natural materials (e.g. wool, cotton, silk, flax, hemp), synthetic materials (e.g. polyester, acrylic, nylon) and recycled materials (Shirvanimoghaddam et al., 2020). Among several types of textile waste, cotton stands out as a particularly promising candidate for sustainable valorisation through pyrolysis. Cotton, a natural cellulose-based fibre, has a high volatile content and calorific value, making it well-suited for thermochemical conversion processes (Esteve-Turrillas & Guardia, 2017). Unlike synthetic wastes, which may release toxic compounds such as dioxins and furans during pyrolysis, cotton undergoes cleaner thermal degradation yielding valuable products such as bio-oil (Nanda & Berruti, 2021).

Several studies reported on the characteristics of CFW such as proximate analysis, elemental composition via ultimate analysis and higher heating value (HHV). The proximate analysis shows that, the CFW contains 6.33 %, 34.33 % and 59.33 % of moisture, volatile matter and fixed carbon, respectively (Tujjohra et al., 2025). While the ultimate analysis reported by (Hanoğlu et al., 2019) shows cotton fabric exhibit 41.7 % carbon, 5.94 % hydrogen, 51.8 % oxygen and 0.575 % of nitrogen. Based on the reported findings, it shows that the cotton fabric material is suitable to use as feedstock for char production with high fixed carbon and high carbon content. However, the volatile matter also shows high (34.33%) which have potential to produce bio-oil products. The natural textile which rich in cellulose should behave like other biomass material during pyrolysis (Czajczyńska et al., 2017). The calculated average calorific value of these textile wastes was 22 MJ/kg which is greater than wood (Bagheri et al., 2020). Therefore, there is enormous potential in exploiting natural textiles from waste as low-cost feedstock for bioenergy production.

2.5.2 Plastic Waste

Plastic is considered as one of the most important innovations because of its essential properties, such as low cost, light weight, flexibility, durability, corrosion resistance, and high machinability (Sardon & Dove, 2018). The global use of plastics is expected to increase from 464 million tons in 2020 and up to 884 million tons in 2050. There is about 4725 million tons of plastics potentially accumulated in stock in 2050 since year 2000 (Dokl et al., 2024).

Most of the plastic waste is not biodegradable than other organic matters, thus landfill dispose is not a sustainable solution. The incineration is one of ways for plastic disposal but the release of toxic gas like dioxin and furans from this process is gain community concerns (Chang, 2018). Due to large benefits of plastic in daily life, especially on plastic packaging, pyrolysis process offers promising technology to convert harmful chemicals to value added products like biofuels. The MSW is composed mainly of lightweight plastic packaging materials, such as polyethylene (PE), polypropylene (PP) and polystyrene (PS) (Jeswani et al., 2021) and PP contributes the most plastic waste which is about 40 % among others (Adrados et al., 2012). Figure 2.6 shows the common types of plastic sources.

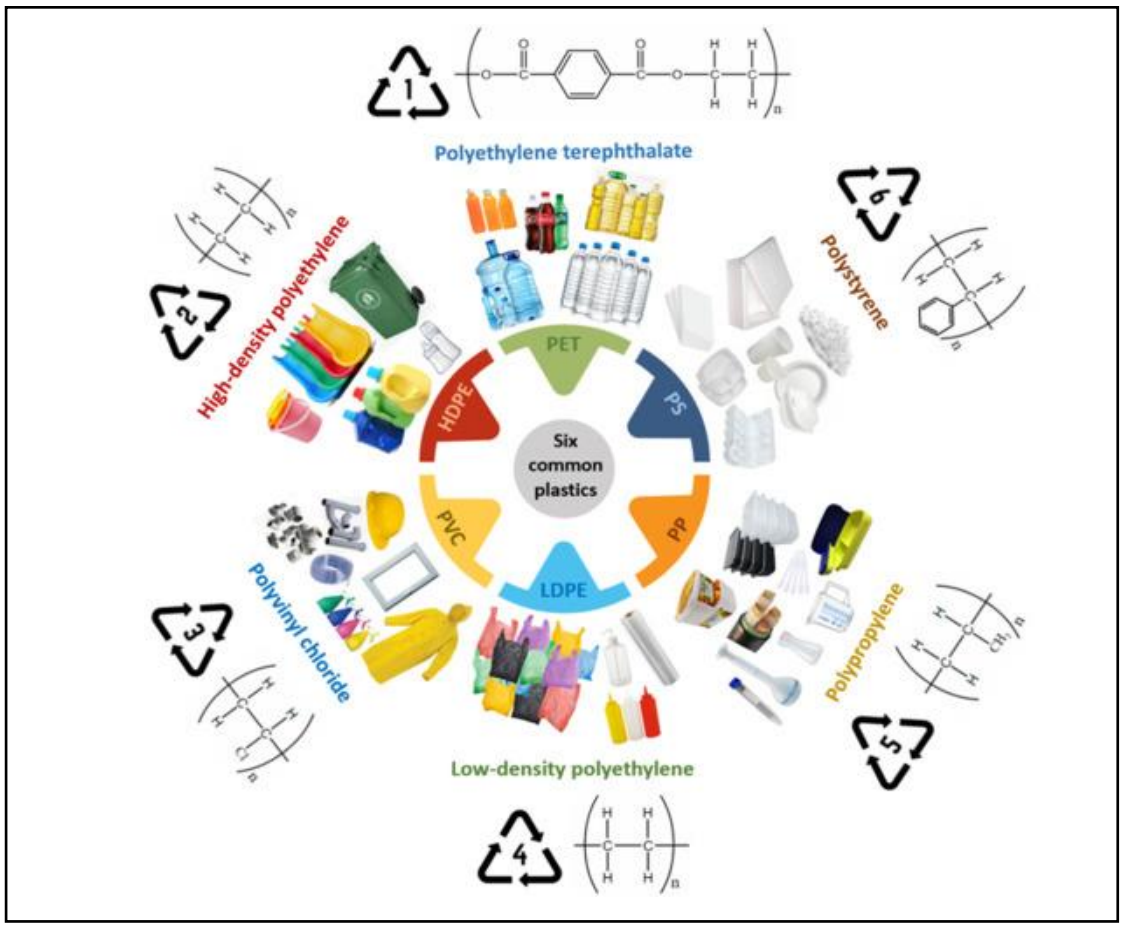

Figure 2.6 Common Type of Plastic Sources

Source: (Chang, 2023)

PP is the second most widely used plastic after PE, and it often ends up in landfills (Parku et al., 2020). PP is a thermoplastic polymer made from propylene monomers, and it has a soft surface with low friction (Uzoejinwa et al., 2018). PP poses characteristics of strong chemical and thermal resistance due to its saturated linear hydrocarbon chain structure. PP also reported to remain stable when exposed to acids or bases and shows high electrical resistance (Fivga & Dimitriou, 2018). These characteristics make PP versatile and are used in many applications such as packaging, furniture, and laboratory equipment.

The proximate analysis shows that PP exhibits remarkable higher volatiles matter (96.9 %) with exceptionally low fixed carbon (1.6 %). While CHNOS elemental analysis shows high in carbon (84.7 %), hydrogen (14.3 %), and incredibly low in oxygen (0.15 %), nitrogen (0.67 %), and sulphur (2.1 %). In addition, PP contains HHV that can reach 46.05 MJ/kg (Chang, 2023). With these characteristics, PP is suitable to be used as feedstock for bio-oil production via pyrolysis process. Thermal recycling of

PP can upcycle waste into liquid fuels and chemicals while reducing the carbon footprint (Chasioti & Zabaniotou, 2024).

There are many researchers that explored the conversion of plastic waste to biofuel and recently, the research has been extended to co-feed with biomass waste. The co-feeding plastic and biomass shows positive synergy to enhance production of bio-oil (Akancha et al., 2019; Al-Maari et al., 2021; Alam et al., 2020; Chen et al., 2016; Dewangan et al., 2016; Muelas et al., 2020). The plastic is rich in hydrogen, thus complementing the biomass drawbacks of high oxygen content with hydrogen to carbon effective ratio (H/C_{eff}) range between 0–0.3. Low H/C_{eff} contributes to more coke and low-quality bio-oil. With addition of plastic, it provides additional hydrogen for further biomass cracking (Shafaghat et al., 2019). Therefore, recycling PP waste with biomass in pyrolysis provide high advantage to improve biomass pyrolysis alone.

2.6 Catalytic Co-pyrolysis

2.6.1 Principle of Co-pyrolysis

Co-pyrolysis is a thermal decomposition process that involves the simultaneous conversion of two or more feedstocks under an inert atmosphere. Unlike single feed pyrolysis, where only one material such as biomass or plastic undergoes thermal degradation. Co-pyrolysis exploits the interactions between different feedstocks to produce improved product yields and qualities (Sharma et al., 2023). The combination of biomass and plastics has attracted considerable attention because it not only addresses challenges in waste management but also enhances the overall efficiency of energy recovery through interactions between the two materials (Bhushan et al., 2025). Other advantages include reduce cost by eliminating the additional treatment of the bio-oil (Han et al., 2014), less carbon emission than fossil fuels (Uzoejinwa et al., 2018), recover essential chemicals and reduced fossil fuels dependency (Yaman et al., 2021).

H/C_{eff} is used as indicator to explain the amount of hydrogen in the specific compound. Table 2.3 shows the elemental analysis of several biomass, plastics and mixture of biomass-plastics used in pyrolysis.

Table 2.3
Elemental Analysis of Several Biomass, Plastic and Mixture Used in Pyrolysis

Biomass/Plastic	Elemental analysis, %						References
	C	H	O*	N	S	H/C_{eff}	
Cotton textile	41.69	5.94	51.80	0.57	0	0	(Hanoğlu et al., 2019)
Flax waste	42.5	6.9	50.6	0	0	0.16	(Wang et al, 2021)
Pine sawdust	48.12	6.09	45.4	0.25	0.14	0.1	(Xue et al., 2018)
Yellow poplar	47.8	6.3	45.8	0.2	0	0.14	(Park et al., 2018)
PP	85.7	14.3	0	0	0	2	(Ryu et al., 2020)
HDPE	85.4	14.6	0	0	0	2.05	(Park et al., 2018)
LDPE	86.35	13.58	0	0	0.074	1.89	(Zheng et al., 2020a)
Walnut shell /LDPE	66.7	9.5	20.1	0.3	0.2	1.24	(Yu et al., 2021)
Moringa oleifera /waste face mask	65.56	11.43	12.14	9.14	1.73	1.44	(Tamilarasan et al., 2024)

Note: PP (Polypropylene), HDPE (High density polyethylene), LDPE (Low density polyethylene).
O*: calculated by equation.

Biomass usually poses H/C_{eff} <0.3 indicates hydrogen deficient and hardly obtains quality bio-oil. On the other hand, if H/C_{eff} >1 shows the feedstock contains enough hydrogen for selective reaction and produces quality bio-oil. H/C_{eff} of plastic is higher than 1, which is suitable to mix with biomass for bio-oil enhancement (Ahmed et al., 2020). The H/C_{eff} result indicates that biomass is hydrogen deficient and plastic is hydrogen rich material. Thus, plastic can be used as hydrogen donor in biomass pyrolysis.

Biomass and plastic have different thermal degradation behaviours. Thermal analysis showed that holo-cellulose biomass degraded at 220 °C – 400 °C, while plastic occurs at higher temperature (420 °C – 520 °C) (Esso et al., 2022; Seah et al., 2023). Despite the distinct thermal degradation ranges of biomass and plastics, synergistic interactions occur through overlapping reaction environments and secondary radical-mediated processes. During decomposition of the biomass, plastic is in its melted state and some interaction between biomass and melted plastic may occur (Esso et al., 2022). Melted plastic provides hydrogen to biomass. The volatiles released from biomass contains radicals that can abstract hydrogen from plastic. The positive synergetic was reported to occur at 500 °C – 550 °C in co-pyrolysis of sugarcane leaves (SCL) and LDPE (Charusiri et al., 2022).

The synergistic interaction of biomass and plastic can be explained by two step mechanisms: (1) the free radicals generated from the pyrolysis of biomass initiate the β-scission of the polymers, inhibiting the intermolecular and intramolecular H transfer, producing aliphatic hydrocarbons and reduced alkadienes; (2) the H transfers from the polymers reacting with the biomass-derived radicals to form stable compounds (Wee et al., 2023). This mechanism accelerates biomass decomposition and significantly lowers char yield (Gowda et al., 2025). During early stage at lower temperature, biomass releases many reactive radicals during its decomposition, which accommodate the scission of plastic chain. Thus, the synergistic interaction between biomass free radicals and the product from plastic pyrolysis leads to effective cracking of long polymer chains (Supramono et al., 2020; Xu & Zhu, 2023).

Moreover, the interaction of biomass and plastic during co-pyrolysis process can be elucidated via TGA (Alam et al., 2020). During co-pyrolysis, biomass started to decompose early from 250–350 °C and the molten plastic restricted the volatile from biomass to be released. When the temperature gradually increased to 550 °C, observed more degradation occurred and stabilized above 550 °C indicating complete degradation of the blends (Sophonrat et al., 2018). At extremely elevated temperatures, accelerated pyrolysis and reduced hydrogen donation weaken the interaction effect, promoting condensation and aromatization. These conditions also favour cracking of oxygenated compounds, increasing gas yield while reducing carbon yield of petrochemical formation (Zhang et al., 2014). The interaction of biomass and plastic can be explained by illustration in Figure 2.7.

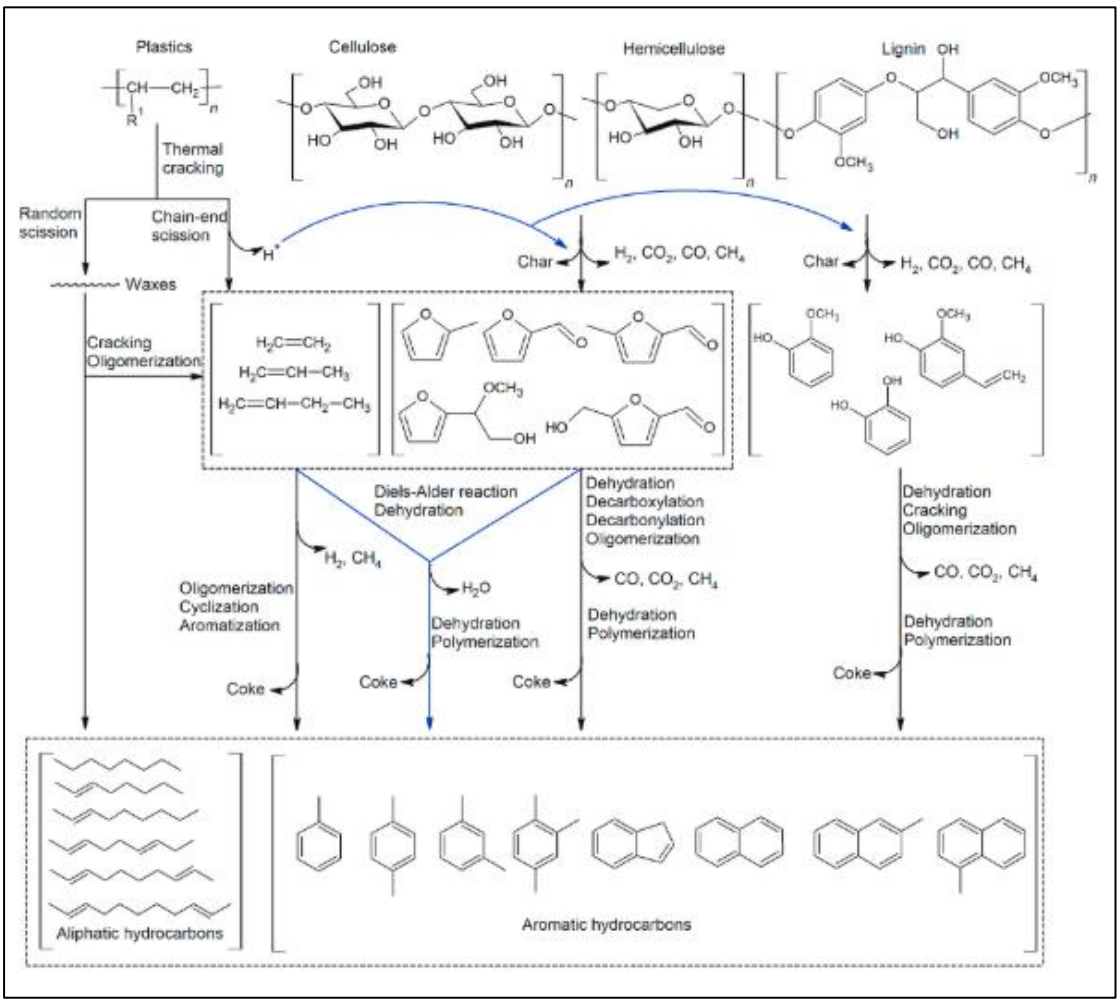

Figure 2.7 Plausible Reaction Mechanism During Co-Pyrolysis of Biomass and Plastic

Source: (Zhang et al., 2016)

Wee et al., (2024) investigated the synergistic co-pyrolysis of oil palm empty fruit bunches (EFB) and surgical face mask (SFM) wastes using TGA. The differences between experimental and theoretical values (ΔW_{TGA} and ΔW_{DTG}) were calculated at EFB:SFM ratios of 4:1, 1:1, and 1:4. The results showed that the 1:1 ratio exhibited positive synergy within the temperature range of 180–320 °C, indicating that sufficient hydrogen from SFM enhanced the degradation rate. Similarly, Jamaluddin et al., (2026) reported that a 50:50 mixture of coffee grounds (CG) and polypropylene (PP) produced the most pronounced synergistic effect during co-pyrolysis. A negative synergy in bio-oil yield was observed at a lower PP content (25%), accompanied by increased gas production. This indicates that secondary interactions between CG and PP derived volatiles influence product distribution depending on the feedstock ratio. The

synergistic interaction promotes higher hydrocarbon formation through the interaction of biomass-derived radicals with hydrogen-rich species from PP.

2.6.2 Bio-oil Upgrading using Catalyst

Biomass pyrolysis alone often produces low-quality bio-oil due to its high oxygen content, acidity, viscosity, and low heating value (Aghamiri & Lahijani, 2024). Introducing hydrogen-rich materials such as plastics improves both yield and hydrocarbon formation (Park et al., 2018). This improvement occurs because bio-oil upgrading relies on reducing oxygenated compounds through deoxygenation reactions such as dehydration, decarboxylation, and decarbonylation in the presence of catalysts (Ahmed et al., 2020). As a result, desirable HC are formed while water (H_2O), carbon dioxide (CO_2), and carbon monoxide (CO) are released as by-products (Terry et al., 2021). The reaction involved in catalytic upgrading of bio-oil is shown in Table 2.4

Table 2.4
Reaction Involved in Catalytic Upgrading of Bio-oil (Mortensen et al., 2011)

Reaction type	Reactant structure	Product structure
Cracking	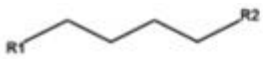	
Decarbonylation	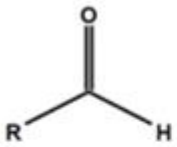	
Decarboxylation	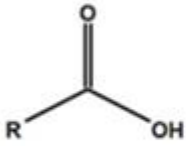	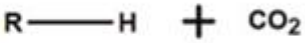
Hydrocracking	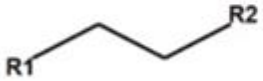	
Hydrodeoxygenation		
Hydrogenation		

Plastics supply the necessary hydrogen pool for stabilizing oxygenated intermediates from biomass, which enhances hydrocarbon production during co-pyrolysis (Hassan et al., 2019). PP, LDPE, and HDPE are particularly suitable, as their hydrogen content reaches 13–14 wt.% (Table 2.3). With these feedstocks, the heating value of upgraded bio-oil increases to about 30–40 MJ/kg, approaching that of petro-diesel (42–46 MJ/kg) (Kusrini et al., 2018).

Catalytic co-pyrolysis offers further advantages over thermal processes. The interaction between biomass and plastics, together with catalytic activity, directs selective reactions and prevents undesirable by-products (Lu et al., 2025). Plastics promote deoxygenation of biomass-derived compounds, while oxygenates from biomass suppress heavy wax formation typical of plastic pyrolysis (Kanduri & Seethamraju, 2023). Catalysts enhance macromolecular cracking, yielding light hydrocarbons and aromatics, while reducing toxic substances and non-condensable (Sekyere et al., 2023). This interaction produces bio-oil with lower oxygen content, improved stability, and higher energy value, making it suitable for fuel and chemical applications.

During the process, vapours from biomass and plastics first undergo co-pyrolysis and then catalytic cracking. On the catalyst surface and within its pores, lighter hydrocarbons are formed through selective pathways that lower the energy demand of decomposition. Oxygenated organics are converted into hydrocarbons via deoxygenation, cracking, oligomerization, and aromatization (Suriapparao & Tejasvi, 2022). The catalyst also drives secondary reactions that improve the selectivity of desired products (Hassan et al., 2019). In this way, catalytic co-pyrolysis establishes itself as a sustainable, efficient, and selective approach for valorising biomass and plastic waste (Li et al., 2024).

2.7 Heterogeneous Catalysts for Co-pyrolysis

Catalytic co-pyrolysis of biomass with plastics demonstrates clear benefits compared to conventional thermal pyrolysis. The interaction of the two feedstocks plays a crucial role which are the hydrogen-rich plastics provide additional hydrogen to drive deoxygenation reactions, while oxygen-containing biomass intermediates suppress the formation of heavy waxes during polymer breakdown (Gomes et al., 2025; Kanduri & Seethamraju, 2023). The use of catalysts further enhances these interactions by

facilitating cracking of large molecules, thereby increasing the yield of light HC and aromatic HC and simultaneously lowering the release of harmful by-products and gas emissions (Li et al., 2024). Thus, the bio-oil exhibits higher stability, and possesses superior fuel and chemical qualities. Heterogeneous catalysts have gained wide attention due to their advantages over homogeneous systems. They can be reused, are simple to separate from the product, do not corrode equipment, minimize contamination of the oil, reduce operational expenses, and maintain high selectivity while being environmentally benign (Al-Salem et al., 2017). The subsequent section highlights several heterogeneous catalysts that are frequently applied in pyrolysis. Figure 2.8 shows the interaction between biomass, plastic, and catalyst in the catalytic co-pyrolysis process.

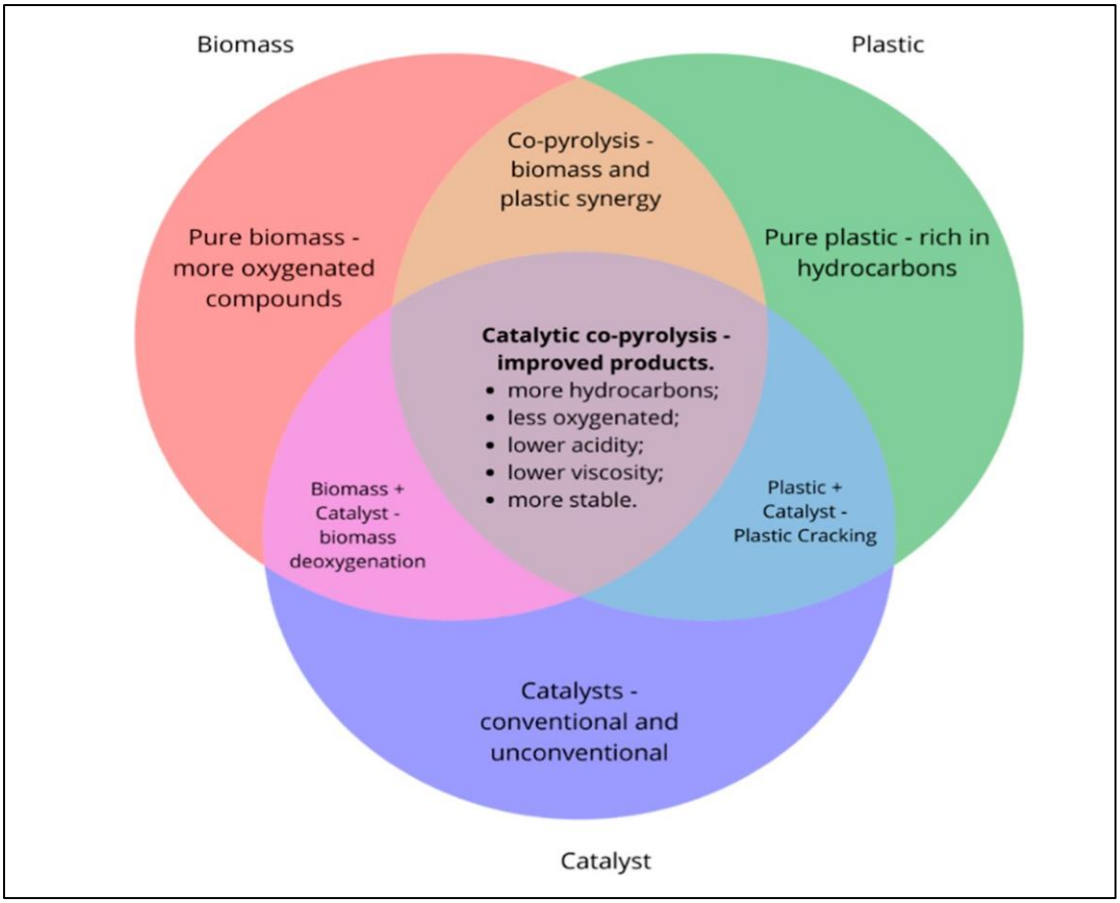

Figure 2.8 Interaction Between Biomass, Plastic and Catalyst in The Catalytic Co-Pyrolysis Process

Source: (Gomes et al., 2025)

2.7.1 Role of Catalysts in Bio-oil Upgrading

Catalytic co-pyrolysis has been widely recognized for its ability to enhance selectivity and yield of high-value hydrocarbons. This improvement arises from the capacity of catalysts to control reaction pathways, tailor mechanisms, and accelerate reaction kinetics. Catalysts promote several key reactions that improve bio-oil quality. Deoxygenation occurs through hydrodeoxygenation, decarboxylation, and decarbonylation, removing oxygen in the form of H_2O, CO, or CO_2 (Tan et al., 2024). Catalysts also facilitate cracking reactions, breaking down large oxygenates and polyolefin molecules into lighter hydrocarbons with higher fuel value (Zhang et al., 2023). Furthermore, hydrogenation and hydrodeoxygenation (HDO) reactions saturate double bonds and eliminate oxygen with hydrogen, resulting in more stable products (Kim et al., 2024). Additional reactions such as aromatization and isomerization convert unstable oxygenates into stable aromatic and branched hydrocarbons, which are desirable for fuel applications (He et al., 2023).

The use of appropriate catalysts not only reduces the oxygen content in bio-oil but also improves its chemical stability, making it more comparable to conventional fossil fuels. This catalytic action decreases the formation of undesirable by-products, reduces acidity, viscosity, and minimizes solid residue generation. Therefore, enhancing the suitability of bio-oil for refining and industrial applications (Alcazar-Ruiz et al., 2023). Catalysts also lower the activation energy required for pyrolysis, accelerating decomposition and improving both yield and quality of the resulting oil. Different catalysts exhibit selective effects on product distribution, which increase HC content and enrich high-value compounds in bio-oil. Thus, improves the overall economic feasibility of biomass pyrolysis (Qiu et al., 2022). These catalytic functions are particularly important when applied to biomass and plastic co-pyrolysis, where synergistic effects between feedstocks and catalysts determine the efficiency and value of the final products. To achieve an efficient deoxygenation process, metal oxides catalysts have been widely employed (Kariim et al., 2023).

2.7.2 Metal Oxides Catalyst

Metal oxides play a crucial role in biomass pyrolysis due to their unique catalytic functionalities, which influence the composition and stability of bio-oil. Their wide

availability, cost-effectiveness, and non-toxic nature make them attractive catalysts for bio-oil upgrading (Sun et al., 2025). Metal oxide is solid catalyst and extensively use as active phase or support for various organic reaction (Ooi et al., 2019). Their inherent properties, such as surface acidity, redox activity, and high thermal stability, promote cracking, deoxygenation, and hydrocarbon formation (Ouedraogo & Bhoi, 2020). It presents sufficient porosity, high dispersion, good adsorption and anti-carbon deposition (Zheng et al., 2022). These characteristics allow large molecule to penetrate and be converted into small volatiles (Gholizadeh & Hu, 2022).

There are three classification of oxide-based catalyst that commonly reported in catalytic pyrolysis which are acid catalyst, basic catalyst and transition metal catalyst (Tawalbeh et al., 2021). Metal oxides can be classified as alkali metal oxides (MgO, CaO), acidic metal oxides (Al_2O_3, SiO_2 and Al_2O_3–SiO_2), transition metal oxides (ZrO_2, ZnO, NiO, TiO_2, Cr_2O_3, Fe_2O_3). The classification of the metal oxide is shown in Figure 2.9 Each of metals poses its unique characteristics to be selective on different targeted product.

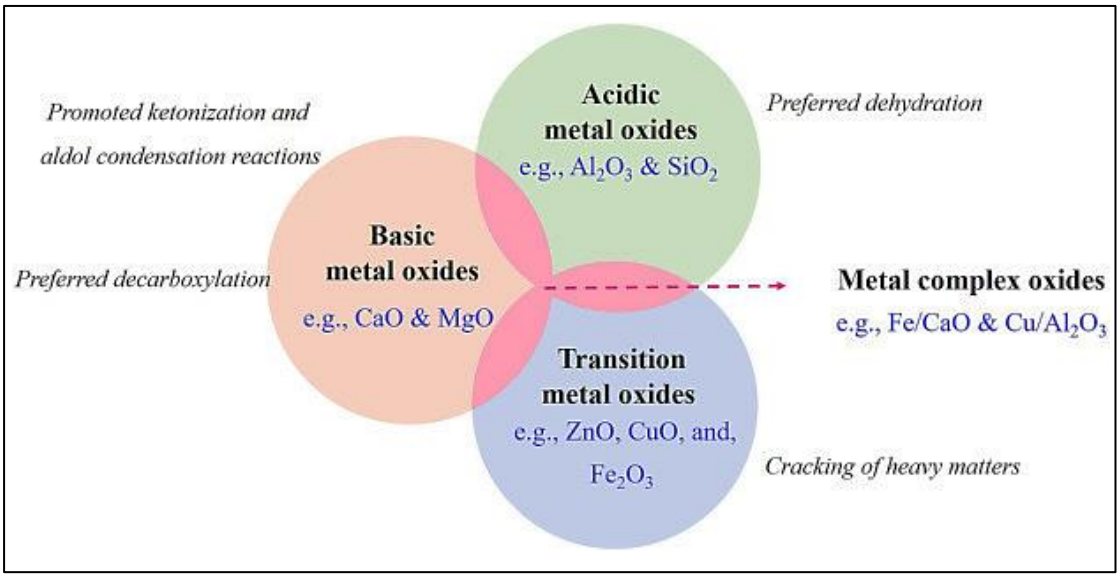

Figure 2.9 Classification of Metal Oxide

Source: (Chen et al., 2019)

Acid catalysts such as Al_2O_3 shows the most investigated acidic metal oxide and widely use in cracking and deoxygenation during pyrolysis. Their Lewis and Brønsted acid sites promote the cleavage of C–O and C–C bonds, leading to a reduction in oxygenated compounds and an increase in hydrocarbon and aromatic selectivity (Zheng et al., 2020). Moreover, acid catalyst cush as Al_2O_3 and SiO_2, promoted the formation

of tar. The acidic oxides could help to promote polymerization and cracking reactions (Zhang et al., 2018). Acid catalysts such as Al_2O_3 have high catalytic activity, specific surface area, temperature resistance, and superior dispersion make it suitable to be used as metal support. According to Ooi et al., (2019), Al_2O_3 support has been widely used in deoxygenation reaction with various metal including noble metal and transition metal in different feedstocks. The activity and stability of metal supported catalyst is strongly affected by the support acidity and interaction between metal support (Yoon et al., 2019).

Basic metal oxides such as calcium oxide (CaO) and magnesium oxide (MgO) have been extensively applied in biomass pyrolysis and co-pyrolysis due to their ability to neutralize acidic intermediates and promote carbon–carbon coupling reactions. Basic sites catalyse aldol condensation, ketonization, and ketylation reactions, which effectively remove oxygen from pyrolysis vapours while conserving hydrogen in the liquid product. This pathway predominantly generates CO_2 rather than CO, which is more efficient in terms of carbon and hydrogen retention within the bio-oil (Kalogiannis et al., 2018; Sun et al., 2025). The role of CaO is particularly well-documented. CaO catalysts selectively remove carboxylic acids and phenolics, reducing acidity and enhancing the hydrocarbon fraction in the oil (Chen et al., 2017). In co-pyrolysis studies, Ni–CaO composites have been shown to significantly improve oil quality by reducing acid number and enhancing calorific value (Lin et al., 2018). Similarly, MgO has been observed to increase alkene selectivity and reduce aldehyde and ketone contents, contributing to higher energy density oils. Recent work has also shown that CaO can increase alcohol content while reducing oxygenates, further stabilizing bio-oil composition (Tamilarasan et al., 2024). Overall, basic oxides are effective for stabilizing bio-oils by reducing oxygen content, acidity, and water formation, making them valuable for improving fuel quality. However, their cracking efficiency is typically lower than acidic oxides, often resulting in heavier product distributions.

Transition metal oxides, including those of nickel (NiO), titanium (TiO_2), cobalt (Co_3O_4), cerium (CeO_2), iron (Fe_2O_3), and manganese (MnO_2), offer unique catalytic behaviour due to their multiple valence states and redox properties. These features allow them to participate in oxidation-reduction cycles, hydrogen transfer reactions, and selective cracking, making them highly versatile in pyrolysis and co-pyrolysis systems (Sun et al., 2025). Different transition metals impart distinct effects on product distribution. For instance, TiO_2 and NiO have been shown to suppress excessive

cracking, thereby increasing tar or heavy oil yields. Co, V, and Mn-based oxides promote the formation of heavier oils, whereas Ni, Ce, Cr, Cu, and Fe-based catalysts favour lighter oil fractions (Zhang et al., 2019). The redox activity of these oxides enhances deoxygenation efficiency and enables the production of alcohols, ketones, furans, and phenolics, contributing to a diversified product profile. Figure 2.10 shows the bio-oil yield and product selectivity for different transition metal oxides.

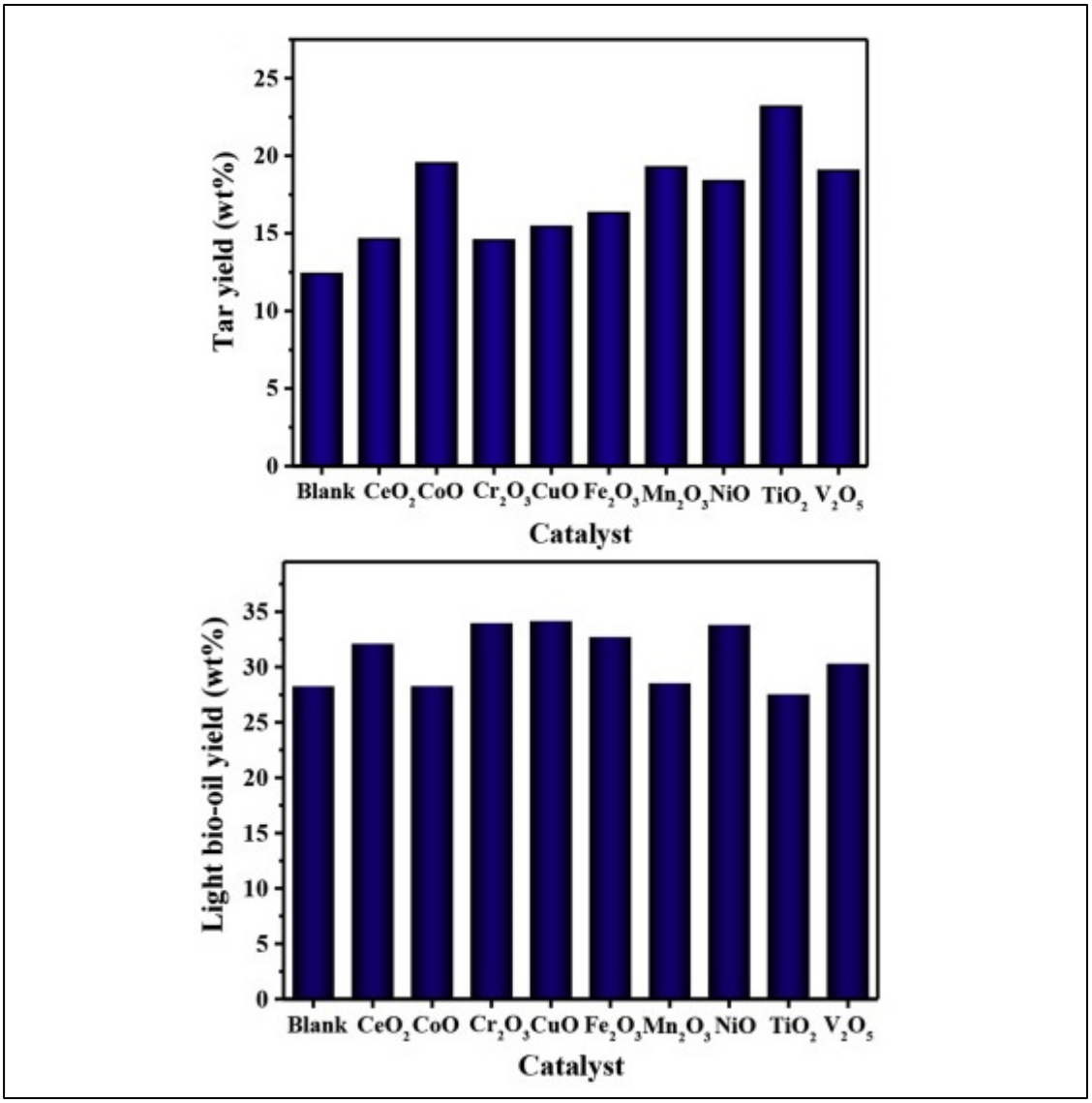

Figure 2.10 Bio-Oil Yield and Product Selectivity for Different Transition Metal Oxides

Source: (Zhang et al., 2019)

Bifunctional and mixed metal oxides integrate acidic, basic, or redox properties into a single material, thereby overcoming the limitations of individual oxides. Spinel-type catalysts, such as MgCr, MgAl, and MgFe oxides, exemplify this approach. These

materials combine basic properties from MgO with redox or structural modifications from trivalent metals (e.g., Al, Cr, Fe), resulting in enhanced surface area, pore structure, and multifunctional catalytic activity (Atanda et al., 2021). MgCr spinel oxides, for example, demonstrate effective deoxygenation while maintaining high aromatic HC yields, attributed to their high surface area and large pore volume. Similarly, MgFe and MgAl spinels have shown strong potential in deoxygenation and carbon efficiency during pyrolysis of lignocellulosic biomass (Atanda et al., 2020). When supported on zeolites such as ZSM–5, these mixed oxides further enhance cracking and aromatic conversion by combining mesoporous accessibility with microporous shape-selectivity. Several transition metals (Ce, Co, La, Pd, Mo, Ni, Ru) supported on Al_2O_3 showed that Pd/Al_2O_3, Ce/Al_2O_3, and Ni/Al_2O_3 were most effective in promoting deoxygenation. Additionally, the catalysts have potential to reduce PAHs formation, highlighting their advantage for bio-oil upgrading (Kaewpengkrow et al., 2017). The synergistic action of bifunctional oxides results in improved oil yield, higher selectivity to aromatics, reduced acidity, and enhanced overall stability of bio-oil. These advantages make them highly attractive for industrial applications where balanced performance between yield and oil quality is required.

2.7.3 Industrial Solid Waste Catalyst in Pyrolysis and Co-pyrolysis

The utilization of industrial solid waste (ISW) as a source of catalysts has received increasing attention due to its low cost, high abundance, and intrinsic catalytic properties. Many ISW streams such as red mud (RM), fly ash (FA), steel slag (SS), aluminium dross (AD), and sludge contain valuable metal oxides including Fe_2O_3, Al_2O_3, CaO, TiO_2, MgO, and SiO_2. These oxides act as active sites for cracking, hydrogen transfer, and oxygen removal (Qiu et al., 2022; Wang et al., 2022). Unlike synthetic catalysts, ISW provides an environmentally friendly alternative by valorising hazardous residues while simultaneously upgrading biomass-derived fuels. Furthermore, ISW-based catalysts can be applied directly after pretreatment (calcination) or used as precursors to synthesize tailored catalytic materials such as zeolites (Hassan et al., 2019) and biochar catalyst (Ma et al., 2023).

Several studies have been conducted using various ISW as catalyst. Ahmed et al., (2022) studied the effect of RM incorporated with ZSM catalyst. RM is a waste material which is rich in Fe generated from Bayer process. The findings show that it exhibits higher catalytic activity than mesoporous ZSM. The combination causes tuning the acid site and

basic sites, which promotes both dehydration and decarbonylation as well as the H/C_{eff} of oil to 1.28, thus making it as compatible fuel.

Hassan and Hameed (2023) reported that using hydroxyapatite-zeolite (HAP-ZE) catalyst prepared from steel waste in co-pyrolysis was able to produce 71.19 % of bio-oil yield with favour the production of hydrocarbon, alcohol and inhibit acid production. The presence of CaO, SiO and Al_2O_3 as bifunction catalyst promote deacidification of bio-oil via neutralization, thermal cracking, and catalytic cracking. SB and HDPE intermediates, and the deoxygenation reaction of SB- derived oxygenates with HDPE-derived free radical via hydrogenation and dehydration reactions over its active sites.

Other study by Kamil et al., (2017) showed that the bio-oil produced from modified AD has better bio-oil yield than untreated AD. It was also reported that the increase in bio-oil was possibly attributed to the active metal which mainly contains Al_2O_3 and Fe_2O_3 and after acid treatment which improve acidity and textural properties of the catalyst. Furthermore, the same author explored the use of molten slag (MS) as catalyst in pyrolysis of waste cooking oil. Similar findings were observed, where MS with acid washing resulted in increased of bio-oil yield and the bio-oil was selective to low carbon number (Kamil et al., 2020). The improvement is observed due to the increased acidity of modified catalyst with increased Fe_2O_3 active metal (94.7 %) compared to raw MS.

Industrial sludge, a by-product of wastewater treatment and metallurgical processes, has emerged as a promising ISW catalyst. Sun et al., (2020) demonstrated that sludge-derived char could enhance plastic pyrolysis, increasing monocyclic aromatic selectivity up to 75.3 %. The catalytic effect is attributed to the ash components, which promote aromatization of chain hydrocarbons while limiting condensation of heavier aromatics. Acidic sites such as aluminium phosphates and dehydrogenation-active species (P=O groups and sulphides) facilitate dehydrogenation, hydrogen transfer, and Diels–Alder reactions. Meanwhile, basic, and redox-active species like CaO and Fe compounds assist in hydrogenation and ring-opening, thereby preventing excessive polyaromatic formation. Table 2.5 shows the types of ISW used as catalyst in pyrolysis. Furthermore, Table 2.6 summarizes the advantages and limitations of several reported heterogeneous catalysts that would justify the new catalyst in this work.

Table 2.5
ISW Type Used as Catalyst in Various Appication

Type of ISW	Sources	Metal	Application	Yield/selectivity	References
Red mud	Bayer process for aluminium production	Fe_2O_3, Al_2O_3, TiO2, and CaO	Bio-oil production (co-pyrolysis)	65.7 % HC	(Ahmed et al, 2022)
Coal fly ash	Coal combustion in thermal power plants	SiO_2 and Al_2O_3	HC rich bio-oil yield (co-pyrolysis)	84.02 % hydrocarbons	(Padil et al., 2025)
Molten slag	Iron and steel making	CaO, Fe, and silicates	Bio-oil production (co-pyrolysis, pyrolysis)	71.19 % bio-oil, 16 % bio-oil	(Hassan & Hameed, 2023), (Kamil et al., 2020)
Aluminium dross	Primary and secondary aluminium production	Al_2O_3 and other oxides	Bio-oil production (pyrolysis)	14.9 % bio-oil	(Kamil et al., 2017)
Industrial sludge	Wastewater treatment plant, electroplating	Fe, Cu, Ni, Sludge biochar	H_2 production and HCl removal (pyrolysis), aromatic from plastic waste (pyrolysis)	42.18 % of H_2, 80–85 % HCl removal, 75.3 % aromatic selectivity	(Jia et al., 2025), (Sun et al., 2020)

Table 2.6
The Advantageous and Limitations of Various Heterogeneous Catalyst to Produce Bio-oil in Biomass Pyrolysis and Co-pyrolysis

Catalyst	Feedstock	Operating Conditions	Advantageous	Limitations	Remarks	References
CaO	Moringa oleifera (MO) and waste face mask (WFM)	[a]450 °C, [b]15 °C/min, [c]15 min, [d]Na, [e]0.2:1	High bio-oil yield (52%) compared to MO alone and reduce oxygenates and acid.	Selective to alcohol than hydrocarbons	Using commercial catalyst, reusability not reported	(Tamilarasan et al., 2024)
(MgO, NiO, Bi_2O_3, CuO, ZnO)–Al_2O_3 (Synthesis: wet impregnation)	Sawdust	[a]550 °C, [b]35 °C/min, [c]60min, [d]N_2, [e]1:6	Highest HC produced using Bi_2O_3–Al_2O_3. MgO–Al_2O_3 produced highest phenol.	Low bio-oil yield	Reusability not reported, focus on phenol, HC and aromatic HC.	(Singh et al., 2023)
Ga–ZSM-5, Co–ZSM-5, Cu–ZSM-5, Fe–ZSM-5 and Ni–ZSM-5	Sawdust/Polystyrene plastic	[a]500 °C, [b]10 °C/min, [c]20 min, [d]N_2, [e]2:1	The addition of metal oxides on ZSM-5 has increased bio-oil yield up to 68% (Co-ZSM-5) and increase aromatic HC with the highest of >70% (Fe-ZSM-5)	Reduce surface are and pore volume.	Reusability not reported.	(Dyer et al., 2022)
USY (5.3) USY (11)	Flax waste (textile), Polyethylene (PE), polypropylene (PP)	[a]650 °C, [b]10 °C/ms, [c]20 s, [d] NA, [e]1.5:1	Furan intermediate was promoted almost 6 times using USY catalyst compared to non-catalytic pyrolysis and co feed with PE (20 %) shows highest aromatic HC selectivity (81.9%).	Small pore diameter could promote pore blockage	Using commercial catalyst, reusability not reported.	(Wang et al., 2021)

Catalyst	Feedstock	Operating Conditions	Advantageous	Limitations	Remarks	References
Pd, Ni, Ce, Ru, La, Co, Mo (5wt%)–Al_2O_3 (synthesis: wet impregnation)	Jathropha curcas	[a]600 °C, [b] NA, [c]30s, [d] He, [e]10:1	Tremendous reduction of oxygenate compounds (73 % to 10 %) using catalyst. >70 % conversion to HC with metal/catalyst. <2 % PAH was obtained.	High catalyst utilization is not cost effective	Using commercial catalyst, reusability not reported.	(Kaewpengkrow et al., 2017)
Ce, Co, Cr, Cu, Fe, Mn, Ni, Ti, V–oxides (Synthesis: Solgel)	Poplar wood	[a]500 °C, [b] NA, [c]30min, [d] N_2, [e] NA	Max. tar yield is 25 % produce by TiO_2. Cr, Cu, Ce, Fe, Ni-oxides promotes light bio-oil.	Low bio-oil yield on single metal oxides.	Reusability not reported.	(Zhang et al., 2019)
HZSM	Palm empty fruit bunches (EFB) and surgical face mask (SFM)	[a]500 °C, [b] 10,20,50,100 °C/min, [c] NA, [d]N_2, [e]10:1	The catalytic activities show achieving high reduction of activation energy and difference in enthalpy of 13.54 % and 14.94 %, respectively.	High catalyst utilization is not cost effective	Reusability not reported.	(Wee et al., 2024)
MgB_2O_4 B= Fe, Al, La, Y, Ga, Cr (Synthesis: HT)	Wheat straw	[a]500 °C, [b] NA, [c] NA, [d]N_2, [e]1:3	$MgCr_2O_4$ the most effective in oxygen removal relative to quality of bio-oil produced. Promote highest AH and lower oxygen content in bio-oil. MgCr, MgAl, MgFe, MgY, MgGa produce among highest HHV (28-32 MJ/kg)	Low aromatic product	Reusability not reported.	(Atanda et al., 2021)

Catalyst	Feedstock	Operating Conditions	Advantageous	Limitations	Remarks	References
(Ca, Mn, Fe, Co, Ni, Zn)–Al_2O_3 (Synthesis: co-precipitation)	Sugar beet pulp	[a]550 °C, [b] NA, [c] 10 min, [d]He, [e]1:10	Ni–Al_2O_3 produced highest HC yield (25.26 %) and moderate aromatic HC yield.	Moderate HC yield and high acidity	Reusability not reported.	(Özbay et al., 2025)
(W, Al, Mn)–NbO (Synthesis: citrate gel method)	Beechwood chip	[a]500 °C, [b] NA, [c] NA, [d]N_2, [e]1:1	All modified catalyst modified chemical composition and lower the oxygen content in bio-oil. Mn-NbO performance closed to HZSM although poses different properties.	Moderate acidity and low aromatic HC.	Reusability not reported.	(Locatel et al., 2021)

Note: [a] Pyrolysis temperature, [b] Heating rate, [c] Pyrolysis time, [d] Sweeping gas, [e] Catalyst-to-feedstock ratio. HT (hydrothermal), NA (not available)

2.8 The Basis for Metal Selections (Cr, Ti, Al)

Based on literature studies, various metals were considered as options in the synthesis of catalyst in this work. Several works reported on chromium-based catalysts to be actively used for hydrocarbon and bio-oil production. Cr–Al_2O_3 has well established in hydrogenation reaction of alkanes and has been commercialized in industry (Weckhuysen & Schoonheydt, 1999). Zhang et al., (2019) reported Cr_2O_3 was able to produce higher bio-oil yield compared to non-catalytic bio-oil specially to promote light hydrocarbon. Furthermore, Cr_2O_3 is thermally stable under reductive atmosphere. In work reported by Atanda et. al., (2021) showed the addition of Cr in spinel-based catalyst poses higher aromatization capability and lower oxygen content compared to other tested. Smirnov et. al., (2019) found adding Cr additive in Ni-SiO catalyst increase the activity of hydrodeoxygenation of anisol conversion due to high acidity and increase corrosion resistance. Carriel Schmitt et. al., (2019) observed the higher strength of acid site in Ni-Cr catalyst promoted conversion of beech wood to ketones, organic acids, sugars and alcohols in fast pyrolysis bio-oil hydrotreatment.

Titanium oxide is a reducible oxide with good chemical stability, zero toxicity and low cost (Ooi et al., 2019). TiO_2 is well known for its strong metal support interaction properties and poses high oxophilicity that is capable of facile oxygen abstraction. Thus, it is suitable for deoxygenation activity (Kay Lup et al., 2017). The TiO_2 also shows good conversion of poplar wood to heavy oil with minimal coke formation and has high thermal stability (Zhang et al., 2019). The deoxygenation activity also observed higher using ex-situ configuration on cellulose pyrolysis (Ida et al., 2020). Fan et al., (2020) reported on HZSM5 modified with various Ti-species for catalytic activity. The results show that TiAH5 (anatase species) actively converts biomass to gasoline additive while Ti3H5 actively become diesel additive bio-oil. Terry et al., (2023) reported that Ni-Mo/TiO_2 and Ni/Al_2O_3 catalysts enhanced hydrocarbon production due to their high acidity, which promoted deoxygenation, cracking of oxygenated compounds, and PP decomposition during catalytic co-pyrolysis.

Aluminium oxide has been reported to show high catalytic activity, poses high specific surface area, temperature resistance and superior dispersion (Ooi et al., 2019). These characteristics allowed Al_2O_3 to be functional as active phase and support. Atanda et al., (2020) combined Al_2O_3 with spinel-ZSM5 and found Al_2O_3 provides well balanced deoxygenation degree and producing bio-oil with acceptable carbon

efficiency. In the study reported by Zhang et al., (2018) showed Al_2O_3 provide significant production of tar due to catalyst acidity compared to basic catalyst. Kaewpengkrow et al., (2017) reported Al_2O_3 as catalyst and support in deoxygenation activity of physic nut residue. Various transition metal/Al_2O_3 catalyst were evaluated, and result showed the deoxygenation activity was the highest at higher Jathropa: catalyst ratio (1:10) of Al_2O_3 catalyst and metal/Al_2O_3. The study indicates the oxygenates compound had reduced significantly. The addition of transition metal on Al_2O_3 support promotes aromatic besides hydrocarbon, while Al_2O_3 catalyst active in cracking activity. Iliopoulou et al., (2023) investigated the use of Al_2O_3 and Mn–Al_2O_3 supported catalysts in the catalytic pyrolysis of olive mill waste for bio-oil production. The incorporation of Al_2O_3 either as a catalyst or support, improved bio-oil quality by enhancing deoxygenation, resulting in less than 3% oxygen in the organic phase and reduced acidity. In contrast, Wang et al., (2020) reported that the pyrolysis of polycarbonate using a Fe–Ce–Al_2O_3 catalyst predominantly produced monoaromatic hydrocarbons (MAHs) and phenolic compounds in the bio-oil. Tang et al., (2025) reported Ni/CaO–Al_2O_3 catalyst has improved catalytic cracking to produce more hydrogen and short HC in catalytic co-pyrolysis of tobacco stem and polypropylene plastic.

The waste derived catalyst has also shown effectiveness in pyrolysis. Kamil et al., (2017) use AD as catalyst in catalytic pyrolysis of waste cooking oil. AD contains combination of metals, the most substances are Al_2O_3, Cl, Fe_2O_3, and K_2O. The Al_2O_3 catalyst provides good characteristics of surface area, surface morphology, thermal stability, and acidity which has potential to be utilized as low-cost catalyst. Other researchers reported on extraction of Al_2O_3 from AD and used as catalyst support for glycerol dry reforming reaction (Roslan et al., 2021). The characteristics of EGA support, which have high surface area, well dispersion of metal on EGA support and small crystallite size, enhanced the conversion of glycerol which showed EGA has suitable characteristics as catalyst support.

Chow et al., (2018) used sludge ash as catalyst in co-pyrolysis of sludge and palm empty fruit bunch fibre. The ash contains alkali and alkaline earth metals such as Mg, K and Ca have promoted the degradation of biomass. The findings elucidate the decomposition of biomass and sludge catalysts has shifted the reaction pathways, where enhanced the phenol production with improved acidity of bio-oil. Kai et al., (2025) studied the self-sourced CaO/biochar composite from papermill sludge pyrolysis. The

findings reveal the pyrolysis of papermill sludge in the presence of CaO/biochar catalyst able to be reduced the oxygenates compound especially acid and ester in bio-oil. Aluminium recovered from sludge also has been applied as a catalyst in various processes, including microbial fuel cells (Thulluru et al., 2025), antibiotic degradation (Revilla et al., 2025), and hydrogen production (Liu et al., 2025). These studies reported good catalytic performance, leading to improve reaction efficiency. Therefore, aluminium-rich sludge has significant potential as a sustainable source of aluminium for catalyst development.

Considering the good potential from various combinations of metals mentioned above, the screening and elimination were done to focus the study on the development of heterogeneous catalysts that consist of Cr, Ti, and EA. The properties, activity, and catalyst reusability of the metal oxides (Cr, Ti)–based EA support in catalytic co-pyrolysis from CFW and PPW have not been reported. Moreover, the availability of the materials and cost are additional factors motivating the selection of the metals in this work. The summary of metal oxides catalyst consists of metals (Cr, Ti, and Al) selected for this study are shown in Table 2.7.

Table 2.7
Summary of Metal Oxides Catalysts Consist of Metals (Cr, Ti and Al) Selected for Present Study

Catalyst	Feedstock	Performance	Remark	References
Cr_2O_3	Poplar wood	35 % light oil yield. Less coke formation.	Promote cracking	(Zhang et al., 2019)
$MgCr_2O_4$	Wheat straw	11 % bio-oil yield. 20 % O_2 content in bio-oil.	Promote deoxygenation and aromatic	(Atanda et al., 2021)
Ni–Cr	Beech wood	50.2 % upgraded oil phase	Higher activity due to higher acid strength.	(Schmitt et al, 2019)
$NiCr_{10}$–SiO_2	Anisol Furfural	100 % cyclohexane from anisole. 95 mol % THFA from furfuryl.	Reduce erosion and corrosiveness.	(Smirnov et al., 2019)
TiO_2	Poplar wood	24 % heavy oil yield.	High in anti-carbon deposition.	(Zhang et al., 2019)
TiO_2	Cellulose	69 % deoxygenated product and high aromatic product	Promote deoxygenation	(Ida et al., 2020)

Catalyst	Feedstock	Performance	Remark	References
TiAH5 Ti3H5	Rapeseed shell	30.84 % bio-oil yield (TiAH5) 31.79	Promote deoxygenation and aromatic.	(Fan et al., 2020)
MgAl–ZSM5	Pinewood	25 % bio-oil, 32 % oxygen in bio-oil.	Promote deoxygenation, promote aromatic.	(Atanda et al., 2020)
Al_2O_3	Poplar wood	22.5 % tar yield. 32.9 % oxygen in bio-oil	Promote cracking on acidic catalyst.	(Zhang et al., 2018)
Ni/Ca–KWBC	municipal sewage sludge/cotton stalks	highest H_2 yield (5.03 mmol/g) and production rate (20.30 %)	Promote H_2 reforming	(Liu et al., 2025)
Ni/Mo–TiO_2 Ni/Al_2O_3	Oil palm trunk/ PP	Increased hydrocarbons and reduce oxygenates compound	Promote deoxygenation and cracking	(Terry et al., 2023)
Ni/EGA	Glycerol	22 % glycerol conversion. 15 % hydrogen yield.	Promote cracking	(Roslan et al., 2021)
Fe–Ce/Al	Polycarbonate waste	3-fold increase in targeted MAHs	Promote direct deoxygenation	(Wang et al., 2020)
Ni/CaO–Al_2O_3	Tobacco stem/PP	Increase aliphatic HC (Ni/Ca25)	Promote cracking	(Tang et al., 2025)

2.9 Catalyst Synthesis using Wet Impregnation Method

The wet impregnation is a method that widely used for catalyst preparation because it is simple, economical, and scalable for industrial applications (Chen et al., 2021; Colelli et al., 2025). In this process, a solution of the desired metal precursor, either aqueous or organic, is applied to a porous support such as Al_2O_3, SiO_2, or TiO_2. These materials exhibit high specific surface areas, high porosities, and high thermal and mechanical stability and come in a variety of pore sizes, which enhance catalyst performance (Munnik et al., 2015). The procedure involves contacting the support with the precursor solution, enabling the active metal species to diffuse into the porous network of the material (Afolabi & Onwona, 2023).

Following impregnation, the material is typically subjected to drying process to remove the solvent and heated at moderate temperature. Then the material is undergoing calcination or reduction steps, where it heated under controlled conditions to convert

the metal precursors into their active oxide or metallic forms. These thermal treatments help to anchor the active phase onto the support, improve metal dispersion, and tailor physicochemical properties such as surface area, acidity, and redox characteristics. The final catalytic performance depends strongly on parameters such as precursor type, solvent, pH, impregnation time, and post-treatment conditions.

Several catalysts have been successfully synthesized using the wet impregnation method for diverse applications. For instance, bimetallic (Ni, Cu, Zn, Ag, and Fe) strontium oxide (SrO)-loaded hierarchical Y–zeolite catalysts have been prepared for co-pyrolysis reaction and shows improvement in mesoporosity of the catalyst (Dada et al., 2022). Similarly, Ni–MCM–41 catalysts synthesized by wet impregnation have demonstrated excellent performance in co-pyrolysis reaction due to the addition of Ni effectively modulate the physicochemical properties of MCM–41 (Shi et al., 2020). In CO_2 reduction, carbon beads (CB) and addition of calcium (Ca/CB) via wet impregnation showed that the Ca well dispersed on CB surface (Devarajan & Madhavan, 2023). Figure 2.11 shows the steps in wet impregnation of Ca/CB for CO_2 reduction process.

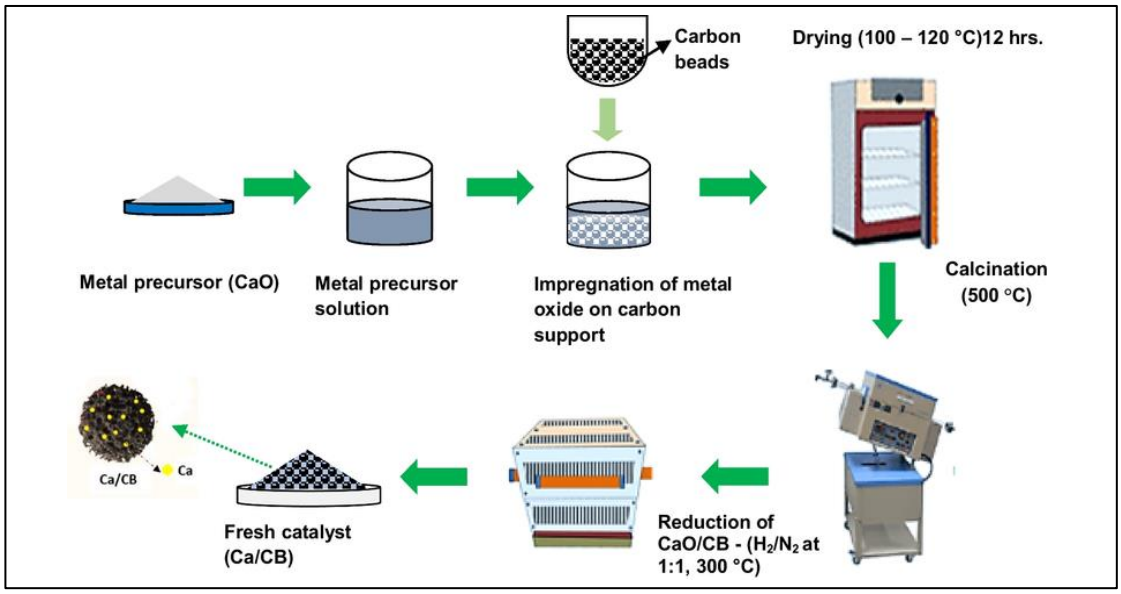

Figure 2.11 Wet Impregnation Method in CB and Ca/CB For CO_2 Reduction Process

Source: (Devarajan & Madhavan, 2023)

2.10 Effect of Catalyst Preparation Conditions

Several studies have reported that the preparation conditions play a crucial role in tuning both the physicochemical properties and catalytic activity. The subsequent sub-sections discuss three critical parameters, which are metal loading, calcination temperature, and calcination time.

2.10.1 Effect of Metal loading

The effect of metal loading in catalytic co-pyrolysis on product yield and bio-oil component distributions is significant. Several studies have been conducted to evaluate the effectiveness of metal loading in improving the catalyst activity.

Zulkafli et al., (2023) investigated the metal loading of Zn and Ga over electric arc furnace slag (EAFS) catalyst. It was reported that the 5 wt.% Zn loading provide maximum bio-oil yield compared to others (10, 15 and 20 wt.% Zn loading). However, for Ga loading, it showed that 15 wt.% of Ga loading achieved the maximum bio-oil yield which 5.67 % lower than 5 wt.% of Zn loading. The finding also shows that HC and alcohol have been the most compound found in bio-oil by 5 wt.% Zn (43.96 % and 15.78 %). While in 15 wt.% Ga, the ester shows dominant with 50.68 % followed by HC. Therefore, it concludes that the metal loading for each catalyst provides different catalytic activity.

Maneechakr & Karnjanakom, (2021) also investigate the effect of different metal (Ni, Cu, Fe)-doped carbon catalyst at different metal loadings (5 %, 10 %, 15 %, 20 %) towards bio-oil production. The bio-oil yield was found at maximum when 15 % of metal loading was doped to carbon, which increased the HC compound in bio-oil to 65–75 %. The acidity of the catalyst played a significant role to promote dehydration and decarbonylation reaction, therefore increased bio-oil, and HC yield. 15 % Ni-Carbon shows the best catalytic activity with 72 % of HC produced.

Nandakumar et al., (2023) has extensively investigated the catalysts activities for various metals (Ni, Mn, Zn) at different metal loadings (1 %, 5 %, 10 %) over HZSM–5 catalysts in the co-pyrolysis of wheat straw and HDPE. Figure 2.12 shows the comparison of several types of metal at different metal loadings.

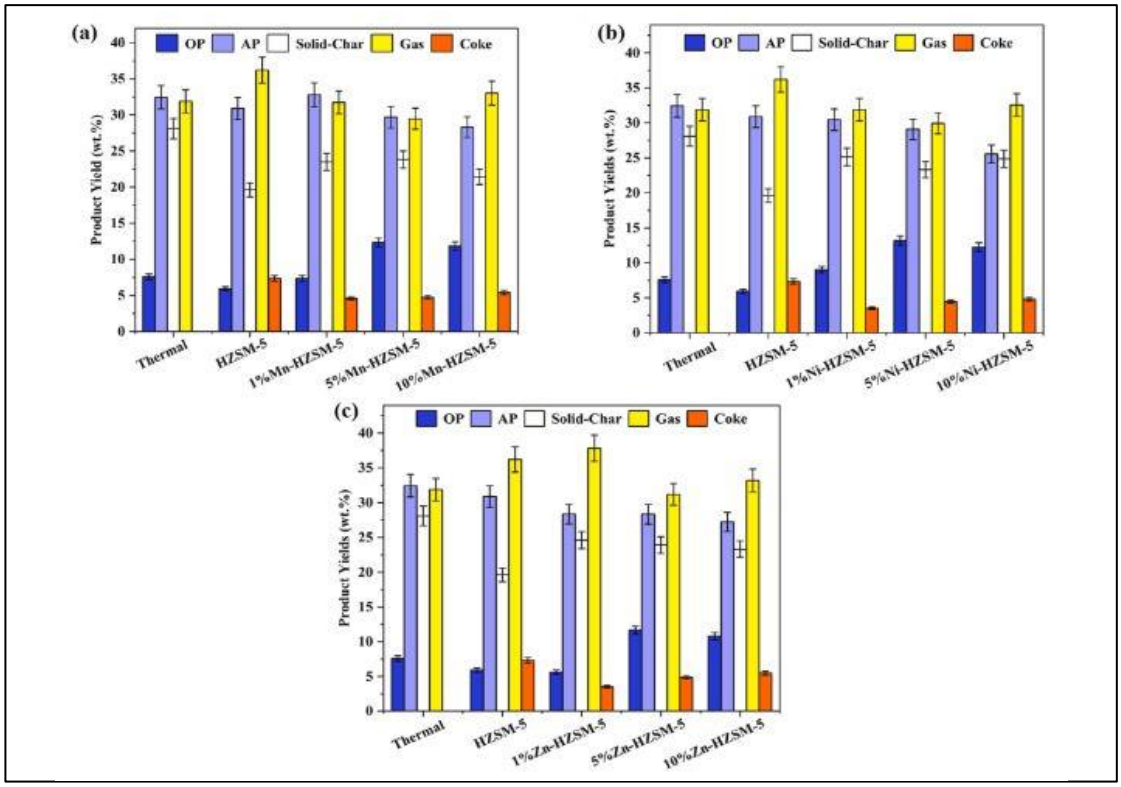

Figure 2.12 Comparison Product Yield of (a) Mn (b) Ni (v) Zn at Different Metal Loadings over HZSM–5 Catalyst

Source: (Nandakumar et al., 2023)

The result shows that the metal loading has significantly improved the organic phase (OP) for all metals at higher metal loadings with 10 % Ni–HZSM–5 generated liquid product containing max percentage of organic phases (32.38 %) followed by 5% Ni (31.20 %), 10% Mn (29.45 %), and 5% Zn (29.16 %) respectively. In addition, total liquid yield achieved 42.57 % and 42 % for 5 % Ni–HZSM–5 and 5 % Mn–HZSM–5. Likewise, the remaining metal-loaded HZSM–5 produced liquid yields within the range of ~38–40 %. However, aromatic HC was reported to increase at lower metal loading, which the highest was reported to be achieved at 25.12 % for 1 % Zn–HZSM–5. Therefore, the metal-modified catalysts enhanced the organic phase fractions formations with the upgrading HC and aromatic HC which strongly correlated with the acidity of the catalyst.

2.10.2 Effect of Calcination Temperature

Calcination temperature plays a critical role in catalyst synthesis because it determines the structural, chemical, and textural properties of the catalyst. Higher calcination temperatures influence catalyst activity, and several studies have demonstrated improvements in catalytic activity with optimized conditions. Wang et al., (2022) observed that Ni–RM catalysts calcined at lower temperatures (400–600 °C) showed better surface area and metal dispersion compared to those calcined at higher temperatures (700–900 °C). At elevated temperatures, sintering and agglomeration occurred, which reduced the number of active sites and decreased catalytic activity. As a result, the conversion gradually declined from a maximum of 100 % at calcination temperatures below 600 °C to lower values at higher calcination temperatures. Figure 2.13 shows the surface morphology by SEM and transmission electron microscopy (TEM) image for Ni–RM catalyst at different calcination temperatures. The SEM and TEM images show the agglomeration of Ni at higher calcination temperature.

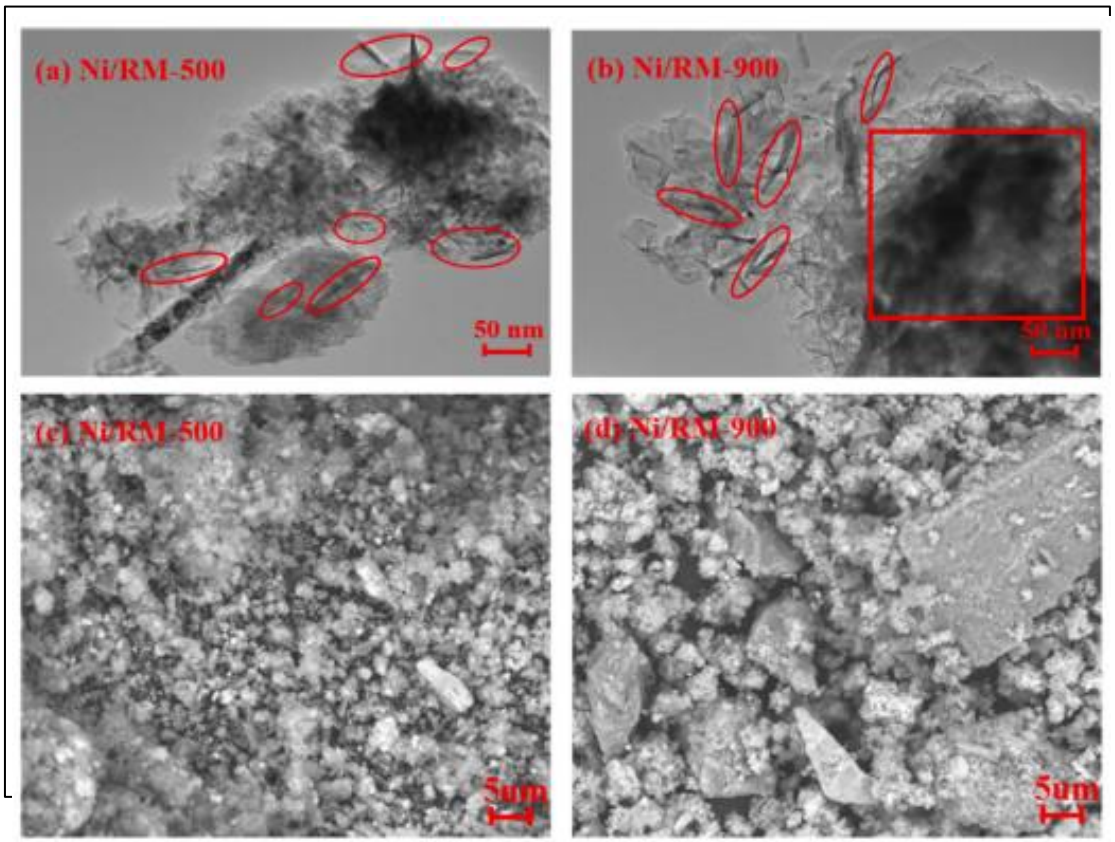

Figure 2.13 SEM and TEM Image for Ni–RM at Different Calcination Temperature
Source: (Wang et al., 2022)

Another study showed that calcination temperature significantly influenced the catalyst structure and consequently its activity. Isha et al., (2022) reported that the liquid yield from HDPE pyrolysis decreased with increasing calcination temperature, while the formation of solid wax was promoted. It was observed a sharp reduction in surface area when the catalyst was calcined above 500 °C, which suppressed cracking reactions and limited the formation of shorter-chain hydrocarbons. Similarly, Li et al., (2019) demonstrated that calcination temperature strongly affected catalyst structure. Increasing calcination temperature gradually decreased the Brunauer-Emmett-Teller (BET) surface area, average pore diameter, and total pore volume. At higher temperatures, sintering became apparent as particle size increased from 20–50 nm to larger aggregates, as confirmed by surface morphology. It was found that, Ni/MgO calcined at 850 °C achieved the highest conversion (98 %) compared to Ni/MgO–650 (84 %), whereas further increasing the calcination temperature to 950 °C reduced conversion back to 84 %. Ni/MgO–850 exhibits optimal catalytic performance due to the synergistic interaction between metallic Ni active sites and the basic MgO support. This is further enhanced by higher dispersion of surface Ni atoms and appropriate basicity. In contrast, excessive calcination shows by Ni/MgO–950 leads to structural deterioration and reduced catalytic activity.

Recently, Chen et al., (2022) investigated the calcination temperature effects of CaO derived from carbide slag catalyst on cotton stalk pyrolysis. The result shown that calcination temperature (650–950 °C) significantly influences catalyst structure and performance. The lower temperatures suppress sintering and enhance basicity, resulting in improved hydrocarbon yield and bio-oil quality, while higher temperatures promote sintering and increase oxygenated compounds.

2.10.3 Effect of Calcination Time

The calcination time also plays a significant role in determining catalyst activity, stability, and selectivity. Insufficient calcination may leave residual precursors or incomplete crystallization, while prolonged calcination can cause sintering, loss of surface area, and changes in phase composition.

The calcination time between 1 h to 7 h was investigated for Pd–Fe–Co–Ce/FSC catalyst. The highest chemical oxygen demand (COD) removal rate was obtained for calcination time of 3 h. Longer durations reduced performance, likely due to excessive

metal particle growth and loss of active surface area (Zhang et al., 2020). Another study investigated on calcination time of CaO derived from chicken eggshells from 10 min to 350 min in transesterification of waste cooking oil. The optimum calcination time was obtained at 210 min, which produced 94.7 % of biodiesel yield. At this condition, the CaO was completely formed. Lower calcination time showed lower yield due to incomplete formation of CaO from calcium carbonate ($CaCO_3$), conversely higher calcination time cause catalyst deactivation due to sintering (Lani et al., 2019).

Calcination time also possibly changes the particle size of the catalyst. Chava et al., (2021) showed that calcination time (4–20 h at 800 °C) strongly governs Ni particle size and dispersion on Ni/γ-Al_2O_3 monolith catalysts. Short calcination time (4–10 h) yields larger, less uniform Ni particles, whereas prolonged calcination time (20 h) promotes spinel formation ($NiAl_2O_4$). Therefore, enhancing metal–support interactions and producing finer, well-dispersed Ni particles after reduction. The resulting smaller particle size increases active site availability, thereby improving catalytic performance, with calcination time of 20 h exhibiting the highest activity. On the other study, Alhalili & Smiri, (2022) observed the nano particle size distribution of TiO_2 NPs shifted tremendously when calcined at 1 h and 5 h. Longer calcination time (5 h) has reduced to particle size from average 85nm to 25nm. Figure 2.14 shows the SEM images and particle size distributions of TiO_2 NPs.

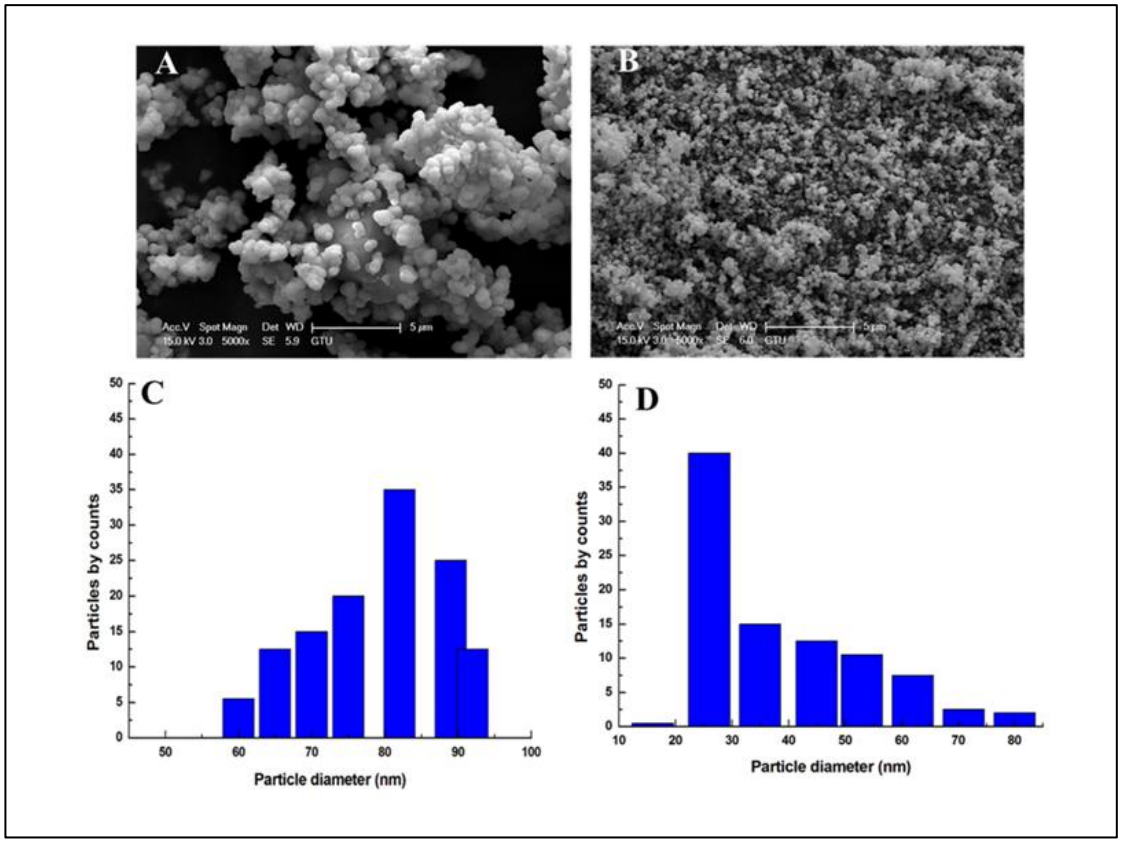

Figure 2.14 SEM and Particle Size Distributions of TiO_2 Nps

Source: (Alhalili & Smiri, 2022)

2.11 Effect of Pyrolysis Process Conditions on Catalyst Activity

Several studies have reported that the process conditions play a crucial role in catalyst activity. The subsequent sub-sections discuss four critical parameters, which are pyrolysis temperature, biomass-to-plastic ratio, feedstock-to-catalyst ratio, and pyrolysis time.

2.11.1 Pyrolysis Temperature

Ahmad et al., (2024) reported a significant increase in bio-oil yield from 26 % to 61 % as the temperature rose from 350 °C to 450 °C, with the maximum yield of 63 % achieved at 550 °C. The temperature range of 350–450 °C is critical for decomposition of complex components formed between biomass and plastic, promoting the formation of lighter volatile compounds and enhancing liquid yield. This increase is accompanied by a substantial reduction in char yield (57% to 10%) and a moderate rise in gas yield, indicating enhanced volatilisation and primary decomposition

reactions. Beyond 450 °C, the marginal improvement in oil yield suggests the onset of secondary cracking reactions, which favour gas formation and limit further increases in liquid products.

Similarly, Ryu et al., (2020) investigated the thermal degradation behaviour of organosolv lignin (OL) and PP, both individually and during co-pyrolysis, using TGA analysis. The derivative thermogravimetry (DTG) results indicated that PP degraded at a higher maximum temperature (T_{max}, 478 °C) compared to OL (T_{max}, 393 °C), while the OL/PP mixture showed a peak degradation temperature of 489 °C. These findings indicate that the selection of an optimum pyrolysis temperature is crucial to ensure complete decomposition of all feedstocks. Therefore, the 550–600 °C is suitable temperature range for achieving complete thermal degradation and maximizing bio-oil production. Figure 2.15 illustrates the DTG curves of OL, PP, and OL/PP degradation with temperature obtained from TGA analysis.

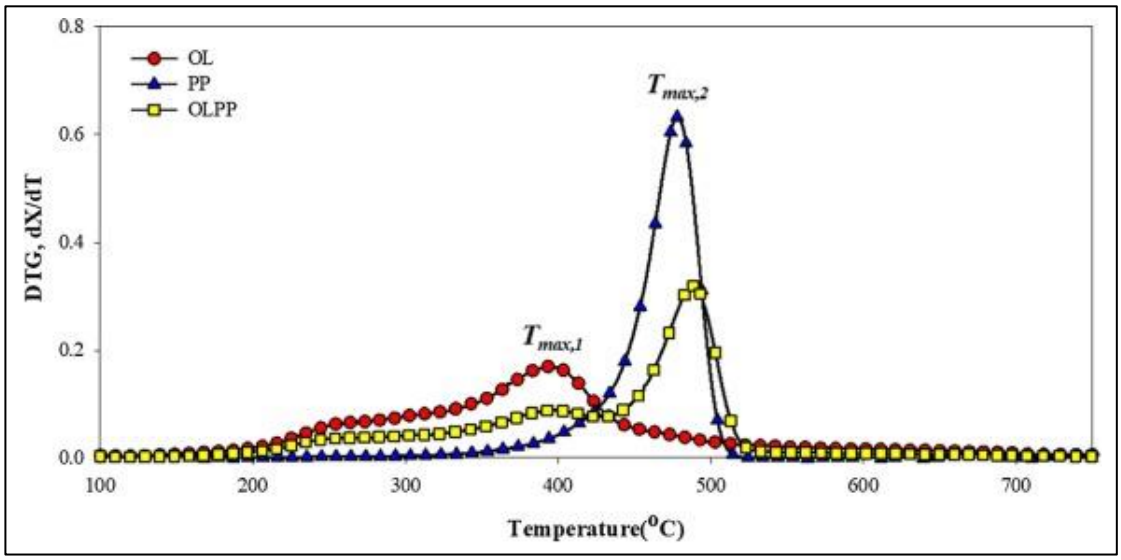

Figure 2.15 DTG Curve of OL, PP and OL/PP Degradation over Temperature
Source: (Ryu et al., 2020)

Panicker et al., (2025) reported that a higher pyrolysis temperature of 650 °C was the optimal condition for the co-pyrolysis of coconut shell (CNS) and polystyrene (PS) due to its selectivity toward hydrocarbon formation. At this temperature, the bio-oil contained 33 % hydrocarbons and only 13 % acidic compounds, compared to 6 % and 4 % hydrocarbons and 20–17 % acidic compounds at 450 °C and 550 °C, respectively. These findings show that lower temperatures favour the formation of

oxygenated compounds, while higher temperatures (650 °C) enhance hydrocarbon production in the presence of a catalyst.

Jin et al., (2022) investigated the co-pyrolysis of pine and PE using a ZSM–5 catalyst at different temperatures (500 °C, 600 °C, and 700 °C) and observed variations in carbon chain distribution. At lower temperature (500 °C), a substantial amount of long-chain aliphatic hydrocarbons was produced, which restricted the diffusion of large molecules into the catalyst pores for further reactions. In contrast, higher pyrolysis temperatures enhanced thermal cracking, generating vapours rich in lighter components. Therefore, the small molecules could easily access the pores and converted into aliphatic HC. Moreover, further raising the temperature to 700 °C has increased in aromatic HC, reaching 58.1 %. Although increasing temperature enhanced cracking activity and promoted the formation of aliphatic HC and aromatic HC, excessively high temperatures tend to increase gas formation, thereby reducing the yield of the desired bio-oil (Al-Maari et al., 2025; Hassan et al., 2019; Razzak et al., 2025).

2.11.2 Effect of Biomass-to-Plastic Ratio

The BP ratio is another parameter that studied by several researchers. The addition of plastics in catalytic biomass increased the formation of aliphatic HC and aromatic HC. Wang et al., (2021) reported on the increased of aromatic HC when 80 % of PE was mixed with flax waste. The increase of aromatic HC is due to the abundance of hydrogen donors produced from PE that reacted with furans via Diels-Alder reaction. The addition of plastic promoted an increased in the H/C_{eff} of the system, increased the hydrocarbon content and promoted the Diels Alder reaction (Wang et al., 2019; Zheng et al., 2020). The similar finding was reported by Jin et al., (2022), where increased PE to pine ratio has increased the aromatic HC selectivity.

Other study reported that higher BP ratio leads to reduce the bio-oil production but increased char and gas yield. High char is due to increased amount of biomass during co-pyrolysis since the char is from biomass feedstock (Dyer et al., 2022). In different work, Dyer et al., (2021) reported on the reduction of oxygenated components in bio-oil as reflected to the high HDPE and PS in the BP mixture. However, Fu et al., (2024a) found that, bio-oil yield is reduced by increased the HDPE ratio and the gas was produced significantly. This indicates that the catalyst exhibited efficient catalytic performance in inducing deep cracking of HDPE, promoting gas generation. In contrast,

the monoaromatic hydrocarbon (MAH) production is increased by 10.4 % when the HDPE increased from 30 % to 50 %. Figure 2.16 shows the product distributions and bio-oil component distribution of CS–HDPE in catalytic pyrolysis.

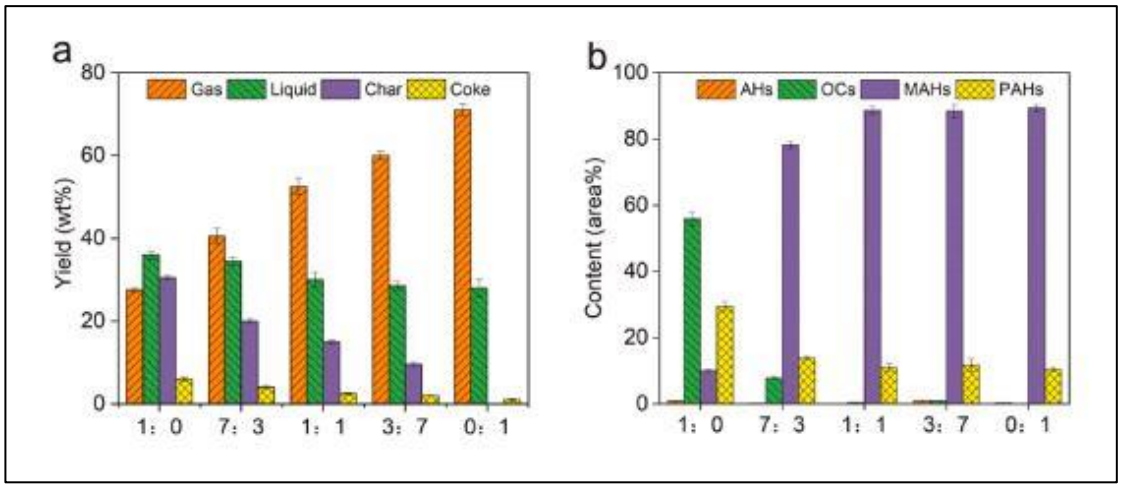

Figure 2.16 (a) Product Distributions (b) Bio-oil Component Distribution of CS–HDPE in Catalytic Pyrolysis

Source: (Fu et al., 2024b)

Kanduri & Seethamraju, (2023) investigated on the effect of biomass/plastic mass ratios of 1:2, 1:1, and 2:1 in the catalytic co-pyrolysis of biomass (Groundnut shells) and plastics (LDPE and HDPE) in the presence of FCC catalyst. The findings revealed that, for biomass-LDPE (B-LDPE) and HDPE (B-HDPE) in ex-situ configuration produced 37 wt.% and 36 wt.% bio-oil yield at 1:2 ratio, respectively. At higher plastic ratio (1:2), the presence of monoaromatic in B-LDPE slightly higher (19.61 % C) than B-HDPE (17.73 %C). The monoaromatics yield increased with increasing the biomass fraction (1:2 to 2:1) in the feed. However, an increase in PAH and char yields were also observed for both B-LDPE and B-HDPE.

Duan et al., (2017) reported that varying the BP ratio influenced the conversion of oxygenates to hydrocarbons, as illustrated in Figure 2.17. The aromatic yield increased significantly, reaching approximately 40 % when the linear low-density polyethylene (LLDPE) mass ratio was 50 %, indicating that a xylan-to-LLDPE ratio of 1:1 is optimal for aromatic production. In contrast, the formation of polycyclic aromatic hydrocarbons (PAHs) decreased markedly with higher LLDPE content. The enhancement in hydrocarbon yield was attributed to the hydrocarbon pool generated

from ketone conversion and LLDPE chain cleavage, while the Diels–Alder reaction facilitated the formation of aromatic compounds.

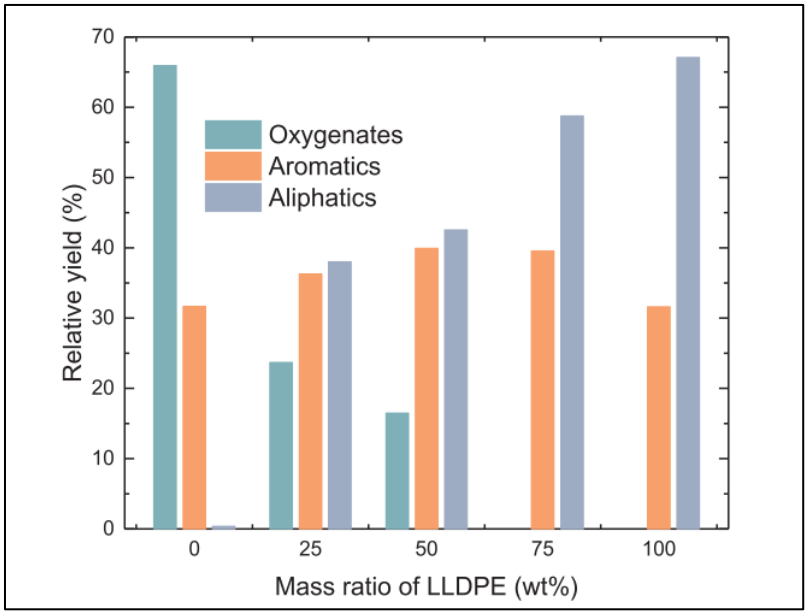

Figure 2.17 Effect of LLDPE Mass Ratio in Bio-Oil Component Distribution
Source: (Duan et al., 2017)

2.11.3 Effect of Feedstock-to-Catalyst Ratio

The F/C ratio is other key parameter influencing catalytic activity and product distribution during the co-pyrolysis of biomass and plastics. This ratio determines the degree of contact between the feedstock vapours and active catalytic sites, directly affecting the extent of catalytic reactions. Several studies have been conducted that varies the F/C ratio. Al-Maari et al., (2025) investigated the effects of F/C ratio in co-pyrolysis of low-density polyethylene (LDPE) with palm oil empty fruit bunch (EFB) waste using a natural clinoptilolite catalyst. The result revealed that, the increased in catalyst amount increased the bio-oil yield which the highest obtained at 1:5 (72.6 %) and produced highest HC yield (77.8 %). However, increasing the catalyst loading beyond the optimum level led to a significant decrease in hydrocarbon yield, while the acidic compounds were eliminated. Similarly, Hassan et al., (2019) reported that increasing the feedstock-to-catalyst ratio slightly reduced bio-oil yield while promoting gas formation, with a maximum hydrocarbon content of 74.55 % achieved at a 6:1 ratio before declining at higher loadings. Increasing catalyst loading also prolonged the

residence time of pyrolysis vapours within the catalyst pores, enhancing cracking and deoxygenation reactions that favoured aromatic hydrocarbon formation.

Some of the researchers have targeted to produce aromatic HC via catalytic co-pyrolysis of biomass and plastics. Duan et al., (2017) studied the co-pyrolysis of lignin and PP in the presence of HZSM-5 catalyst at different F/C ratio. Figure 2.18 shows the product yield and component distributions of F/C ratio. The highest aromatics is observed at 1:1 F/C ratio, while significantly reduced the oxygenates compound as shown in Figure 2.18(c) and Figure 2.18(b), respectively.

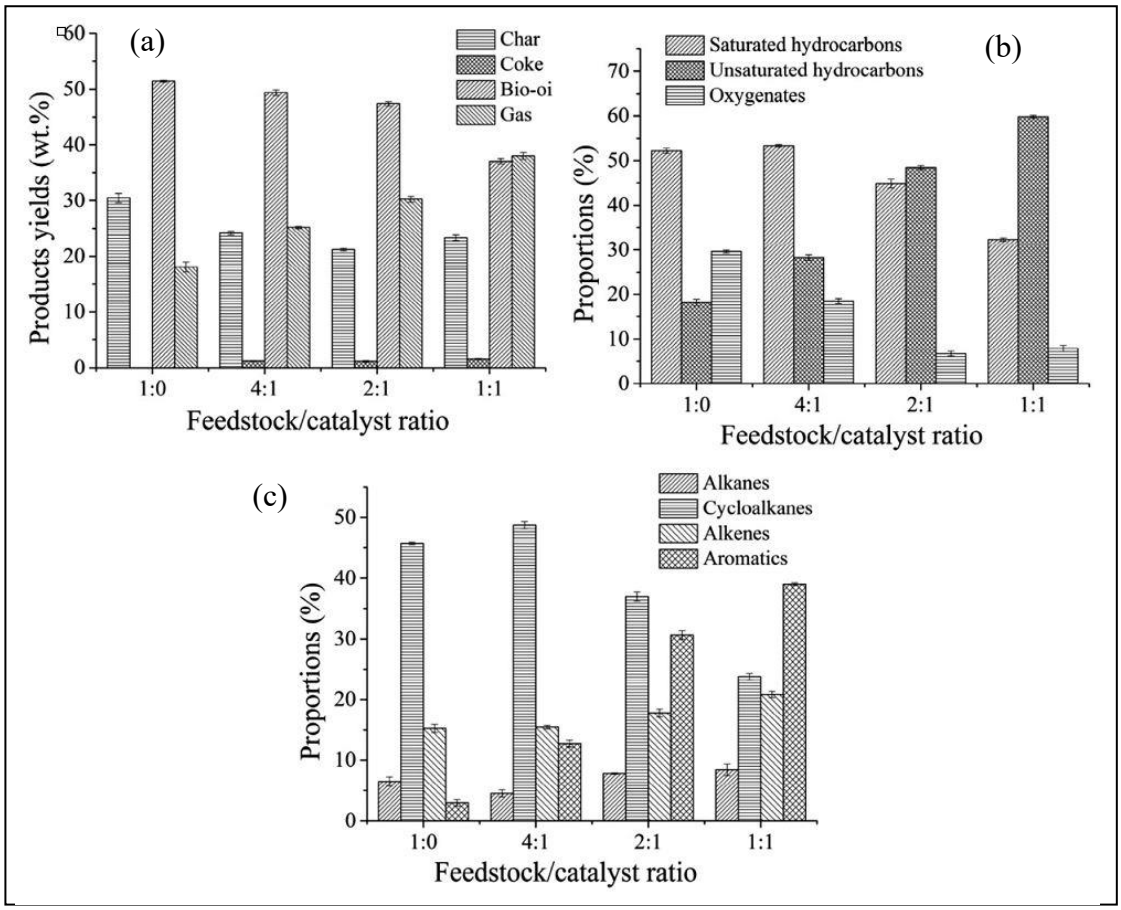

Figure 2.18 Effect of F/C Ratio in Catalytic Activity (a) Products Yield (b-c) Bio-oil Component Distribution

Source: (Duan et al., 2017)

The selectivity toward aromatic compounds increased as more active sites became available for aromatization and oligomerization reactions. The presence of sufficient active sites also enhanced deoxygenation activity, thereby reducing oxygenated compounds and increasing hydrocarbon production. The results also showed on the reduction of bio-oil yield while increasing the catalyst ratio. This

possibly due to enhancement of secondary cracking, which promoted gas formation. The similar trend is reported by Ding et al., (2018) which studied the effect of feedstock-to-catalyst (CaO:HZSM–5) ratio during co-pyrolysis of hemicellulose and LLDPE. The findings reveal that decreased F/C ratio promoted the aromatic production and aliphatic HC from 31.66 % and 0.38 % to 64.14 % and 9.82 %, respectively. Wang et al., (2025) investigated the F/C ratio of HS–ZSM in the co-pyrolysis of neem sawdust (NS) and LDPE. The increase in catalyst loadings (0.5g; 1g and 1.5g) showed the increment of aromatics from 18 % to 42.4 %, while suppressing olefin and oxygenates. The enrichment in acids sites at higher catalyst loadings has facilitated the Diels–Alder reaction of olefins and furans to yield aromatics.

2.11.4 Effect of Pyrolysis Time

Pyrolysis time is an important parameter that strongly influences the product yield and composition during catalytic co-pyrolysis of biomass and plastics. It governs the extent of thermal degradation, cracking, and secondary reactions that determine the balance between liquid, gas, and solid products. Understanding the effect of reaction time is therefore essential to identify the optimum duration that maximizes bio-oil yield while minimizing excessive cracking and catalyst deactivation.

Ahmad et al., (2024) investigated the effect of pyrolysis time on product yield and reported that the bio-oil yield increased from 50 % to 61 % as the reaction time extended from 20 to 30 min. The prolonged pyrolysis time allowed greater feedstock exposure, which facilitated cracking reactions and generated smaller molecular fragments, thereby enhancing liquid yield. However, excessive reaction time promoted over-cracking, leading to increased gas formation.

Similarly, Charusiri et al., (2022) examined the influence of pyrolysis time on the catalytic co-pyrolysis of sugarcane leaves and low-density polyethylene (SCL–LDPE) using a copper-doped HZSM–35 catalyst. The bio-oil yield increased from 29.22 % to 36.99 % at 45 min but gradually declined at longer pyrolysis time. The reduction in yield was attributed to catalyst deactivation caused by pore blockage and the deposition of carbonaceous materials. Furthermore, prolong pyrolysis time enhanced secondary cracking and thermal degradation, resulting in higher gas production. Figure 2.19 illustrates the effect of pyrolysis time on catalyst activity during the co-pyrolysis of SCL–LDPE.

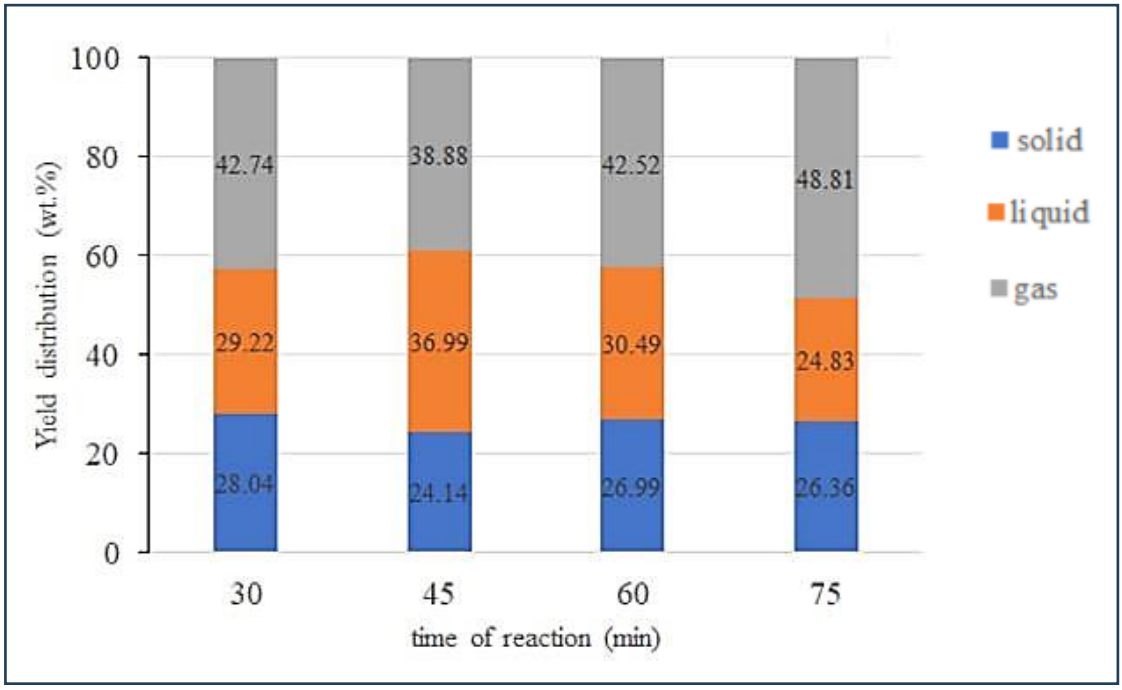

Figure 2.19 Effect of Pyrolysis Time of Co-Pyrolysis of SCL–LDPE on Catalyst Activity

Source: (Charusiri et al., 2022).

In a related study, Charusiri et al., (2023) observed that pyrolysis times below 45 min were insufficient to degrade large HC molecules from both spent lubricating oil (SLO) and LDPE into smaller compounds. Consequently, limits the diffusion of volatiles into the catalyst pores for further cracking. At 60 min, thermal degradation was more effective, producing a higher proportion of shorter linear alkanes. However, at prolonged pyrolysis times (90 min) caused excessive cracking and yielding a high gas fraction (43.82 %). Catalyst deactivation due to pore blockage and surface material deposition further contributed to the decline in liquid yield at longer pyrolysis time.

2.12 Catalyst Reusability and Regeneration

Catalyst reusability and regeneration are critical factors in evaluating the long-term efficiency and economic viability of catalytic co-pyrolysis processes. There are several studies that have investigated catalyst reusability and regeneration behaviour during pyrolysis process.

Maneechakr & Karnjanakom (2021) investigate the reusability of different types of catalysts for 5 cycles. The results showed the HC yield dropped significantly after 5th runs, which resultant from the reduce catalytic activity. This is due to the catalyst

deactivation caused by the blocked pores where the poison molecules adsorbed on the surface of resulted in less active sites available for reaction. Therefore, prevent volatiles reaching the active sites and hinder catalytic reaction. The regeneration of the catalyst has been reported to remove adsorbed material on the catalyst. The observation is further supported by Ahmed et al., (2022), whereby demonstrated that absorbed material on the catalyst surface during catalytic co-pyrolysis can accumulate within catalyst pores and block active sites. Therefore, restricted the diffusion path and reduced catalyst activity. Regeneration through oxidative treatment removes these adsorbed deposits, thereby allowed the accessibility of active sites and improving catalytic activities. Similarly, Zhang et al., (2016), reported on the regeneration of the catalyst after co-pyrolysis of Douglas fir sawdust and LDPE. The result showed the carbon yield of liquid organic was decline with repeated use. The slight decrease in liquid yield from 40.54% (fresh) to 36.77% after the fifth cycle indicates that the catalyst retained its activity with some loss of active sites. This reduction is attributed to irreversible mesopore blockage caused by deposited species, which alters the catalyst surface. The blockage of pores restricts access to active sites and inhibits reactions such as Diels–Alder pathways, thereby reducing the liquid yield.

Hafriz et al., (2022) investigated the reusability and regeneration of deoxygenation of WCO using KSi catalyst. The regeneration study was conducted for 2 cycles, which are identified as KSi–RG1 for regeneration cycle 1 and KSi–RG2 for regeneration cycle 2. For reusability test, each of the fresh (KSi) and reusability cycles were conducted five consecutive runs to observe the product yield of the deoxygenation of WCO. The reusability and regeneration test is displayed in Figure 2.20. The results showed that the pyrolysis oil yield decreased from 51.8 % in the first run to 29.5 % in the fifth run when using the fresh catalyst. The reduction of the catalytic activity is due to the deposited materials on the catalyst surface caused poisoning and pore blockage. Consequently, hindered the interaction between volatile compounds and the active site. In the regenerated catalyst, the oil yield dropped to 46.0 % and 40.3 % for KSi–RG1 and KSi–RG2, respectively. After five consecutive runs of the reused catalyst, the oil yield declined greatly in both regeneration cycles as material accumulation on the catalyst surface deteriorated its activity. As a result, the yield decreased from 46.0 % to 24.5 % in regeneration cycle 1 and from 40.3 % to 21.1 % in regeneration cycle 2, where cycle 1 and cycle 2 represent different reaction. However, each regeneration process recovered part of the catalyst activity by removing surface impurities.

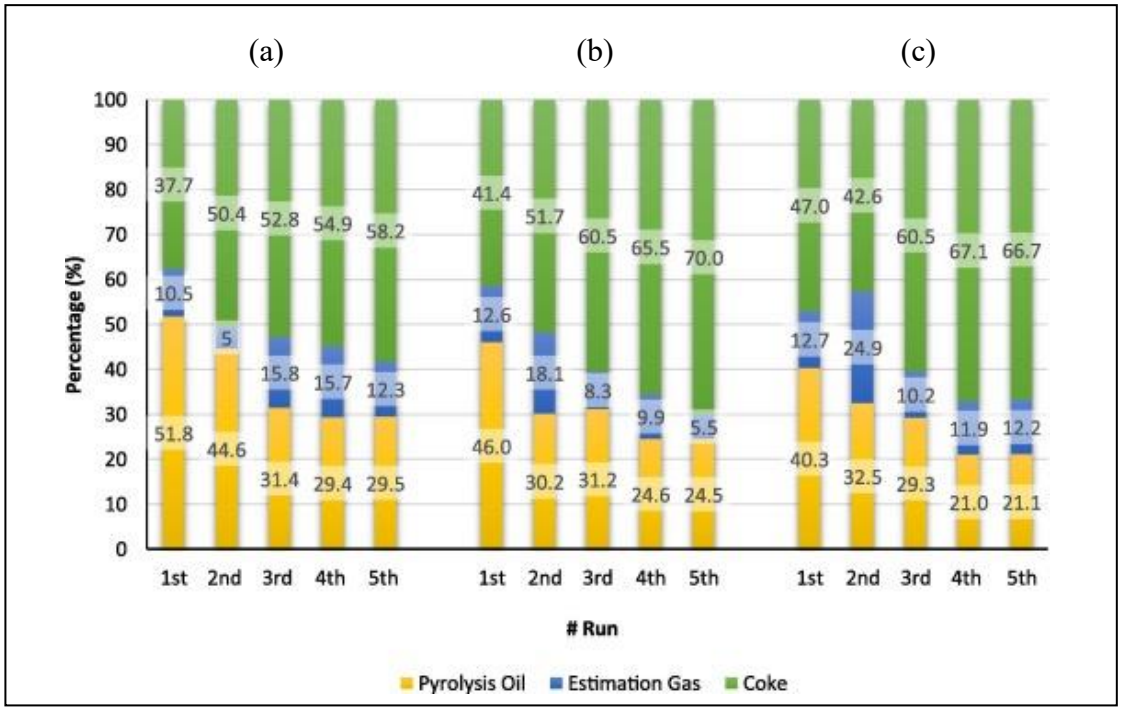

Figure 2.20 Reusability and Regeneration of Catalyst in Deoxygenation of WCO (a) KSi (b) KSi–RG1 (c) KSi–RG2

Source: (Hafriz et al., 2022)

2.13 Kinetic Model of Biomass-Plastics in Catalytic Co-pyrolysis

Kinetic analysis is used to determine the rate law of the pyrolysis reaction and elucidate the reaction pathway. The kinetic model provides fundamental insight into the reaction mechanism and serves as essential information for future scale-up studies. The kinetic study usually conducted conduct at non-isothermal conditions at various heating rates using TGA. Thermogravimetric (TG) and derivative thermogravimetric (DTG) analyses provide valuable understanding into the decomposition mechanism and reaction pathways during pyrolysis. The resulting curves illustrate the mass loss rate as a function of temperature, which can be used to interpret the kinetics of the thermal degradation process.

The model-fitting method determines kinetic parameters by assuming a specific reaction mechanism or model to describe the conversion process. The Coats-Redfern (CR) method is among the most widely used model-fitting techniques due to its simplicity and ability to describe complex thermal degradation reactions with reasonable accuracy. The CR method uses a single heating rate to fits experimental data to mathematical models, such as chemical reaction and diffusion, random nucleation, geometric, power law and phase boundary to estimate the activation energy (E, kJ/mol),

pre-exponential factor (A, s^{-1}) and the reaction order (Shagali et al., 2023). Activation energy represents the minimum energy required to initiate bond cleavage during a reaction, while the pre-exponential factor reflects the frequency of effective molecular collisions and thus the reaction rate (Shahdan et al., 2022). Numerous studies have employed the CR method to examine interactions in the co-pyrolysis of biomass and plastics under both catalytic and non-catalytic conditions. Beyond estimating kinetic parameters, these analyses also offer insight into the associated reaction mechanisms.

Jamaluddin et al., (2026) used the CR method to model the kinetics of coffee grounds (CG), polypropylene (PP), and their blends. Thermogravimetric analysis was used to evaluate thermal behaviour across two temperature ranges (150–350 °C and 350–500 °C) and fitted to different reaction models. The results showed that first-order and diffusion models best described the degradation behaviour, with activation energies ranging from 66–190 kJ/mol. Notably, the CG/PP blend exhibited lower activation energies compared to the individual feedstocks, indicating enhanced reaction efficiency due to synergistic interactions. Mirzaei et al., (2026) applied the CR method to study the co-pyrolysis of microalgae Chlorella vulgaris (CV) and polyvinyl chloride (PVC). The analysis was conducted over 150–585 °C, and the data were fitted to various reaction models. The variation in kinetic models observed for CV, PVC, and their blends highlights the complex and multi-stage nature of thermal decomposition, particularly in mixed feedstock systems. For CV, the degradation behaviour is best approximated by a higher-order reaction model (F_n, $n \approx 4.1$). For PVC, the mechanism varies with conversion: the initial stage is best described by a nucleation model (A2), followed by a first-order model (F1) in the intermediate stage, and a second-order model (F2) in the final stage. While for the CV/PVC blend, the early stage follows a nucleation model (A2), transitioning to a first-order model (F1) at intermediate conversion. The activation energy for CV, PVC and CV/PVC blends ranging between 111.77–300.35 kJ/mol.

In catalytic co-pyrolysis of biomass and plastics, many studies have reported lower activation energies compared to non-catalytic systems due to the ability of catalysts to reduce the reaction energy barrier and promote bond cleavage. Wang et al., (2020) studied the co-pyrolysis kinetics of lignin (LG) and polyethylene (PE) in the presence of transition metal catalysts (Fe, Co, Ni, and Mn) using a first-order kinetic model fitted to TG data. The catalytic systems exhibited significantly lower activation energies (7.79–93.76 kJ/mol) than the non-catalytic LG/PE blend (29.61–101.43

kJ/mol). This behaviour was attributed to the catalytic role of transition metals in generating reactive oxygenated intermediates, facilitating polymer depolymerization, and strengthening interactions between biomass and plastic derived species. Similarly, Zheng et al., (2022) observed reduced activation energies during catalytic co-pyrolysis of bamboo and LDPE, with the CeZrAl catalyst producing the lowest value of 61.01 kJ/mol compared to 151.07 kJ/mol for the non-catalytic blend. The reduction indicates that the catalyst accelerated biomass conversion and improved the reaction rate, while a first-order reaction model well described the degradation behaviour. In contrast, Shahdan et al., (2022) reported a higher activation energy for catalytic co-pyrolysis of empty fruit bunch (EFB) and HDPE using treated rice husk ash (RHA-T) compared to the non-catalytic system, with a difference of 22.52 kJ/mol. Nevertheless, the catalytic system showed a pre-exponential factor approximately seven times higher than that of EFB/HDPE, indicating a much faster reaction rate that compensated for the higher energy barrier. The previous study regarding to kinetic analysis is summarized in Table 2.8.

Table 2.8
Comparison of Kinetic Parameters and Reaction Models for Biomass/Plastic Co-Pyrolysis With and Without Catalysts Using The Coats Redfern Method

Feedstock (catalyst)	**Model**	**Activation Energy (E, kJ/mol)**	**Pre-exponential factor (A, min^{-1})**	**Reference**
Coffee ground/PP	Diffusion	66.22 – 116.72	9.19×10^{1} – 3.68×10^{4}	(Jamaluddin et al., 2026)
Microalgae Chlorella vulgaris /PVC	Nucleation & first order	111.77 – 167.92	NA	(Mirzaei et al., 2026)
Lignin/PE (Fe, Co, Ni, and Mn)	First order	7.79 – 93.76	2.38×10^{-2} – 1.03×10^{6}	(Wang et al., 2020)
Bamboo/LDPE (CeZrAl)	First order	61.02	1.395×10^{6}	(Zheng et al., 2022)
Empty fruit bunch/HDPE (RHA-T)	Diffusion	84.91	9.66×10^{7}	(Shahdan et al., 2022)

Note: Polypropylene (PP), polyvinyl chloride (PVC), polyethylene (PE), high density polyethylene (HDPE), not reported (NA)

2.14 Summary

This chapter has reviewed previous and current studies on bio-oil production from biomass and plastics through catalytic pyrolysis. The review revealed significant research gaps in developing an effective heterogeneous catalyst that can exhibit high catalytic activity under moderate operating conditions, good reusability, and enhance the overall kinetics of the process.

Globally, the continuous increase in MSW, particularly biomass and plastic fractions, has become a serious environmental issue. The high dependence on fossil fuels further worsens the GHG emission and environmental degradation. Consequently, converting biomass and plastic waste into bio-oil through catalytic co-pyrolysis offers a sustainable route for waste valorisation and renewable fuel production. CFW is a cellulose-rich biomass, and PPW is a hydrogen-rich polymer, were identified as promising feedstocks. Previous studies were reported on the combination of biomass and plastic enables good interactions, where hydrogen transfer from PPW compensates for the oxygen deficiency in CFW, thus improving bio-oil yield and quality.

The literature has also emphasized the importance of catalysts in improving product selectivity via cracking, deoxygenation, and aromatization reactions. Metal oxides have shown enormous potential due to their acid–base properties, and availability. However, there remains a lack of research on utilizing industrial sludge as a low-cost and sustainable aluminium source for catalyst synthesis. Industrial sludge contains valuable metals such as aluminium, which are often underutilized and disposed of as waste. Therefore, this study introduces a novel approach by extracting aluminium from industrial sludge to synthesize metal oxide-supported catalysts, contributing both to waste minimization and circular economy principles.

Despite numerous studies on catalytic pyrolysis, critical knowledge gaps persist regarding the effects of catalyst preparation conditions, process operating parameters, catalyst reusability and regeneration, and reaction kinetics. Previous research has shown that variations in metal loading, calcination temperature, and calcination time significantly alter the catalyst's physicochemical properties, thereby influencing bio-oil yield and composition. However, these effects have not been comprehensively studied for catalysts derived from metal oxides incorporated on extracted aluminium supports, specifically on Cr, Ti and aluminium extracted from industrial sludge. Similarly, systematic studies on catalyst reusability and regeneration remain limited, despite their

importance for practical and sustainable applications. Moreover, a severe lack of kinetic analysis exists for the catalytic co-pyrolysis of CFW and PPW. Kinetic modelling is essential to quantify the reaction rate and identify the energy barrier. The absence of such information has hindered accurate prediction, optimization, and scale-up of the process.

Hence, this study aims to bridge these gaps by developing a metal oxide catalyst supported on aluminium extracted from industrial sludge, optimizing the catalyst preparation and process operating conditions, evaluating catalyst reusability, and conducting a comprehensive kinetic analysis of the catalytic co-pyrolysis of CFW and PPW. The outcomes of this work are anticipated to provide valuable insights into sustainable catalyst design, improved bio-oil production, and an understanding of the reaction kinetics governing catalytic co-pyrolysis.

CHAPTER 3
RESEARCH METHODOLOGY

3.1 Introduction

This chapter discusses the material, and methods used throughout the experimental work. Firstly, is the catalyst development, characterization, and catalyst activity evaluation. Next is the investigation of catalyst activity based on the effect of operating conditions, followed by the catalyst reusability and regeneration study. The kinetic model of the catalytic reaction is also presented. Section 3.2 provides the materials and equipment used in catalytic co-pyrolysis process and characterizations. The details on the synthesis process of metal oxides catalyst are outlined in Section 3.3. Section 3.4 describes the catalytic co-pyrolysis experimental setup. In section 3.5, the method of catalyst reusability and regeneration studies is explained. Lastly, section 3.6, gives information on the kinetic study of catalytic reactions. Figure 3.1 shows the schematic flow chart of the overall experimental work for the present study.

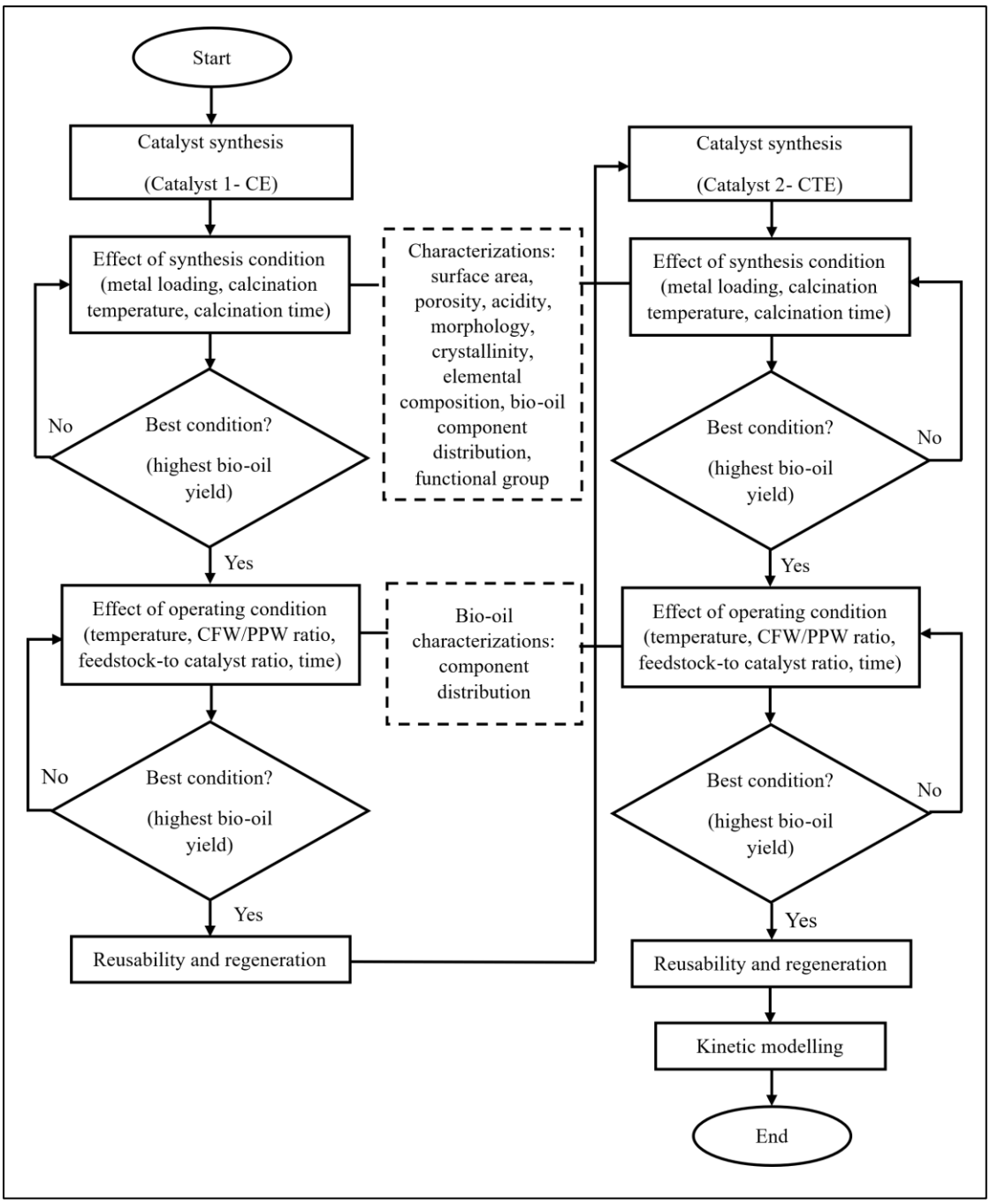

Figure 3.1 Flow Chart for Overall Process of Experimental Work

3.2 Materials and Equipment

The materials used in this study included feedstock, chemicals reagent and gas. All the reagents used were analytical grade unless otherwise specified. The materials and chemicals used in this study are discussed in section 3.2.1 and 3.2.3, respectively. The equipment used in this study are discussed in section 3.2.3.

3.2.1 Raw Material

The feedstocks used in the co-pyrolysis process comprised cotton fabric waste (CFW), which was collected from Toray Penfabric Sdn. Bhd. in Penang, and polypropylene plastic waste (PPW) sourced from discarded commercial PP food containers. The PPW is primarily composed of polypropylene, with minor additives as typically reported in standard polymer formulations. Prior to use in co-pyrolysis process, the CFW and PPW were cut into small pieces, approximately 2 cm x 2 cm. While the raw industrial sludge was collected from Kobe Precision Technology Sdn. Bhd. in Penang. Figure 3.2(a-c) shows the feedstock used in co-pyrolysis and industrial sludge.

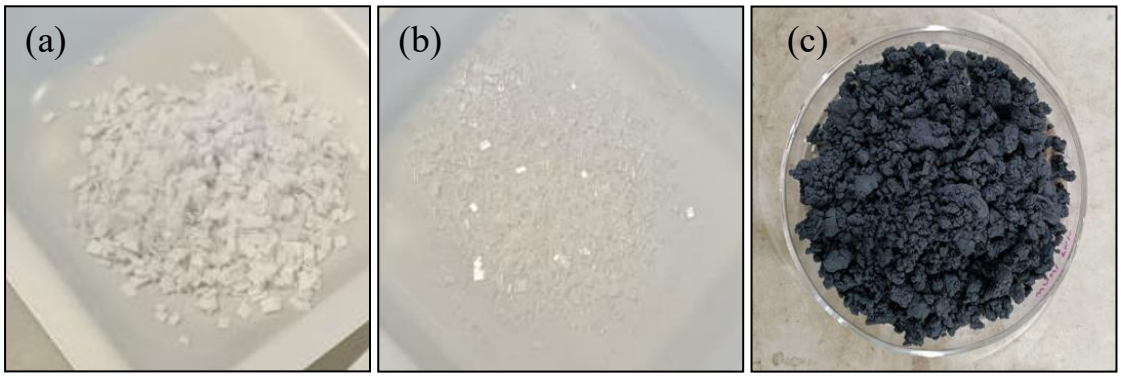

Figure 3.2 (a) Cotton Fabric Waste (CFW) and (b) Polypropylene Plastic Waste (PPW) and (c) Industrial Sludge

3.2.2 Chemicals and Gas

The chemicals used for synthesis catalyst are chromium (III) nitrate nonahydrate (98 % wt./wt.), sulfuric acid (97 % wt./wt.) and ammonium hydroxide solution (25 % wt./wt.) from QreC, and titanium (IV) butoxide (97 % wt./wt.) from Sigma Aldrich. Hexane and methanol were used as solvent while acetone for cleaning purposes. During the pyrolysis process, nitrogen gas (N_2) was used as an inert carrier. The summary of chemicals used is tabulated in Table 3.1

Table 3.1
Chemical Used in The Experiment at Work

No	Chemicals	Purity	Manufacturer	Function
1	Chromium (III) nitrate nonahydrate	98 % wt./wt.	QreC	Catalyst precursor
2	Sulfuric acid	97 % wt./wt.	QreC	Leaching
3	Ammonium hydroxide	25 wt./wt.	QreC	Precipitation
4	Titanium (IV) butoxide	97 % wt./wt.	Sigma Aldrich	Catalyst precursor
5	Hexane	99 % wt./wt.	QreC	Solvent used for catalyst cleaning in reusability study
6	Methanol	99.9 % wt./wt.	QreC	Solvent used to dilute bio-oil for GC-MS sample
7	Acetone	99.9 % wt./wt.	QreC	Cleaning
8	Nitrogen gas	99.999 %	AGS	Pyrolysis inert gas

3.2.3 Equipment

The feedstock was characterized for the proximate analysis using thermogravimetric analysis (TGA) and ultimate analysis using carbon, hydrogen, nitrogen, and sulphur elemental analyser (CHNS). During catalyst development, the equipment used includes universal oven, muffle furnace, vacuum pump, centrifuge and stirring hotplate. The metal composition of the dry sludge, EA, CE, and CTE catalysts were characterized by using x-ray fluorescence (XRF). The x-ray diffraction (XRD) was used to identify the metal crystallinity and phase. Meanwhile the textural properties of the catalyst such as specific surface area, total pore volume and average pore diameter of the catalysts were determined by N_2 adsorption-desorption technique (BET analyser). The morphology of the catalyst was carried out using a scanning electron microscope-energy dispersive x-ray (SEM-EDX). Furthermore, the acidity of the catalysts was investigated using temperature programmed desorption with ammonia (NH_3-TPD). The pyrolysis was conducted in fixed bed microreactor while the weight of the products (char, bio-oil) from pyrolysis process were measured by analytical balance. The bio-oil component distributions and functional groups were identified using gas chromatograph-mass spectrometer (GC-MS) and Fourier transform infrared spectroscopy (FTIR), respectively. The summary of equipment used is tabulated in Table 3.2.

Table 3.2
Equipments Used in The Experiment and Characterization

No	Equipment/instrument	Model	Function
1	Universal Oven	Memmert	Sludge/Catalyst Drying
2	Muffle Furnace	Carbolite	Catalyst calcination
3	Stirring Hotplate	IKA	Metal extraction and catalyst synthesis.
4	Vacuum pump	Rocker	Solution filtration
5	Centrifuge	Kubota	Separating solid-liquid solution
6	Microreactor	Micromeritic	Pyrolysis
7	Thermogravimetric Analyzer (TGA)	Mettler Toledo	Proximate analysis/thermal degradation
8	Carbon, hydrogen, nitrogen, and Sulphur (CHNS) elemental Analyzer	LECO CHNS analyser (Truspec® Micro CHNS, LECO, St. Joseph, MI, USA	Organic elemental composition
9	Energy Dispersive X-ray Fluorescence (XRF)	EDX-XRF, model Bruker M4 Tornado	Metal elemental analysis
10	X-ray Diffraction (XRD)	D8 Advanced, Bruker, USA	Crystalline phase
11	Nitrogen adsorption-desorption	ASAP 2020 Micromeritics	Surface area and porosity measurement
12	Scanning Electron Microscope-Energy Dispersive X-ray Spectroscopy (SEM-EDX)	Hitachi Regulus 8220 and Oxford EDX windowless 100 mm	Surface and microstructure analysis
13	Ammonia Temperatured-Programmed Desorption Analyzer (NH_3-TPD)	Micromeritics Autochem II 2920	Catalyst acidity
14	Fourier Transform-Infrared Spectroscopy (FTIR)	Perkin Elmer Frontier, United States)	Functional group
15	Gas Chromatograph-Mass Spectrometry (GC-MS)	GC-MS-QP2010 Ultra, Shimadzu	Bio-oil composition

3.3 Catalysts Synthesis

The catalyst development consists of preparation of EA, and synthesis of metal oxides catalyst according to synthesis conditions of metal loadings and calcination treatments. The performances in each parameter were based on one factor at time (OFAT). The OFAT approach enables a clear and systematic evaluation of the independent effect of each variable and is widely accepted for developing a fundamental

understanding of individual parameter influences (Taylor et al., 2023). The catalytic activities of each parameter were compared and used to determine the best conditions of the catalyst synthesis based on bio-oil yield. Then, the best conditions on evaluated parameters were used for subsequent parameters study.

3.3.1 Preparation of Extracted Aluminium

The EA was prepared by acid leaching method modified from Roslan et al., (2021). Initially, the semi-solid sludge was dried in an oven at 110 °C for 6 h. The resulting dried sludge (DS) was then ground into fine particles and sieved to obtain a particle size of less than 250 µm. Subsequently, 50 g of DS was subjected to acid leaching using sulfuric acid (H_2SO_4) at a solid-to-liquid ratio of 1:50 (g: mL). The leaching process was conducted at 70 °C for 1 h with continuous stirring at 450 rpm. The leachate was then left overnight, followed by filtration to obtain a clear solution. A 10 % ammonium solution (NH_4OH) was gradually added to the filtrate until reached pH 9, resulting in the formation of a white precipitate. The precipitate was thoroughly washed with deionized water until pH reached neutral and dried at 110 °C for 12 h. Finally, the dried material was calcined in a muffle furnace at 600 °C for 2 h with a heating rate of 5 °C/min. Figure 3.3 displays the EA extraction solution and EA after calcination.

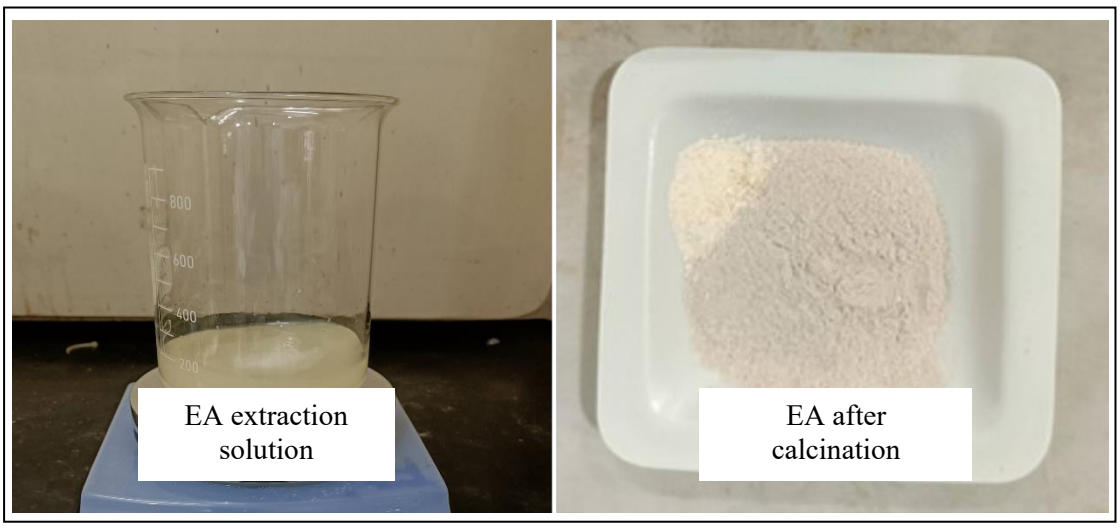

Figure 3.3 EA Extraction Solution and EA After Calcination

3.3.2 Synthesis of Chromium–Extracted Aluminium (CE) Catalyst

CE catalysts with varying Cr loadings (5 wt.%, 10 wt.%, 15 wt.%, and 20 wt.%) relative to the mass of EA were synthesized via the wet impregnation method as displayed in Figure 3.4. The metal loading range of 5 – 20 wt.% was selected based on commonly reported values in catalytic studies (Maneechakr & Karnjanakom, 2021), representing low to moderate loadings. This range enables systematic evaluation of metal content while avoiding excessively low loading with limited active sites and high loading that may affect dispersion.

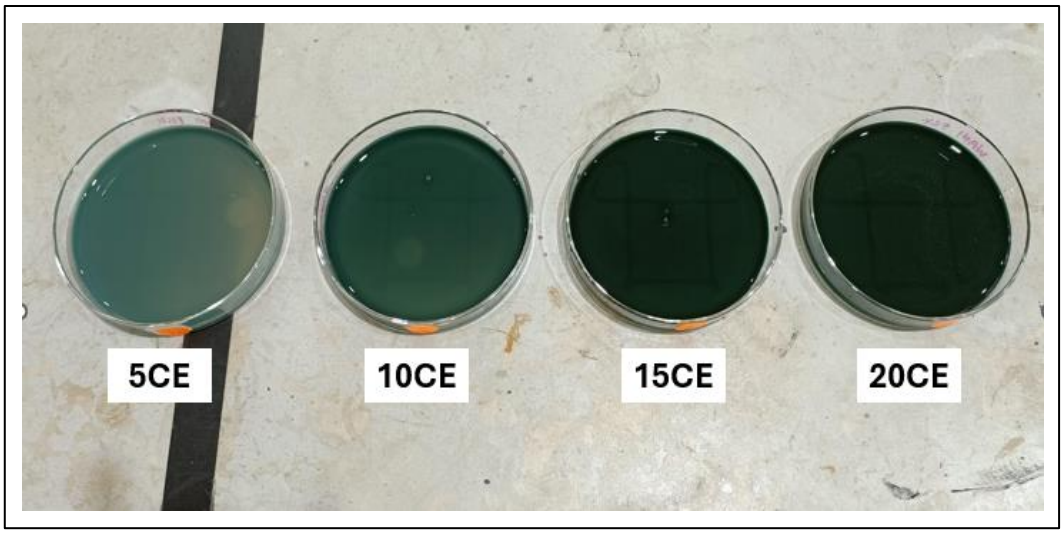

Figure 3.4 CE Catalyst at Different Metal Loadings

In typical synthesis of 5 wt.% loading, 1.154 g of precursor ($Cr(NO_3)_2 \cdot 9H_2O$) was dissolved in deionized water, followed by the addition of 3 g of EA into the solution. The mixture was stirred at 250 rpm using a magnetic stirrer for 4 h at room temperature. The resulting slurry was dried in an oven at 115 °C overnight. After drying completed, the sample was ground into a fine powder and subsequently calcined in a muffle furnace at 600 °C for 5 h with a heating rate of 5 °C/min. The prepared catalyst was designated as 5CE, indicating 5 wt.% Cr loading on EA. The same procedure was applied to synthesis other metal loadings and other synthesis conditions as shown in Table 3.3. The catalyst with varies calcination temperature was denoted as 5CE-T, while calcination time was denoted as 5CE-T-t. The T and t values indicated the variation of calcination temperature and time, respectively.

Table 3.3
Effect of Synthesis Condition for CE Catalyst

Catalyst preparation conditions	Values
Metal loadings (wt.%)	5, 10, 15, 20,
Calcination temperatures (°C)	400, 500, 600, 700, 800
Calcination times (h)	2, 3, 4, 5, 6

3.3.3 Synthesis of Chromium/Titanium–Extracted Aluminium (CTE) Catalyst

The synthesis of CTE catalyst was following the same procedures as CE catalyst. The $Cr(NO_3)_2 \cdot 9H_2O$ precursor was mixed with titanium (IV) butoxide ($Ti(OC_4H_9)_4$) precursor at chromium-to-titanium (Cr/Ti) weight loadings of 0:1, 1:1, 2:1, and 1:2, corresponding to a total metal loading of 15 wt. % relative to the mass of EA. The Cr/Ti weight loading (0:1 to 1:2) were selected based on commonly reported values of metal loading range of 5 – 15 wt.% in catalytic studies (Zulkafli et al., 2023). This range enables evaluation of the balance between catalytic activity and metal dispersion. Figure 3.5 displays the CTE catalysts at different metal loadings.

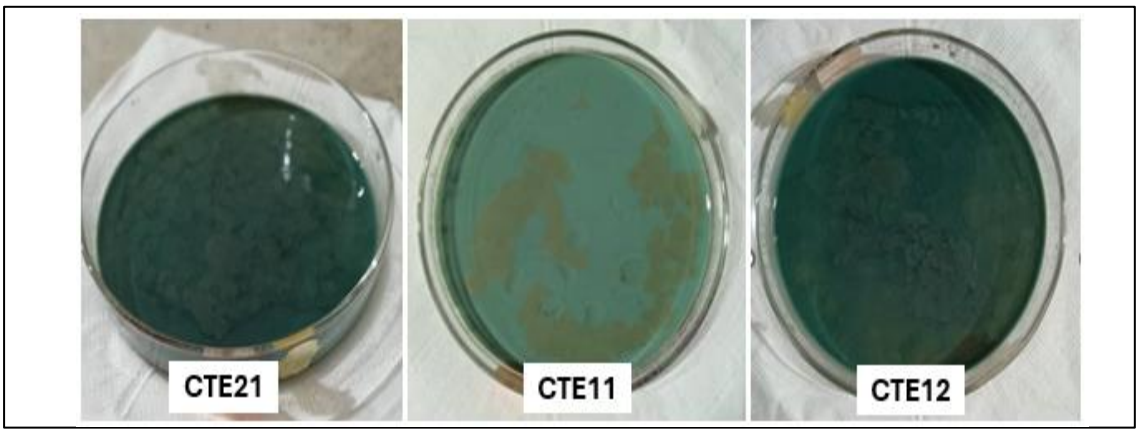

Figure 3.5 CTE Catalyst at Different Metal Loadings

The prepared catalyst was designated as CTE11, indicating 15 wt. % with 1:1 ratio of Cr/Ti loading on EA. In typical synthesis of CTE11 catalyst, 1.732 g $Cr(NO_3)_2 \cdot 9H_2O$ was diluted with 13mL distilled water and stirred slowly. Then, 1.6 mL $Ti(OC_4H_9)_4$ was added dropwise into Cr solution in a beaker and stir slowly prior to add EA on Cr/Ti solution. Subsequently, 3 g of EA was added to the mixture, and continuously stirred at 250 rpm using a magnetic stirrer for 4 h at room temperature. The resulting slurry was dried in an oven at 115 °C overnight. After drying completed,

the sample was ground into a fine powder and subsequently calcined in a muffle furnace at 600 °C for 5 h with a heating rate of 5 °C/min. The same procedure was applied to synthesis of other metal loadings and other synthesis conditions as shown in Table 3.4. The catalyst with varies calcination temperature was denoted as CTE11-T, while calcination time was denoted as CTE11-T-t. The T and t values indicated the variation of calcination temperature and time, respectively. The summary of the procedure describes in section 3.3.2 and 3.3.3 is displayed in Figure 3.6

Table 3.4
Effect of Synthesis Condition for CTE Catalyst

Catalyst preparation conditions	**Values**
Metal loadings (Cr:Ti)	0:1, 1:1, 2:1, 1:2
Calcination temperatures (°C)	400, 500, 600, 700, 800
Calcination times (h)	2, 3, 4, 5, 6

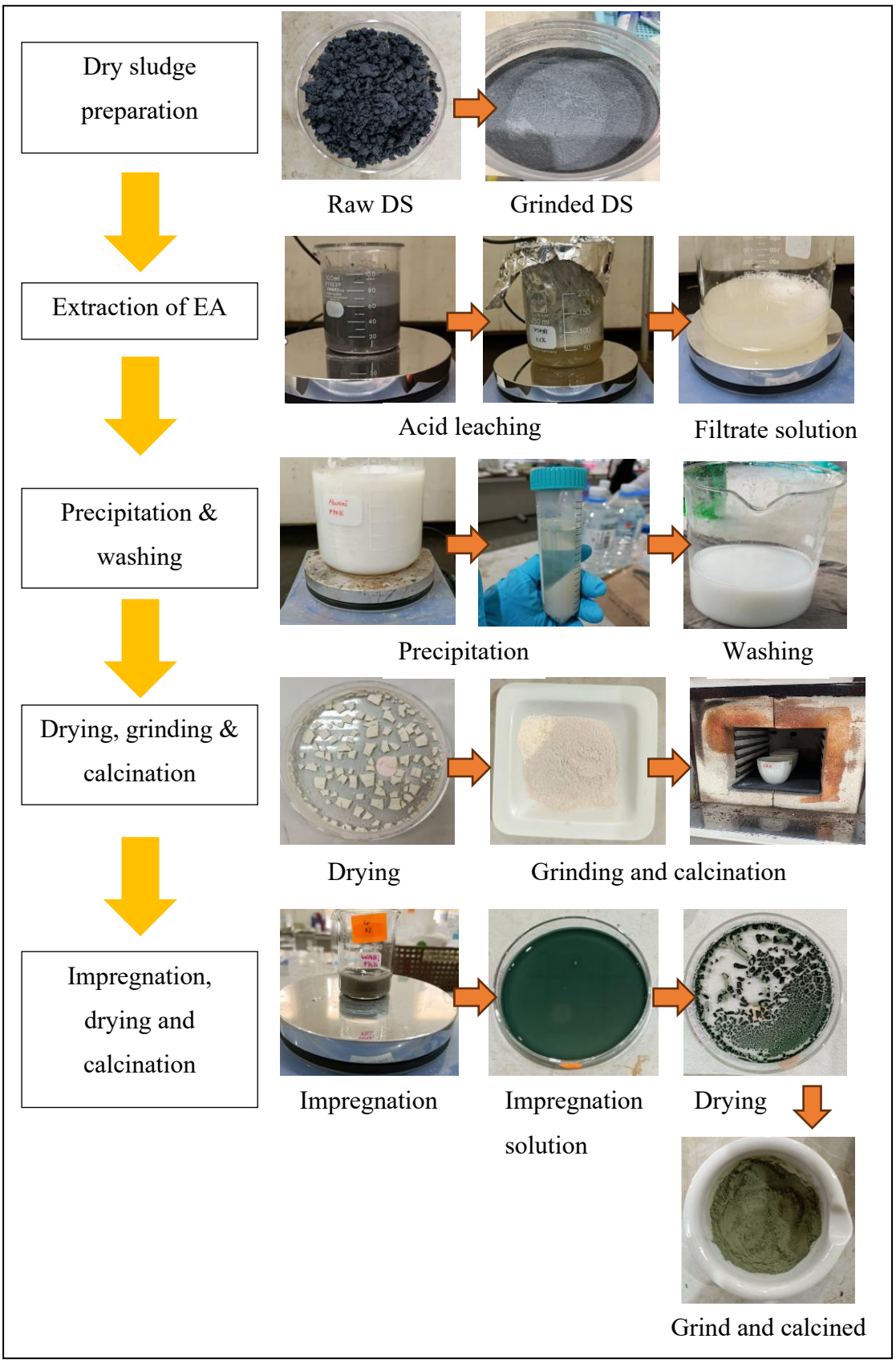

Figure 3.6 Overall Process of Catalyst Development

3.4 Catalyst Characterization

In the development of solid acid catalysts for bio-oil synthesis, several key characteristics are essential to evaluate their catalytic activity. The physicochemical properties including chemical composition, surface area, pore size, pore volume, surface acidity, surface morphology, and crystalline structure were investigated using various analytical techniques. The detailed characterization procedure is outlined in the following sub-sections.

3.4.1 X-ray Fluorescence (XRF)

XRF analysis was employed to determine the elemental composition of DS, EA, CE, and CTE catalysts. The measurements were carried out using a Bruker M4 Tornado XRF spectrometer. Prior to analysis, the samples were prepared as pressed pellets by mixing 1.5 g of powdered sample with 5.5 g of boric acid, followed by compression in a mould to form uniform pellets. The XRF analysis was conducted under vacuum conditions at a maximum power setting of 60 kV and 60 mA, utilizing a rhodium (Rh) x-ray tube. Each sample was exposed to x-ray irradiation for approximately 30 min. The resulting elemental spectra (in keV) were interpreted using SuperQ Panalytical software.

3.4.2 X-ray Diffraction (XRD)

The crystallite structure of the synthesized catalyst was examined by using x-ray Diffraction (XRD) method. The powder XRD patterns of the synthesized catalysts was analysed using XRD, D8 Advanced, Bruker, USA. The voltage and current were set to the desired data collection settings at 40 kV and 40 mA, respectively. The sample was scanned at scanning range of 2θ from 10° to 90° with Cu-Kα radiation (λ = 1.5406 Å) at scan speed of 0.04s. The peaks of the diffractogram were identified using Diffrac.suite software by referring to ICDD database.

3.4.3 Nitrogen Adsorption-Desorption

The nitrogen adsorption-desorption method was employed to analyse the textural properties of the catalyst. The surface area and porosity characteristics of the solid catalyst was determined from the adsorption-desorption isotherms of nitrogen using Micromeritics (Model ASAP 2020, US). Prior to analysis, the sample was degassed at 350 °C for 10 h under vacuum to remove physiosorbed molecules and prevent any significant changes due to surface modification. The degassed sample was then transferred to the analysis system and cooled in liquid nitrogen. The analysis was conducted at 77 K, where successive known amounts of the adsorptive were introduced allowing the system to reach equilibrium at each stage, forming a series of single points on the adsorption isotherm. The specific surface area of the solid catalyst was determined using Brunauer-Emmett-Teller (BET) method, while the pore size distribution (PSD) was analysed using the Density Functional Theory (DFT) technique.

3.4.4 Scanning Electron Microscope with Energy Dispersive X-ray (SEM-EDX)

The surface morphology and elemental distribution (%) of the catalysts were observed by surface scanning electron microscopy-energy dispersive x-ray (FESEM-EDX) using Hitachi Regulus 8220 and Oxford EDX windowless 100 mm model. The SEM scans a focused electron beam over a surface of a sample being analysed. The interaction of the electrons with the sample produces various signals that are collected by the appropriate detectors to form images. Prior to the analysis, the sample in powder form was dried and mounted on aluminium stubs using conductive carbon tape. Images were captured at magnification of x10,000. The surface morphology was analysed using secondary electron and backscattered electrons (SE-BSE) signals. The elemental composition and mapping were further confirmed using EDX detector.

3.4.5 Ammonia Temperatured Programme Desorption (NH_3-TPD)

The NH_3-TPD was employed to evaluate the surface acidity of the catalyst. The amount and temperature range of ammonia desorption provides insights into the total acidity and the strength distribution of acid sites (weak, medium, and strong) on the catalyst surface. The method is based on the measurement of desorption profile of a

preabsorbed probe molecule during control heating. The analysis was conducted using Micromeritics Autochem II 2920. A 50mg of sample was loaded and pre-treated under helium (He) gas stream (50 mL/min) and heated to 350 °C to remove impurities on the surface of the catalyst. A 5 % ammonia–helium gas mixture at 50 mL/min was flown through the sample at ambient temperature until saturated and held for 60 min before the sample was purged with the He gas. Subsequently, the ammonia (NH_3) desorption was monitored by TCD at temperatures ranging from 50 °C to 700 °C.

3.5 Experimental Procedure

The catalytic activity of the synthesized catalysts was assessed through the co-pyrolysis of CFW and PPW in a fixed-bed reactor. The product yields were quantified based on weight measurements. While the bio-oil component distributions and bio-oil functional group were analysed using gas chromatography–mass spectrometry (GC-MS) and Fourier transform infrared spectroscopy (FTIR), respectively.

3.5.1 General Operating Condition of Co-pyrolysis Reactions

A total of 1 g of feedstock, comprising a 1:1 weight ratio of CFW to PPW was prepared and loaded with an equal amount of catalyst (feedstock-to-catalyst ratio at 1:1) in the fixed-bed reactor. Nitrogen gas (N_2) was continuously supplied at a flow rate of 50 $mL \cdot min^{-1}$ to ensure an inert atmosphere and to function as a carrier gas for transporting volatile products from the reactor. The reactor was heated from an ambient temperature to 500 °C and maintained at this temperature for 60 min. The heating rate was automatically controlled to reach the desired temperature set point. A wax trap and a condenser, maintained at 120 °C and – 4 °C respectively, were used to cool and condense the volatiles. Quenching was not applied, as rapid cooling at – 4 °C in the integrated condenser was sufficient within the continuous system. Throughout the experiment, the operating conditions including the CFW-to-PPW ratio (1:1), feedstock-to-catalyst ratio (1:1), pyrolysis temperature (500 °C), and reaction time (60 min) were kept constant. Upon completion of the reaction, the reactor was allowed to cool, after which the condensed products collected from the wax trap and condenser were combined and weighed as bio-oil, while the residual solid char was also collected and

weighed (Zulkafli et al., 2024). The experiment was conducted twice to ensure the reliability and reproducibility of the results.

3.5.2 Fixed-bed Reactor System

The pyrolysis system consists of a tubular column equipped with electrical heating and cooling systems. The vertical fixed bed reactor column was constructed of 316 stainless steels with internal diameter and height of 2 cm and 5 cm, respectively. The column was arranged into ex-situ configuration to separate feedstock and catalyst. The upper stage consisted of feedstock (CFW and PPW) while to the bottom stage contained catalysts. Both stages were separated by quartz wool. The N_2 gas flowed through the feedstock and catalyst until it reached the outlet. The inert gas of nitrogen was used to ensure no oxygen was presence during the reaction. The temperature, level and pressure of the systems were controlled by PID controllers. After the reaction was completed, pyrolysis products such as bio-oil and residual char were collected and weight to calculate the yield. The products yield was calculated using equation 3.1 – 3.3 (Zulkafli et al., 2024).

$$\text{Char (wt.\%)} = \frac{W_{\text{char}}}{W_{\text{feedstocks}}} \times 100 \tag{3.1}$$

$$\text{Bio-oil (wt.\%)} = \frac{W_{\text{bio-oil}}}{W_{\text{feedstocks}}} \times 100 \tag{3.2}$$

$$\text{Gases (wt.\%)} = 100 - (\text{bio-oil yield}) - (\text{char yield}) \tag{3.3}$$

The bio-oil was collected in wax-trap and condenser (bio-oil), while the residual char was collected after each experiment. After each pyrolysis is completed, the reactor system was washed with acetone to remove impurities and avoid contamination for subsequent experimental run. The catalytic co-pyrolysis of CFW and PPW was conducted using experimental setup shown in Figure 3.7.

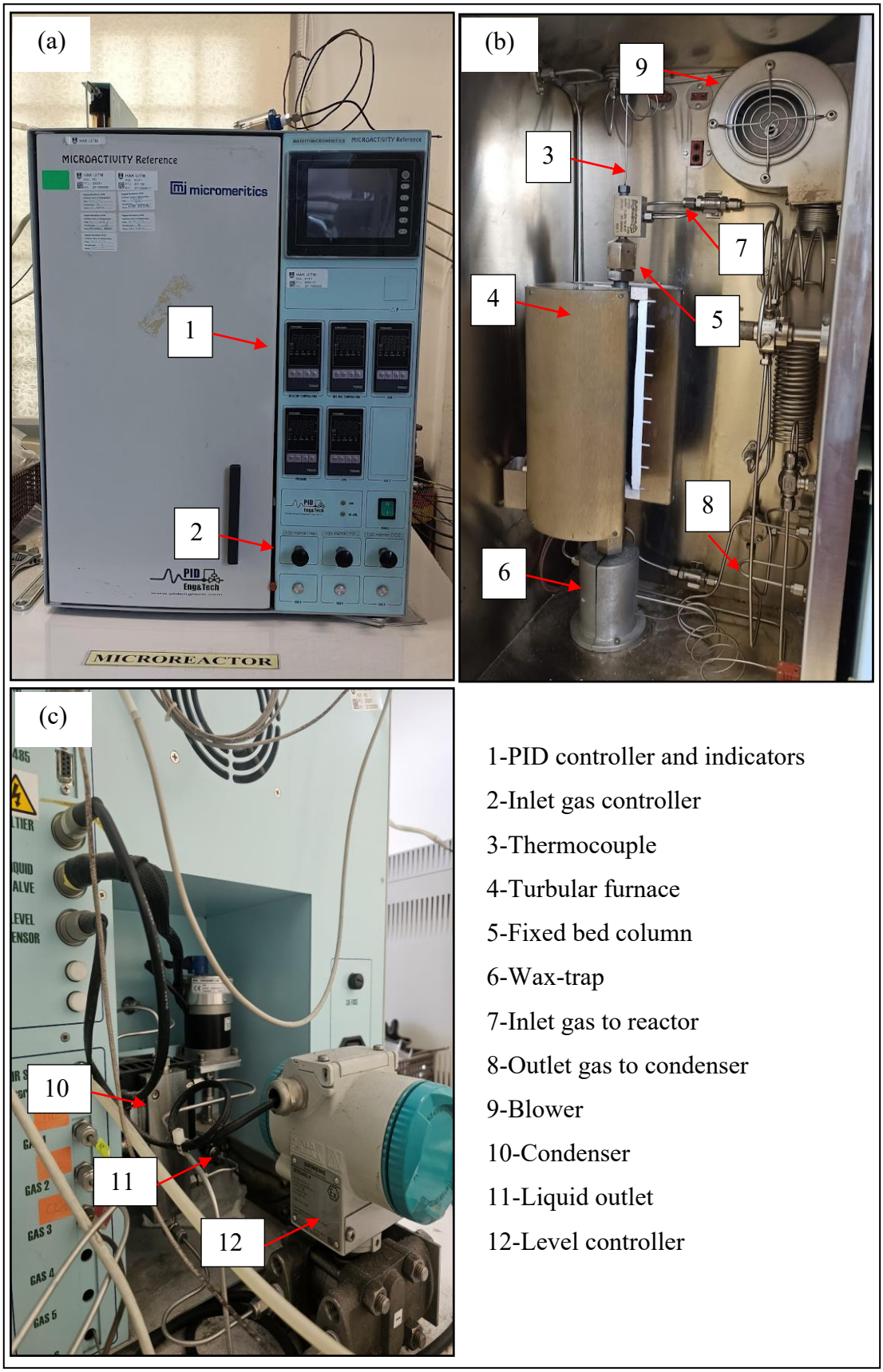

Figure 3.7 Experimental Setup for The Reaction System (a) Reactor Controllers (b) Gas Flow and Heating System (c) Condenser System

3.5.3 Experimental Study on Effect of Catalysts Synthesis Conditions

The co-pyrolysis of CFW and PPW was conducted at constant operating conditions to evaluate the effect of catalyst synthesis conditions as outline in Table 3.4 and Table 3.5. In a typical experimental run, a total of 1 g of feedstock (CFW/PPW) was loaded with 1 g of catalysts in fixed bed reactor. The reactor was conducted at constant operating condition of pyrolysis temperature (500 °C), CFW/PPW ratio (50:50), F/C ratio (1:1), and pyrolysis time (60 min). Upon completion of the reaction, the products gas, char, and bio-oil were collected and measured.

3.5.4 Experimental Study on Effect of Process Operating Conditions

In the study of process operating conditions, the pyrolysis temperature, CFW/PPW ratio, F/C ratio and pyrolysis time were considered. The parameter was varied according to Table 3.6. The product yield for char, bio-oil and gas was calculated using equations 3.1–3.3. The constant process parameters used in this study is same as parameter used during evaluation of catalytic activities for catalyst synthesis, which includes 500°C pyrolysis temperature, 50:50 CFW/PPW ratio, 1:1 F/C ratio and 60 min of pyrolysis time. The catalytic activities of each parameter were compared and used to determine the best conditions of the process operating conditions based on bio-oil yield. Then, the best conditions on evaluated parameters were used for subsequent parameters study.

Table 3.5
Experimental Conditions for Catalyst Reaction Study for CE and CTE Catalyst

Operating conditions	**Range of values**
Pyrolysis temperature (°C)	450, 500, 550, 600, 650
Pyrolysis time (min)	15, 30, 45, 60, 75
CFW/PPW ratio	80:20, 60:40, 50:50, 40:60, 20:80
F/C ratio	2:1, 1:1, 1:1.5, 1:2

3.6 Feedstock and Product Characterization

3.6.1 Thermogravimetric Analyzer (TGA)

The proximate analysis was conducted using thermal gravimetric analyser model TGA/ SDRA51e, Mettler Toledo. The analysis is used to measure the mass changes in the sample and identify the quantity of moisture, volatile matters, fixed carbon and ash by time and changes of temperature. The proximate analysis was performed in accordance with ASTM D 5142-02a. The sample was ramped from 30 to 950 °C, at heating of 20 °C/min under inert gas (nitrogen), followed by switching to oxidative gas (air) flowing at 100 ml/min until the heating completes up to 1100 °C. The H/C effective and calorific value was calculated based on equation 3.4 (Alcazar-Ruiz et al., 2022) and Dulong equation 3.5 (Xu et al., 2022).

$$H/C_{eff} = \frac{H - 2O - 3N - 2S}{C} \tag{3.4}$$

$$HHV\ \left(\frac{MJ}{kg}\right) = 0.3578C + 1.1357H - 0.0845O + 0.0594N + 0.119S \tag{3.5}$$

3.6.2 Gas Chromatography-Mass Spectrometer (GC-MS)

The chemical compound of liquid product was identified using gas chromatography-mass spectrometry (GC-MS, model QP2010 Ultra, Shimadzu). The product distribution of bio-oil was performed using BPX5 capillary column (29.5 m × 0.25 mm × 0.25 mm). High purity helium (99.99 %) was used as carrier gas with flow rate of 1.0 mL/min. About one microliter of bio-oil sample was injected into GC with split ratio of 2:1. The oven temperature was set at 50 °C for 2 min, then ramped at rate of 3 °C/min to 280 °C and held isothermally for 20 min. Identification of the compounds from chromatographic peaks was achieved according to the NIST library. Semi-quantitative and classification of each compound was performed to determine the bio-oil component distributions.

3.6.3 Fourier Transform Infrared (FTIR) Spectroscopy for Bio-oil Analysis

The functional group of chemical compounds in bio-oil was characterized using FTIR spectroscopic analysis. The FTIR analysis was performed using Perkin Elmer Frontier, Unites State with ACD/Spectrus Processor 2020.2.0 software. A small quantity of the sample was placed onto attenuated total reflectance (ATR) crystal, and the sample is then subjected to infrared radiation across the broad spectral range of 4000 cm^{-1} to 600 cm^{-1}. The resulting spectrum reveals transmittance peaks corresponding to specific vibrational modes of molecular bonds to identify key functional groups.

3.7 Catalyst Reusability and Regeneration

The reusability and regeneration test of the as-synthesized catalysts were conducted at best operating conditions which obtained based on the maximum bio-oil yield produced during co-pyrolysis of CFW and PPW. In the reusability test, the spent catalyst was washed with solvent (hexane) before use for the next co-pyrolysis process. The catalyst activity in terms of bi-oil yield was observed for 3 cycles. In regeneration study, the catalyst that was recovered from the first reaction cycle of catalytic reaction, wash with hexane and calcined with air using muffle furnace at the best synthesis conditions for calcination. Then, the catalyst is ready to be used for the next co-pyrolysis reaction. The cycle was repeated until 3 cycles.

3.8 Kinetic Modelling

The kinetic modelling of solid materials during co-pyrolysis of CFW–PPW was adapted to analyse the behaviour of the solid-state experimental condition. In solid state the overall process can be represented by general kinetic decomposition equation in a constant heating rate (β) by equation 3.6 (Zaker et al., 2019).

$$\text{feedstock /catalyst} \xrightarrow{k(t)} \text{residue + volatiles (gas and tar)} \tag{3.6}$$

The reaction rate of non-isothermal solid decomposition $d\alpha/dt$ is a function of progress of the reaction, is described by equation 3.7 and the conversion of feedstock

α, can be calculated by equation 3.8 (Mohamed et al., 2023). Where W_o (mg) is the initial weight, W_f (mg) is the weight at the end of reaction and W_t is the weight at time (t).

$$\frac{d(\alpha)}{dt} = k(T)f(\alpha) = A\,exp\left(\frac{-E}{RT}\right)(1-\alpha)^n \tag{3.7}$$

$$\alpha = \left(\frac{W_o - W_t}{W_o - W_f}\right) \tag{3.8}$$

The primary goal of pyrolysis and co-pyrolysis kinetic modelling is to calculate the kinetic parameters which are activation energy value (E) and pre-exponential factor value (A) as well as the reaction mechanism *f*(α) using mathematical model. The k(T) is dependent on the activation energy (E) as describe by Arrhenius law. The temperature (T) is a reaction temperature in kelvin, k is rate constant, A is the pre-exponential factors (s^{-1}), E is the activation energy (kJ/mol) and R is the gas constant (0.008314 $mol^{-1}\cdot K^{-1}$). The *f*(α) is a differential form of the kinetic mechanism and usually is expressed as $(1-\alpha)^n$, where n is the reaction order and α is a dimensionless measurement of the amount of reactant that have been converted into products (Zaker et al., 2019).

Equation 3.7 is the basic kinetic formulation for computing the kinetic parameters based on TGA data. Non-isothermal TGA method is most often selected over the isothermal TGA method since fewer data are required to determine the reaction kinetics (Luo et al., 2020). The value of n, E and A, in equation 3.7 were determined using parameter estimation technique using n^{th} order reaction model. The equation 3.7 was solved using ODE solver (ode23s) in MATLAB to simulate the evolution of conversion rate over time. The parameter estimation was carried out through numerical integration of a rate based ordinary differential equation (ODE) and optimization to minimize error between experimental and simulated conversion rates. The detail steps involved in kinetics modelling of co-pyrolysis of CFW and PPW is elucidated in section 3.8.1, 3.8.2 and 3.8.3.

3.8.1 TGA Data Collection and Pre-processing

The pyrolysis of CFW and PPW alone, the co-pyrolysis of CFW–PPW with 50 wt. % mixture and co-pyrolysis of CFW–PPW with CTE21-700-5 catalyst were

conducted using TGA instrument. A 10 mg ± 0.8 of samples was load into aluminium crucible in TGA. The degradation of the feedstock was conducted at constant heating rate (β) of 40 °C/min and was thermally heated from 30 °C to 900 °C with nitrogen flow of 50 mL/min. The TG and derivative thermogravimetric (DTG) of each sample were recorded and the active decomposition phase from DTG plot during the degradation was used to determine the kinetic model. The t, T and α data were identified and calculated to load in algorithms based on kinetics model describe in equation 3.7 (Mohamed et al., 2023).

3.8.2 Parameter Estimation of Kinetics Parameter (E, A, and n)

The decomposition kinetics in equation 3.7 were modelled using the general n^{th} order rate law. The equation was solve numerically using ode 23s solver to simulate the evolution of dα/dt. In the parameter estimation, the objective function was defined to minimize the sum of square errors (SSE) between the experimental and simulation as described in equation 3.9 (Cheung et al., 2001).

$$SSE=\sum_{i=1}^{N}\left(\alpha_{exp,i}-\alpha_{sim,i}\right)^2 \tag{3.9}$$

The fmincon function with the interior-point algorithm in MATLAB was used for minimization and subject to the following boundaries of lower bound and upper bound:

1. $A \in [\,10^1, 10^6]\ s^{-1}$
2. $E \in [\,1, 200]$ kJ/mol
3. $n \in [\,0.1, 3]$

The algorithm used to execute the determination of kinetic parameters via parameter estimation technique is presented in Figure 3.8. The algorithm used in MATLAB was provided in **APPENDIX 3**.

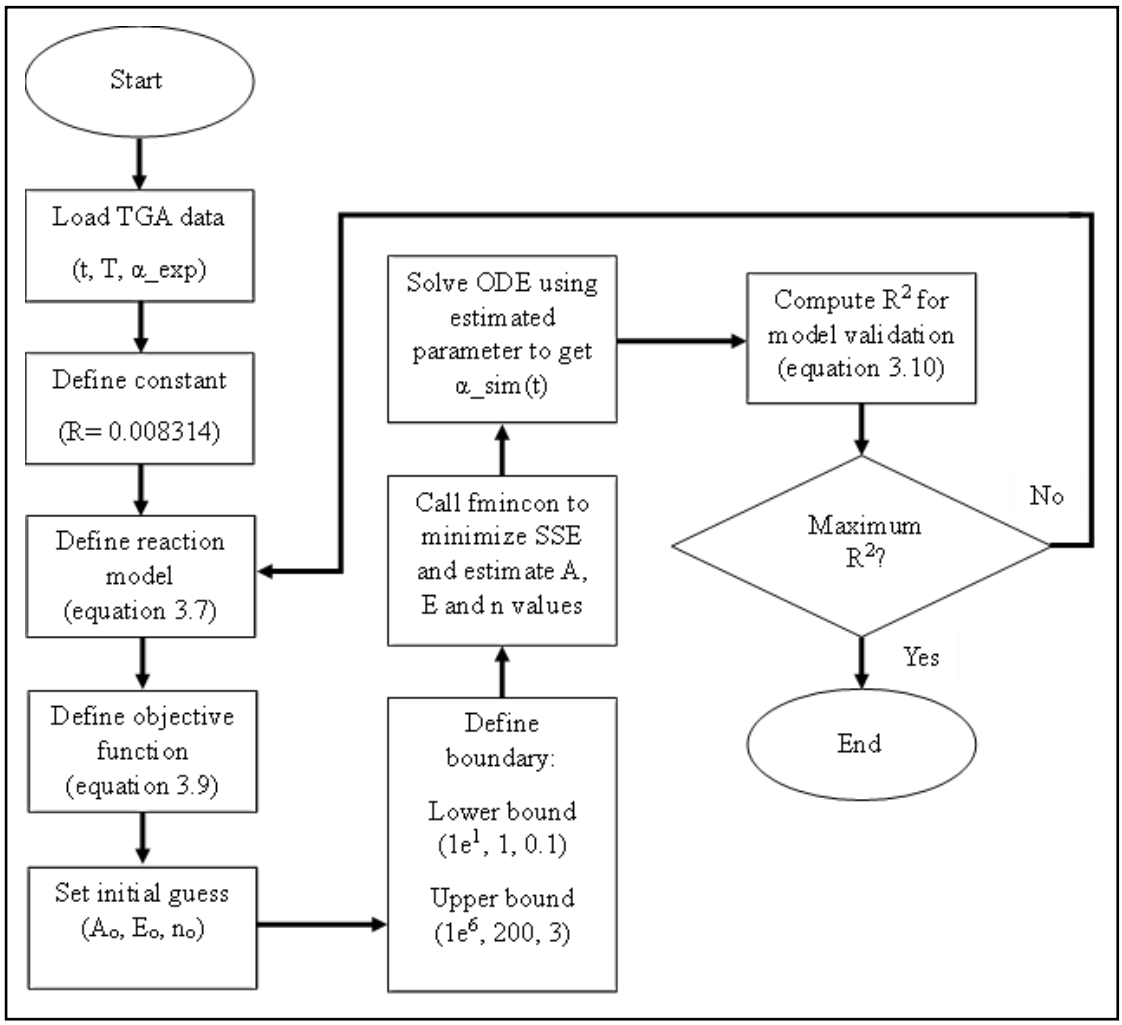

Figure 3.8 Flowchart Algorithm of Kinetic Model using Parameter Estimation Technique

3.8.3 Model Validation

The model with optimum E, A and n parameters was simulated and compared with the experimental data. The coefficient of determination (R^2) was used to validate the model accuracy and calculated as expressed in equation 3.10 (Zaker et al., 2021). The $\bar{\alpha}_{\text{exp}}$ is the mean of the experimental conversion rates, $\alpha_{\text{exp},i}$ is the experimental conversion rates and $\alpha_{\text{sim},i}$ is the simulation conversion rate. A regression plot of experimental and simulated data was used to evaluate the model accuracy. The R^2 is in range between 0 and 1. The best fitted at $R^2 > 0.95$ was chosen to obtain the E, A, and n values.

$$R^2 = 1 - \frac{\sum_{i=1}^{N}(\alpha_{exp,i} - \alpha_{sim,i})^2}{\sum_{i=1}^{N}(\alpha_{exp,i} - \bar{\alpha}_{exp})^2} \tag{3.10}$$

3.9 Summary

The catalytic pyrolysis of biomass and plastic (CFW and PPW) is highlighted in this chapter. The EA is extracted from aluminium sludge and modify with Cr and Ti with catalyst synthesis formulation denoted as CE and CTE, respectively using wet impregnation technique. The synthesis conditions such as metal loading, calcination temperature and time were varied in each synthesis method. The catalyst activities were evaluated during co-pyrolysis of biomass and plastic in fixed bed reactor. The best catalyst from synthesis conditions was subjected to series of reaction that varies in pyrolysis conditions including pyrolysis temperature, CFW/PPW ratio, F/C ratio, and pyrolysis time. The feedstock, catalyst and products were analysed using appropriate analysis technique and equipment. Then the reusability and regeneration capability of the catalyst was identified. Finally kinetic model for CFW, PPW, CFW/PPW and CFW/PPW with catalyst were obtained through parameter estimation technique. The results obtained from the analysis are discussed in chapter 4.

CHAPTER 4
RESULTS DISCUSSION

4.1 Introduction

This chapter presents the results and discussion obtained from experimental works involving the aluminium extraction from industrial sludge, catalysts synthesis, characterization, and catalytic activities in the reaction of co-pyrolysis of cotton fabric waste (CFW) and polypropylene plastic waste (PPW) to produce bio-oil. The results also include the reusability investigation of the synthesized catalysts and the kinetic modelling of the catalytic reactions. The research findings are discussed accordingly as outlined below:

a) Feedstocks characterization based on proximate analysis, ultimate analysis, and thermal gravimetric analysis (TGA).
b) The catalyst developments for chromium–extracted aluminium (CE) and chromium/titanium–extracted aluminium (CTE)
c) The catalyst activities in the bio-oil production via co-pyrolysis of CFW and PPW based on the effects of preparation conditions (metal loading, calcination temperature, and calcination time)
d) The characterization of the synthesized catalysts, based on the physical and chemical properties (elemental compositions, surface area, porosity, acidity, crystallite structures, and surface morphologies).
e) The catalyst activities in the reaction by variation in the operating conditions (pyrolysis temperature, biomass-to-plastic ratio, feedstock-to-catalyst ratio, and pyrolysis time) for the co-pyrolysis of CFW and PPW.
f) The reusability and regeneration of the as-synthesized catalysts.
g) The kinetic modelling for co-pyrolysis of CFW and PPW, catalysed by CTE catalyst.

4.2 Feedstocks Characterization

4.2.1 Proximate and Ultimate Analysis of CFW and PPW

The characteristics of CFW and PPW were analysed by proximate and ultimate analysis as shown by Table 4.1.

Table 4.1
Proximate and Ultimate Analysis of The Biomass (CFW) and Plastic (PPW)

	CFW	**PPW**
[a]Proximate Analysis		
Fixed carbon	3.9	0.0
Volatile	93.1	97.3
Ash	3.0	2.7
[a]Ultimate analysis		
C	44.7	85.8
H	6.2	13.5
N	0.5	0.1
S	0.0	0.0
O[b]	48.6	0.6
H/C_{eff}	0.0	1.9
HHV (MJ/kg)	17.9	45.8

[a] Dry basis (wt.% db.)

[b] Obtained by different [Oxygen (%) =100 − (C + H + N + S)]

The proximate analysis in dry basis revealed that the feedstock used in co-pyrolysis contains high volatile matter, which are 93.1 % and 97.3 % for CFW and PPW, respectively. This finding indicated the CFW and PPW were suitable to be used as feedstock and can produce more bio-oil during pyrolysis. Moreover, the fixed carbon is only observed for CFW which indicate the residue is from CFW. The moisture content of CFW is below 10 % which indicates the effectiveness of co-pyrolysis. Previous study has shown that the biomass pyrolysis is enhanced when the moisture of the substances is less than 10 % (Ghorbannezhad et al., 2020).

The ultimate analysis shows that the CFW contains high oxygen (48.6 %) which likely to produce oxygenates compound in bio-oil while exceptionally low oxygen (0.6 %) found in PPW. The CHNO composition of CFW and PPW are consistent with

findings from another researcher (Bagheri et al., 2020; Engamba Esso, Yan, et al., 2022; Kwon et al., 2021). The analysis indicates that the low H/C_{eff} value (0.0) of CFW reflects a deficiency of effective hydrogen, which contributes to its low higher heating value (17.9 MJ/kg) due to the high oxygen and low hydrogen content. In contrast, high H/C_{eff} value (1.9) of PPW indicates its richness in carbon and hydrogen and the calorific value is also high (45.8 MJ/kg). Thus, confirming the PPW is appropriate to use as co-feeding material for co pyrolysis with CFW (Nandakumar et al., 2023).

4.2.2 Thermal Degradation Characteristics of Feedstocks using TGA

The weight loss profile of CFW, PPW, and CFW/PPW (50:50) mixtures over temperature in a N_2 atmosphere (inert) obtained by TGA is illustrated in Figure 4.1(a-c). The TG and DTG of CFW was thermally decomposed at two different range as shown in Figure 4.1(a). The first range was thermally degraded early up to 150 °C and can be associated with the loss of water. The second decomposition was observed between 283 °C to 401 °C, and the mass loss rate reaches its maximum at 379 °C in the DTG curve.

The decomposition of PPW happen at single sharp peak between 365 °C to 491 °C and at a maximum DTG peak of 459 °C as shown in Figure 4.1(b), indicating rapid devolatilization with minimal residue. The decomposition temperatures of CFW and PPW were close to those of cellulose and polypropylene studied by Xing et al., (2025), ranging from 290 °C to 375 °C and 390 °C to 480 °C, respectively. The difference rises from the greater bond dissociation energy of C–C bonds in the main chain of plastics, compared to glycosidic bonds in cellulose (Li et al., 2024).

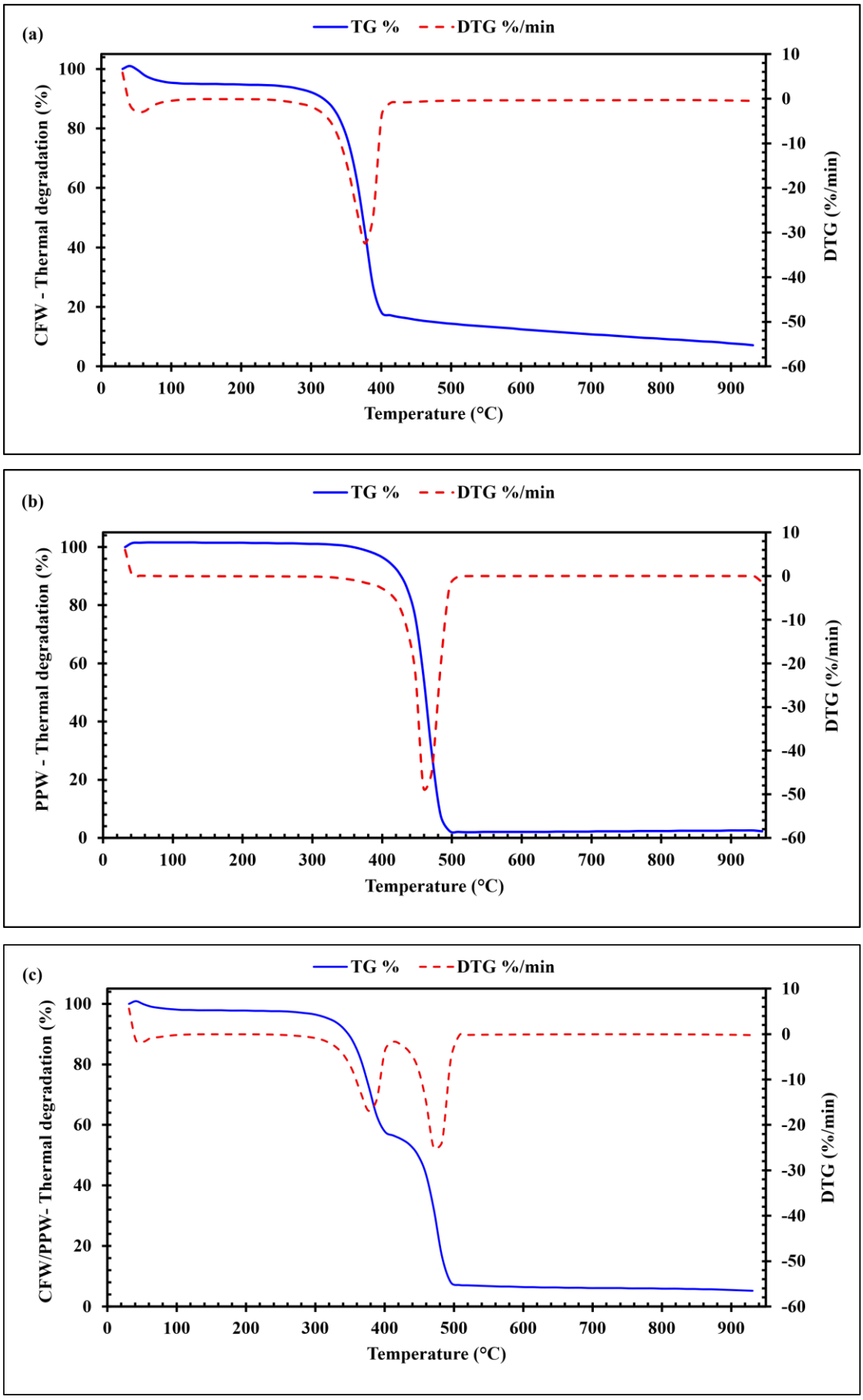

Figure 4.1 TG and DTG of Feedstock (a) CFW (b) PPW (c) CFW/PPW 50:50 Ratio

The TG analysis of the CFW/PPW mixture as shown in Figure 4.1(c) exhibits two distinct weight loss curves. The first corresponds to the primary decomposition of CFW starting at 295 °C, followed by the decomposition of PPW and the remaining CFW, reaching a peak at 476 °C, slightly higher than that of PPW alone. The shift in peak temperatures during co-pyrolysis of CFW (377 °C) and PPW (476 °C) is attributed to the early melting of PPW at approximately 95 °C, which forms a layer around CFW and delays its decomposition. In addition, cellulose in CFW decomposes completely at around 400 °C, and the resulting biochar may hinder heat transfer, leading to a higher decomposition temperature for PPW (Wen et al., 2021). Since the significant loss of CFW and PPW completed near 500 °C, thus pyrolysis temperature is considered at 500 °C for higher bio-oil production from co-pyrolysis of CFW and PPW. Moreover, the difference between the DTG peaks of individual PPW and CFW with CFW/PPW mixture suggests a there is an interaction between CFW and PPW during thermal decomposition, a phenomenon also reported by Zhang et al., (2021). The addition of PP initiated the degradation process, as indicated by the reduction in the initial degradation temperature. However, a shift in the final degradation temperature was observed, due to molten PP encapsulating the chilli straw (CS) particles and delaying their decomposition. Although distinct degradation stages were identified, the synergistic interaction between biomass and plastic is not solely reflected by the maximum mass loss rate but is also evident in the product distribution and kinetic behaviour (Jamaluddin et al., 2026).

4.3 Development of The Metal Oxide Catalysts

4.3.1 Synthesis of Chromium Extracted Aluminium (CE) Catalyst

The CE catalyst was synthesized using a wet impregnation method with different formulations as shown in Table 4.2. All the samples were prepared by fixed calcination condition of 600 °C for 5 h.

Table 4.2
The Catalyst Prepared Using Various Chromium Loading on EA by Weight

			Amount of each metal (g)	
Sample	**Cr loading (wt. %)**	**Catalyst formula**	**Cr**	**EA**
1	0	EA	0	3
2	100	Cr	3	0
3	5	5CE	0.15	3
4	10	10CE	0.3	3
5	15	15CE	0.45	3
6	20	20CE	0.6	3

4.3.2 Effect of Metal Loadings on CE Catalyst Activity

The catalysts were prepared accordingly based on Table 4.2 and were used in the co-pyrolysis of CFW and PPW at constant reaction conditions to compare their activities. The products from the co-pyrolysis, which consist of solids, liquid and gas, were evaluated in terms of their product yield (char, bio-oil, gas) and bio-oil component distributions as shown in Figure 4.2(a-b). The chemical component includes HC, aromatic hydrocarbon (aromatic HC), alcohol, phenols, furans, carbonyl (ketone and aldehyde), acid, sugar, ester, and other oxygenate and non-oxygenate compounds.

The comparison between pyrolysis of CFW alone and co-pyrolysis of CFW/PPW without catalyst indicate that reaction improved the bio-oil yield at 14.7 %. The findings due to the radicals produced from the pyrolysis of CFW alone was not capped by hydrogen due to the absence of hydrogen donor and promoting retrogressive reactions such as repolymerization and condensation. Thus, resulting in high char yield of 17.1 % and incomplete conversion into volatiles. In contrast, the co-pyrolysis of CFW with PPW provides an additional source of hydrogen from the thermal degradation of polypropylene. The availability of hydrogen radicals facilitating the stabilization of biomass-derived radicals. These supressing retrogressive reactions and enhances the formation of condensable volatiles. As a result, the char yield decreases significantly to 9.1%, while the bio-oil yield increases to 46.2% compared to CFW alone. The similar findings is observed in the study conducted by Berthold et al., (2023), where the char was contributed by the retrogressive reaction of unstable O-radicals originated from biomass. The hydrogen transfer from plastics stabilized O-radicals that reducing the char formation.

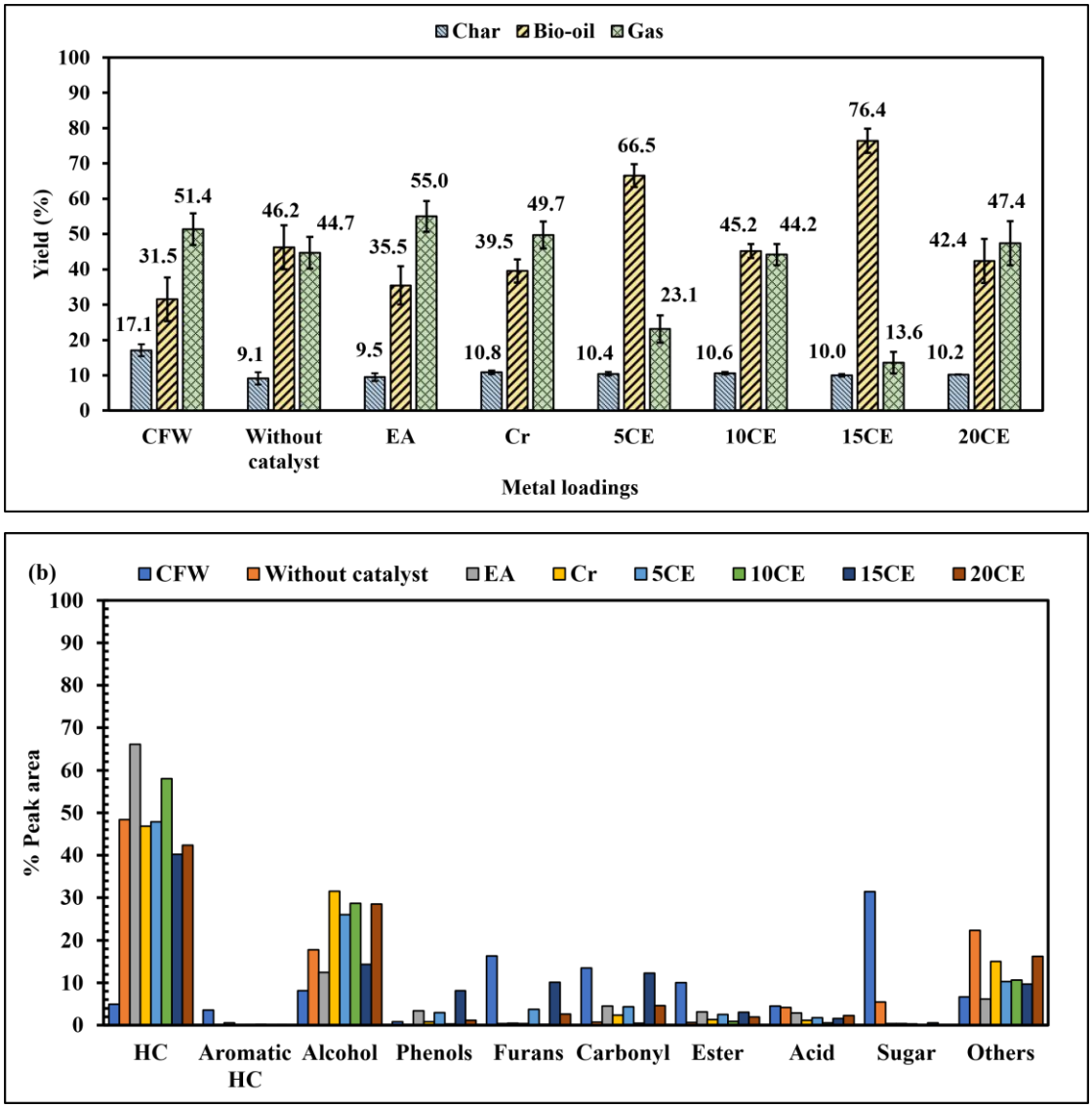

Figure 4.2 Effect of Metal Loadings on CE Catalyst Activity (a) Yield % (b) Bio-oil Component Distributions (Operating Condition: 500 °C Pyrolysis Temperature; 60 min Pyrolysis Time; 50:50 CFW/PPW Ratio; 1:1 F/C Ratio)

Figure 4.2(b) depicted that CFW produced high oxygenated chemical compounds compared to CFW/PPW mixture. CFW which contains cellulose and hemicellulose were decomposed and resulted in oxygenated compounds like anhydro sugars, furans, carbonyl, carboxylic acids, and alcohol as the main product. Wang et. al., (2021) observed that the decomposition of holocellulose from flax textile waste produces more alcohol and carbonyl, as well as a significant quantity of furans. In contrast, degradation of PPW resulted mainly in aliphatic hydrocarbons (HC) (Ojha & Vinu, 2015). Co-pyrolysis of CFW and PPW enhanced the production of hydrocarbons and alcohols. During the process, CFW decomposes earlier to form oxygenated radicals, while PPW degrades at higher temperatures to generate hydrogen-rich radicals. These

species can interact within the overlapping temperature range and during secondary vapor-phase reactions, enabling cross-hydrogen abstraction that stabilizes biomass-derived radicals. This interaction promotes β-scission of cellulose-derived intermediates, leading to the formation of lighter products compared to individual biomass pyrolysis (Suriapparao et al., 2014). Alam et al., (2020) also reported that the synergistic interaction between biomass and plastic mainly occurs during secondary reactions. At lower temperatures, molten plastic may encapsulate the biomass and restrict the release of volatiles. Upon further heating (>280 °C), rapid decomposition of plastic generates volatiles that disrupt this layer, thereby enhancing the release of biomass-derived products.

During the co-pyrolysis of CFW/PPW, various catalysts were investigated which are EA, Cr, and CE with different metal loadings. The activity of EA and Cr catalysts indicates enhanced secondary cracking of the volatiles produced from thermal cracking, although the bio-oil yield was slightly reduced compared to co-pyrolysis without catalysts. The reduction in bio-oil yield is attributed to enhanced secondary cracking and deoxygenation reactions promoted by the catalysts, which convert condensable vapours into non-condensable gases (Luo et al., 2022). However, the incorporation of Cr at 5 wt.% (5CE) and 15 wt.% (15CE) onto EA significantly enhanced bio-oil production. The maximum yield of 76.4 % achieved using the 15CE catalyst. The yield of char from catalytic co-pyrolysis ranges from 9.5 % to 10.8 %. The finding suggests consistent char formation across the CCP reaction. This is possibly due to the feedstocks initially undergo thermal cracking under constant pyrolysis conditions. This process produces primary volatiles and leaves behind a stable char residue before the volatiles pass through the catalyst bed for secondary cracking.

As depicted in Figure 4.2(b), EA catalyst shows the most significant in HC production. However, Cr catalyst promoted HC and alcohol. In general, significant reduction of acid and sugar were observed when using catalyst during pyrolysis. This result is in good agreement with Kaewpengkrow et al., (2017) who reported that the acidity of bio-oil was reduced when introducing transition metal to aluminium support. The formation of aromatic HC when using catalyst is not significant. The EA and Cr catalysts promote cracking and hydrogen transfer reactions rather than aromatization, resulting in a higher yield of aliphatic hydrocarbons. This is consistent with previous studies showing that catalysts with weaker acidity or non-shape-selective structures favour the formation of aliphatic hydrocarbons (Zheng et al., 2022).

The CE catalysts at various loading showed similar catalytic activity except for 10CE and 15CE. 10CE produced higher HC compared to 15CE. However, 10CE produce reduced intermediates such as furans, carbonyls and phenols as opposed to 15CE. High selectivity to phenols was observed in 15CE catalyst compared to other catalysts, which elucidates the transformation of carbonyl and furans into oxygenated aromatics without the deoxygenation pathway (Jaafar et al., 2023).

The acidity and textural properties of catalyst may improve cracking and selectivity of bio-oil. High surface area and pore size facilitated the accessibility to the active sites to overcome limitation of the mass transfer, while acidity enhanced the cracking of oxygenated compounds (Chi et al., 2018). The catalyst characteristics could shift reaction pathways such as dehydration, decarboxylation, decarbonylation and dehydrogenation which consequently will improve the quality of bio-oil. The variation in yield and bio-oil component distributions at various metals and metal loading with regards to its catalyst characteristics are explained in subsequent sections.

The findings show that the presence of plastics together with cellulose could alter cellulose product distribution. Moreover, addition of CE catalysts has upgraded the yield and product distribution of bio-oil. Varies metal loading shows major influence on the yield and bio-oil component distributions. 15CE shows the best catalyst activity with the highest bio-oil yield at 76.4 %. The effect of metal loadings of active metal also showed significant influence in catalytic activities as reported in previous findings by Zulkafli et al., (2023) and Nandakumar et al., (2023).

4.3.3 Functional Groups of The Bio-oil from Co-pyrolysis using CE Catalyst at Different Metal Loadings

The FTIR spectrum of bio-oil obtained via CE catalyst at different metal loadings is shown in Figure 4.3. In general, the spectrum shows similar functional groups.

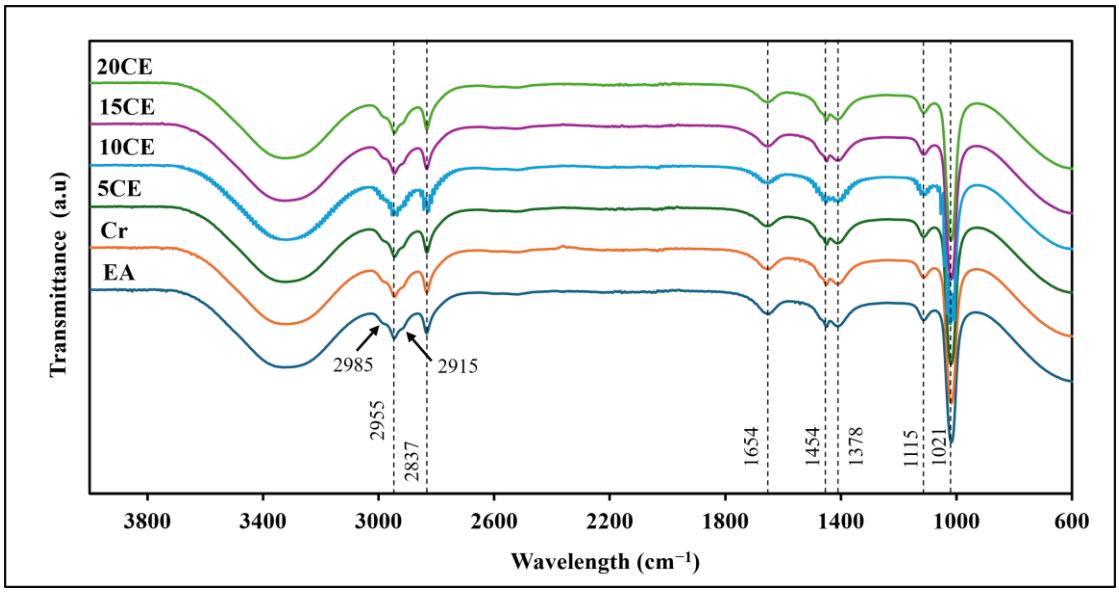

Figure 4.3 FTIR Spectrum of Bio-oil using CE Catalyst at Different Metal Loadings

The major functional group vibrations include O–H stretching (3321 cm^{-1}), C–H stretching and O–H stretching (2990–2831 cm^{-1}), and C=O stretching (1654 cm^{-1}). There are also C–H bending and C=C stretching (1450–1405 cm^{-1}) peaks, C–O stretching and Si–O–Si stretching (1115–1021 cm^{-1}) peaks. A broad peak corresponding to O–H stretching in the range of 3300 to 3600 cm^{-1} possibly attributed to water, alcohol, and aliphatic primary amines formed during co-pyrolysis (Baranitharan et al., 2019; Ojha & Vinu, 2015). The band ranging from 2990 to 2831 cm^{-1} indicates the occurrence of carboxylic acid with an OH bond (Magalhães et al., 2021) and C–H stretching from aliphatic alkane, alkene, or aldehyde (Stuart, 2004). The C=C band detected was considered an alkene group at 1654 cm^{-1} (Baranitharan et al., 2019). The presence of C=O stretching, and N=O stretching indicates the occurrence of amide or nitrite. The spectrum below 1500 cm^{-1} shows the fingerprint region where multiple overlapping waves could occur. The spectrum in the 1450–1405 cm^{-1} range possibly designated for alkane C–H bending. The strong sharp IR spectrum observed at 1021 cm^{-1} reveals most probably the presence of alcohol or phenol in C–O stretching (ranging from 1300 to 1000 cm^{-1}). The IR wave from 1300 to 1000 cm^{-1} also suggests the presence of C–F stretching and Si–O–Si stretching.

4.3.4 Elemental Composition of Dry Sludge, EA and 15CE

The composition of collected dry sludge (DS), EA and 15CE were identified by XRF analysis. The result as represented in Table 4.3, revealed the main compositions in DS contains aluminium (Al) with 57.2 wt.% followed by phosphorus (P), sulphur (S), and silicon (Si), with 18.8 wt.%, 13.6 wt.%, and 8.6 wt.%, respectively, while the rest is insignificant.

Table 4.3
X-ray Florescence Analysis of Dry Sludge and Extracted Aluminum

Element	DS (wt.%)	EA (wt.%)	15CE (wt.%)
Al	57.2	50.8	35.8
Si	8.6	0.1	0.1
P	18.8	10.5	6.1
S	13.6	37.7	18.4
Ca	0.4	0.2	0.1
Cr	0.1	0.1	39.3
Fe	0.6	0.3	0
Cu	0.1	0	0
Zn	0.5	0.4	0.3

The high aluminum content in DS indicates that the sludge contains active metals that can be utilized as catalysts. After the aluminum extraction process, an increase in S content was observed in EA, likely due to the acid leaching procedure involving sulfuric acid. On the contrary, it is observed that Si and P were reduced significantly. The selection of H_2SO_4 acid leaching method has selective to aluminum leaching and remove impurities. The 15CE contains Al and Cr at 35.8 wt.% and 39.3 wt.%, respectively, which validate both metal presence in the as-synthesized catalyst.

4.3.5 Surface Morphology of CE Catalyst at Different Metal Loadings

Figure 4.4 illustrates the surface morphology of EA, Cr and CE catalysts. The image of EA reveals that the crystal poses irregular shapes and consists of facets and edges with rough surfaces.

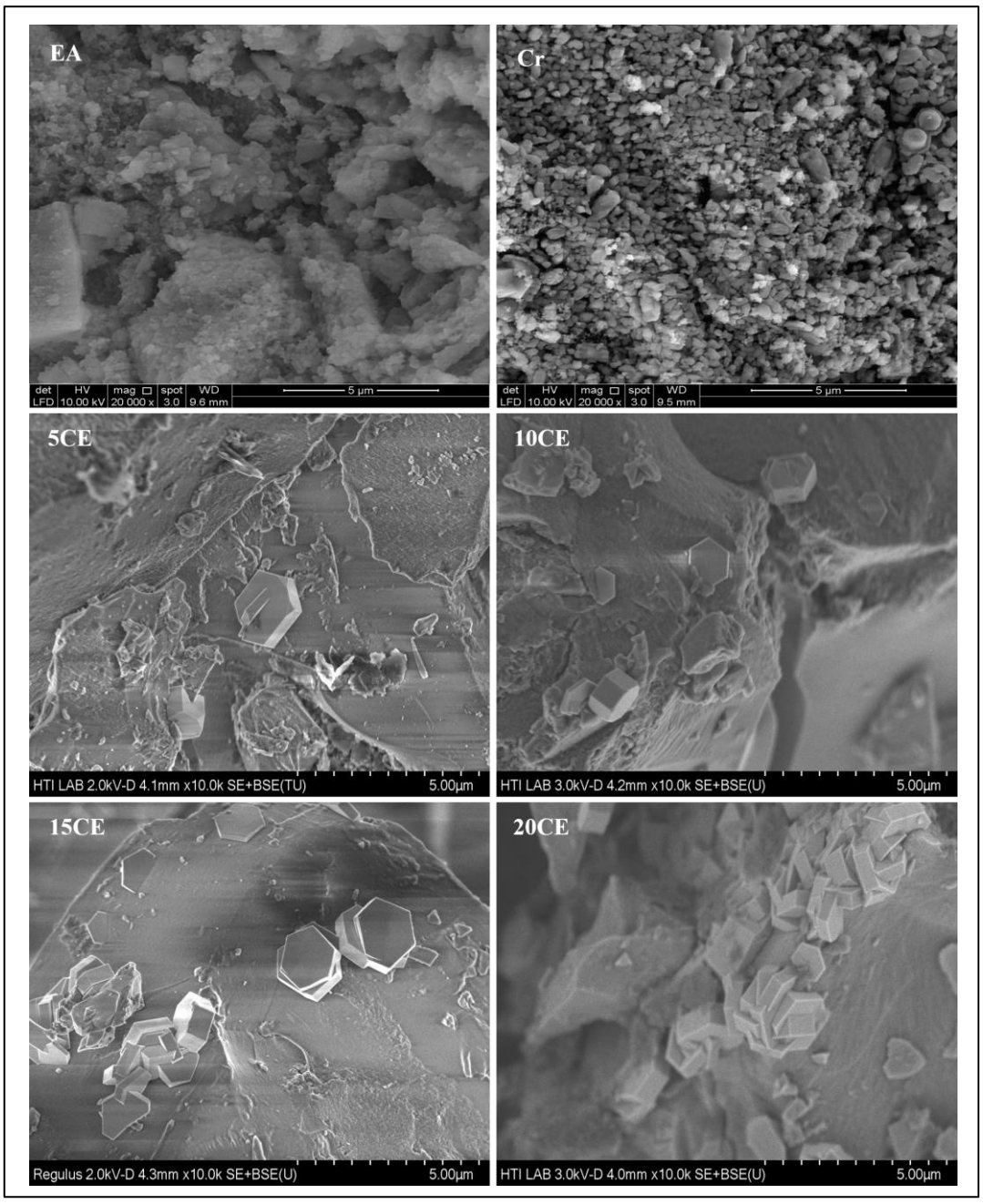

Figure 4.4 SEM Images of Synthesis Catalyst at Different Metal Loadings

Some aggregation of crystal also formed on the surface, possibly due to other impurities such as phosphate and other metals, as displayed in the XRF result. The voids are also observed on the surface, which indicate the porous structure. Meanwhile, the Cr image displays that the Cr crystal is aggregated on the surface of the catalyst, with some having a unique hexagonal shape. The shape of the crystal is irregular, with a rough texture surface. The morphology of CE catalysts is quite close to that of EA and Cr catalysts. It contains irregular shapes and sizes with a rough surface texture. The hexagonal shape of the Cr crystal is also visible. It is clearly seen from the images that

increasing the metal loadings cause the Cr crystal to form aggregation, which could decrease the surface area of the catalyst.

4.3.6 Textural and Acid Properties of CE Catalyst at Different Metal Loadings

The surface area, porosity characteristics, and acid site concentrations of catalysts prepared with varying metal loadings are presented in Table 4.4.

Table 4.4
The Textural and Acidity of Catalyst Prepared Using Various Cr Loading on EA

	Surface Area [a] (m^2/g)	**Total pore volume [a] (cm^3/g)**	**Average pore size [a] (nm)**	**Acidity [b] (mmol/g)**
EA	53.0	0.1186	8.9	3.19
Cr	2.8	0.0296	42.4	0.25
5CE	17.2	0.0539	12.5	3.19
10CE	28.8	0.0464	6.4	3.33
15CE	50.4	0.0536	4.3	3.39
20CE	31.8	0.0366	4.6	3.07

[a] Obtained from N_2 adsorption-desorption
[b] Obtained from NH_3-TPD chemisorption

The trend observed is that the increase in surface area with higher Cr content on EA for 5CE,10CE and 15CE. However, 20CE show that surface area decreases with more Cr loading on EA possibly due to surface aggregates as shown in SEM image in Figure 4.4. The total pore volume shows that 20CE has the lowest pore volume among the CE catalyst. This behaviour is likely due to excessive Cr loading, which promotes agglomeration and deposition of Cr species within the pore channels, leading to partial pore blockage and pore filling (Venegas-Vásconez et al., 2024). The finding also indicate that the Cr incorporated into EA results in higher surface area and pore volume compared to Cr alone. However, EA by itself exhibits the highest surface area and pore volume among all catalysts. EA has surface area of 53 m^2/g and pore volume of 0.1186 cm^3/g with a moderate average pore diameter of 8.9 nm. Among the CE catalyst, 15CE exhibits the highest surface area (50.4 m^2/g), and second highest pore volume which could be one of reason for the good catalytic activity with high bio-oil yield as shown in Figure 4.2(a)

Figures 4.5 and 4.6 illustrate the N_2 sorption isotherms and pore size distribution of the CE catalysts at different metal loadings.

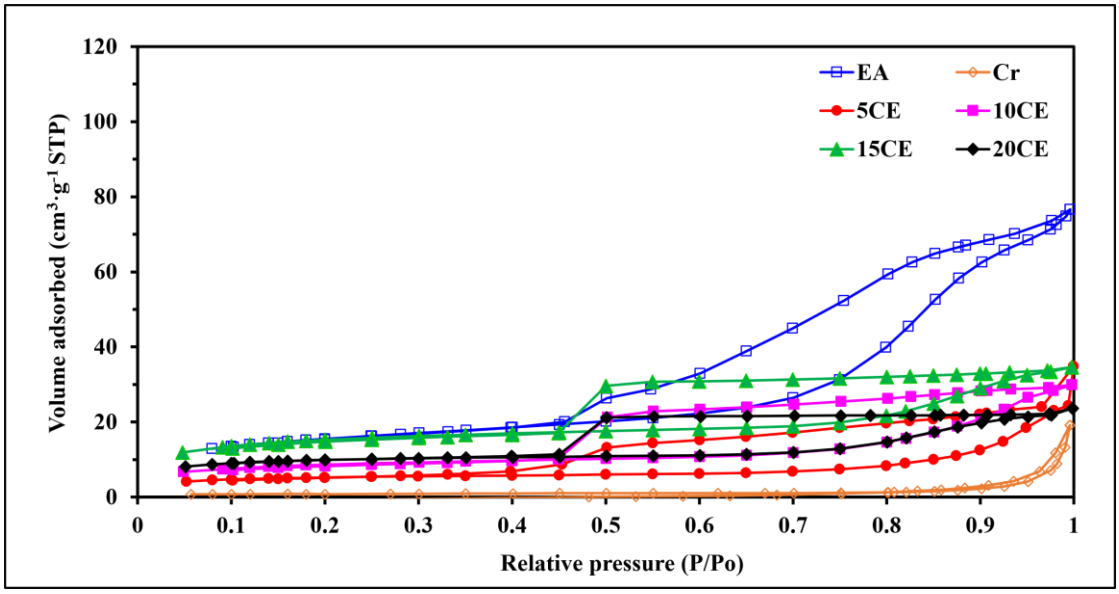

Figure 4.5 N_2 Sorption Isotherm of CE Catalyst at Different Metal Loadings

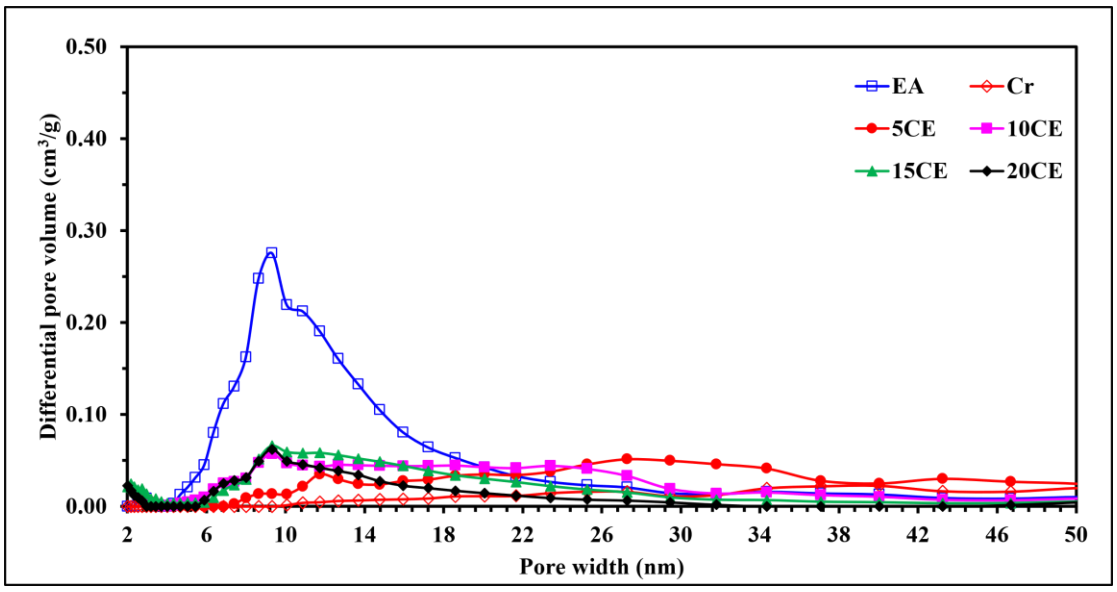

Figure 4.6 Pore Size Distribution of CE Catalyst at Different Metal Loadings

The isotherms correspond to a combination of IUPAC Types III and IV, with a distinct hysteresis loop at relative pressure (p/p_0) > 0.45. Specifically, the Cr catalyst shows a Type III isotherm, indicative of non-porous materials, whereas CE catalysts exhibit Type IV isotherms with H4 hysteresis loops, characteristic of mesoporous structures with ink-bottle-type pores and limited pore connectivity (Thommes et al.,

2015). The pore size distribution for all catalysts, except for Cr, display mesoporosity as evidenced by their respective hysteresis loops.

The acidity and acid site distribution among the catalyst can be observed in Table 4.4 and Figure 4.7, respectively. The NH_3-TPD profiles outline the desorption peaks categorized into weak (<250 °C), medium (250 °C < T < 500 °C), and strong acids (>500 °C) as depicted in works by Phan et.al., (2020). The EA catalyst shows the desorption peak primarily in the weak and medium acidic regions, while introducing Cr onto the EA catalyst shifts the peaks towards the medium and strong acidic regions. This shift indicates alterations in acid site distribution due to the interaction between the introduced Cr metal and EA (Gupta et al., 2022). Furthermore, the introduction of metal catalysts triggers the emergence of new catalytically active acid sites in the strong acidic region. This alteration in acid site distribution aligns with prior research findings by Maneechakr, (2021). However, it is observed only small different in terms of acidity between CE catalysts and EA (range 3.07 – 3.39 mmol/g). The findings indicate that addition of Cr does not contribute significantly to acidity but only shift the acidity region of weak and mild acidity (EA) to mild and strong acidity (CE).

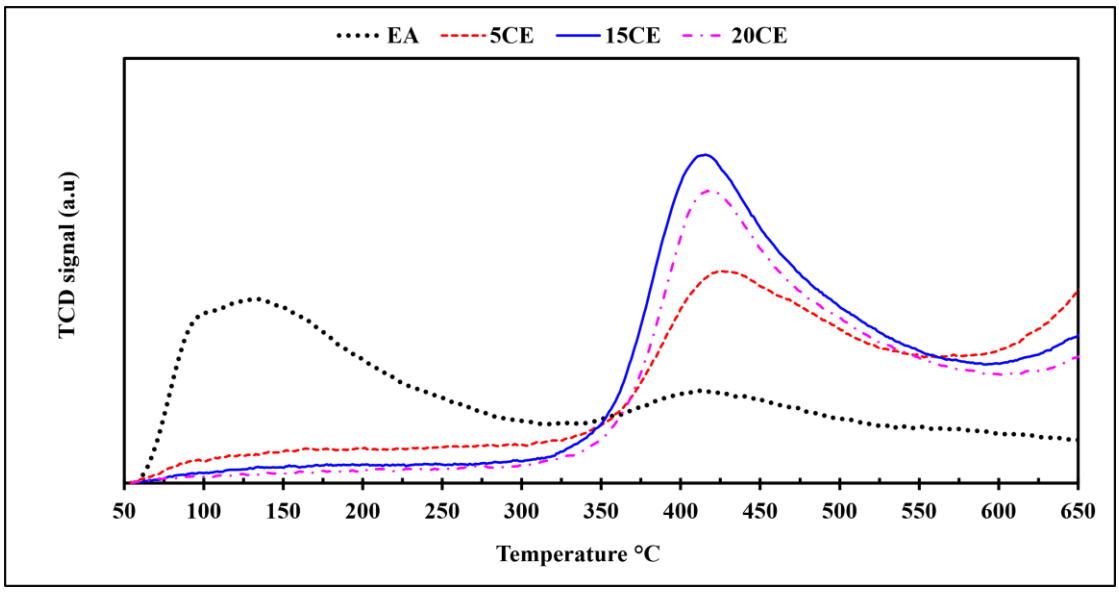

Figure 4.7 NH_3-TPD Desorption Characteristic of CE Catalysts at Different Metal Loadings

4.3.7 Crystallography of Cr, EA and 15CE

The X-ray diffraction (XRD) of Cr, EA, and 15CE are shown in Figure 4.8 The diffractogram depicts the presence of Cr_2O_3 (ICDD No: 01-070-3765) at 2θ = 24.4°, 33.6°, 36.2°, 41.5°, 50.2°, and 54.8° in the Cr sample. The major peaks in EA show the existence of aluminium sulphate (ICDD No: 00-018-0060) at 2θ = 15.1°, 20.9°, 25.3°, 30.6°, 33.5°, 34.2°, and 40.8°. In addition, low-intensity peaks show the presence of aluminium hydroxide (ICDD No: 00-005-0355). Meanwhile, the XRD result of 15CE confirms the presence of chromium oxide (ICDD No: 00-038-1479) at 2θ = 24.4°, 33°, 36.2°, 41.6°, 50.2°, 54.8°, and 65.3°, and low intensity peaks show aluminium chromium oxide (ICDD No: 00-051-1394). All samples are assigned to the rhombohedral phase of the crystal lattice.

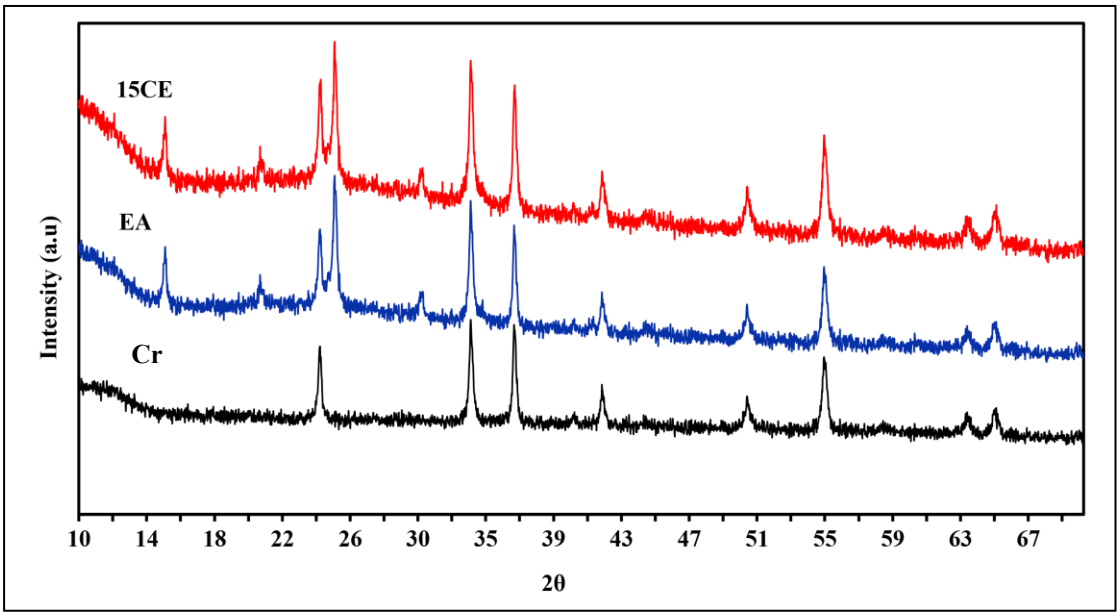

Figure 4.8 X-ray Diffactogram of EA, Cr, 15CE

4.3.8 Effect of Calcination Temperature on 15CE Catalyst Activity

The catalyst activity can be significantly affected by calcination. The effect of calcination temperature of the 15CE (the best catalyst on Cr metal loading) in catalytic activity and the physico-chemical characteristics are discussed this section. The different calcination temperature of catalyst is denoted as 15CE-T, where T indicates calcination temperature. Figure 4.9 (a-b) exhibits the catalyst activity based on product yield and bio-oil component distributions at various calcination temperatures.

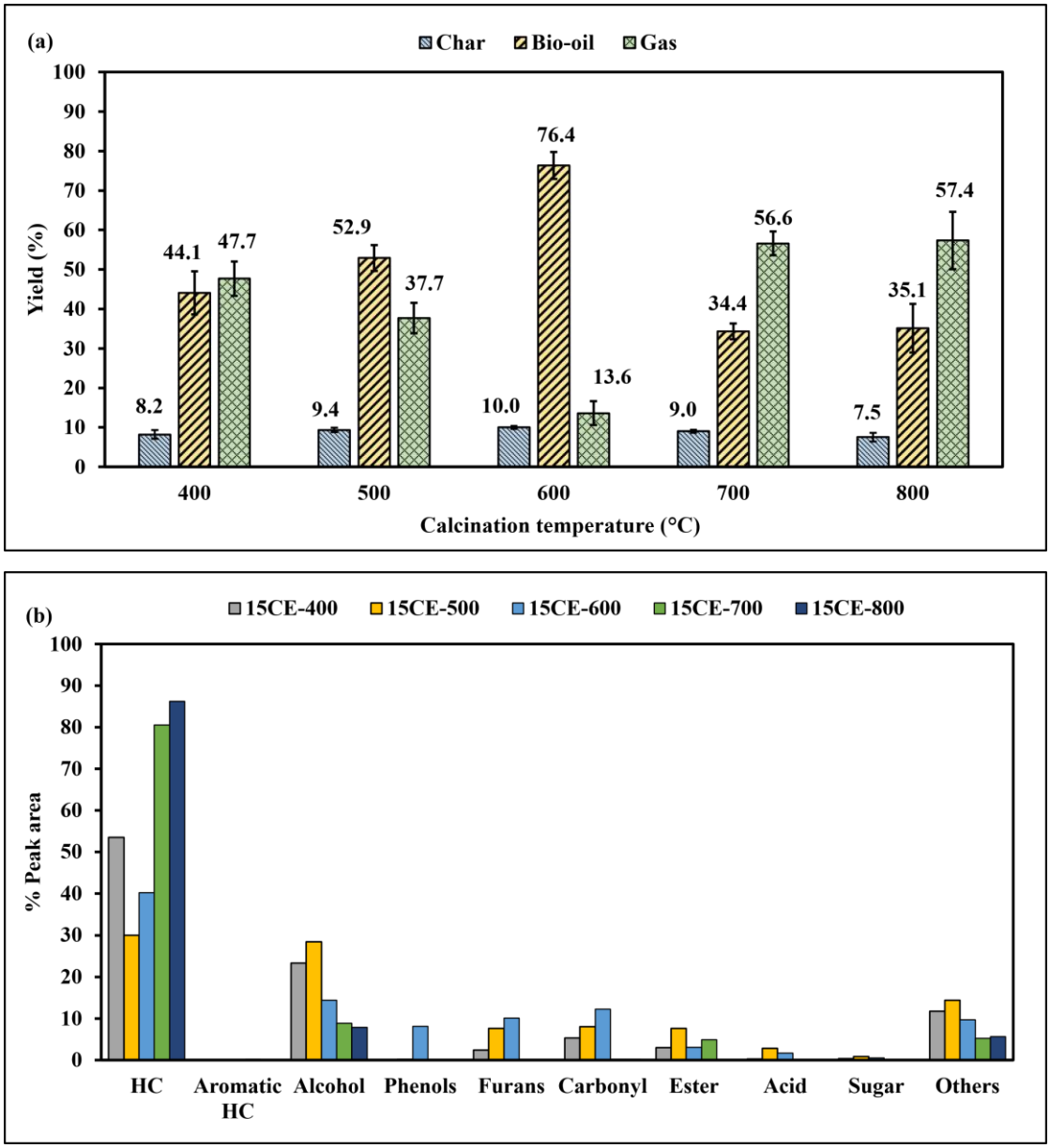

Figure 4.9 Effect of Calcination Temperature on 15CE Catalyst Activity (a) Yield % (b) Bio-oil Component Distributions (Operating Condition: 500 °C Pyrolysis Temperature; 60 min Pyrolysis Time; 50:50 CFW/PPW Ratio; 1:1 F/C Ratio)

The results demonstrated that calcination temperature has a significant effect on the catalyst activity. The increased calcination temperature from 400 °C to 600 °C has shown good activity with increment in bio-oil yield from 44.1 % to 76.4 %. However, further increased calcination temperature to 700 °C and 800 °C causes decrease activity where bio-oil yield is reduced and slightly constant. The finding possibly due to the changes in characteristics of catalyst that enhanced the gas yield instead of bio-oil yield at higher calcination temperature, especially the development of pores and surface area. The excessive cracking and rapid deoxygenation reaction contribute to form more gases

product and aliphatic HC as shown in Figure 4.9 (a) and 4.9 (b), respectively. A high surface area allows the active metal to be more widely dispersed on the support, which can enhance its catalytic activity by providing more active sites for cracking and deoxygenation reaction (Lin et al., 2023; Roy et al., 2022).

During pyrolysis, the feedstocks undergo a series of thermochemical reactions such as dehydration, decarbonylation, cracking, condensation, and polymerization which facilitate the breakdown of complex molecules into hydrocarbons (Razzak et al., 2025). Among the various calcination temperature, the 15CE-600 catalyst demonstrated the highest bio-oil yield (Figure 4.9(a)), with light oil aliphatic hydrocarbons (HC) constituting major fraction as shown in Figure 4.9(b). This observation aligns with findings by Zhang et al., (2019), where it was reported that Cr catalysts favour the production of light bio-oil when calcined at 600 °C.

The increase in calcination temperature (400 °C, 500 °C, and 600 °C) shows that the catalyst activities promoted the formation of furans and carbonyl compounds. However, 15CE-700 shows that the catalyst activity resulted in the suppression of furans and carbonyls and a shift toward hydrocarbon formation. Notably, phenolic compounds were only detected at the 600 °C condition. These trends suggest that lower calcination temperatures facilitate the generation of oxygenated intermediates, whereas higher temperatures promote deoxygenation and hydrocarbon production. The strong influence of calcination temperature on catalyst structure and physicochemical properties plays a critical role in catalytic activity.

Li et al., (2019) reported that varying the calcination temperature of Ni/MgO catalysts between 650 °C and 950 °C significantly altered their efficiency in upgrading lignin-derived bio-oil. Their optimal catalyst, 15 % Ni/MgO–850, achieved a 97 % selectivity in converting guaiacol to cyclohexanol. Similarly, at higher calcination temperatures, 15CE-700 and 15CE-800 exhibited enhanced deoxygenation activity by effectively converting oxygenated compounds such as phenols, furans, acids, carbonyls, and sugars into aliphatic HC, accompanied by a reduction in alcohol and other oxygenates.

4.3.9 Functional Groups of Bio-oil using 15CE Catalyst at Different Calcination Temperature

The IR spectrum of bio-oil produced using CE catalyst at different calcination temperature as shown in Figure 4.10. A broad peak is observed at 3600 – 3000 cm^{-1}, indicating the presence of hydroxyl component (alcohol or water) (Xu et al., 2020). There are also few peaks detected at range 2831 cm^{-1} to 2985 cm^{-1} indicating aliphatic structure (C–H stretch). The compound possibly alkane and aldehyde (Li et al., 2025). Several peaks were detected at double bond region (2000–1600 cm^{-1}), possibly corresponds to C=O stretching (carbonyl group) or C=C bond of olefin (Li et al., 2025). At fingerprint region (below 1600 cm^{-1}), several peaks are also observed. The peaks between 1400-1500 cm^{-1} possibly the presence of C–H bends and overlapping with the presence of ester (1460–1300 cm^{-1}) (Mishra et al., 2022). The weak peaks at 1115 cm^{-1} and strong peaks at 1022 cm^{-1} possibly shows the presence of alcohol, ethers, acids, and ester (C–O) bond.

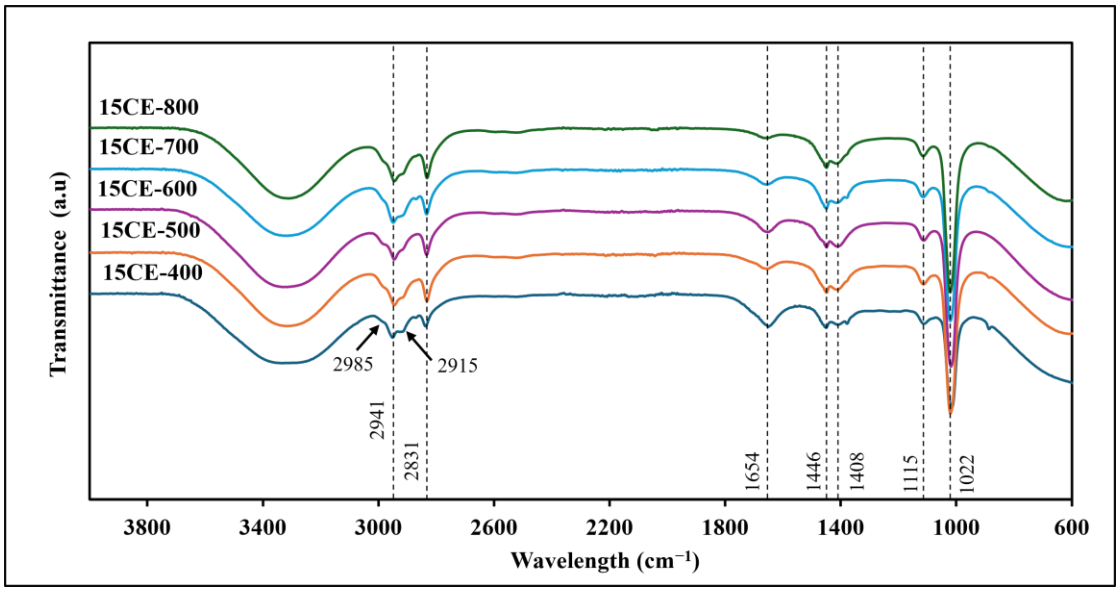

Figure 4.10 FTIR Spectrum of Bio-oil Uses 15CE Catalyst at Different Calcination Temperature

4.3.10 Surface Morphology of 15CE Catalysts at Different Calcination Temperature

Figure 4.11 illustrates the surface morphology of CE catalyst at different calcination temperatures, where it shows the Cr crystal impregnated onto the EA surface. Nonetheless, the morphology of the CE catalyst has noticeable changes at different calcination temperatures. For 15CE-400, the Cr particle is not clearly seen on the EA surface compared to the other CE catalysts. It is possibly due to the Cr crystal growth is inhibited at lower temperatures. In contrast, a notable increase in Cr particles is evident for 15CE-700 and 15CE-800, beside the development of voids and surface cracks on EA. The growth of particles when increase the calcination temperature is align with similar observations reported in previous study (Husain et al., 2024; Langa et al., 2025).

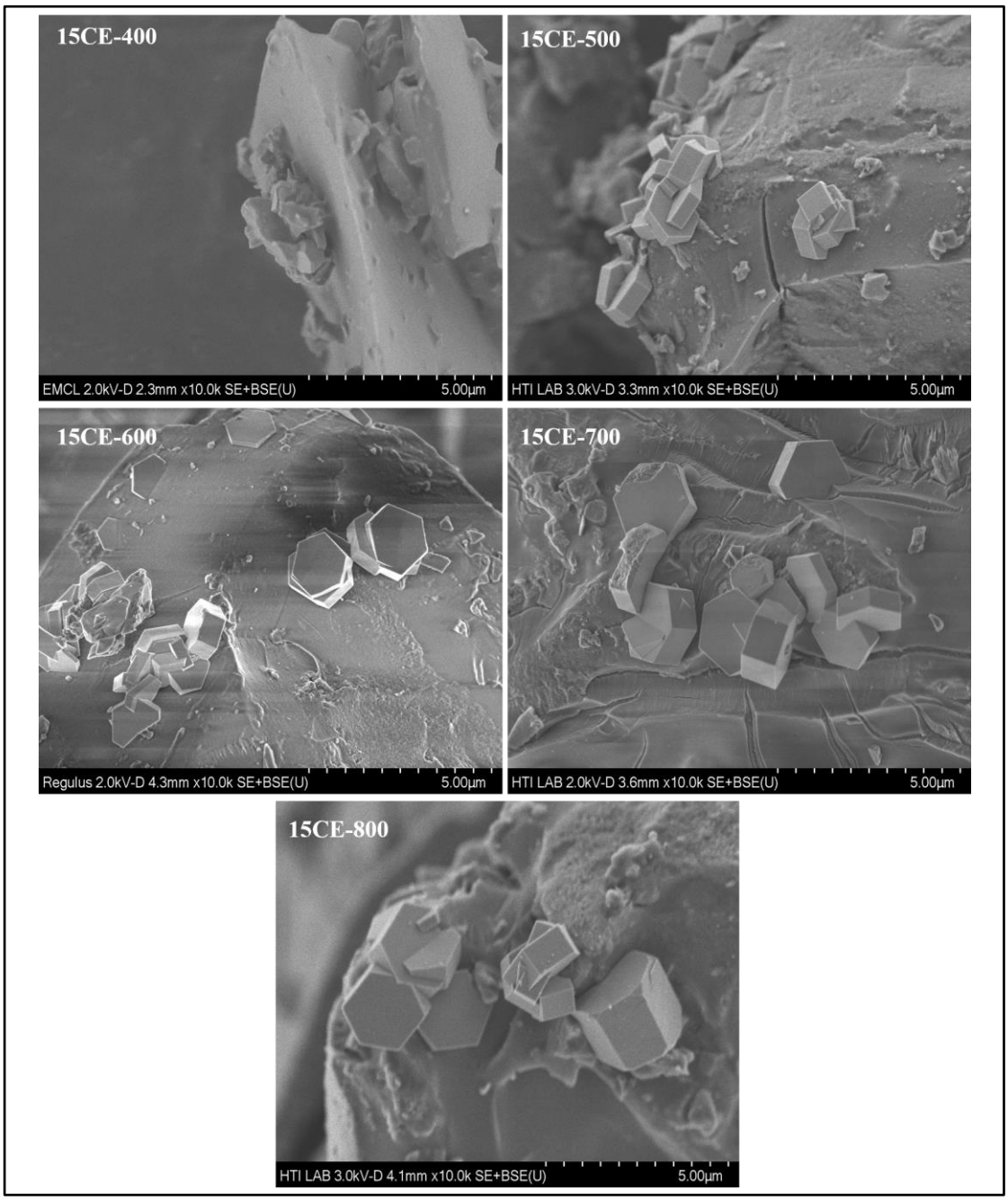

Figure 4.11 SEM Images of CE Catalysts at Different Calcination Temperature

4.3.11 Textural and Acid Properties of 15CE Catalyst at Different Calcination Temperature.

Table 4.5 demonstrates the textural properties and acid sites concentrations of the CE catalyst at different calcination temperature.

Table 4.5
Textural Properties and Acid Sites Concentrations of The CE Catalysts at Different Calcination Temperature

	Surface Area [a] (m^2/g)	**Total pore volume [a] (cm^3/g)**	**Average pore size [a] (nm)**	**Acidity [b] (mmol/g)**
15CE-400	10.9	0.0133	4.9	6.4
15CE-500	5.2	0.0053	4.1	-
15CE-600	50.4	0.0536	4.3	3.4
15CE-700	94.1	0.2024	8.6	-
15CE-800	82.9	0.2547	12.3	1.2

[a] Obtained from N_2 adsorption-desorption
[b] Obtained from NH_3-TPD chemisorption

The catalyst surface area increased at higher calcination temperature for instance 15CE-400 is at 10.9 m^2/g where 15CE-700 is at 94.1 m^2/g. However, there is slight reduction in surface area at 82.9 m^2/g for 15CE-800. The total pore volume and average pore size of catalyst also increased at higher calcination temperature, whereby 15CE-400 is at 0.0133 cm^3/g and 4.9 nm, respectively compare to 15CE-800 is at 0.2547 cm^3/g and 12.3 nm, respectively. Low calcination temperatures possibly lead to incomplete precursor decomposition and reduced active site density, while excessively high temperatures can cause metal sintering, lowering surface area and altering support morphology (Subhan Azeem et al., 2025).

The textural properties of the catalyst at different calcination temperature can be further explained by isotherm and pore size distribution as depicted in Figure 4.12 and 4.13, respectively.

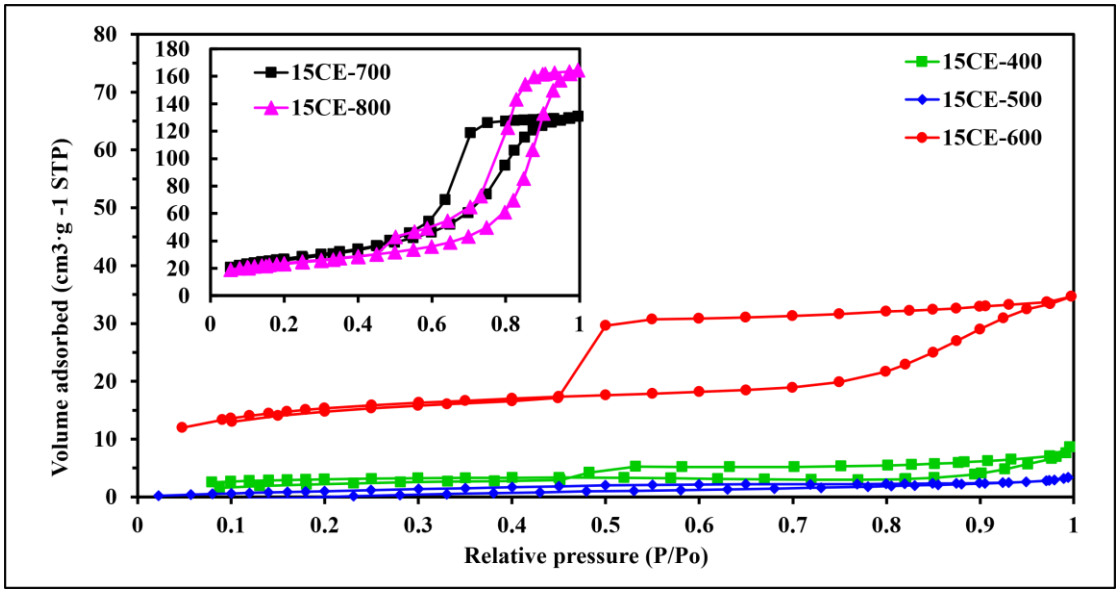

Figure 4.12 N_2 Sorption Isotherm of CE Catalyst at Different Calcination Temperatures

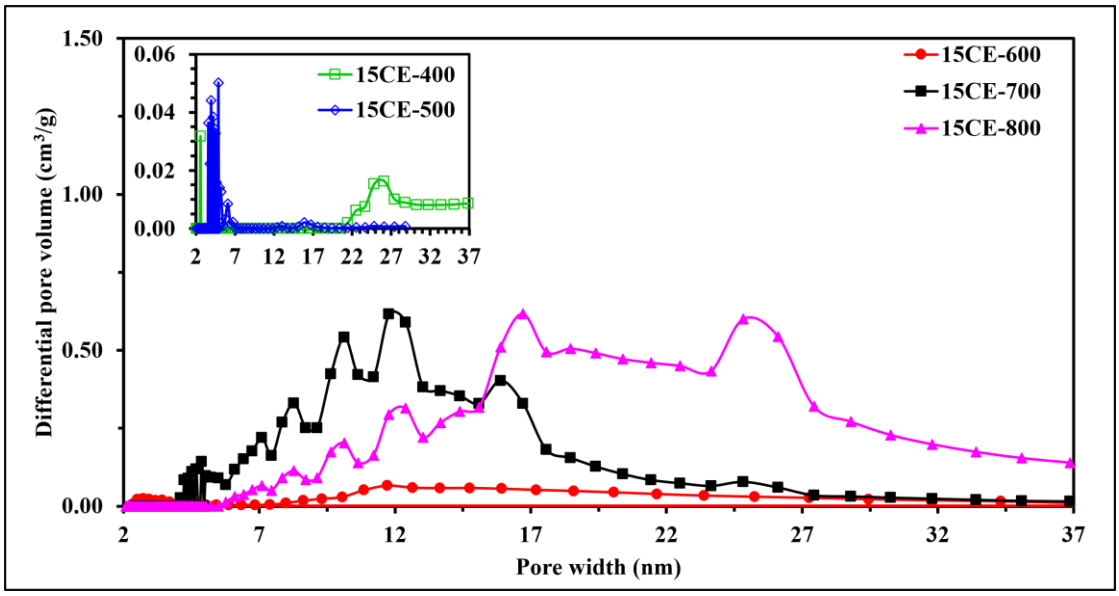

Figure 4.13 Pore Size Distribution of CE Catalyst at Different Calcination Temperatures

The isotherms of CE catalysts at different calcination temperature exhibit type IV IUPAC classification with different hysteresis loop (H4 and H2) as shown in Figure 4.12. The 15CE-600 catalyst showed type IV isotherms with hysteresis loop H4 that suggest the mesoporous material with ink-bottle type pores with minimal network effect. On the other hand, 15CE-700 and 15CE-800 catalyst illustrated the hysteresis loop H2, that suggest pore blocking with larger neck width (Thommes et al., 2015). The

other catalysts (15CE-400 and 15CE-500) showed very low adsorption of N_2 gas indicates non-porous material (Alrozi et al., 2023).

Different calcination temperature also causes the changes in pore size distribution as depicted in Figure 4.13. The pore size is observed to be distributed at mesopores range of 2 nm to 50 nm. These values supports that the pores are mesoporous, and the porosity increases with calcination temperature. The catalysts showed an increase in pore volume coupled with an increase in pore size especially at lower pore size value. Among the CE catalysts, the 15CE-700 and 15CE-800 showed a well-developed pore structure with higher pore volumes at range 2 nm to 27 nm and 2 nm to 37 nm, respectively. However, 15CE-600 shows the pore size distributed between 7 nm to 37 nm with low pore volume with average size at 4.3 nm. Higher calcination temperatures significantly alter pore size distribution by enhancing sintering and grain growth (Prayitno et al., 2025). Increased thermal energy accelerates atomic diffusion, causing smaller pores to merge into larger ones, shifting the pore size distribution toward larger mesopores and macropores (R. Han et al., 2022).

The total acidity and the strength of acid at various calcination temperature were measured by NH_3-TPD are shown in Table 4.5 and Figure 4.14, respectively.

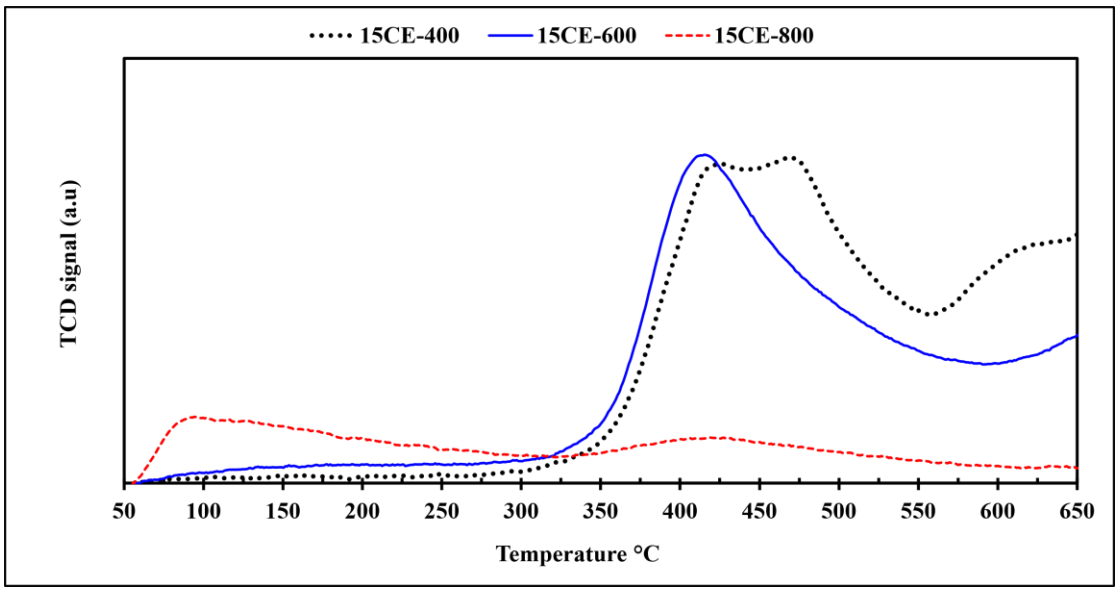

Figure 4.14 NH_3-TPD Desorption Characteristic of As-Synthesis Catalyst at Different Calcination Temperatures

From Table 4.5, the results indicated that the total acid of CE catalyst significantly decreased with the increase of calcination temperature. The 15CE-400 catalyst shows total acidity at 6.4 mmol/g, while 15CE-600 and 15CE-800 shows 3.4 mmol/g and 1.2 mmol/g, respectively. Moreover, the observation on the NH_3-TPD profiles in Figure 4.14 which signifies the strength of the acidity shifted from strong acid to weak acid sites by increasing the calcination temperature. It is aligned with the findings of Ding et. al., (2020), where the catalyst lost it acidity at higher calcination temperatures. The tremendous reduction of acid amount and acid strength possibly due to the dehydroxylation of CE catalyst when temperature is higher than 600 °C (Lu et al., 2005).

4.3.12 Effect of Calcination Time on 15CE-600 Catalyst Activity

The effect of calcination time of the 15CE-600 catalyst in catalytic activity and the physico-chemical characteristics is discussed this section. The different calcination time of catalyst is denoted as 15CE-600-t, where t indicates calcination time. Figure 4.15(a-b) displayed the effect of calcination time in products yield and bio-oil component distribution, respectively.

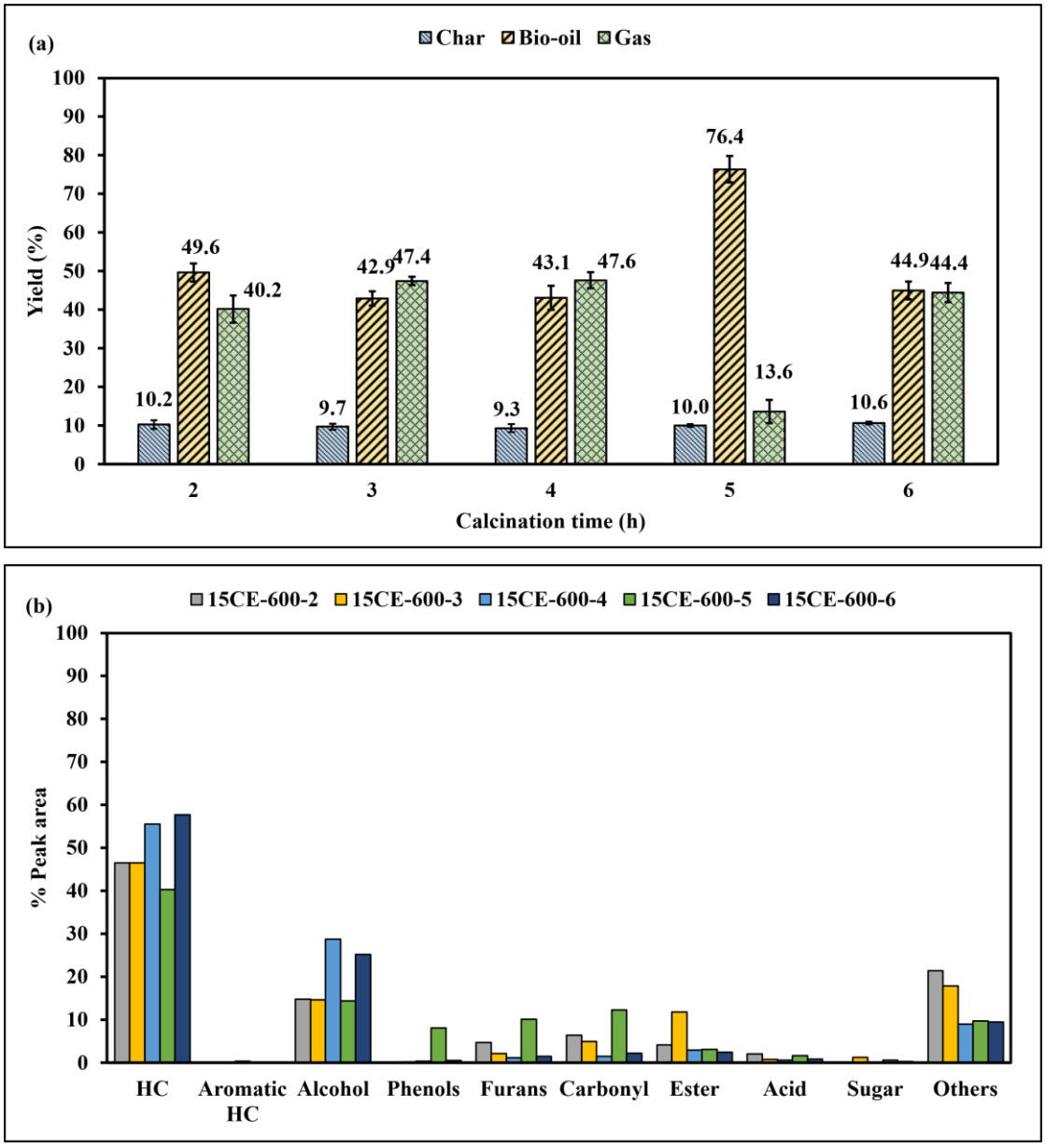

Figure 4.15 Effect of Calcination Time on 15CE-600 Catalyst Activity (a) Yield % (b) Bio-oil Component Distributions (Operating Condition: 500 °C Pyrolysis Temperature; 60 min Pyrolysis Time; 50:50 CFW/PPW Ratio; 1:1 F/C Ratio)

Figure 4.15(a) indicates that CE catalyst calcined 2 h to 4 h (15CE-600-2, 15CE-600-3, 15CE-600-4), poses good activity with bio-oil yield of 49.6 %, 42.9 % and 43.1 %, respectively. However, there is distinct increment in bio-oil yield at 76.4 % for 15CE-600-5, which implies better catalytic activity for calcination at 5 h. Further increment to 6 h for 15CE-600-6 show decreased in bio-oil yield to 44.9 %. The findings reveal that, shorter calcination time possibly leads to incomplete removal and decomposition of substances from CE catalyst which affect surface area, porosity and cause less adhesion crystal structure to the surface support of the catalyst (Yipeng et al.,

2017; Zhang et al., 2020). During calcination, the decomposed substances from precursor materials are removed from the sample leaving only the metal element to synergize and form a strong bond. Sufficient calcination time leads to the formation of homogenously dispersed metal oxides with many active surface sites (Johari et al., 2025). The Cr active metal was agglomerated on the EA surface after 6 h of calcination that reduced the catalytic activity. Most probably, it was due to the sintering effect at longer calcination time (Chava et al., 2021; Olutoye & Hameed, 2010).

Figure 4.15(b) shows that the co-pyrolysis using CE catalysts mostly produce aliphatic HC and alcohol. The catalyst 15CE-600-4 and 15CE-600-6 produce more aliphatic HC and alcohol compared to other CE catalysts. Another observation is that CE catalysts at higher calcination time (15CE-600-4, 15CE-600-5, 15CE-600-6) shows reduction in production of ester. The catalyst 15CE-600-5 promote co-pyrolysis to produce higher carbonyls, phenols and furans compare to other CE catalysts. The furans are most probably produced on the surface of the catalyst where sufficient active sites to convert sugar to furans. While phenols and aromatic HC possibly produced in the pores (Wang et al, 2018). However, the competitive reactions between phenolation and aromatization reaction possibly cause high in phenols than aromatic HC (Chen et al., 2024).

4.3.13 Functional Groups of Bio-oil using 15CE-600 Catalyst at Different Calcination Time

Figure 4.16 shows the FTIR spectra of bio-oil from co-pyrolysis of CFW and PPW using CE catalyst at different calcination time.

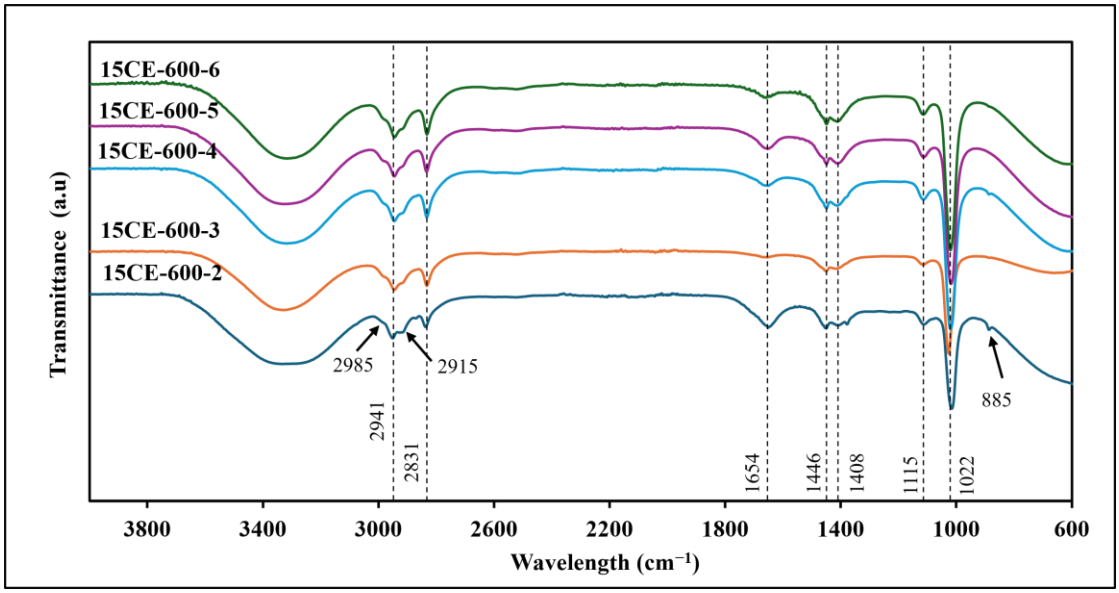

Figure 4.16 FTIR Spectrum of Bio-oil using 15CE-600 Catalyst at Different Calcination Time

The similar IR spectra is observed in bio-oil from co-pyrolysis at different calcination time as compound to calcination temperature. Thus, indicate that different catalyst calcination temperature and time does not change the product compound. The presence of these compounds was demonstrated in IR spectra of O–H stretching (3309 cm^{-1}), C–H stretching, O–H stretching (2949–2827 cm^{-1}), C=O stretching primary amide or C=C stretching of alkene (1654 cm^{-1}), alkane C–H bending and ester (1458–1401 cm^{-1}), C–O stretching (1115-1021 cm^{-1}), and possibly Si–O–Si stretching (1115–1021 cm^{-1}) (Li et al., 2025; Mishra et al., 2022; Stuart, 2004).

4.3.14 Surface Morphology of 15CE-600 Catalyst at Different Calcination Time

Figure 4.17 illustrates the morphology of 15CE catalyst at various calcination time. Generally, the Cr crystallite was observed to appear on the surface of EA. However, early calcination time at 15CE-600-2 and 15CE-600-3 show the fine Cr crystallite and well dispersed on surface of EA. The Cr crystallite is more visible and larger at 15CE-600-4. While at 15CE-600-5 and 15CE-600-6, the Cr crystallite started to agglomerate and grow.

As can be seen in Figure 4.17, the compact surface is seen at 15CE-600-4 compared to the 15CE-600-3 indicated the densification of EA that possibly impact the surface area and porosity of the catalysts. While agglomeration observed at 15CE-600-6 caused the lower dispersion of Cr crystallite on the surface of EA. The agglomeration

particles would be formed by coagulation and sintering (Zhang et al, 2020). Thus reduce the accessibility towards active sites and reduce catalytic activity (Said et al., 2024).

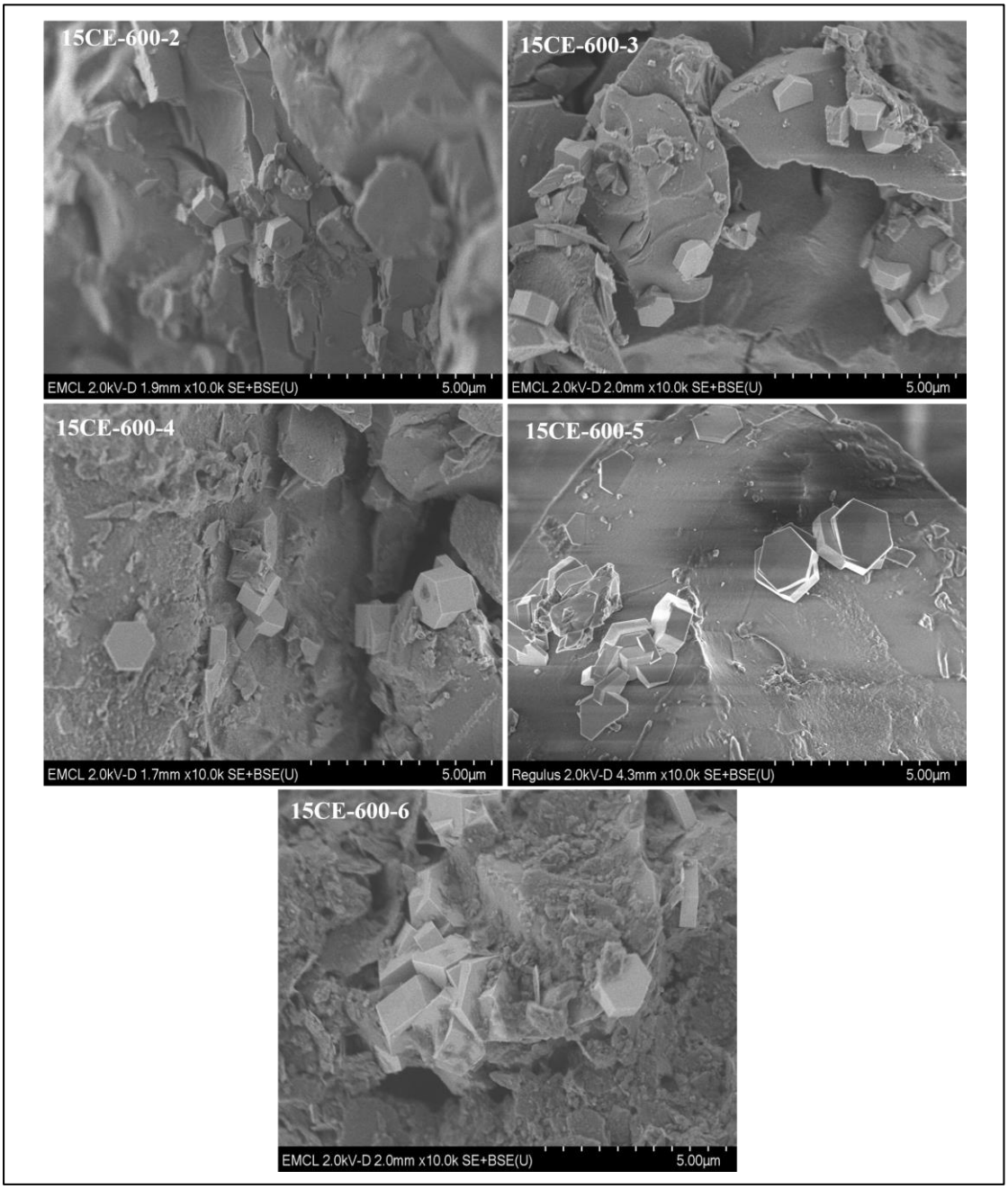

Figure 4.17 SEM Images As-Synthesis 15CE-600 Catalyst at Various Calcination Treatment

4.3.15 Textural and Acid Properties of CE Catalyst at Different Calcination Time

Table 4.6 demonstrates the textural properties and acid sites concentrations of the CE catalyst at different calcination time.

Table 4.6
Textural Properties and Acid Sites Concentrations of 15CE-600 Catalysts at Different Calcination Time

	Surface Area [a] (m^2/g)	**Total pore volume [a] (cm^3/g)**	**Average pore size [a] (nm)**	**Acidity [b] (mmol/g)**
15CE-600-2	17.9	0.0142	3.2	4.0
15CE-600-3	24.2	0.0223	3.7	-
15CE-600-4	2.2	0.0080	14.6	-
15CE-600-5	50.4	0.0536	4.3	3.4
15CE-600-6	10.2	0.0219	8.6	3.4

[a] Obtained from N_2 adsorption-desorption
[b] Obtained from NH_3-TPD chemisorption

The surface area and total pore volume are observed to increase when increase calcination time from 2 h to 3 h. The surface area shows increment from 17.9 m^2/g to 24.2 m^2/g, while the pore volume also increased from 0.0142 cm^3/g to 0.0223 cm^3/g for 15CE-600-2 and 15CE-600-3, respectively. However, the textural properties unveil a distinct reduction in the surface area and total pore volume of 15CE-600-4 to 2.2 m^2/g and 0.0080 cm^3/g, respectively. The reduction possibly attributed to the removal of hydroxyl, nitrate and other organic compounds at early stages of calcination hours (2 h to 3 h) caused the destruction of pore structure (Ahmed et al., 2022) before the pore reopening and CE structure reorganization as evident in 15CE-600-5. The surface area and total pore volume of 15CE-600-5 shows increased to 50 m^2/g and 0.0536 cm^3/g, respectively. The prolong the calcination time at 15CE-600-6, cause the surface area and total pore volume decrease as the Cr particles started to agglomerate. The extension of the calcination time will promote the aggregation of particles and induce the increase in the size of particle (Xu et al., 2024). The textural properties of the catalyst on different calcinations time can be further explained by isotherm and pore size distribution showed by Figure 4.18 and 4.19, respectively.

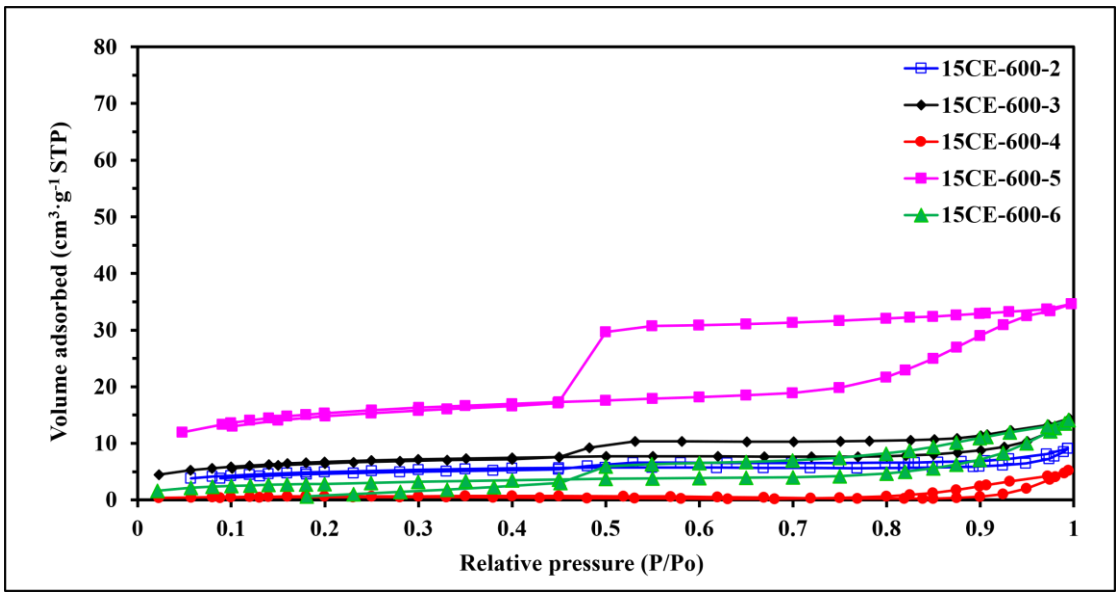

Figure 4.18 N_2 Sorption Isotherm of 15CE-600 Catalysts at Different Calcination Time

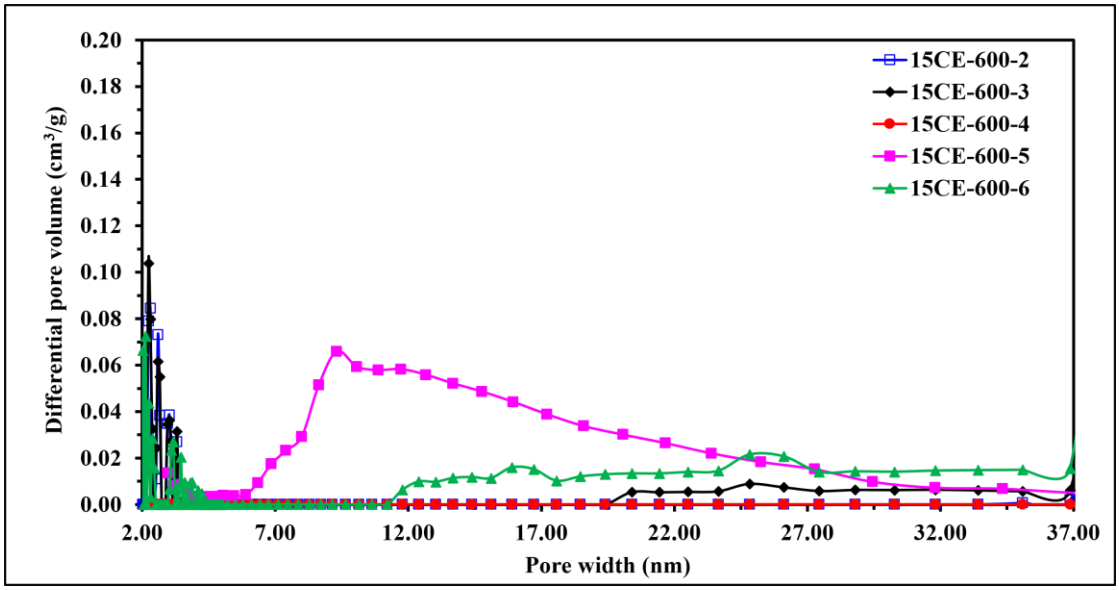

Figure 4.19 Pore Size Distribution of 15CE-600 Catalysts at Different Calcination Time

Figure 4.18 displays the N_2 adsorption isotherms for 15CE-600 catalysts at different calcination time. The isotherm exhibits a type IV isotherm with an H4 type hysteresis loop which associated with mesopore structure except for 15CE-600-4. Moreover, the pore size in Figure 4.19 indicates there is tiny pore (2 nm–4 nm) observed for 15CE-600-2 and 15CE-600-3, which suggests indicates the removal of organic substances is incomplete. While this tiny pore shows destruction at 15CE-600-4, where is no pore distributed in mesopore range on the catalyst surface. However, it can be seen

the pore started to develop when calcine at 5 h (15CE-600-5) between 7 nm–37 nm and the pore size increased as it shifts to larger size between 12 nm–37 nm (15CE-600-6) due to agglomeration of Cr particle.

Table 4.5 indicates the total acid amount slightly reduced from 4 mmol/g to 3.4 mmol/g, for 15CE-600-2 and 15CE-600-5 respectively and maintained at 3.4 mmol/g when prolonged the calcination time to 6 h (15CE-600-6). Figure 4.20 reveals the acid strength is sustained at medium to strong acid site with different calcination time. Thus indicates the calcination time is not much influence the acidity.

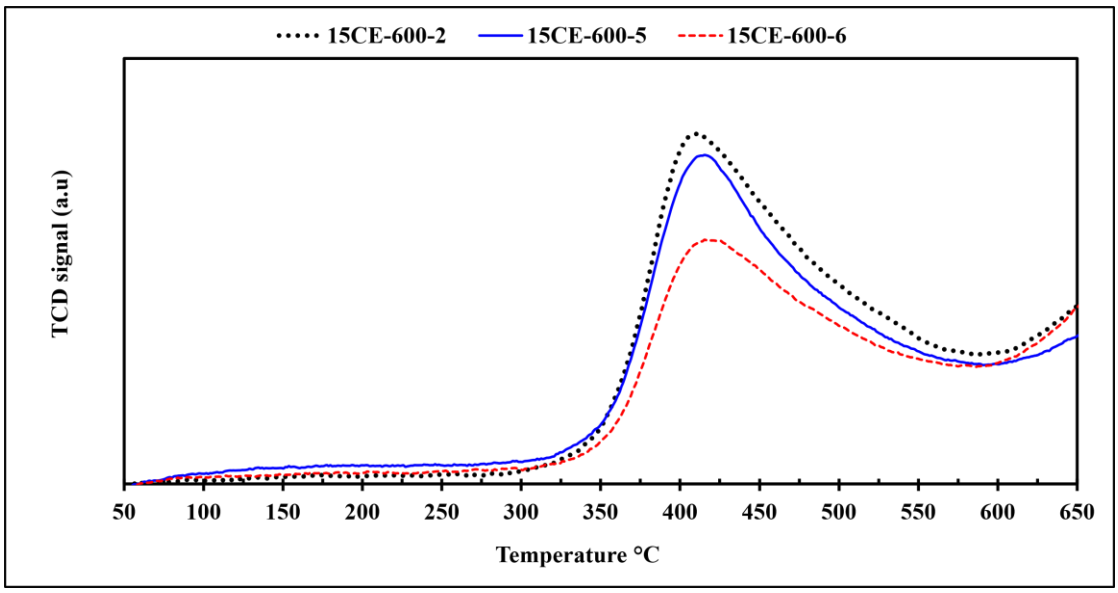

Figure 4.20 NH_3-TPD Desorption Characteristic of As-Synthesis Catalyst at Different 15CE-600 Calcination Times

4.4 Influence of Operating Conditions of Co-pyrolysis CFW and PPW using CE Catalyst

The efficiency and product distribution of catalytic co-pyrolysis are largely dependent on key process parameters, including pyrolysis temperature, cotton fabric waste-to-polypropylene waste (CFW/PPW) ratio, feedstock-to-catalyst (F/C) ratio, and pyrolysis time. These parameters are evaluated under constant process conditions of 500 °C pyrolysis temperature, a 50:50 CFW/PPW ratio, a 1:1 F/C ratio, and a pyrolysis time of 60 min. These conditions were selected based on the effect of parameter studies by maximizing bio-oil yield. The subsequent sections will provide a detailed analysis of the influence of each parameter on the catalytic co-pyrolysis process. The best

condition catalyst from effect of synthesis conditions which is 15CE-600-5 is used in the investigation on effect of operating parameters.

4.4.1 Effect of Pyrolysis Temperature on 15CE-600-5 Catalyst Activity

The effect of pyrolysis temperature on 15CE-600-5 catalyst activity was investigated at constant operating conditions of CFW/PPW ratio (50:50), F/C ratio 1:1 and pyrolysis time 60 min at different pyrolysis temperature (450 °C, 500 °C, 550 °C, 600 °C, and 650 °C. Figure 4.21 (a) and 4.21 (b) show the product yield and bio-oil component distributions, respectively. The char yield is observed to relatively stable at about 10 % except the highest char (12.5 %) is observed at 450 °C across the entire temperature range. The bio-oil yield shows the increment from 38.8 % to 76.4 % as the temperature increases from 450 °C to 500 °C. However, further temperature elevation exhibit reducing trend in bio-oil yield and remain slightly unchanged after 600 °C.

At earlier stage (450 °C to 500 °C), the temperature range is essential for breaking the long polymer of CFW and PPW into shorter polymer that enhanced oil yield. However, when the temperature raised further, the decomposition of CFW/PPW blend was completed (Sophonrat et al., 2018) and undergo secondary cracking of volatiles. The lighter components underwent further cracking to form gases component such as CO, CO_2, H_2, and CH_4, thus observed high in gases yield at elevated temperatures (Sun et al., 2025). Notably, a peak bio-oil yield of around 76.4 % was achieved at a pyrolysis temperature of 500 °C. However, the gas yield displayed an inversed pattern of bio-oil. The gas yield is observed in increment trend by increase pyrolysis temperature from 550 °C. The lowest bio-oil yield was recorded at 450 °C, which is attributed to a partial degradation of the feedstock with highest char residue (Al-Maari et al., 2025).

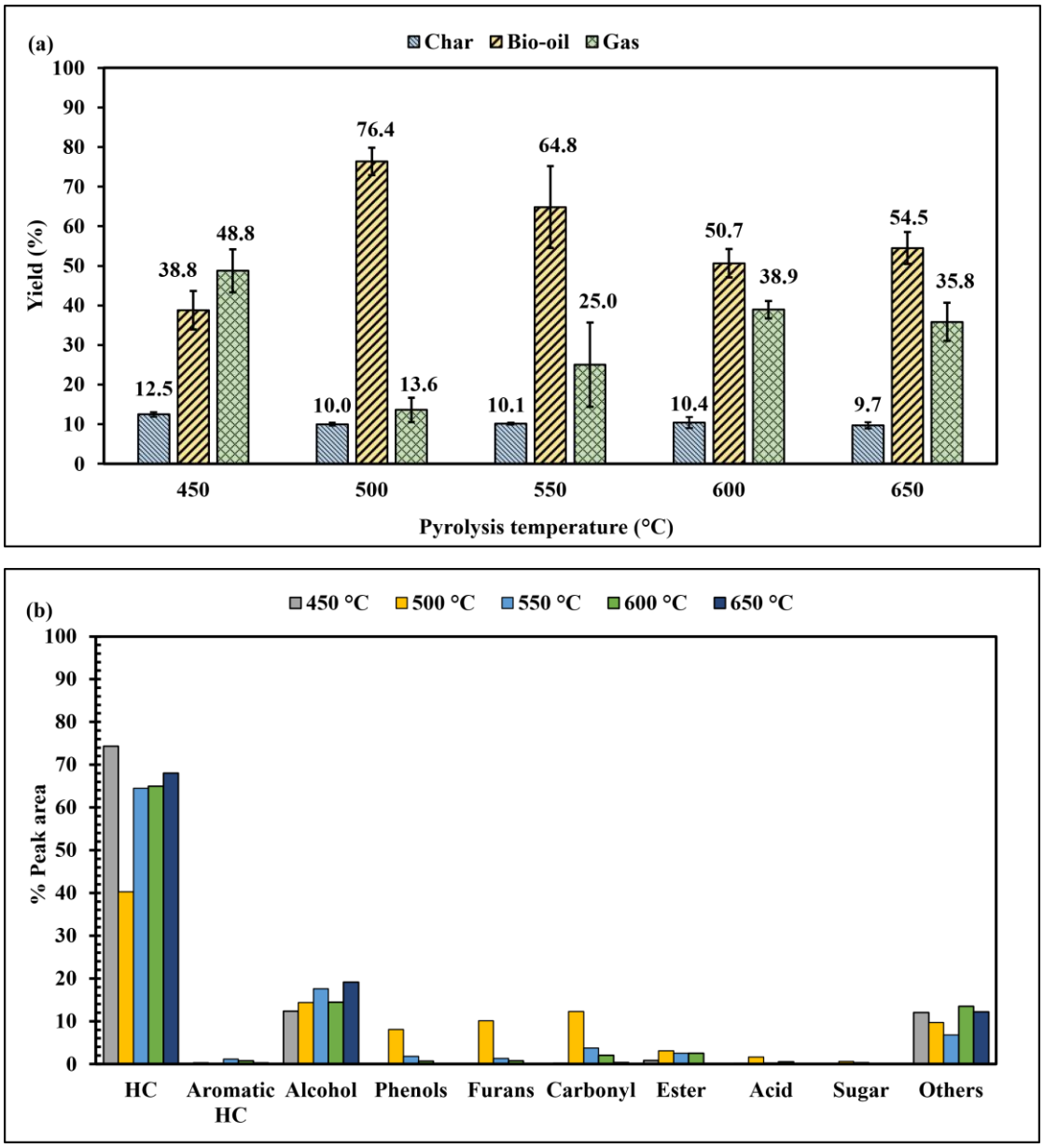

Figure 4.21 Effect of Pyrolysis Temperature on 15CE-600-5 Catalyst Activity (a) Yield % (b) Bio-oil Component Distributions (Operating Condition: 450 °C, 500 °C, 550 °C, 600 °C, 650 °C Pyrolysis Temperature; 60 min Pyrolysis Time; 50:50 CFW/PPW; 1:1 F/C Ratio)

Figure 4.21(b) illustrates the bio-oil component distributions at various pyrolysis temperatures. Most of the sugar compound was dehydrated to form other compounds as early as 450 °C. The hydrocarbon was dominated and followed by alcohol and other oxygenated organic compounds including phenols, furans, carbonyl, ester, and acids. At 500 °C, notably the intermediate product of furans, phenols and carbonyls was formed, and the aliphatic HC was tremendously dropped almost half of aliphatic HC formed at 450 °C. At 500 °C, the CFW undergoes rapid depolymerization

and fragmentation, leading the formation of oxygenated compounds and hydrocarbon mostly form by PPW was facilitating the secondary reaction (Jin et al., 2022).

The high formation of carbonyl and alcohol might be attributed to retro-aldol condensation of saccharides derived from cellulose deconstruction (Zhang et al., 2021). Besides that, employing 15CE catalyst in the co-pyrolysis of CFW/PPW enhanced formation of furans, phenols, and carbonyls at 500 °C. Further increase the temperature above 500 °C, the intermediate is consumed remarkably and forms higher hydrocarbon compound. It is possibly via cracking, condensation, dehydration, and aromatization. The aromatic hydrocarbon was form at higher temperature probably due to the aromatization reaction of carbonyl (Wang et al., 2020).

4.4.2 Effect of CFW/PPW Ratio on 15CE-600-5 Catalyst Activity

The effect of CFW/PPW ratio on 15CE-600-5 catalyst activity was investigated at constant operating conditions of pyrolysis temperature 500 °C, F/C ratio 1:1 and pyrolysis time 60 min at different CFW/PPW ratio (80:20, 60:40, 50:50, 40:60 and 20:80). Figures 4.22(a) and 4.22(b) show the product yield and bio-oil component distributions, respectively.

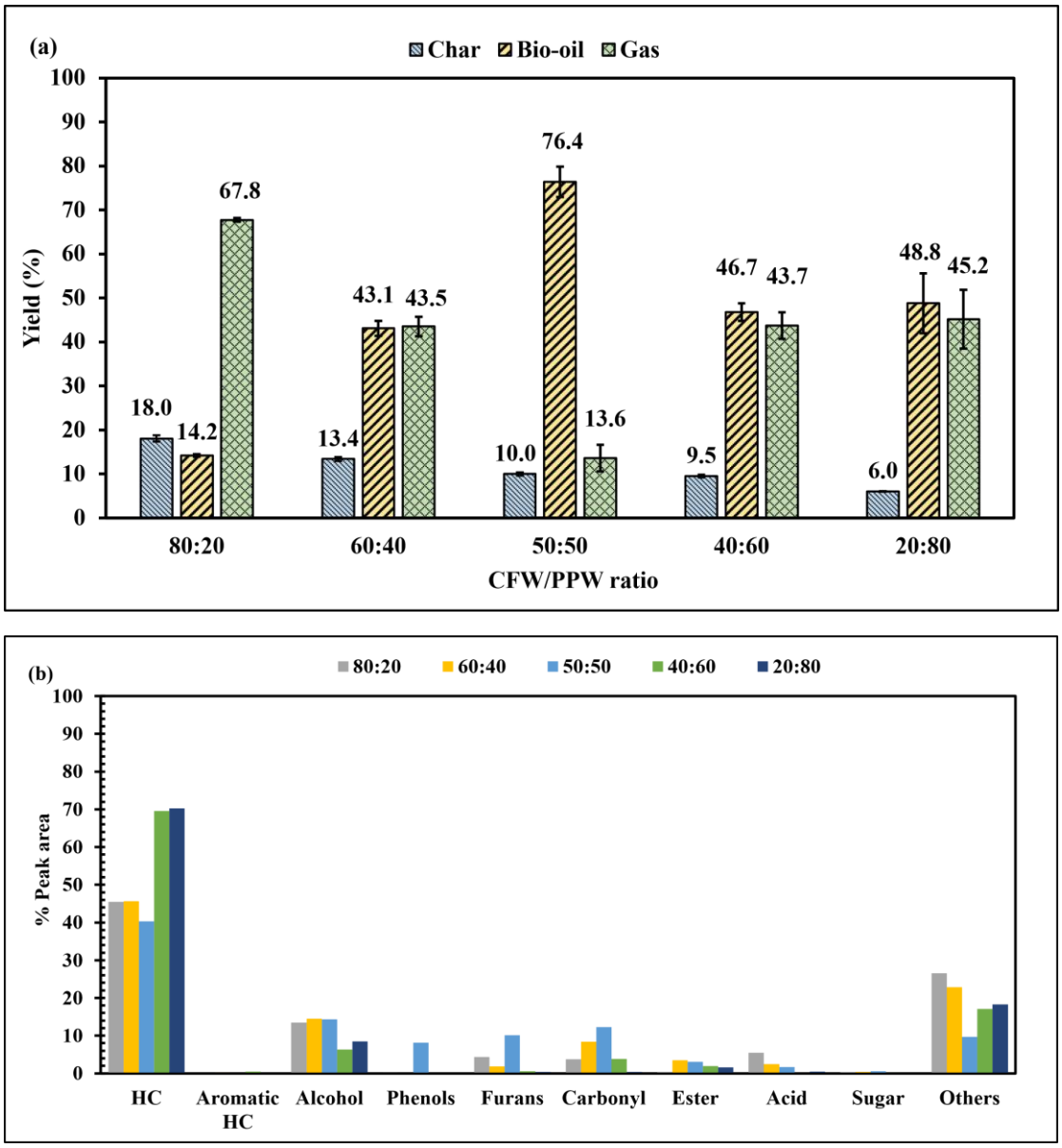

Figure 4.22 Effect of CFW/PPW Ratio on 15CE-600-5 Catalyst Activity (a) Yield % (b) Bio-oil Component Distributions (Operating Condition: 500 °C Pyrolysis Temperature; 60 min Pyrolysis Time; 80:20, 60:40, 50:50, 40:60, 20:80 CFW/PPW Ratio; 1:1 F/C Ratio)

The result in 4.22(a) shows the bio-oil yield increased from 14.2 % to the highest peak of 76.4 % as the ratio of PPW increased to 50 % (CFW/PPW ratio of 50:50). Subsequent increased of PPW caused the bio-oil yield dropped to 46.7 %. It is also notable that the trend of char and gas yield were opposite to bio-oil yield. The significant low yield of char was observed when low CFW was co-feed with PPW. The char is mainly a residue of CFW after pyrolysis, meanwhile at 500 °C, most of the PPW has been degraded into volatiles, and more gases was produced as the percentage of PPW in the feedstock increased (Ahmad et al., 2024). Shafaghat et al., (2019) also found

reduction of char yield when higher co-feed ratio of plastic during catalytic co-pyrolysis of empty fruit bunches (EFB) with PP over meso-MFI catalyst from 24.62 % to 11.46 % (75:25 to 25:75 of EFB:PP). The higher proportion of PPW might produce more hydrogen particles and thus weakened the polymerization reaction of oxygenates (Duan et al., 2017). At initial stage, the degradation of CFW at lower temperatures has initiated the chain scission of plastic polymer chains. The unstable free radicals from CFW pyrolysis absorbed the hydrogen and inhibited the polymerization and cross-linking reactions, thereby bio-oil is selective to hydrocarbon formation and suppressing char formation (Duan et al., 2017; Kumar & Srinivas, 2020).

As depicted in Figure 4.22(b), hydrocarbon and alcohol are the primary products in the bio-oil. The aliphatic hydrocarbon content increased with the decreasing CFW/PPW ratio. At the same time, higher PPW reduce the oxygenated chemical compounds and shows a formation of aromatic. At higher CFW/PPW ratios, the bio-oil composition tends to shift toward oxygenated intermediates. This occurs because CFW degradation produces a high amount of anhydro sugars. These anhydro sugars are large molecules that hinder diffusion into the catalyst pores, limiting further conversion into hydrocarbons and aromatics. As a result, the molecules likely adsorb onto the catalyst surface, where then undergo dehydration to form furans and small oxygenated compounds (Kumar & Srivinas, 2020).

Conversely, the aliphatic HC was increased tremendously at 60 % and 80 % of PPW. The formations of hydrocarbon especially olefin and aromatic possibly undergo various pathways and primarily attribute to the interaction of furans (cellulose from CFW) and PPW derived olefin. A slightly increase in aromatic hydrocarbons (0.5 %) at 40:60 CFW/PPW ratio was also observed with a decrease in furans, suggesting that the Diels–Alder reaction was enhanced, and more furans were being converted into aromatic compounds as the amount of PPW increased. (Wang et al., 2021).

4.4.3 Effect of F/C Ratio on 15CE-600-5 Catalyst Activity

The effect of F/C ratio on 15CE-600-5 catalyst activity was investigated at constant operating conditions of CFW/PPW ratio 50:50, pyrolysis temperature 500 °C and pyrolysis time 60 min at different F/C ratio (2:1, 1:1, 1:1.5, and 1:2). Figures 4.23(a) and 4.23(b) illustrate the product yield and bio-oil component distributions under different F/C ratio, respectively.

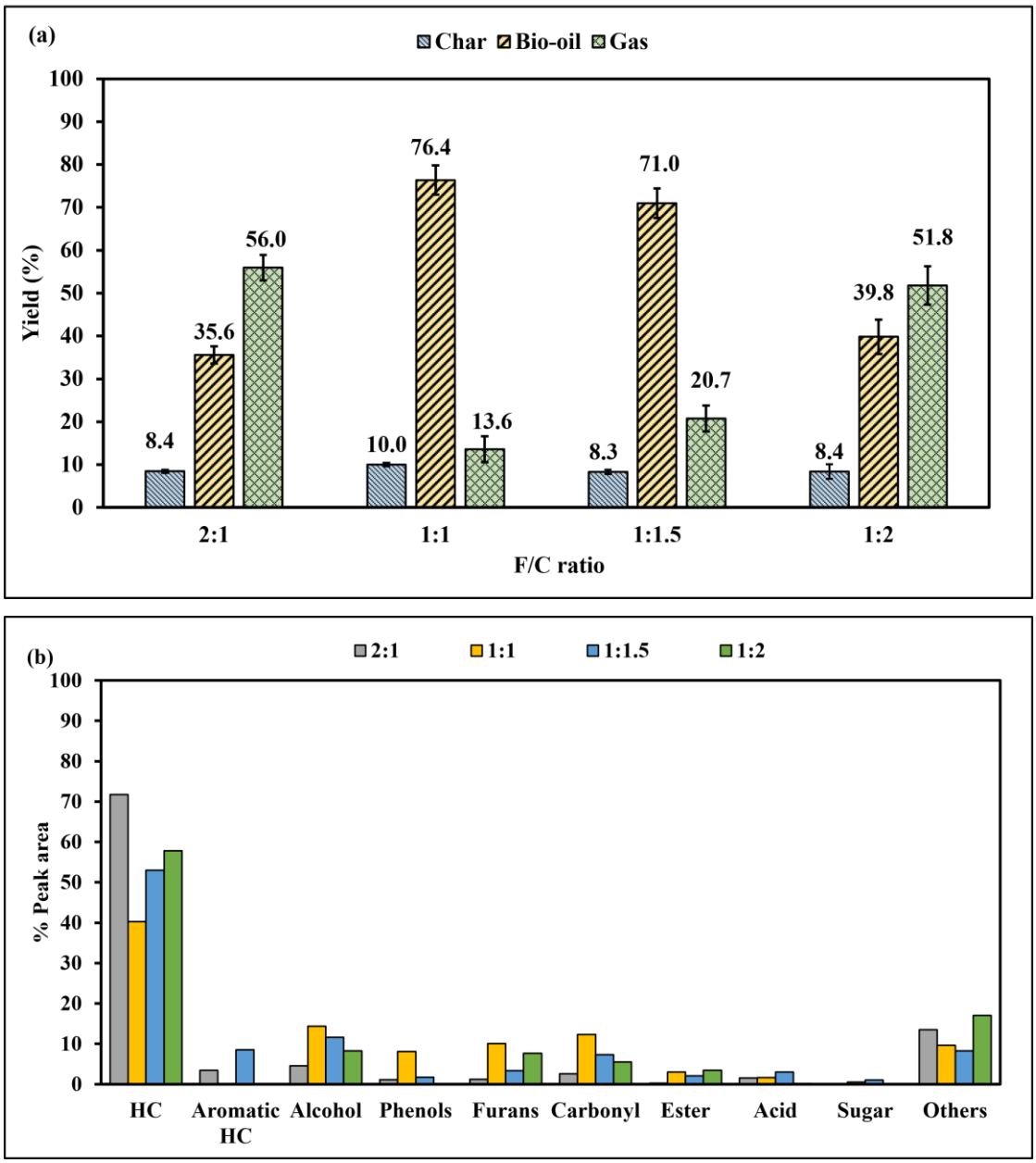

Figure 4.23 Effect of F/C Ratio on 15CE-600-5 Catalyst Activity (a) Yield % (b) Bio-oil Component Distributions (Operating Condition: 500 °C Pyrolysis Temperature; 60 min Pyrolysis Time; 50:50 CFW/PPW Ratio; 2:1, 1:1, 1:1.5, 1:2 F/C Ratio)

The maximum bio-oil yield of 76.4 % was obtained by using 1:1 FC ratio. The increase in bio-oil yield with higher catalyst loading (from 2:1 to 1:1) can be attributed to the greater availability of active sites, which enhances the interaction between pyrolysis vapours and the catalyst surface. This promotes secondary reactions such as cracking and deoxygenation, leading to increased formation of condensable hydrocarbons (Wang et al., 2025). However, further increment catalyst amount resulted the decreasing trend in producing bio-oil and more gases were produced. Several studies

on the catalytic co-pyrolysis of biomass and plastics have reported that increasing catalyst loading generally leads to a reduction in bio-oil yield, primarily due to the excessive cracking of pyrolysis vapors into gases (Muhammad & Manos, 2021; Wang et al., 2025; Xue et al., 2018). This is often accompanied by an increase in hydrocarbon content in bio-oil, attributed to the availability of more active sites and sufficient pore structures that promote deoxygenation and aromatization reactions (Hassan & Hameed, 2023).

Catalyst loading at different F/C ratios significantly affected the production of aliphatic HC, aromatic HCs, and oxygenated compounds in the bio-oil as shown in Figure 4.23(b). The highest aliphatic HC content was observed at an F/C ratio of 2:1, possibly due to effective deoxygenation by plastic-derived radicals and selective conversion of oxygenates by the catalyst (Chen et al., 2020). However, the lower catalyst amounts limited vapor to catalyst contact, reducing cracking and resulting in heavier hydrocarbons. At an F/C ratio of 1:1, aliphatic HC production decreased due to increased formation of furans, phenols, and carbonyls. When catalyst loading increased (F/C 1:1.5 and 1:2), aliphatic HC content gradually rose, with aromatic HC peaked at 1:1.5. This is likely due to greater active site availability and enhanced Diels–Alder and dehydration reactions, which promoted aromatics and reduced oxygenates (Li et al., 2025)

4.4.4 Effect of Pyrolysis Time on 15CE-600-5 Catalyst Activity

The effect of pyrolysis time on 15CE-600-5 catalyst activity was investigated at constant operating conditions of pyrolysis temperature 500 °C, CFW/PPW ratio 50:50, and F/C ratio (1:1) at different pyrolysis time (15 min, 30 min, 45 min, 60 min and 75 min). Figures 4.24(a) and 4.24(b) illustrate the product yield and bio-oil component distributions under different pyrolysis time, respectively.

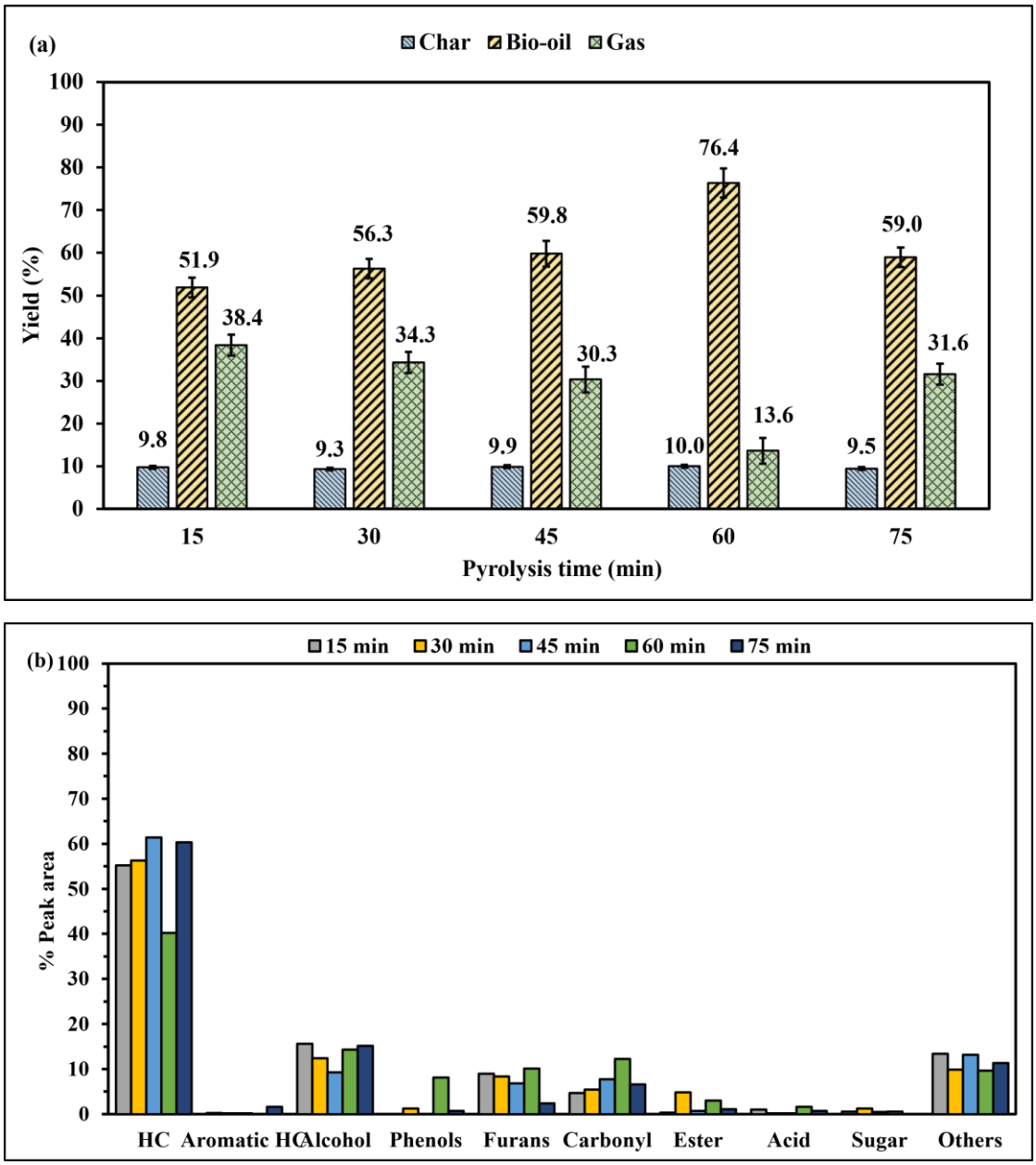

Figure 4.24 Effect of Pyrolysis Time on 15CE-600-5 Catalyst Activity (a) Yield % (b) Bio-oil Component Distributions (Operating Condition: 500 °C Pyrolysis Temperature; 15, 30, 45,60,75 min Pyrolysis Time; 50:50 CFW/PPW Ratio; 1:1 F/C Ratio)

Bio-oil yield increased significantly from 51.9 % at 15 min to 76.4 % at 60 min, then declined to 59.0 % at 75 min. Gas yield followed an opposite trend, decreasing to 13.6 % at 60 min before rising again, while char yield remained relatively constant at 9.3–10.0 %. These results suggest that prolonged exposure of feedstock in pyrolysis enhances bio-oil yield up to an optimum time, beyond which secondary cracking increases gas production (Ahmad et al., 2024). Longer residence times improve feedstock conversion by allowing complete thermal decomposition and cracking of

volatiles. However, extended durations beyond the optimal point may reduce liquid yield (Genuino et al., 2024). Char yield was largely unaffected, as major devolatilization occurs early. At 500 °C, most PPW decomposes fully, while CFW stabilizes as solid residue (Vuppaladadiyam et al., 2019). While catalysts influence vapor-phase reactions, their impact on char is minimal once they have formed.

The chemical composition of bio-oil products during catalytic co-pyrolysis of CFW and PPW illustrated in Figure 4.24(b) indicates the increment of aliphatic HC composition as pyrolysis time increased. However, the catalytic reaction favours the formation of oxygenates such as alcohol, phenols, furans, and carbonyl when the pyrolysis time was prolonged to 60 min. The high formation of carbonyls and alcohols might be attributed to retro-aldol condensation of sugar derived from cellulose degradation (Zhang et al., 2021). After 75 min, the furans possibly undergo Diels-Alder cycloaddition with olefin to form bicyclic intermediates that rapidly dehydrate and dehydrogenate to aromatic HC since the composition of aromatic increased (He et al., 2023).

4.4.5 Reusability and Regeneration on 15CE-600-5 Catalytic Activity

Figure 4.25 shows the catalytic activity on 15CE-600-5 catalyst for reusability and regeneration study after three cycles. The result indicates significant reduction in catalytic activity during reusability test, where the bio-oil yield reduced from 76.4 % to 21.6 % and 21.5 % for cycle 2 and cycle 3, respectively. The finding indicates 71.8 % reduction in catalytic activity, which possibly due to coke deposition that hinder the accessibility to the active sites on catalyst surface (Barbosa et al., 2021). The adsorbed material deposition blocks pore channels and cover catalyst surface, which significantly reduces accessible surface area and active sites. Therefore, limits the vapor-catalyst interaction.

However, regeneration test showed improved catalytic activity which increased to 58.5 % and 56.7 % bio-oil yield for cycle 2 and cycle 3, respectively. The finding suggest that the regenerated catalyst has undergone thermal treatment via calcination to remove the impurities on the catalyst. During regeneration, calcination removes the coke deposits, reopens the pores, and partially recovers access to active sites, which improves catalytic activity. However, the activity is not fully recovered due to possible

irreversible changes such as sintering. Thus, regeneration shows better catalytic activity compared to reusability test.

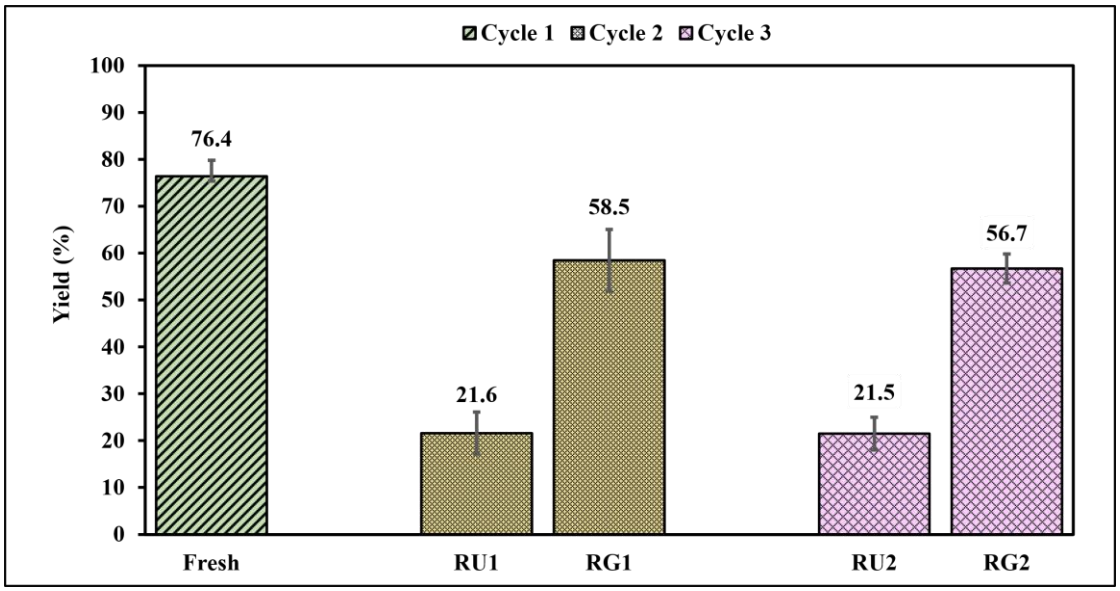

Figure 4.25 Reusability and Regeneration Study on 15CE-600-5 Catalyst Activity (Operating Condition: 500 °C Pyrolysis Temperature; 60 min Pyrolysis Time; 50:50 CFW/PPW Ratio; 1:1 F/C Ratio)

4.4.6 Concluding Remarks for CE Catalyst and Justification for Development of CTE Catalyst

The formulated of CE catalyst exhibited strong potential for the catalytic co-pyrolysis of CFW and PPW for bio-oil production. It significantly enhanced bio-oil yield, achieving a maximum of 76.4 % compared to only 46.2 % for reaction without catalyst. The resulting bio-oil was rich in aliphatic HC, accompanied by notable concentrations of oxygenated intermediates including alcohol, furan, phenol, and carbonyls. The best condition catalyst in the effect of catalyst preparation condition shows that 15 % of Cr loading on EA and calcination at temperature of 600 °C and time of 5 h which is 15CE-600-5. The effect of operating condition shows that the best condition is obtained at 500 °C, 60 min, 50:50 CFW/PPW ratio and 1:1 F/C ratio. The reusability study shows that the catalyst activity declined after the second and third cycles of reusability which suggesting blockage of active sites. Catalyst regeneration was able to improve performance by removing surface blockages, thereby recovering catalytic activity to a considerable extent. Despite this, there is potential for the catalyst to be improve further to increase both product yield and upgraded the bio-oil quality.

The development of CTE was pursued by integrating Ti into CE catalyst to improve textural properties, acidity that may increase the catalyst activity and reusability.

Several works were reported on the high catalytic activity of TiO_2 in different applications. The nano TiO_2 was used as catalyst in hydrothermal liquefaction (HTL) of oil sludge to produce H_2 and light aliphatic HC through hydrocracking (Dang et al., 2021). In pyrolysis of poplar wood, TiO_2 showed higher ability to supress the extensive cracking of primary product resulting in increased of tar yield and reduced gas product yield. (Zhang et al., 2019). The Ti based catalyst not only performed in single metal but also showed the good catalytic activity in composite catalyst. Xu et al., (2023) had reported on using hybrid catalyst of Zr-doped $TiOSO_4$ nanocomposites showed excellence selectivity towards aliphatic HC and enhanced substantial production of toluene compared to non-catalytic pyrolysis of oil shale.

4.5 Development of the Chromium/Titanium-Extracted Aluminium (CTE) Catalysts

The CTE catalysts were synthesized via the wet impregnation method using different formulations. Based on the best conditions of 15CE-600-5 catalyst, the total metal loading was fixed at 15 wt.% while varying the Cr/Ti ratios. The 15 wt.% loading was selected as it previously demonstrated the highest catalytic activity, yielding the maximum bio-oil. All catalyst samples were calcined at fixed temperature of 600 °C and 5 h. Table 4.7 shows the composition of Cr, Ti, and EA in CTE catalyst preparation.

Table 4.7
The Catalyst Prepared at Different Chromium Loadings on EA by Weight

Sample	Cr loading (wt.%)	Ti loading (wt.%)	Catalyst formula	Amount of each metal (g)		
				Cr	Ti	EA
1	0	100	TiO_2	0	3	0
2	0	15	Ti-EA	0	0.45	3
3	10	5	CTE21	0.3	0.15	3
4	7.5	7.5	CTE11	0.225	0.225	3
5	5	10	CTE12	0.15	0.3	3

4.5.1 Effect of Metal Loading on CTE Catalyst Activities

Figure 4.26(a–b) shows the catalytic activity of titanium oxide (TiO_2), titanium-extracted aluminium (Ti-EA), and CTE catalysts with different metal loadings on product yield and bio-oil composition from co-pyrolysis of CFW and PPW.

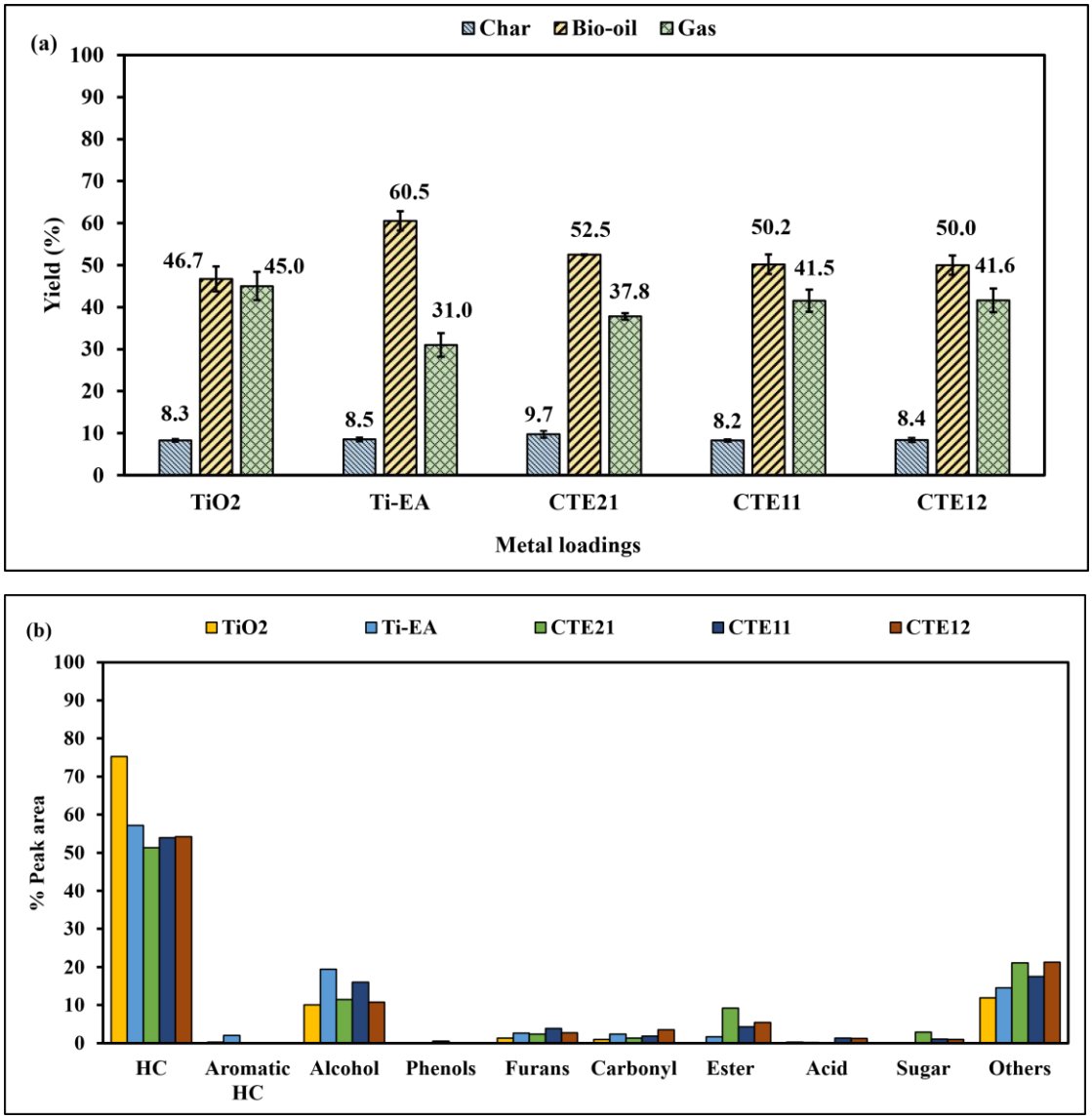

Figure 4.26 Effect of Metal Loadings on CTE Catalyst Activity (a) Yield % (b) Bio-oil Component Distributions (Operating Condition: 500 °C Pyrolysis Temperature; 60 min Pyrolysis Time; 50:50 CFW/PPW Ratio; 1:1 F/C Ratio)

Based on the findings, Ti-EA catalyst achieved bio-oil yield of 60.5 % compared to only 46.7 % using TiO_2 catalyst. The findings show incorporation of Ti onto EA able to contribute to better catalytic activity for Ti-EA catalyst. The char yield is similar for reaction using CTE catalyst ranging from 8.2 % to 9.7 %. The stable char is observed

indicating that char formation is primarily governed by thermal decomposition of the feedstock rather than catalytic effects. This observation is consistent with Xu et al., (2024), whereby it was reported that the bio-char yield remains largely unchanged under indirect catalyst contact. The catalyst mainly enhances secondary decomposition of pyrolysis volatiles rather than influencing primary char formation. However, the gas yield increased, as co-pyrolysis reaction using CTE catalyst with increment of Ti loadings. CTE21, CTE11 and CTE12 obtained gas yield 37.8 %, 41.56 % and 41.6 %, respectively. Also, CTE catalyst obtained more than 50 % bio-oil yield compared to TiO_2 catalyst which suggest incorporated Cr/Ti onto EA able to promote better activity. The trend of CTE catalysts show that CTE21 obtained higher bio-oil yield at 52.5 % compared to 50.2 and 50 % using CTE11 and CTE12, respectively. Previous studies by Zhang et al., (2019), Schmitt at al., (2020) and Atanda et al., (2020) shows utilizing Cr catalyst improved catalytic activity.

Figure 4.26(b) shows bio-oil component distribution, where all catalyst has high aliphatic HC and alcohol, whereas reduced oxygenate product. The trend of CTE catalyst indicates increment in aliphatic HC as Ti loading increased for CTE21, CTE11and CTE12. Previous study used Ti catalyst also shows high aliphatic HC (Fan et al., 2022; Nwankwor et al., 2021). Although CTE21 produced lower aliphatic HC and alcohol than CTE11 and CTE12, it generated more esters. This increase resulted from different catalytic pathways, where esterification occurred through the reaction of alcohol with carboxylic acids in the presence of acids catalyst (Dawodu et al., 2019). The characterizations of their physical and chemical properties were pursued for further correlation into their behaviour as catalysts, which are discussed in subsequent sections.

4.5.2 Functional Groups of Bio-oil using CTE Catalyst at Different Metal Loadings

The FTIR spectra of the bio-oil at different catalysts metal loadings are displayed in Figure 4.27, similar pattern of IR wave indicating common functional group. The broad IR spectra wave at range 3200-3600 cm^{-1} suggests the O–H stretch compound, probably aromatic O–H and alcohol. The hydrocarbons contain C–H, =C–H, C=C also identified and appears at various IR spectra (2955–2872 cm^{-1}, 1378 cm^{-1}, 1115 cm^{-1}, 1021 cm^{-1}, 2160 cm^{-1}, 1654 cm^{-1}, 1454 cm^{-1}) (Dawodu et al., 2019; Stuart, 2004; Xue et al., 2017). Oxygenate compounds found mainly appear at range 1650-

1800 cm^{-1} as C=O bond shows the presence of carbonyls, ester, anhydride, and furans. The obvious sharp IR spectra at 1115 cm^{-1} show the presence of alcohol, phenol (C–O bond), or aromatic (C–H bond). There is also possibility on nitrogen compound such as nitril as observed in peak 1648 cm^{-1}.

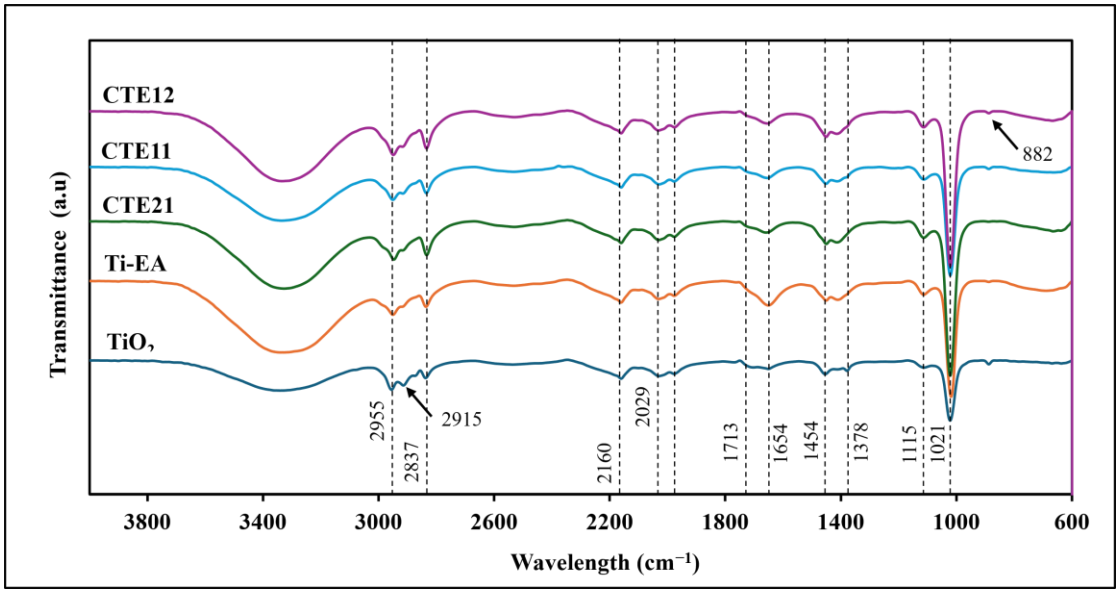

Figure 4.27 FTIR Spectrum of Bio-oil using CTE Catalyst at Different Metal Loadings

4.5.3 Elemental Composition of TiO_2, Ti-EA and CTE21

Table 4.8 displays the elemental compositions of TiO_2, Ti-EA and CTE21 catalysts.

Table 4.8
X-Ray Florescence Analysis of TiO_2, Ti-EA and CTE21

	Al	Si	P	S	Ca	Cr	Ce	Fe	Zn	Mg	Na	Ti	Cu
TiO_2	0.0	0.2	0.0	0.0	0.0	0.0	0.0	0.0	0.0	0.0	0.1	99.7	0.0
Ti-EA	48.5	0.3	5.9	17.6	0.1	0.0	0.0	0.1	0.0	0.2	0.1	27.2	0.0
CTE21	28.5	0.3	4.4	44.4	0.1	16.4	0.1	0.0	0.3	0.1	0.1	5.2	0.1

TiO_2 shows that the sample contains 99.7 wt.% of Ti. While the Ti-EA shows high Al and Ti elements, which are 48.5 wt.% and 27.2 wt.%, respectively, with other components such as P and S. However, the CTE21 catalyst shows the significant composition of S (44.4 wt.%), followed by Al (28.5 wt.%), Cr (16.4 wt.%), Ti (5.2

wt.%) and P (4.4 wt.%). Thus, possibly the strong metal support interactions among Ti-EA catalyst due to high Ti and Al contribute to the high bio-oil yield (Kay Lup et al., 2017). In addition, Ti is known to have high oxophilicity which increase the tendency to deoxygenation activity and coupling with EA increases the acidity of the catalyst. According to Kepp, (2016), high oxophilicity metals such as Ti and Al, have tendency to facile oxygen abstraction. At the same time, each metal contains high acidity, caused enhancement in hydrocarbon production.

4.5.4 Surface Morphology of CTE Catalyst at Different Metal Loadings

Figure 4.28 illustrates the surface morphology of TiO_2, Ti-EA and CTE catalysts at different metal loadings. There is a uniform crystalline structure with aggregated particles that indicate high crystallinity for TiO_2 catalyst. In contrast, Ti-EA shows a modified texture with more irregular and aggregated structures, suggesting the effect of modification with EA on the surface morphology. All the CTE catalysts shows well dispersed particles and maintain a relatively porous structure. In contrast, CTE12 exhibit smoother surface with less roughness and fewer pores. While the higher Cr loading in CTE21 results in enhanced porosity. These structural differences indicate that CTE21 provides more accessible active sites, which facilitate deoxygenation reactions and promote greater hydrocarbon formation during CFW–PPW co-pyrolysis, consistent with findings that aggressive deoxygenation and improved hydrocarbon yields correlate with increased catalyst porosity (Mo et al., 2023).

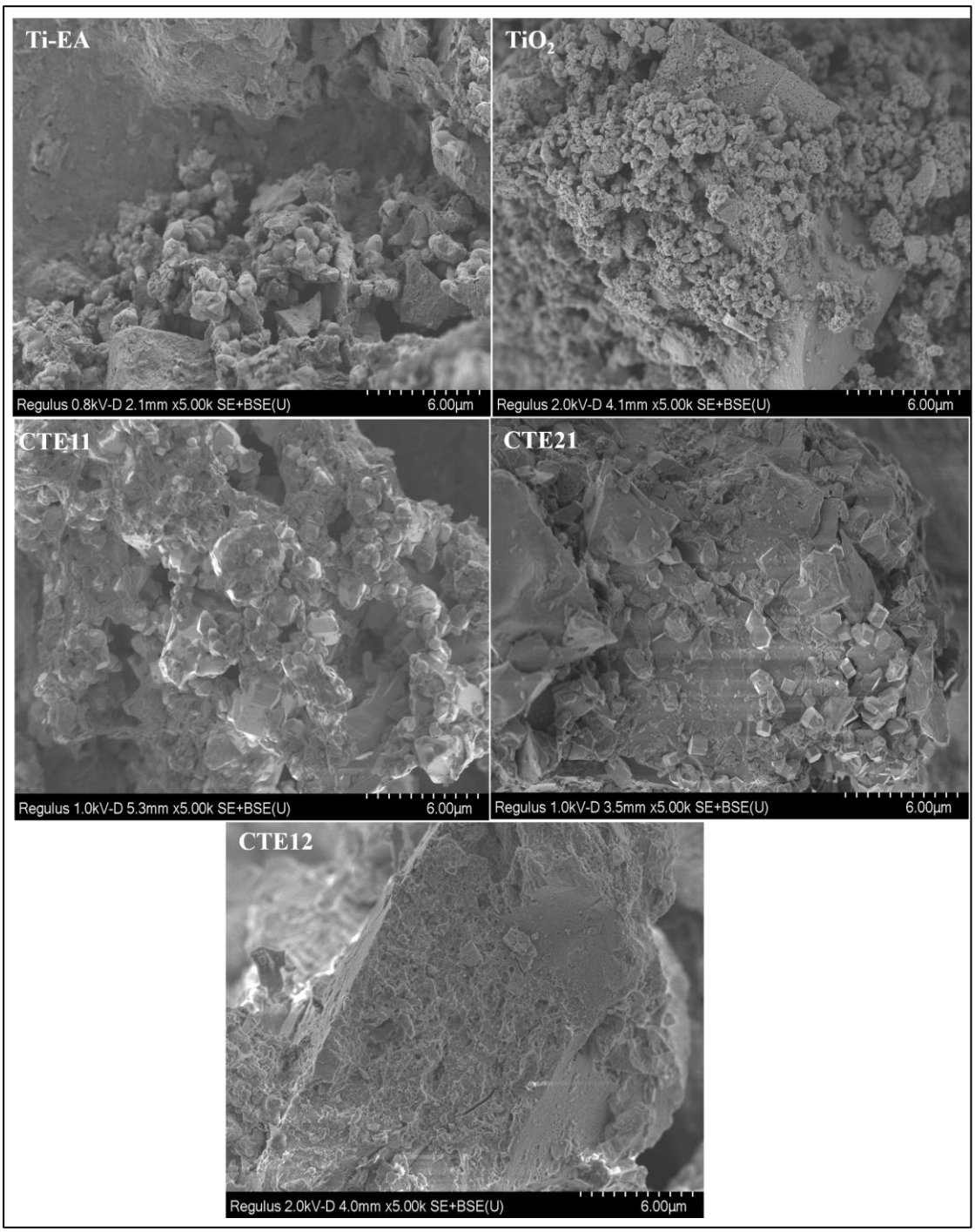

Figure 4.28 SEM Images of Synthesis Catalyst at Different CTE Metal Loadings

4.5.5 Textural and Acid Properties of CTE Catalyst at Different Metal Loadings

The surface area, porosity characteristics, and acid site concentrations of CTE catalysts prepared with different metal loadings are presented in Table 4.9.

Table 4.9
The Textural Properties and Acidity of CTE Catalysts at Various Metal Loadings

	Surface Area [a] (m^2/g)	**Total pore volume [a] (cm^3/g)**	**Average pore size [a] (nm)**	**Acidity [b] (mmol/g)**
TiO_2	3.8	0.0351	36.6	-
Ti-EA	4.6	0.0189	16.5	3.72
CTE21	46.7	0.0696	6.0	1.03
CTE11	7.5	0.0222	11.8	3.56
CTE12	31.1	0.0460	5.9	-

[a] Obtained from N_2 adsorption-desorption
[b] Obtained from NH_3-TPD chemisorption

The catalyst CTE21 has the highest surface area and pore volume and second lowest pore size compared to CTE11 and CTE12. The result indicates different Cr loading at CTE catalyst contribute to the change of textural properties and catalyst activity. As reported, CTE also shown to have the highest bio-oil yield. It is known that highest surface area and pore volume promote better catalytic activity due to more active site for reaction to occur. TiO_2 and Ti-EA have much lower surface area compared to CTE catalyst. The finding indicates incorporation of Cr into CTE catalyst contribute to increment of surface area. Previous studies on propane dehydrogenation reported 5Cr–SBA–15 have high surface area (Tedeeva et al., 2025). Ti-EA has low surface area and pore volume. However, its acid of 3.72 mmol/g is above to CTE21 at 1.03 mmol/g. This could explain the high bio-oil yield obtained using Ti-EA, where indicates catalyst acidity also contribute to catalyst activity not just surface area. (Moonsrikaew & Duangchan, 2022).

N_2 sorption isotherm analysis in Figure 4.29 demonstrates the CTE catalysts displayed the behaviour of isotherm type IV with hysteresis loop H2. The type IV isotherms indicates the CTE catalysts are mesopores with blocking in a narrow pore neck with larger size distribution (Thommes et al., 2015). Conversely, for TiO_2 and Ti-EA are type III indicate nonporous catalysts. The mesopore characteristics of CTE catalysts increased the surface area and allowed the volatiles to access to the active metals.

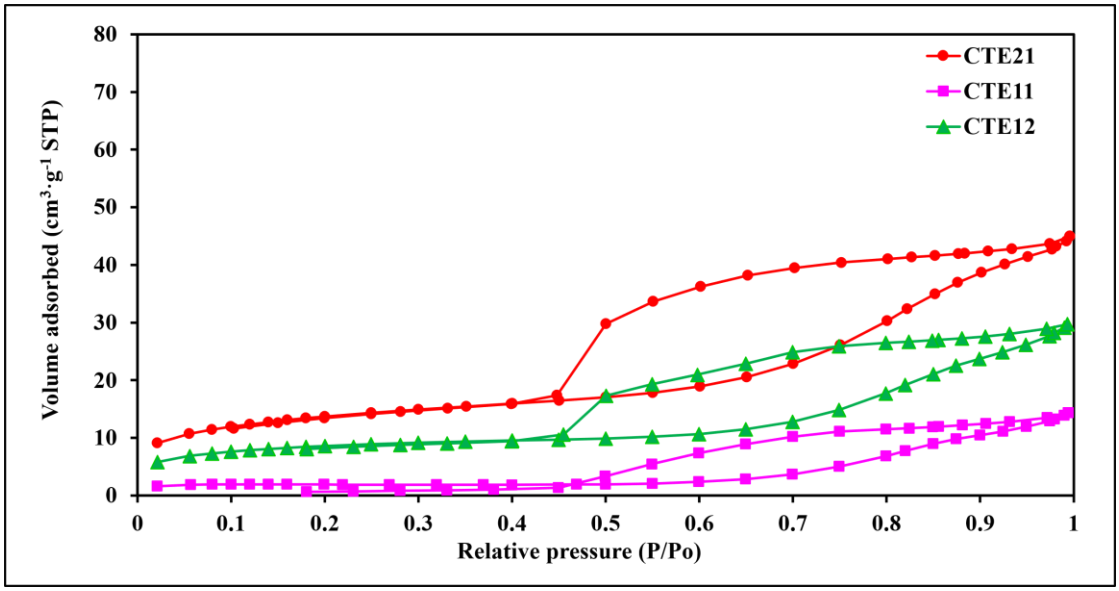

Figure 4.29 N_2 Sorption Isotherm of CTE Catalyst at Different Metal Loadings

Figure 4.30 shows the pore size distribution of the CTE catalysts, TiO_2 and Ti-EA. The CTE21, CTE11, and CTE12 have pore size at range between 2–34 nm, which exhibit a mesopores structure with a dominant pore size ranging between 7–20 nm. The mesopore characteristics possibly facilitates molecular diffusion and enhances accessibility of active sites (Li et al., 2025). While Ti-EA shows pore size distribution in range between 16–30 nm with the differential pore volume less than 0.02 cm^3/g, possibly attributed to the spacing within the rugged small particles (Alrozi et al., 2023).

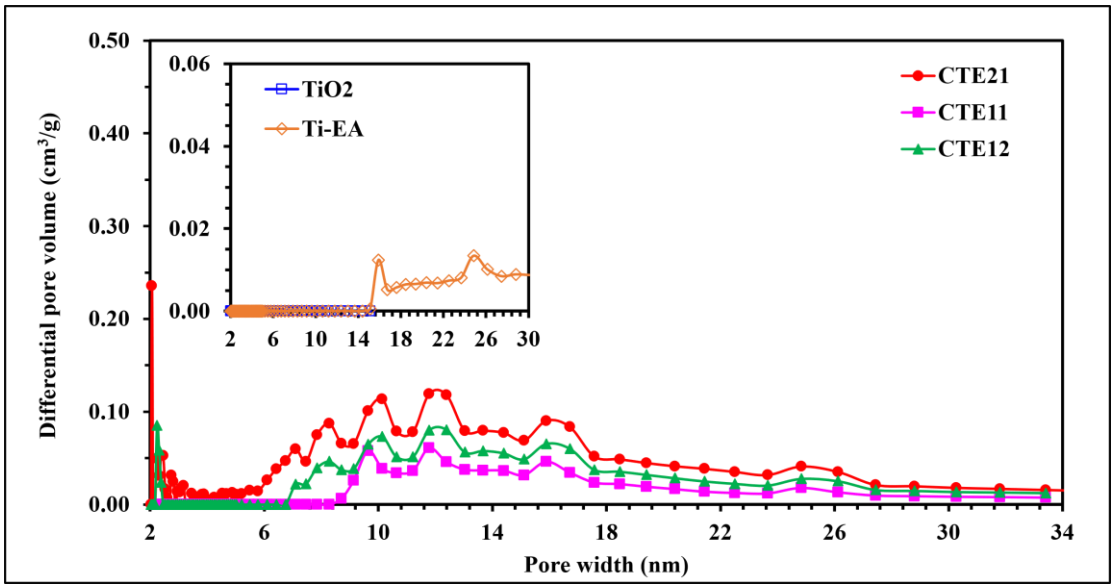

Figure 4.30 Pore Size Distribution of CTE Catalyst at Different Metal Loadings

Figure 4.31 shows TPD profiles of the CTE catalysts. The acidity also increased with the mixture of Cr and Ti incorporated onto EA.

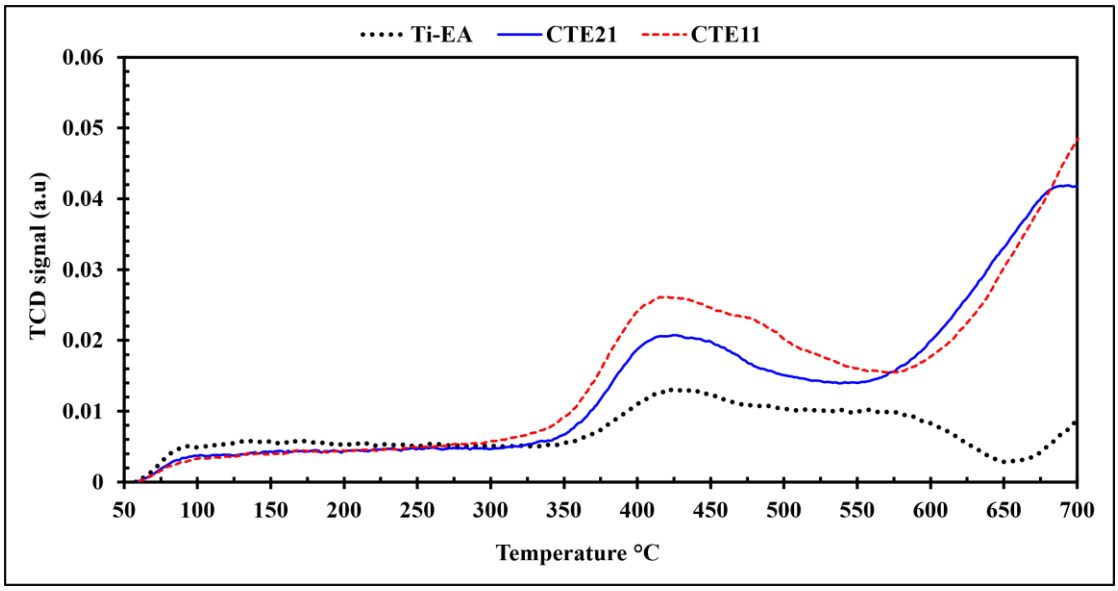

Figure 4.31 NH_3-TPD Desorption Characteristic of As-Synthesis Catalyst at Different CTE Metal Loadings

The CTE21 and CTE11 catalysts shows desorption peaks around 350 – 500 °C and > 650 °C corresponds to medium and strong acid sites. The Ti-EA catalyst also shown the peak appeared at 400 – 450 °C and 550 – 600 °C indicates the medium and strong acid sites. Thus, CTE21, CTE11 and Ti-EA show the high total acid as reported in Table 4.9, which has improved the catalytic activity during co-pyrolysis of CFW–PPW.

4.5.6 Crystallography of TiO_2, Ti-EA and CTE21

Figure 4.32 displays the XRD diffraction patterns of TiO_2, Ti-EA and CTE21 catalyst.

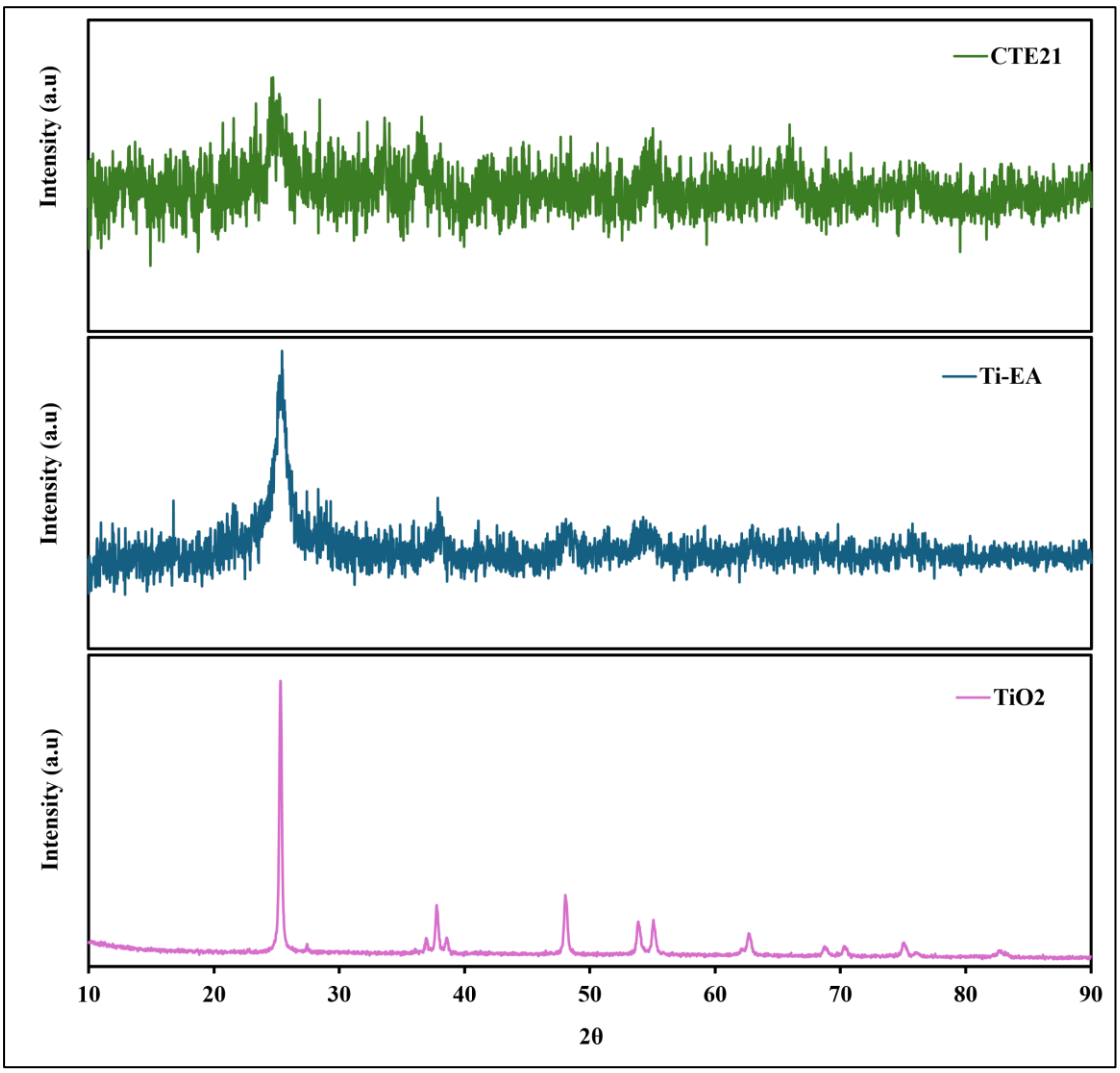

Figure 4.32 X-ray Diffactogram of TiO_2, Ti-EA, CTE21

The TiO_2 with 79.5 % crystallite shows the sharp peaks at 2θ of 25.4°, 37.8°, 36.9°, 38.5°, 48.1°, 55.1°, 62.8°, and 68.8°, are attribute to anatase TiO_2 phase compared to reference (ICDD No: 75-1537) (El-Desoky et al., 2020; Peng et al., 2016). The similarity between the XRD features of TiO_2 indicates it was formed in its pure anatase crystalline structure. The incorporation of Ti into EA presents the additional XRD diffraction peaks at 2θ of 14.9°, 21.4°, 30.5°, 47.9°, 65.1°, 75.7°, and 85.6°, indicate the presence of aluminium in different forms such as aluminium sulphate (ICDD No. 98-003-4816), aluminium oxide (ICDD No. 98-002-3782) and boehmite (ICDD No. 98-002-3618). There are also observed the overlapping peaks among aluminium forms with TiO_2 peaks at 2θ of 25.4°. While CTE21 catalyst unveils the peak at 2θ of 14.9°, indicates the presence of Cr_2O_3 other than TiO_2, and other aluminium forms. The Ti-EA and CTE21 signifies the amorphous structure.

4.5.7 Effect of Calcination Temperature on CTE21 Catalyst Activity

CTE21 was chosen for further investigation on char, bio-oil and gas yield as shown in Figure 4.33(a) and bio-oil component distributions in Figure 4.33(b). The calcination temperatures were evaluated between 400–800 °C. Figure 4.33(a) shows the char yield, from 7.9 % to 10.8 % which demonstrate only small variation, suggesting stable thermal decomposition under constant operating conditions. The bio-oil and gas yields varied considerably with calcination temperature. CTE21-400, calcined at 400 °C, produced 61.8 % bio-oil, while the yield declined to 51.8 % for CTE21-500. As the calcination temperature increased from 500 °C to 700 °C, the catalytic activity increased where the bio-oil yield rose to a maximum of 63.4 %, before decreasing again to 52.9 % at 800 °C. In contrast, the gas yield declined from 39.6 % for CTE21-500 to 27.5 % for CTE21-700 and subsequently increased to 39.2 % for CTE21-800. This indicates that calcination at 700 °C promotes the cracking of large molecules to shorter molecules, while at 800 °C shows formation of gases increased indicates over cracking of bio-oil components into non-condensable gases (Xu et al., 2022). Thus, CTE21-700 emerges as the best calcination temperature for maximizing bio-oil production.

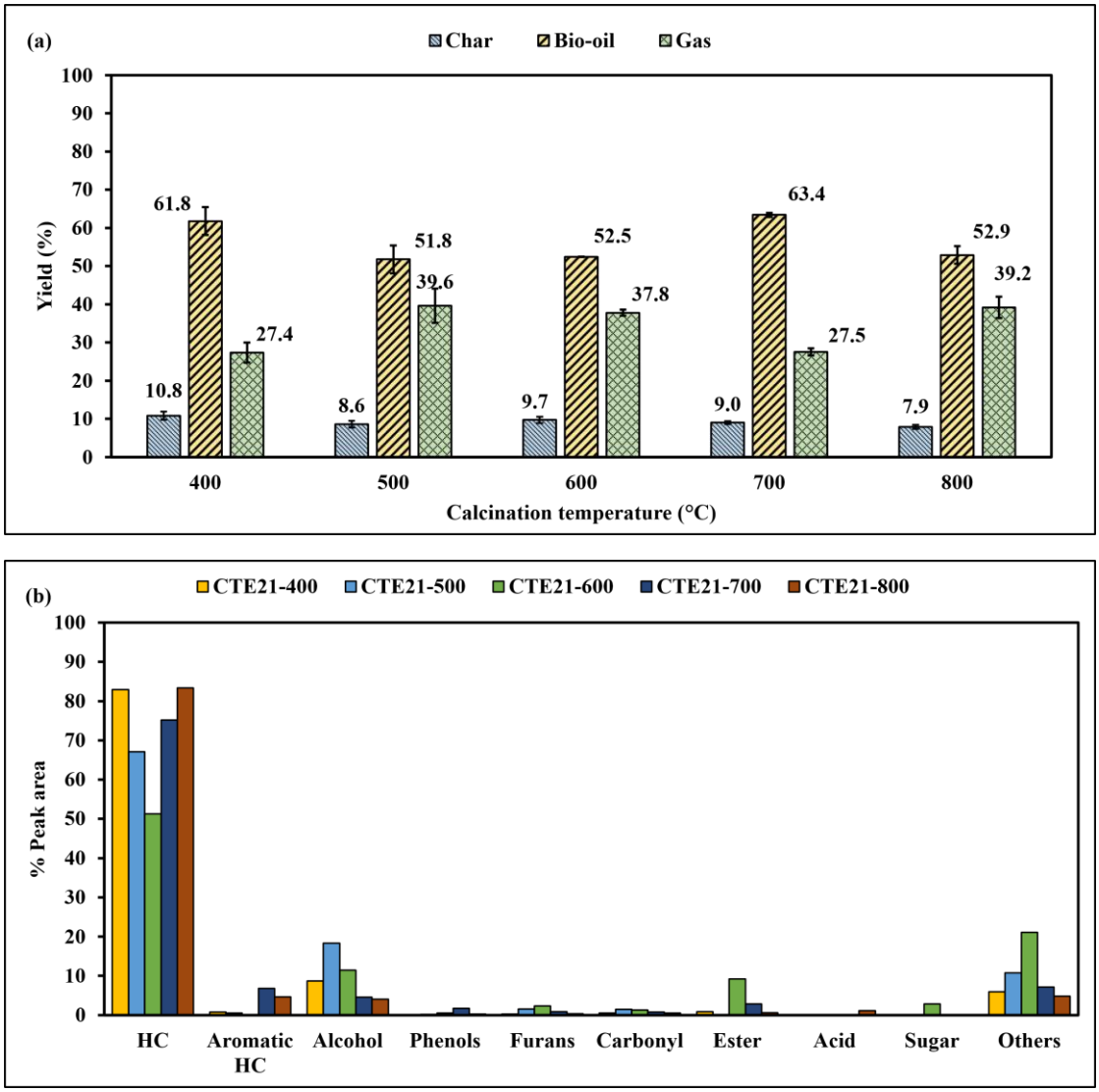

Figure 4.33 Effect of Calcination Temperature on CTE21 Catalyst Activity (a) Yield % (b) Bio-oil Component Distributions (Operating Condition: 500 °C Pyrolysis Temperature; 60 min Pyrolysis Time; 50:50 CFW/PPW Ratio; 1:1 F/C Ratio)

Figure 4.33(b) displays the bio-oil component distributions at different calcination temperature of CTE21 catalyst. The major bio-oil compound detected were aliphatic HC and alcohol. The other oxygenates significantly reduced specifically aldehyde and acid. Moreover, the sugar compound also mostly converted into smaller molecules in a form of aliphatic HC or other oxygenate compounds. The trend shows that increased calcination temperature from 400 °C (CTE21-400) to 600 °C (CTE21-600) reduced the aliphatic HC production. Further increased calcination temperature for CTE21-700 and CTE21-800 conversely increased the aliphatic HC production and observed the formation of aromatic aliphatic HC. The higher calcination temperature tends to cause the structural changes and facilitate the development of active sites on

the surface, which promote the deoxygenation reaction to aliphatic HC production (Harith et al., 2022). The deoxygenation reactions actively occurred and removed oxygenated compound via decarboxylation, decarbonylation, dehydration and demethoxylation (Chen et al., 2022).

The strong acidity associated with the CTE21-700 catalyst possibly drives the cracking and deoxygenation reaction and facilitating with large surface area, pore size and volume that ease the diffusion of larger molecules into the pores and active sites. Therefore, prominently converted to aliphatic HC and aromatic HC. Previous study has reported that the aromatic HC and phenols were enhanced via hydrodeoxygenation (including decarbonylation and decarboxylation) likely due to enriched and stronger acid sites (Wang et al., 2018). Sarker et. al., (2020) and He et. al., (2018) also emphasized on the influence of medium and strong acidity in promoting aliphatic HC and aromatic production. Therefore, CTE21 calcined at 700 °C (CTE21-700) is the best calcination temperature for the catalyst used in the co-pyrolysis of CFW and PPW as it generates the highest bio-oil yield up to 63.4 %.

4.5.8 Functional Groups of Bio-oil using CTE21 Catalyst at Different Calcination Temperature

Figure 4.34 demonstrate the FTIR spectra for bio-oil obtained from the reaction via CTE21 catalysts at different calcination temperature. Generally, all catalyst exhibits similar pattern of IR wave. The IR wave signifies similar peaks to the reference CTE21-600 catalyst as discussed previously in Figure 4.27. A broad band around 3400 cm^{-1} corresponded to O–H stretching vibrations of alcohol and phenol, while the peak near 1700 cm^{-1} indicated carbonyl compounds such as ketones and aldehydes. Absorptions in the range of 2920–2850 cm^{-1} were assigned to aliphatic C–H stretching of alkanes and alkenes, whereas the bands near 1600 cm^{-1} reflected aromatic C=C vibrations. The C–O stretching of alcohol, ether, and ester was also detected between 1050 and 1150 cm^{-1}. Despite the presence of these common groups, the intensity of oxygenated functional bands decreased with increasing calcination temperature, while the aromatic C=C vibrations became more pronounced. Nevertheless, some minor peaks were formed and diminished when calcined at different temperatures. There are peaks that start to appear at 2872 cm^{-1}, clearly shows the presence of aliphatic alkane C–H when increased the calcination temperature. The pronounce of very sharp IR wave at 1115

cm^{-1} attributed to the existence of aromatic C–H, alcohol C–O bond and ester C–O bond (Stuart, 2004).

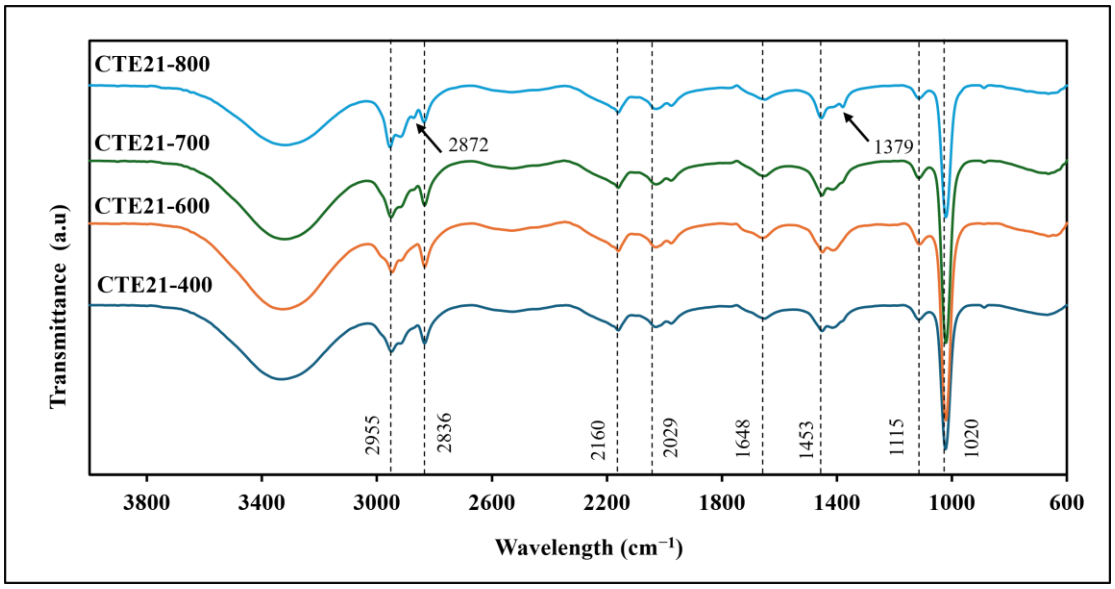

Figure 4.34 FTIR Spectrum of Bio-oil Uses CTE21 Catalyst at Different Calcination Temperature

4.5.9 Surface Morphology of CTE Catalysts at Different Calcination Temperature

The surface morphology of the catalysts subjected to different calcination treatments was examined using SEM, as shown in Figure 4.35. It is observed that, the calcination temperature notably affects metal crystal formation. Figure 4.35 shows distinct morphological differences among the CTE21 catalysts. At 400 °C, Cr crystals are poorly exposed on the EA support, indicating limited crystallization. In contrast, at 600–700 °C, Cr crystals appear clearly and disperse well, suggesting that higher temperatures overcome activation barriers and promote grain growth with larger particles (Johari et al., 2025). The Ti crystals are not clearly seen in the SEM images, likely due to their smaller particle size and more uniform dispersion on the EA support. EDS mapping of CTE21-700 further confirms the presence and dispersion of Cr, Al, and Ti on the catalyst surface as shown in Figure 4.36 These findings demonstrate that calcination temperature influences the structural morphology of the catalyst, thereby affecting its activity. Higher calcination temperatures enhance the growth of active metals and remove impurities, which facilitates the diffusion of volatiles into the pores and across the catalyst surface.

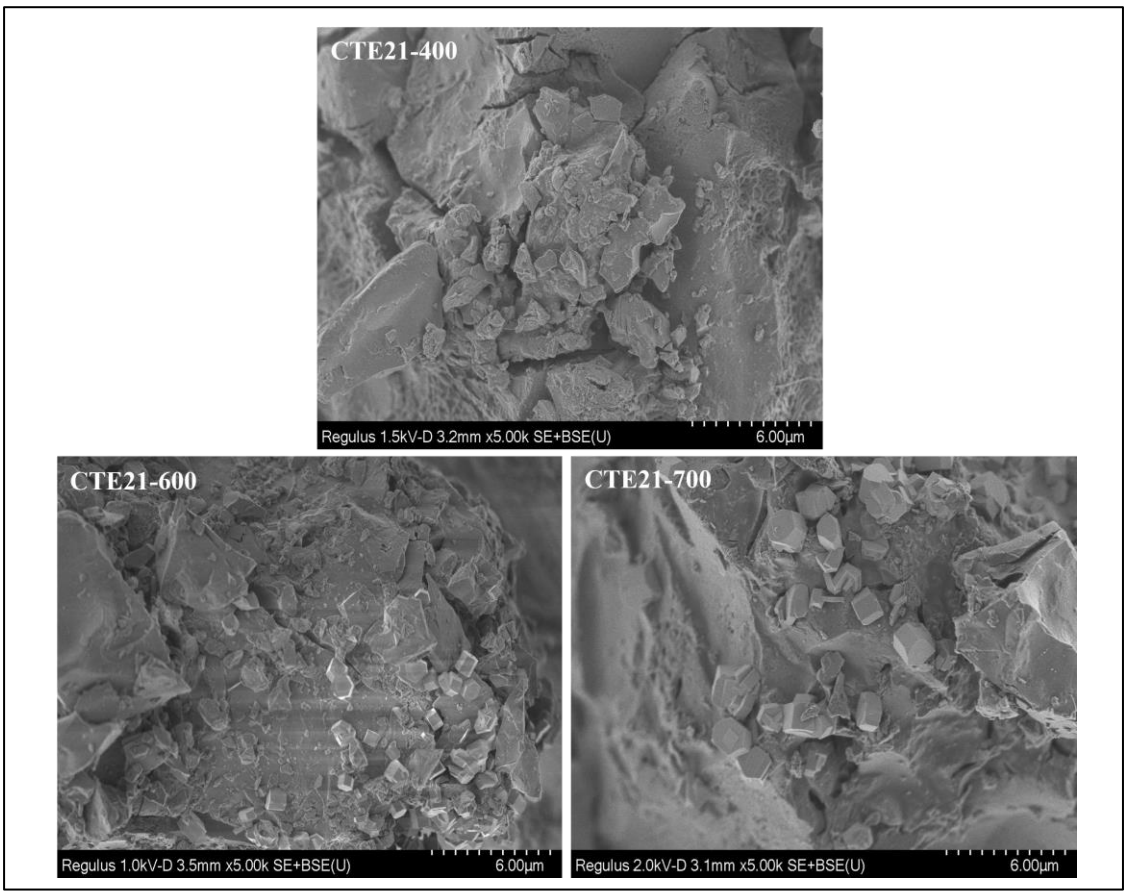

Figure 4.35 SEM Images of CTE21 Catalyst at Different Calcination Temperature

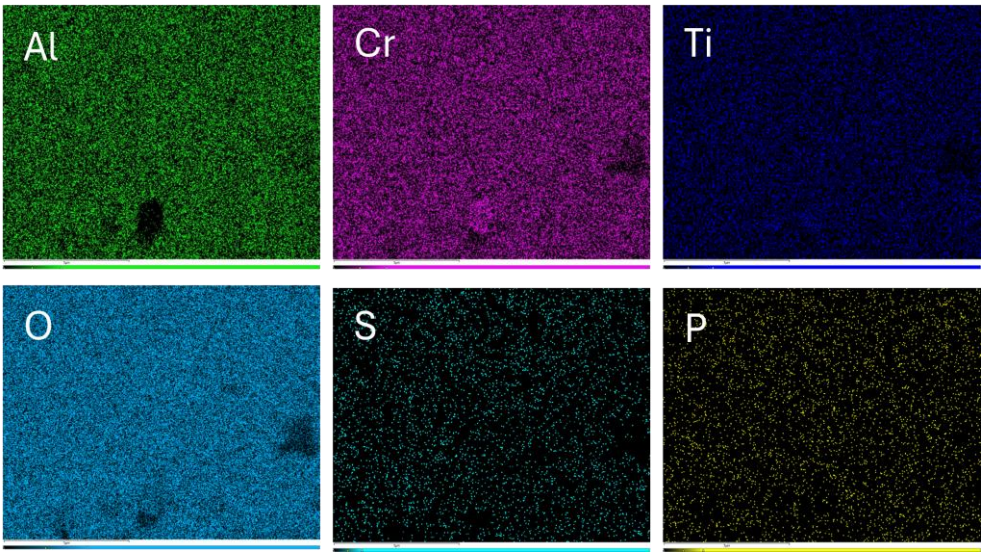

Figure 4.36 Elemental Mapping of CTE21-700

4.5.10 Textural and Acid Properties of CTE21 Catalyst at Different Calcination Temperature

Table 4.10 displays the textural properties and acid sites concentrations of the CTE21 catalyst at different calcination temperature. BET analysis shows that CTE21-400 and CTE21-500 have low surface areas (4.9 and 2.9 m^2/g) and low total pore volumes (0.0108 and 0.0086 cm^3/g). When the calcination temperature increased from 500 °C to 700 °C (CTE21-500 to CTE21-700), the surface area rose sharply from 2.9 to 71.2 m^2/g. However, it declined to 40.2 m^2/g for CTE21-800. The total pore volume followed the same trend, increasing to 0.2539 cm^3/g at CTE21-700 before decreasing to 0.1664 cm^3/g at CTE21-800.

Table 4.10
Textural Properties and Acid Sites Concentrations of The CTE21 Catalysts at Different Calcination Temperature

	Surface Area [a] (m^2/g)	**Total pore volume [a] (cm^3/g)**	**Average pore size [a] (nm)**	**Acidity [b] (mmol/g)**
CTE21-400	4.9	0.0108	8.9	-
CTE21-500	2.9	0.0086	11.8	5.31
CTE21-600	46.7	0.0696	6.0	1.03
CTE21-700	71.2	0.2539	14.3	3.91
CTE21-800	40.2	0.1664	16.6	-

[a] Obtained from N_2 adsorption-desorption
[b] Obtained from NH_3-TPD chemisorption

The observed trends possibly result from incomplete removal of volatile impurities at lower calcination temperatures and from sintering effects such as lattice collapse and channel overlap at higher calcination temperatures. These effects reduce surface area and pore volume, thereby reducing the accessibility of active sites in the CTE catalysts (Zha et al., 2024). Thus, the high surface area and pore volume possibly indicate enhanced catalytic activity, as reported for CTE21-700 which achieved the maximum bio-oil yield of 63.4 %. Similar observations, where increased surface area and mesoporosity improves accessibility to active sites, diffusion of pyrolysis vapours, and product yields are widely reported for mesoporous catalysts (Tian et al., 2024; Wang et al., 2025).

The textural properties of the catalyst at different calcination temperatures can be further explained by the isotherm and pore size distribution shown in Figures 4.37 and Figure 4.38, respectively.

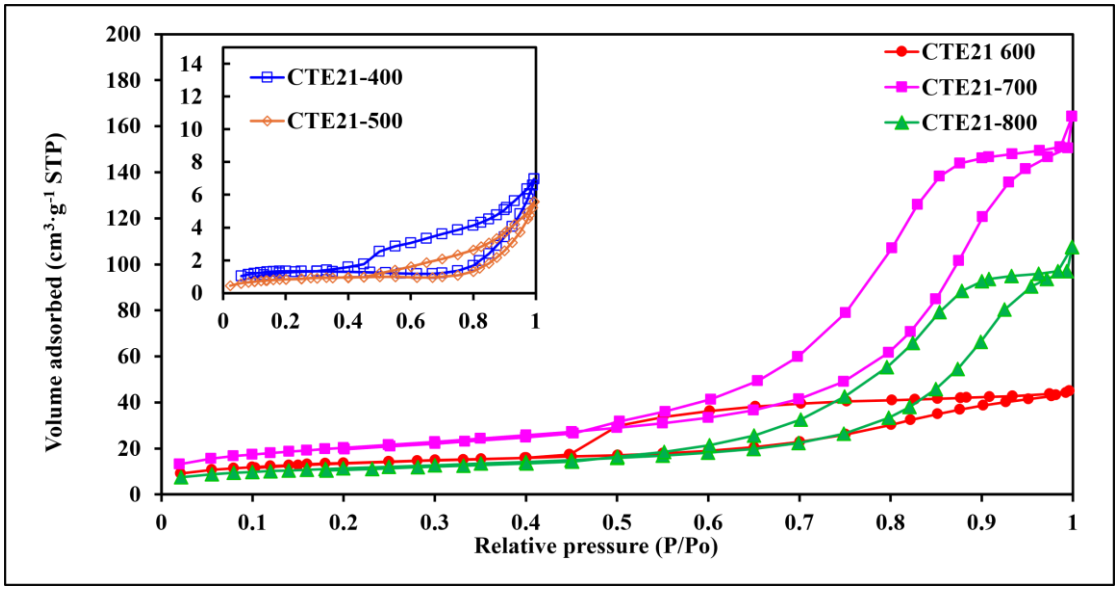

Figure 4.37 N_2 Sorption Isotherm of CTE21 Catalyst at Different Calcination Temperatures

The adsorption–desorption isotherms of CTE21 catalysts display H4 hysteresis loops typical of type IV isotherms, indicating a mesoporous structure. CTE21-400 and CTE21-500 adsorb relatively low volumes of N_2, reflecting smaller surface area and pore volume, as reported in Table 4.10. With increasing calcination temperature, both surface area and pore volume increase. However, excessive calcination leads to sintering of fine crystals and cluster agglomeration, reducing surface area and pore volume (Li et al., 2018; Zou et al., 2017). The average pore size of the CTE catalysts ranges from 6 to 16 nm, confirming their mesoporous nature. For CTE21-700 and CTE21-800, pore sizes extend from 4 to 36 nm, broader than those of CTE21-400, CTE21-500, and CTE21-600. These variations in pore size distribution indicate that calcination temperature strongly influences pore formation within the catalyst (Isha et al., 2022), consistent with the SEM surface morphology shown in Figure 4.35.

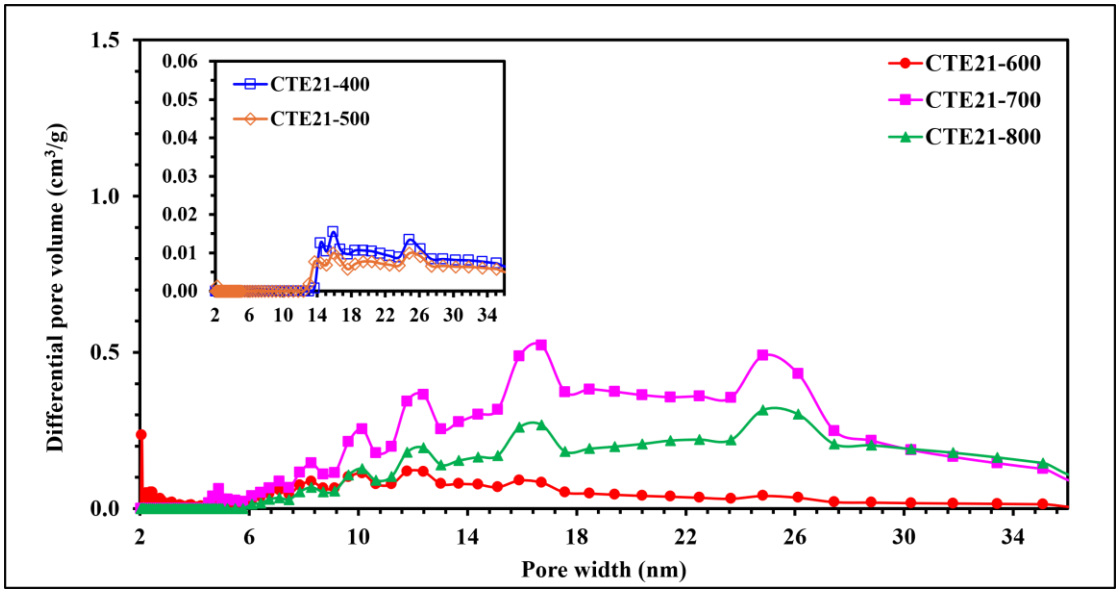

Figure 4.38 Pore Size Distribution of CTE21 Catalyst at Different Calcination Temperatures

Figure 4.39 shows distinct peaks in the NH_3-TPD curves of the CTE catalyst. These peaks correspond to weak and medium acidic site for all CTE catalyst except for CTE21-600 only at medium acid site.

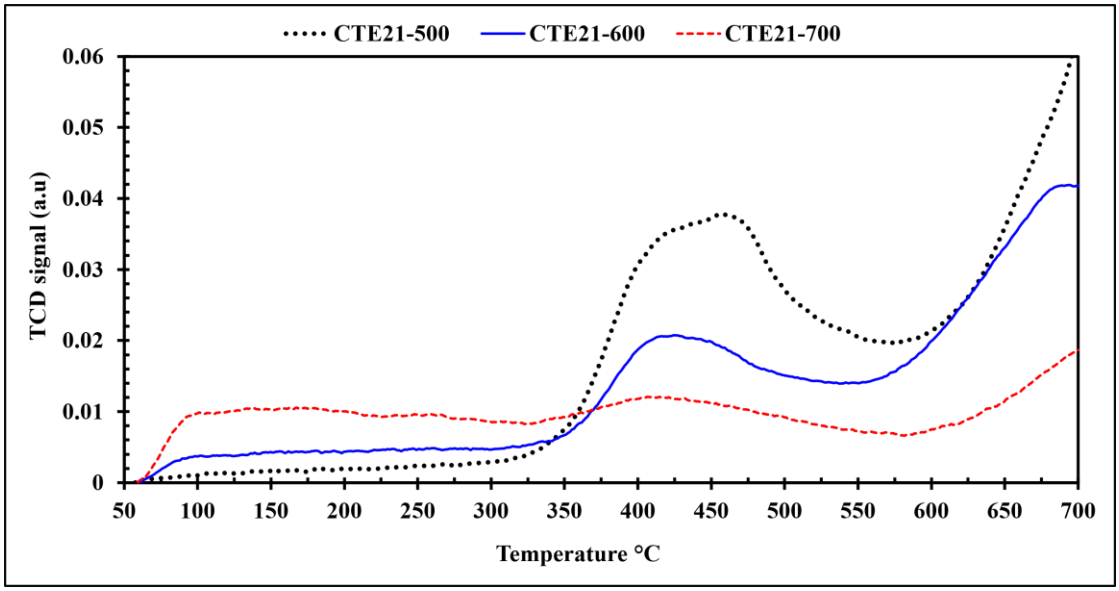

Figure 4.39 NH_3-TPD Desorption Characteristic of As-synthesis Catalyst at Different CTE21 Calcination Temperatures

Table 4.10 presents the acidity values of CTE catalysts at different calcination temperatures. CTE21-500 exhibited the highest acidity (5.31 mmol/g), whereas CTE21-600 showed the lowest value (1.03 mmol/g). Acidity plays a crucial role in directing

product distribution toward aliphatic HC, as supported by Figure 4.33(b), where the aliphatic HC formation was pronounced for CTE21-500 but significantly reduced for CTE21-600 in line with the decrease in acidity. For CTE21-700, the acidity was 3.91 mmol/g, with acid sites mainly distributed across low and medium strength regions. This distribution indicates that medium acidity combined with accessible acid sites can contribute to selective aliphatic HC and aromatic HC formation. Previous studies have reported similar findings. Yang et al., (2019) highlighted that acid sites can promote hemicellulose deoxygenation within large pore networks, leading to aromatic HC formation. Similarly, Rezaei et al., (2017) demonstrated that mesoporous catalysts with high acidity facilitate the production of light olefins during co-pyrolysis.

4.5.11 Effect of Calcination Time on CTE21-700 Catalyst Activity

CTE21-700 was chosen for further investigation on char, bio-oil and gas yield at different calcination time as shown in Figure 4.40(a) and bio-oil component distributions in Figure 4.40(b). The calcination time were evaluated between 15 min to 75 min.

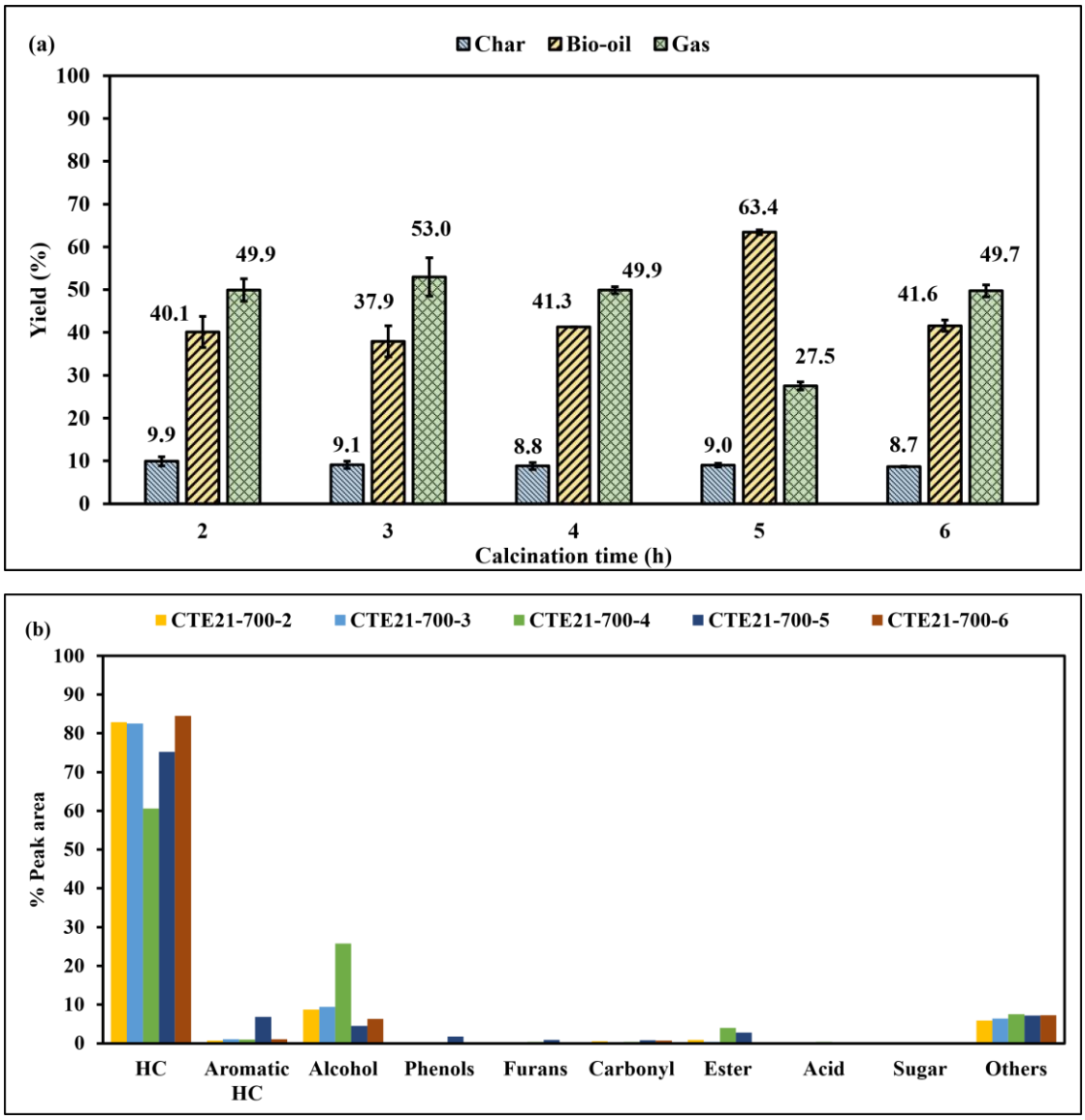

Figure 4.40 Effect of Calcination Time on CTE21-700 Catalyst Activity (a) Yield % (b) Bio-oil Component Distributions (Operating Condition: 500 °C Pyrolysis Temperature; 60 min Pyrolysis Time; 50:50 CFW/PPW Ratio; 1:1 F/C Ratio)

The catalytic activity is also affected by different in calcination time as shown in Figure 4.40(a). The char yield is stable between 8.7 % to 9.9 %, as discussed previously due to stable thermal decomposition under constant operating conditions. As calcination time increased from 2 h (CTE21-700-2) to 4 h (CTE21-700-4), the bio-oil yield fluctuates at 37.9 % to 41.3 % and reached a maximum of 63.4 % at 5 h before declined to 41.6 % at 6 h (CTE21-700-6). These variations in product yield can be attributed to change in particle size and morphology of the CTE21-700 catalysts, which in turn influence porosity and textural properties (Stefanidis et al., 2016). The sharp increase in CTE21-700-5 suggests that residual impurities such as water and volatile compounds are removed, creating pores that enhance the diffusion of volatiles and

improve catalytic activity (Zha et al., 2024). In contrast, longer calcination promotes metal agglomeration, which reduces surface area and pore volume, thereby lowering catalyst performance (Prayitno et al., 2025; Sulaiman & Rohana, 2016).

Figure 4.40(b) presents the bio-oil component distribution of the CTE21-700 catalyst at different calcination times, where aliphatic HC and alcohol are the dominant composition. For CTE21-700-4, the aliphatic HC yield decreased sharply while alcohol formation increased relative to the other catalysts. Extending the calcination time to 6 h increased aliphatic HC production, indicating improved catalytic activity. It is observed that, the CTE21-700-5 catalyst produced the highest composition of aromatic hydrocarbons. This enhancement can be attributed to the synergistic effect of larger accessible surface area and sufficient acidity, which facilitate better dispersion of active phases and the exposure of stronger acid sites, thereby promoting hydrocarbon selectivity (Harith et al., 2022; Sarker et al., 2020) .

4.5.12 Functional Groups of Bio-oil using CTE21-700 Catalyst at Different Calcination Time

Figure 4.41 shows the FTIR spectra that revealed the presence of the functional group in the bio-oil at different calcination time. The spectra show similar patterns, confirming the presence of common functional groups as reported previously in Figure 4.27.

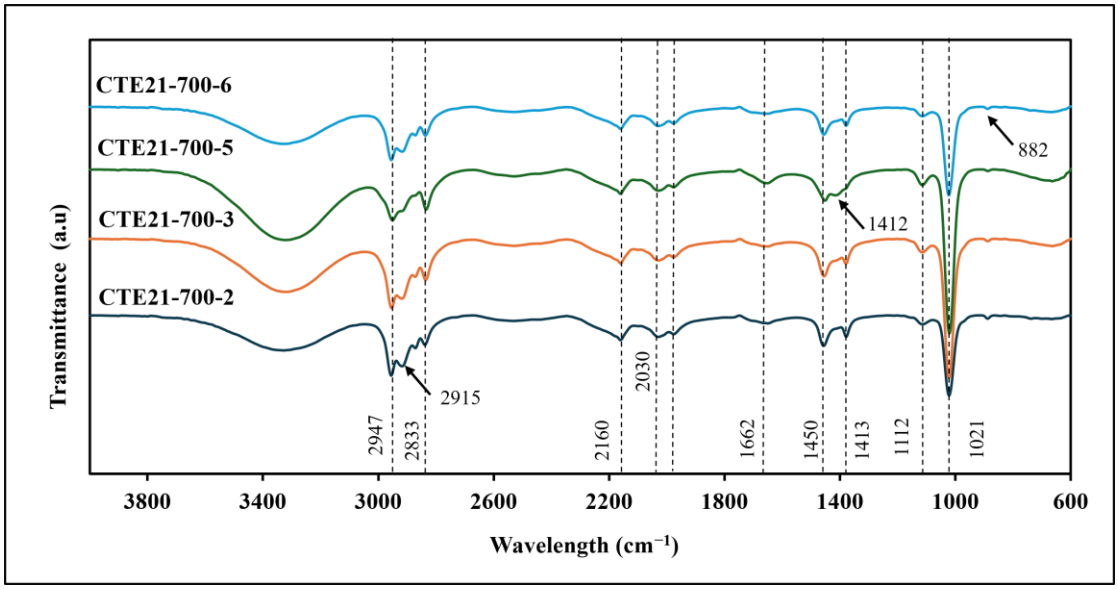

Figure 4.41 FTIR Spectrum of Bio-oil Uses CTE21-700 Catalyst at Different Calcination Time

The FTIR spectra of the bio-oils show common functional groups, including O–H stretching (3200 to 3600 cm^{-1}), C=O stretching (1700-1750 cm^{-1}), aromatic C–H (1275-1000), C=C (1430-1600 cm^{-1}), and C–O stretching (1050–1150 cm^{-1}). All CTE21-700 exhibit similar patterns, indicating comparable compound classes. However, the intensity varies with calcination time. CTE21-700-4 shows stronger O–H and C=O bands, suggesting higher alcohol and carbonyl content, consistent with lower hydrocarbon selectivity. In contrast, CTE21-700-5 exhibits weaker oxygenated signals and stronger aromatic bands, confirming improved deoxygenation and enhanced hydrocarbon formation due to its higher surface area and acidity.

4.5.13 Surface Morphology of CTE-700 Catalysts at Different Calcination Time

Figure 4.42 displays the distinct catalyst morphology that has been formulated at different calcination time (CTE21-700-3, CTE21-700-5, and CTE21-700-6). The SEM images show that the calcination time influence the particle morphology especially on the crystallinity of the particles.

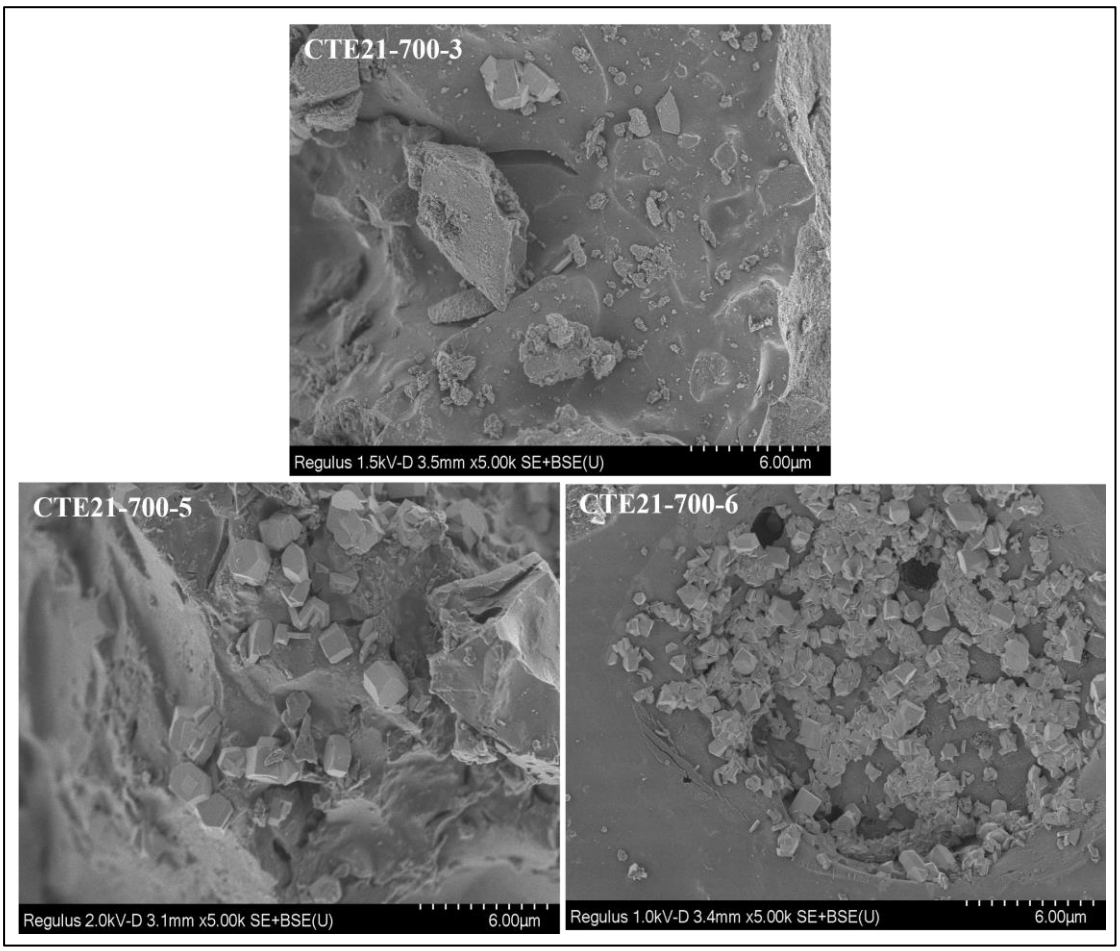

Figure 4.42 SEM Images of Synthesis of CTE21-700 Catalyst at Different Calcination Time

CTE21-700-3 shows scattered particles of irregular shape and size on a smooth support. The presence of large plate-like structures indicates incomplete crystallization, which limits contact with active sites during catalytic reactions. In contrast, the SEM image of CTE21-700-5 shows hexagonal particles attached to the EA surface, indicating high crystallinity, enhanced particle growth, and greater surface area. However, extending the calcination time to 6 h (CTE21-700-6) caused agglomeration of the active metals, which reduced the catalyst surface area. The SEM image also shows evidence of sintering. The agglomerated particles likely formed through coagulation and sintering (Zhang et al., 2020),which reduces access to active sites and lowers catalytic activity (Said et al., 2024).

4.5.14 Textural and Acid Properties of CTE21-700 Catalyst at Different Calcination Time

The analysis of textural properties shows in Table 4.11, reveals that the CTE21-700-5 catalyst exhibits the highest surface area (71.2 m^2/g) and large pore volume (0.2539 cm^3/g) compared to other CTE21-700 catalysts.

Table 4.11
The Textural Properties and Acidity of Catalysts at Different CTE21-700 Calcination Time

	Surface Area [a] (m^2/g)	Total pore volume [a] (cm^3/g)	Average pore size [a] (nm)	Acidity [b] (mmol/g)
CTE21-700-2	40.3	0.1178	11.7	-
CTE21-700-3	33.7	0.1009	12.0	3.93
CTE21-700-4	42.3	0.1073	10.1	-
CTE21-700-5	71.2	0.2539	14.3	3.91
CTE21-700-6	34.3	0.1042	12.1	3.46

[a] Obtained from N_2 adsorption-desorption
[b] Obtained from NH_3-TPD chemisorption

This result indicates that 5 h calcination is the optimum duration for developing favourable surface characteristics that enhance catalytic activity during co-pyrolysis. Among the CTE21-700 catalysts, CTE21-700-3 shows the lowest surface area, followed by CTE21-700-6, due to partial decomposition and agglomeration, as confirmed by their morphology. These findings suggest that sufficient calcination time promotes the formation of uniformly distributed metal oxides with abundant active surface sites, leading to higher catalytic activity. The 5 h calcination enhanced surface area (71.2 m^2/g) and active sites, resulting in higher bio-oil yield. Therefore, CTE21-700 calcined for 5 h (CTE21-700-5) achieved the best catalytic activity, producing bio-oil with a yield of 63.4 %. Recent work by Aliwi et al., (2025), obtained surface area of 96.74 m^2/g for Al based metal oxides calcined at longer calcination time (6 h). High calcination time is important thermal treatment to promote porous structure with sufficient active sites for good catalytic activity.

The N_2 sorption isotherm in Figure 4.43 shows the CTE21-700 catalyst exhibit type IV isotherm with H4 hysteresis loop according to IUPAC classification, which confirm its mesoporosity structure. The result reveals in Figure 4.44 indicates the CTE-700 catalyst lies in mesopore region range with CTE-700-5 shows the highest

volume among the catalyst. The biggest pore diameter of 14.3 nm, is observed in CTE21-700-5, which have excellence agreement with the highest mesopore volume of 0.2539 cm^3/g.

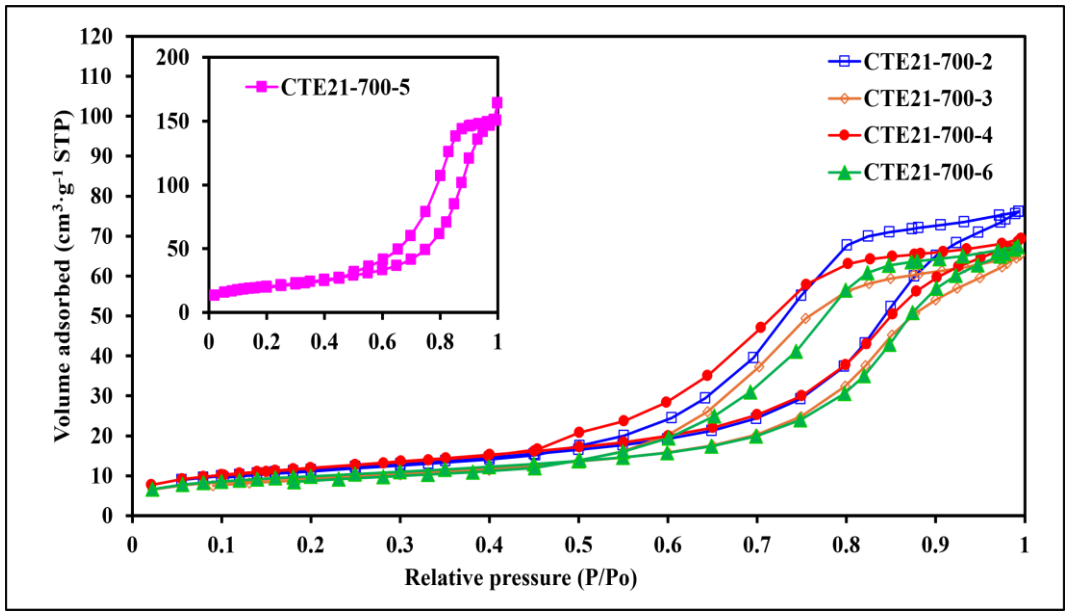

Figure 4.43 N_2 Sorption Isotherm of CTE21-700 Catalysts at Different Calcination Time

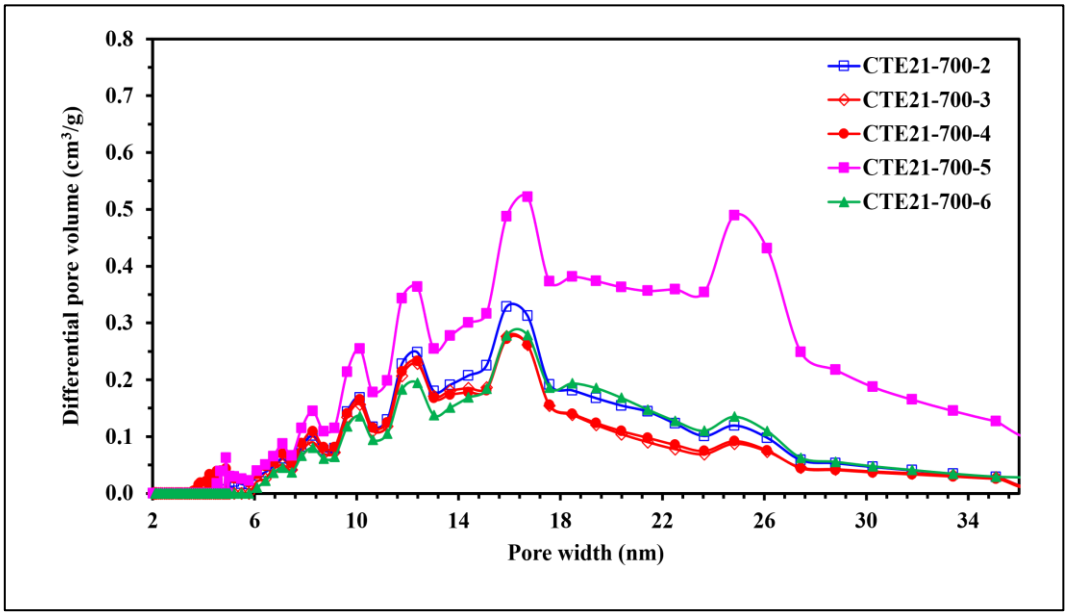

Figure 4.44 Pore Size Distribution of CTE21-700 Catalyst at Different Calcination Time

Figure 4.45 shows the major acid strength peaks corresponding to weak, medium, and strong acids. All catalysts exhibit a similar acidity pattern, indicating that calcination time does not significantly alter their acidity.

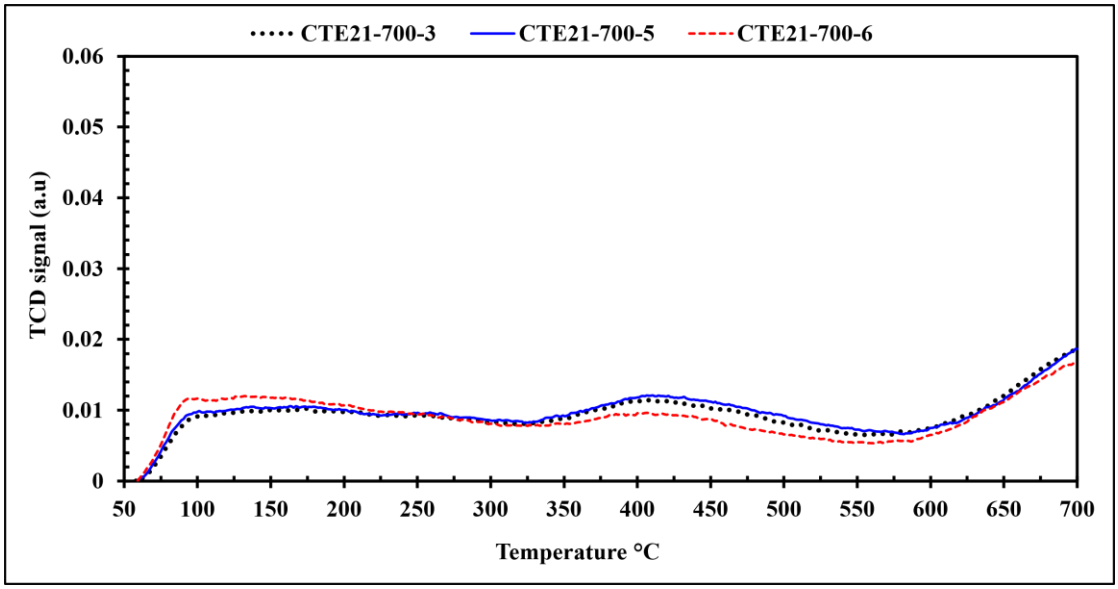

Figure 4.45 NH_3-TPD Desorption Characteristic of CTE21-700 Catalyst at Different Calcination Time

The total acidity values for CTE21-700-3, CTE21-700-5, and CTE21-700-6 are 3.93 mmol/g, 3.91 mmol/g, and 3.46 mmol/g, respectively, showing only slight differences. Consequently, the catalytic activity remains comparable, except for CTE21-700-5, which demonstrates higher bio-oil production due to its larger surface area and greater porosity.

4.6 Influence of Operating Conditions in The Co-pyrolysis of CFW and PPW using CTE Catalyst

In previous subsection 4.5, were discussed the catalytic activity with different catalyst synthesis conditions. The CTE21-700-5 has shown good activity among the CTE catalysts and obtained the maximum bio-oil yield (63.4 %) with diminished oxygenates compound. In subsequent section, the effect of process parameters such as pyrolysis temperature, CFW/PPW ratio, F/C ratio, and pyrolysis time on catalytic activity of CTE21-700-5 catalyst are evaluated.

4.6.1 Effect of Pyrolysis Temperature on CTE21-700-5 Catalyst Activity

The effect of pyrolysis temperature on CTE21-700-5 catalyst activity was investigated at constant operating conditions of CFW/PPW ratio (50:50), F/C ratio 1:1 and pyrolysis time 60 min at different pyrolysis temperature (450 °C, 500 °C, 550 °C,

600 °C, and 650 °C. Figure 4.46(a) and 4.46(b) show the product yield and bio-oil component distributions, respectively.

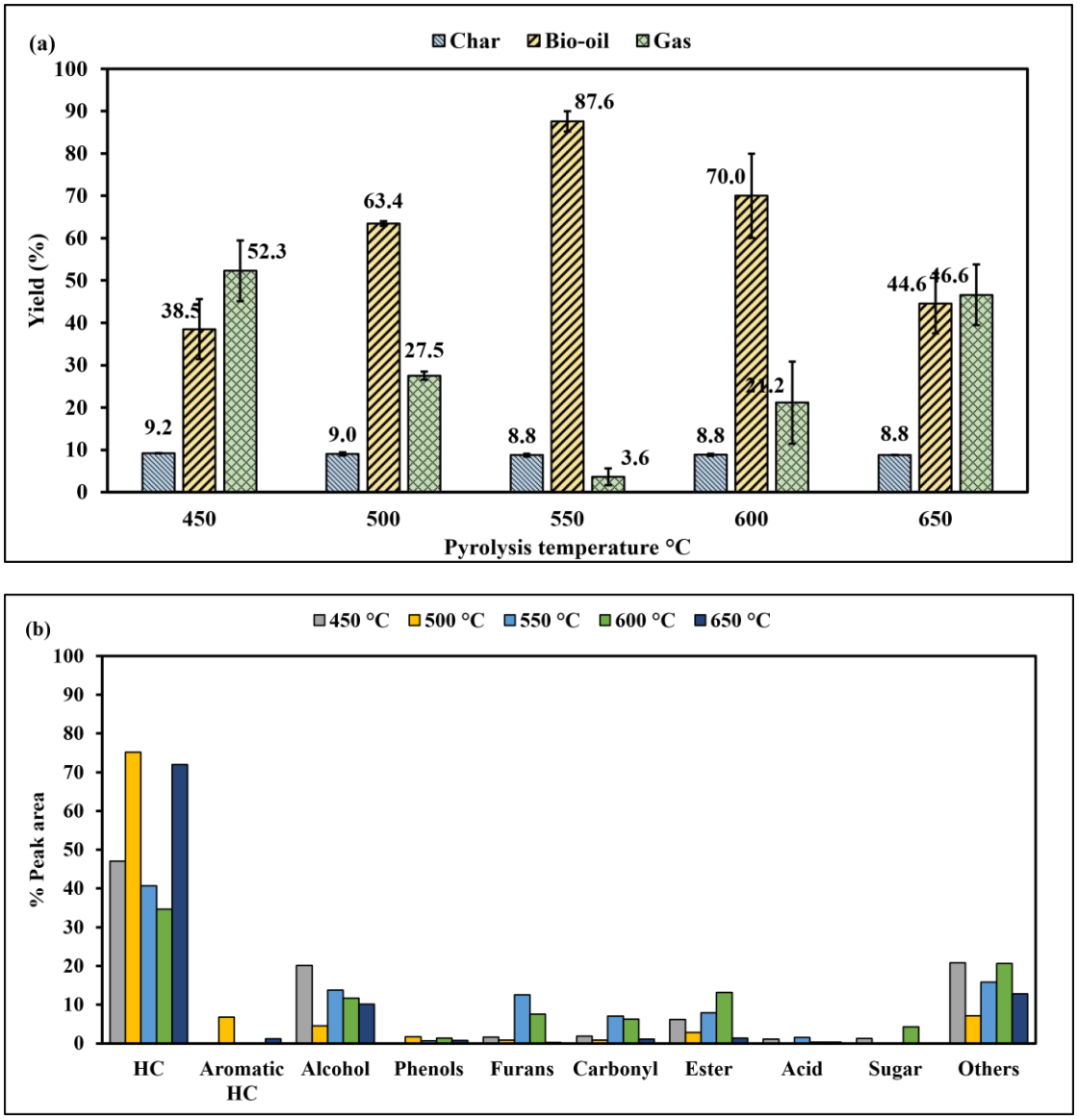

Figure 4.46 Effect of Pyrolysis Temperature on CTE21-700-5 Catalyst Activity (a) Yield % (b) Bio-oil Component Distributions (Operating Condition: 450 °C, 500 °C, 550 °C, 600 °C, 650 °C Pyrolysis Temperature; 60 min Pyrolysis Time; 50:50 CFW/PPW; 1:1 F/C Ratio)

The char yield remains consistent within the range of 8.8–9.2 % across the pyrolysis temperature range of 450–650 °C. This stability is likely due to the ex-situ configuration, where the physical separation of the catalyst and feedstock limits interactions to thermal cracking alone (Xu et al, 2024). However, the bio-oil yield exhibits strong temperature dependence, reaching its optimum at 550 °C. The yield increases steadily from 450 to 550 °C, then decreases at higher temperatures (600 °C

and 650 °C). While the gas yield has shown the opposite trend to the bio-oil yield. The maximum bio-oil yield obtained 87.6 % at 550 °C can be attributed to sufficient heat for the decomposition of both CFW and PPW, along with the catalytic effect of CTE21-700, which provides accessible active sites and suitable acidity (Charusiri et al., 2022). However, above 550 °C, secondary cracking from catalyst accelerates, causing a sharp decline in bio-oil yield to 70.0 % at 600 °C (gas yield 21.2 %) and further to 44.6 % at 650 °C (gas yield 46.6 %). This decline indicates that condensable intermediates undergo excessive cracking, converting into non-condensable gases (Al-Maari et al., 2025; Esso et al., 2022).

The bio-oil component distribution over CTE21-700 as shown in Figure 4.46(b) indicates a clear temperature-dependent shift in catalytic performance. The aliphatic HC is observed to be the main products, followed by alcohol of co-pyrolysis. aliphatic HC formation increases from 450 to 500 °C, indicating that at 450 °C, the plastic begins to melt and suppresses the release of CFW volatiles. At 500 °C, PPW reaches its optimum degradation temperature, releasing additional hydrogen radicals that interact with CFW intermediates to form aliphatic HC and aromatic hydrocarbons. The decline in alcohol further confirms that dehydration transfers hydrogen radicals to form aliphatic HC (Li et al., 2020). At 550 °C and 600 °C, aliphatic HC content decreases significantly, while oxygenates remain dominant, indicating incomplete deoxygenation and limited catalytic upgrading. There is also significant increase in furans, carbonyls, and ester at 550 °C and 600 °C. Figure 4.39 shows that CTE21-700 possesses moderate acidity between 350–500 °C, which diminishes above 550 °C. This decline in acidity reduces deoxygenation efficiency, leading to higher levels of oxygenates such as furans, carbonyls, and alcohol, consistent with Zheng et al., (2017), Yang et al., (2019), and Seo et al., (2024), which highlighted the role of acid site strength in catalytic deoxygenation. At 650 °C, sufficient thermal energy promotes secondary reactions that convert oxygen in bio-oil into non-condensable gases (CO and CO_2), thereby increasing gas yield and aliphatic HC (Charusiri et al., 2022).

4.6.2 Effect of CFW/PPW Ratio on CTE21-700-5 Catalyst Activity

The effect of CFW/PPW ratio on CTE21-700-5 catalyst activity was investigated at constant operating conditions of pyrolysis temperature 550 °C, F/C ratio 1:1 and pyrolysis time 60 min at different CFW/PPW ratio (80:20, 60:40, 50:50, 40:60

and 20:80). Figures 4.47(a) and 4.47(b) show the product yield and bio-oil component distributions, respectively.

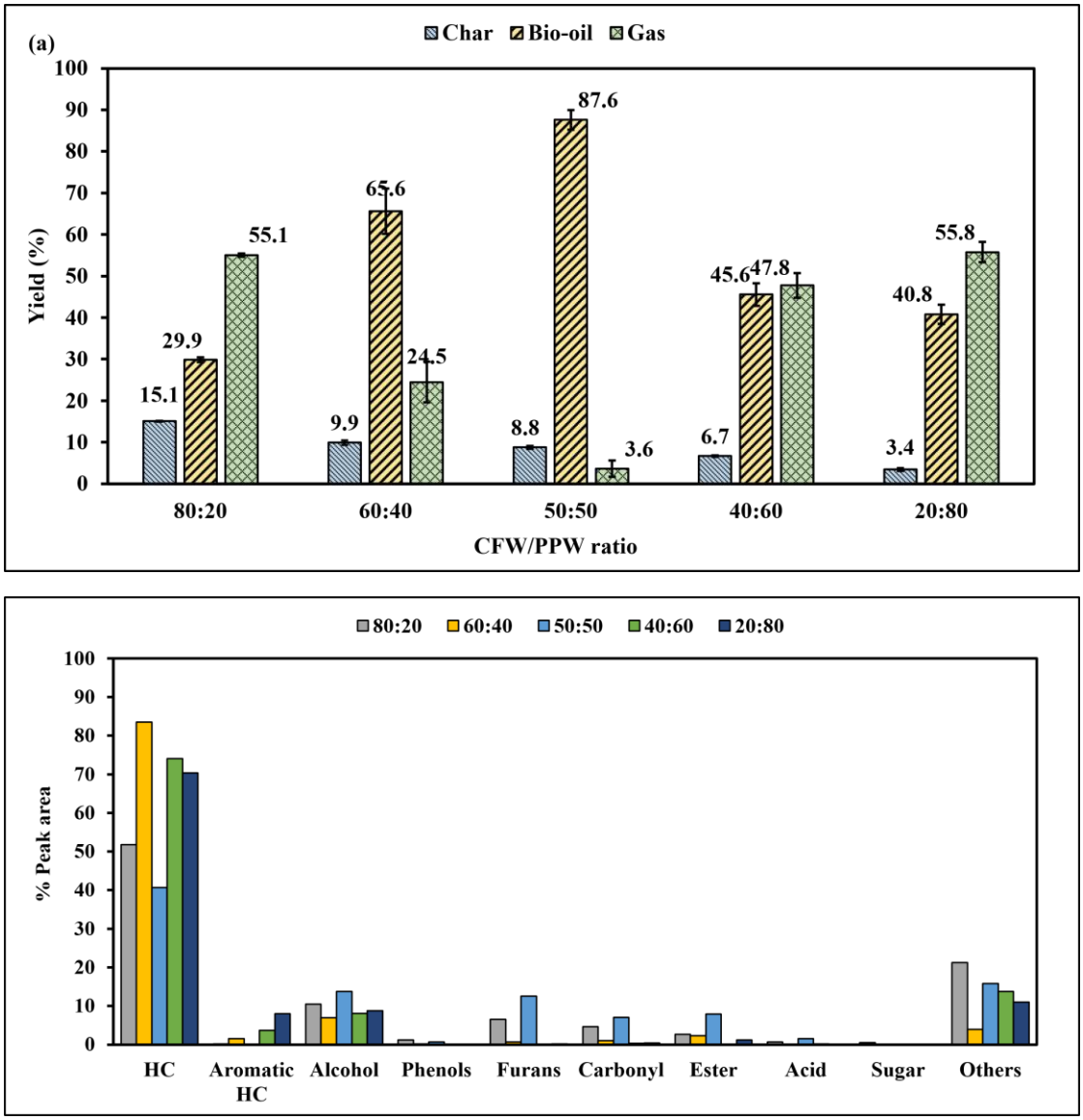

Figure 4.47 Effect of CFW/PPW Ratio on CTE21-700-5 Catalyst Activity (a) Yield % (b) Bio-oil Component Distributions (Operating Condition: 550 °C Pyrolysis Temperature; 60 min Pyrolysis Time; 80:20, 60:40, 50:50, 40:60, 20:80 CFW/PPW Ratio; 1:1 F/C Ratio)

Figure 4.47(a) shows that, as the PPW increased from 20 % (80:20) to 80 % (20:80), the char yield dropped from 15.1 % to 3.4 %, suggesting the char residue is mainly from CFW. PPW acts as a hydrogen supplier that helps accelerate the removal of side chain functional groups, known as the methoxyl groups, which can lead to the reduction of char yield (Hassan & Hameed, 2023). At the pyrolysis temperature (550 °C), most of the PPW have converted to volatiles and the remaining is char residue left

from CFW. The char yield increased with CFW fraction in the feed (Kumar & Srinivas, 2020). Meanwhile, the bio-oil yield increased from 29.9 % to 87.6 % as the CFW/PPW ratio was decreased from 80:20 to 50:50, which indicated that the addition of PPW to CFW during catalytic co-pyrolysis improved the bio-oil yield by increasing the hydrogen supply (Hassan et al., 2019). The similar finding was reported by Sangpatch et al., (2025), where increasing the ratio of palm oil to PP markedly increased the liquid fraction. However, further increased PPW ratio (40:60 and 20:80), cause the bio-oil yield declines, likely because excess plastic alters vapour composition toward lighter fragments and gases while promoting oligomerization that suppress condensable hydrocarbon production (Xu et al., 2021).

Figure 4.47(b) shows on bio-oil component distributions at different CFW/PPW ratio. It is observed that, the proportion of aliphatic HC and alcohol have been the primary product in co-pyrolysis. The aliphatic HC shows increasing trend from 80:20 to 60:40 of CFW/PPW ratio, suggesting the higher PPW ratio possibly increased the aliphatic HC component distribution in bio-oil. High PPW possibly produced more hydrogen radical that can interact with oxygenates intermediate during co-pyrolysis. The presence of excess hydrogen donor from plastic enhanced the overall H/C_{eff} value of the feedstock by keeping the hydrocarbon pool functioning for aliphatic HC production (Hassan & Hameed, 2023). However, increased the CFW/PPW ratio to 50:50, reduced the aliphatic HC and observed high oxygenates especially alcohol, furans, carbonyl, and ester, suggesting the deoxygenation reaction activities was not promoted. The overabundance of hydrogen in the hydrocarbon pool and the high H/C ratio could not adequately react with the oxygenated compounds (Ding et al, 2018). The aliphatic HC and aromatic HC were promoted when ratio of PPW further increased to 40:60 and 20:80, suggesting that the aliphatic HC compound originated from the direct decomposition of PPW and aromatic HC formed via Diels-Alder reaction as evidence on diminished of furans at 40:60 and 20:80.

4.6.3 Effect of F/C Ratio on CTE21-700-5 Catalyst Activity

The effect of F/C ratio on CTE21-700-5 catalyst activity was investigated at constant operating conditions of CFW/PPW ratio 50:50, pyrolysis temperature 550 °C and pyrolysis time 60 min at different F/C ratio (2:1, 1:1, 1:1.5, and 1:2). Figures 4.48(a)

and 4.48(b) illustrate the product yield and bio-oil component distributions under different F/C ratio, respectively.

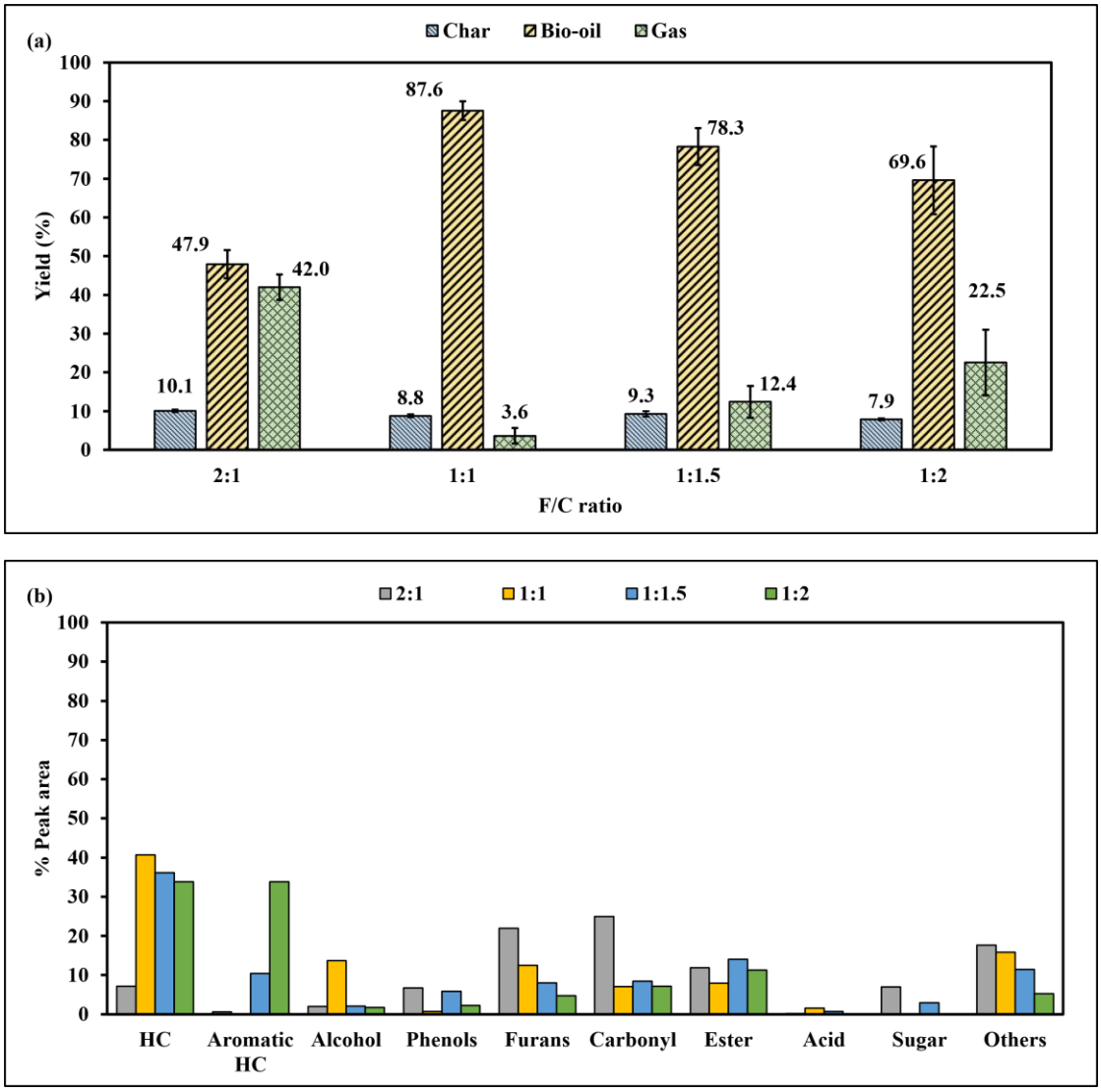

Figure 4.48 Effect of F/C Ratio on CTE21-700-5 Catalyst Activity (a) Yield % (b) Bio-oil Component Distributions (Operating Condition: 550 °C Pyrolysis Temperature; 60 min Pyrolysis Time; 50:50 CFW/PPW Ratio; 2:1, 1:1, 1:1.5, 1:2 F/C Ratio)

Figure 4.48(a) shows that the char yield was achieved minimum at 7.9 % (1:2 F/C ratio) and maximum at 10.1 % (2:1 F/C ratio). Moreover, the sharp increase in bio-oil yield from 2:1 (47.9 %) to 1:1 F/C ratio (87.6 %), indicates the catalyst effectively enhanced the bio-oil yield before the dropped is observed at 1:1.5 (78.3 %) and 1:2 (69.6 %) due to further secondary cracking on catalyst surface with abundant of active sites available for catalytic reaction. The similar findings were reported on increased in catalyst to feedstock ratio cause the increased in bio-oil yield (Ahmed et al., 2020; Al-

Maari et al., 2025). Despite of high bio-oil yield, it is observed that the gas yield shows increasing trend from 3.9 % to 22.5 % when the catalyst is doubled, suggesting increasing catalyst loading prolongs vapor residence inside the catalyst due to mass transfer limitations (Hassan et al., 2019). This extended contact exposes more acidic sites, promotes excessive cracking, reduces bio-oil yield, and increases gas yield.

Figure 4.48(b) shows that the low aliphatic HC and high oxygenate compounds was formed when catalyst loading is at 2:1 F/C ratio. However, the aliphatic HC was slightly increased when increased the catalyst loading at low F/C ratio (1:1, 1:1.5 and 1:2). The aliphatic HC was a primary component in bio-oil accompanied by oxygenates compound namely furans, carbonyl, and ester. Interestingly, the tremendous dropped in alcohol and raised in aromatic HC are also observed at high catalyst ratio. The excessive active sites with accordance to its catalyst ratio (1:1.5 and 1:2), contribute to the dehydration of alcohol to form olefin (Li et al., 2020). Furthermore, the CTE21-700-5 catalyst contains TiO_2 which has been reported to promote the production of aliphatic HC and aromatics (Li et al., 2020). The aromatic HC possibly forms via hydrocarbon pool mechanism and Diels-Alder reaction (Wang et al., 2021). The Diels-Alder routes usually employ solid catalysts for cycloaddition, dehydration, and dehydrogenation to form desirable aromatic monomers (Settle et al., 2017). The reducing in furans and aliphatic HC compound from 1:1 to 1:2, suggesting the Diels-Alder pathways is responsible to aromatic HC.

4.6.4 Effect of Pyrolysis Time on CTE21-700-5 Catalyst Activity

The effect of pyrolysis time on CTE21-700-5 catalyst activity was investigated at constant operating conditions of pyrolysis temperature 550 °C, CFW/PPW ratio 50:50, and F/C ratio (1:1) at different pyrolysis time (15 min, 30 min, 45 min, 60 min and 75 min). Figures 4.49(a) and 4.49(b) illustrate the product yield and bio-oil component distributions under different pyrolysis time, respectively.

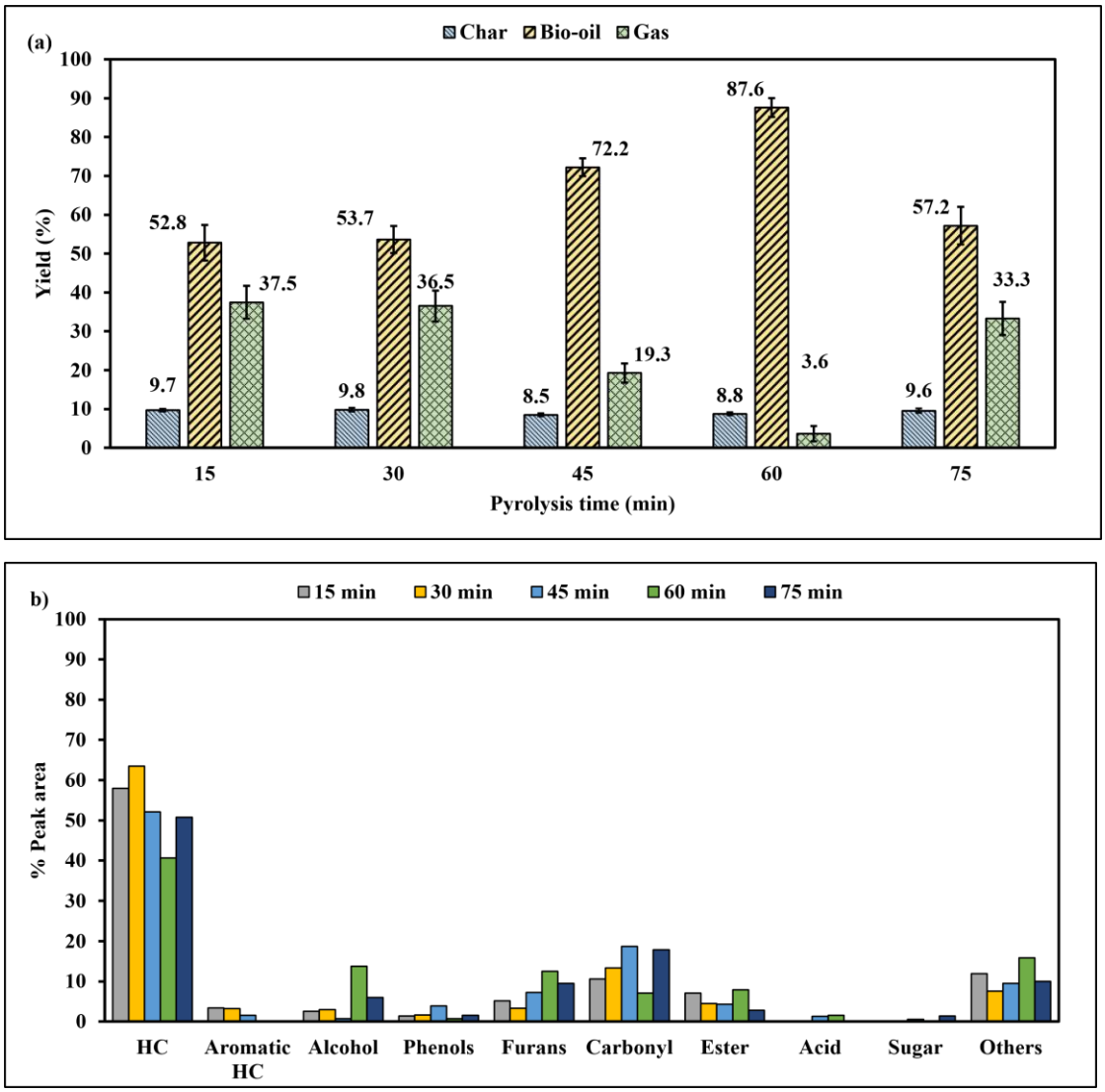

Figure 4.49 Effect of Pyrolysis Time on CTE21-700-5 Catalyst Activity (a) Yield % (b) Bio-oil Component Distributions (Operating Condition: 550 °C Pyrolysis Temperature; 15, 30, 45, 60, 75 min Pyrolysis Time; 50:50 CFW/PPW Ratio; 1:1 F/C Ratio)

Figure 4.49(a) shows the effect of pyrolysis time on the product yield. The char yield shows consistent between 8.5 % to 9.8 %, indicates the char is influenced by the thermal degradation as discussed previously. The consistency of char produced at different pyrolysis time suggest the feedstock completely degraded to volatiles as early as 15 min. Conversely, the bio-oil yield shows a notable change with different pyrolysis time. The slight increment, in bio-oil yield is observed at 15 min (52.8 %) to 30 min (53.7 %) before rose gradually from 30 min to 60 min (87.6 %), indicating the decomposition of CFW and PPW accelerates the formation of volatile and the catalytic reaction also completely occurs (Charusiri et al., 2022). However, as the pyrolysis time increase to 75 min, the bio-oil yield dropped to 57.2 %. As the pyrolysis time proceed

longer, further thermal degradation possibly enhanced the secondary cracking reaction and increasing the gas yield (Yan et al., 2017). There are also possibilities on catalyst deactivation that cause the lower bio-oil yield due to formation of coke from depolymerization and causing blockage on active site (Mullen et al., 2018).

Figure 4.49(b) shows the aliphatic HC dominates the bio-oil component distribution, followed by carbonyl, furans, and ester. While alcohol was rapidly produced after 60 min of pyrolysis time. At early stage, there is observed increase in furans and carbonyls formation, possibly due to thermal cracking of holocellulose compound via dehydration induced by carbonyl formation or fragmentation and retro-aldol condensation reactions (Wang et al., 2021; Zheng et al., 2020).

4.6.5 Reusability and Regeneration of The CTE21-700-5 Catalyst

The reusability and regeneration test for 2 cycles were conducted after fresh catalytic reaction. Figure 4.50 shows the catalytic performances of CTE21-700-5 for reusability and regeneration in catalytic co-pyrolysis of CFW and PPW. There is marked reduction in bio-oil yield from 87.6 % to 53.3 % for fresh and reused cycle 2, respectively. The reduction in catalytic activity during reusability test more likely due to deactivation of the catalyst through deposition of carbonaceous material on the surfaces. The regeneration test shows that improved catalyst activity, where the bio-oil yield achieves 70.2 % at regeneration cycle 1 compared to 87.6 % for fresh catalyst. There is further reduction to 59.5 % after regeneration cycle 2. The finding suggest that regeneration spent catalyst has recovered the catalyst activity. The deposit was removed during regeneration at high temperature calcination and improve the catalytic activity to prolong the lifetime of catalyst (Cheng et al., 2016).

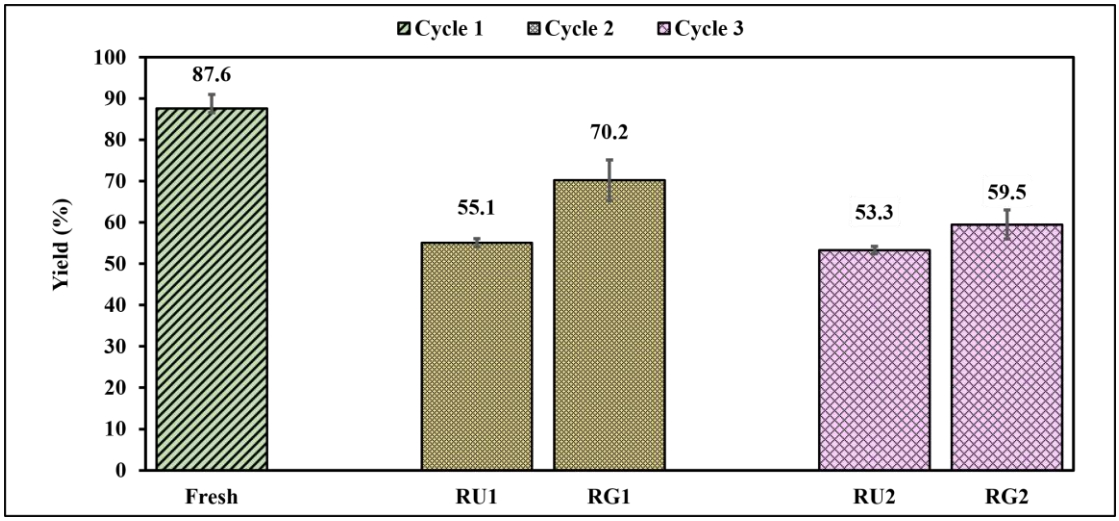

Figure 4.50 Reusability and Regeneration Study on CTE21-700-5 Catalyst Activity (Operating Condition: 550 °C Pyrolysis Temperature; 60 min Pyrolysis Time; 50:50 CFW/PPW Ratio; 1:1 F/C Ratio)

4.7 Concluding Remark for CTE Catalyst Synthesis and Process Evaluation

The improve formulated catalyst, which is CTE catalyst exhibit strong potential to be used in upgrading bio-oil quality. The highest bio-oil yield obtained during co-pyrolysis of CFW and PPW was 87.6 % using CTE21-700-5 catalyst at the best process conditions (pyrolysis temperature: 550 °C, CFW/PPW ratio: 50:50, F/C ratio: 1:1 and pyrolysis time: 60 min). This finding indicates the catalytic activity can be improved by incorporating Cr and Ti on EA. In comparison to 15CE catalyst, the highest yield obtained was 76.4 % at the best process conditions (pyrolysis temperature: 500 °C, CFW/PPW ratio: 50:50, F/C ratio: 1:1 and pyrolysis time: 60 min). The bio-oil component distribution shows comparable quality with 40 % of aliphatic HC was produced together with mixed of oxygenates. It also reveals the acidity and textural properties (surface area, pore volume, and size) play a significant role to this finding. Also, CTE catalyst show better activity during reusability and regeneration test compared to CE catalyst. The CTE21-700-5 higher surface area possibly contributed to the better catalytic activity in the regenerated catalyst compared to 15CE-600-5. Therefore, it can be concluded CTE21-700-5 catalyst is the best catalyst obtained in this study.

4.8 Kinetic Modelling

The kinetic parameters from non-isothermal TGA using n^{th} order reaction model were estimated using parameter estimation techniques. The set of data was obtained for each sample at 40°C/min heating rate with the selection of reaction order (n), $0.1 < n < 3$. The samples were included CFW, PPW, CFW/PPW mixture (1:1) and CFW/PPW mixture with catalyst (F/C ratio 1:1). The typical temperature ranges where the greatest percentage of volatiles mass loss occurred (active zone of pyrolysis) were chosen to calculate kinetic parameters in a single step reaction, including pre-exponential factor (A) and apparent activation energy (E) values. Figure 4.51 presented the DTG profiles which actively degraded the samples at different temperatures.

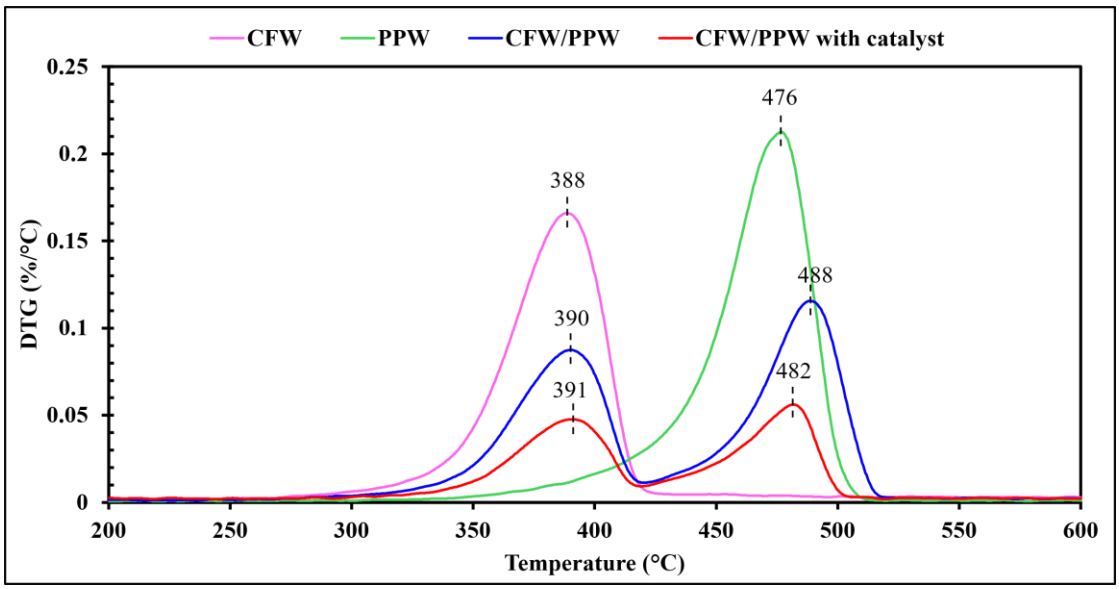

Figure 4.51 DTG Profiles for CFW, PPW, CFW/PPW, and CFW/PPW with Catalyst (Operating Condition: Heating Rate: 40 °C/min, N_2 Flowrate: 50 mL/min)

The thermal degradation of CFW and PPW alone showed an independent peak occurred at 237 – 430 °C and 330 – 510 °C, respectively. The DTG profiles of CFW/PPW presented two peaks, the first and second peak appeared in the temperature range of 280 – 420 °C and 420 – 520 °C, respectively which attribute to the different characteristic of CFW and PPW (Zhang et al., 2016). The first peak corresponds to the decomposition of CFW with simultaneous melting of PPW, while the second peak is attributed to PPW degradation and residual CFW intermediates. The presence of two distinct peaks reflects the different thermal behaviours of the feedstocks. However, shifts in peak position and intensity relative to the individual components indicate

interaction during co-pyrolysis. The reduced degradation rate in the first stage and enhanced degradation in the second stage suggest synergistic effects, likely driven by hydrogen transfer from PPW to oxygenated intermediates from CFW (Singh et al., 2021). Besides, the degradation of CFW/PPW with catalyst shows the degradation of CFW/PPW improved the thermal decomposition temperature range to 420 – 520 °C, reduce peak temperature (482 °C) and accelerate pyrolysis compared to CFW/PPW without catalyst. Zheng et al., (2020a) also presented similar trends and observation. The thermal properties parameters of CFW, PPW, CFW/PPW and CFW/PPW with catalyst are listed in Table 4.12.

Table 4.12
Thermal Properties Parameters of CFW, PPW, CFW/PPW and CFW/PPW with Catalyst

	Temperature (°C)	**Peak temperature (°C)**	**DTG max (%/min)**
CFW	237–430	388	0.166
PPW	330–510	476	0.212
CFW/PPW	280–420, 420–520	390, 488	0.087, 0.116
CFW/PPW with catalyst	290-420, 420-520	391, 482	0.048, 0.056

The kinetic parameters (E and A) show in Equation 3.7 and the n were determined numerically using an NLP solver that minimized the SSE between experimental and simulated data. The kinetic model with the highest R^2 value was selected as the best fit, and the corresponding E, A, and n values were obtained. Figure 4.52 illustrates the correlation between simulated and experimental data used to optimize E, A, and n. The results demonstrate an excellent fit, with R^2 values of 0.99, 0.98, 0.96, and 0.98 for CFW, PPW, CFW/PPW, and CFW/PPW with catalyst, respectively.

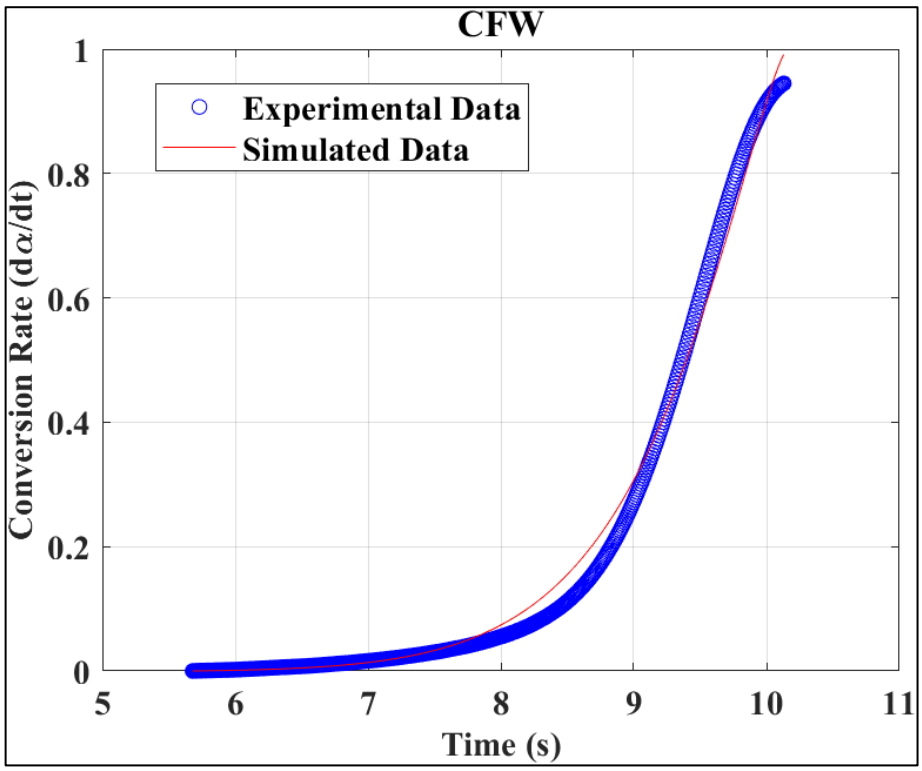
CFW
Experimental Data
Simulated Data
Conversion Rate (dα/dt)
Time (s)
0
0.2
0.4
0.6
0.8
1
5
6
7
8
9
10
11

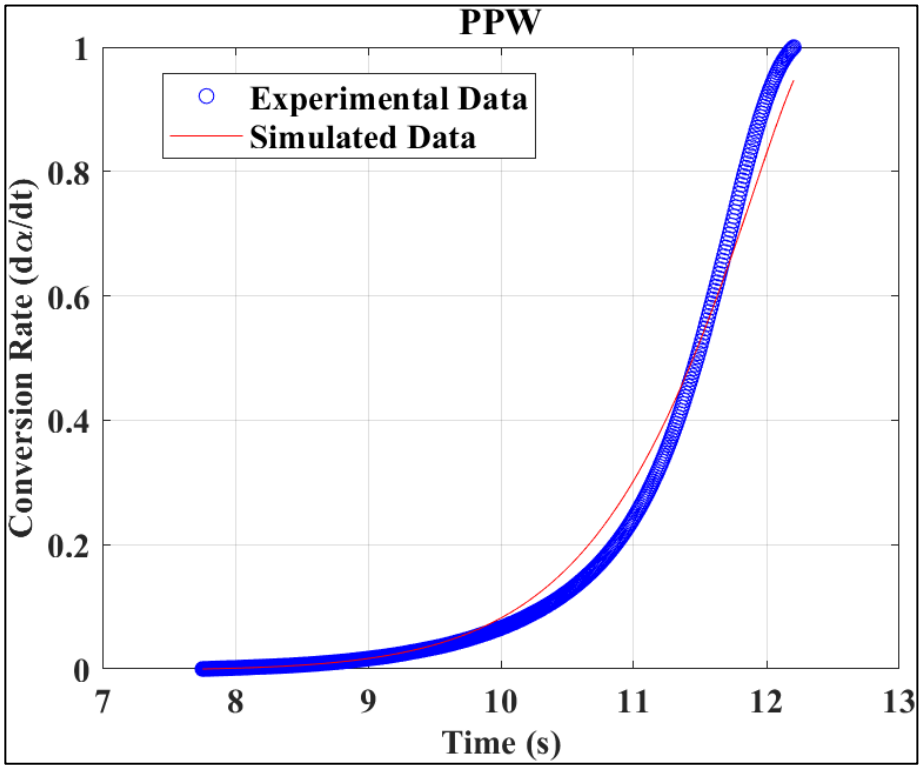
PPW
Experimental Data
Simulated Data
Conversion Rate (dα/dt)
Time (s)
0
0.2
0.4
0.6
0.8
1
7
8
9
10
11
12
13

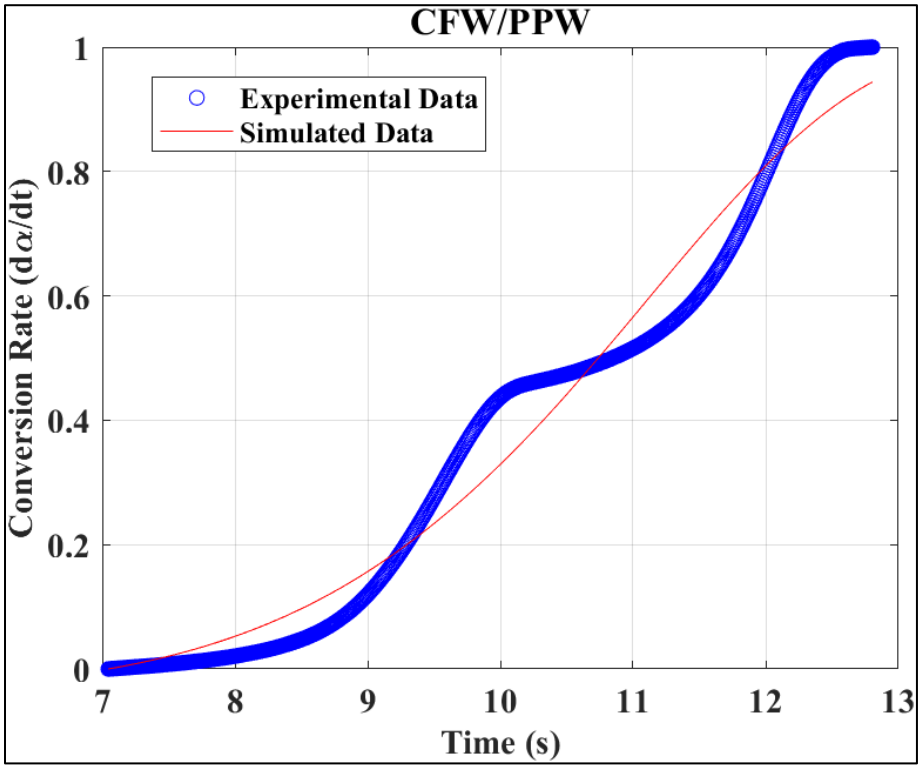

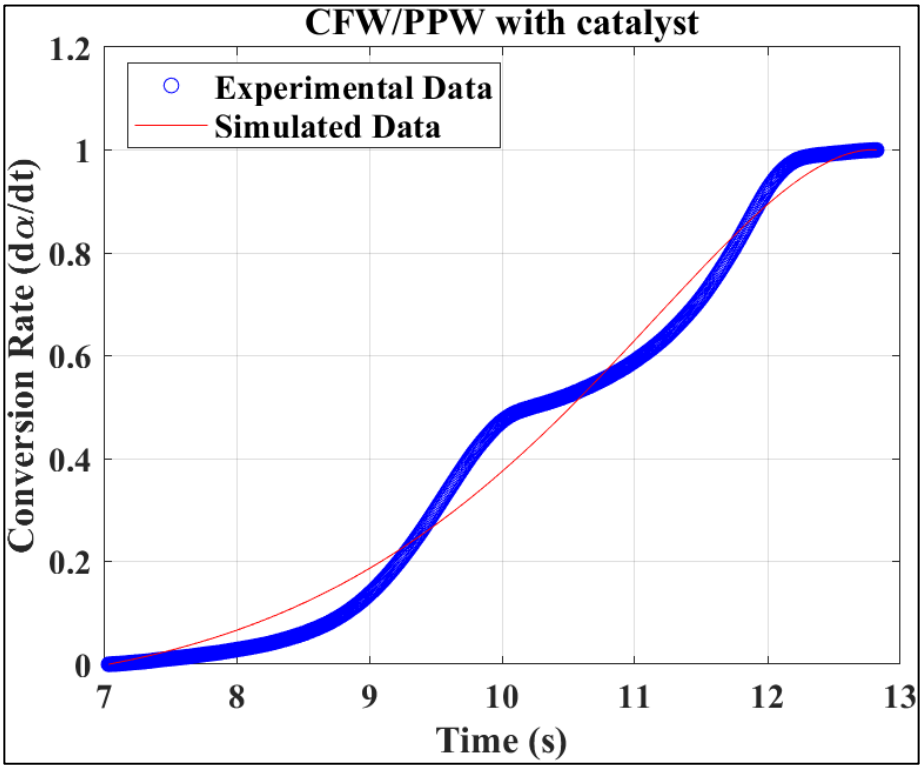

Figure 4.52 Pyrolysis Kinetic Curves of CFW, PPW, CFW/PPW, CFW/PPW with Catalyst (Operating Condition: Heating Rate: 40 °C/min, N_2 Flowrate: 50 mL/min

The kinetic parameters of CFW, PPW, CFW/PPW, and CFW/PPW with catalyst are summarized in Table 4.13.

Table 4.13
Kinetic Parameters for CFW, PPW, CFW/PPW and CFW/PPW with Catalyst

	Temperature (°C)	**E (kJ/mol)**	**A (s^{-1})**	**n**	**R^2**
CFW	237–430	107.74	2.64 x 10^8	0.3	0.99
PPW	330–510	127.80	7.44 x 10^8	0.4	0.98
CFW/PPW	280–520	55.06	4.81 x 10^3	0.8	0.96
CFW/PPW with catalyst	290–520	47.25	1.19 x 10^3	0.5	0.98

The E for CFW was 107.74 kJ/mol, while PPW shows a higher value of 127.80 kJ/mol. The higher E for PPW indicates that polypropylene requires more energy to initiate degradation due to its strong C–C structure that decomposes via free radical chain reaction mechanism (Suriapparao et al., 2014). Conversely, the E of CFW reflects the decomposition of cellulose and hemicellulose, which occurs at lower energy compared to PPW (Gin et al., 2024). Similar findings were obtained from a few researchers, where the plastics required more energy to degrade compared to biomass (Bhushan et al., 2024; Garba et al., 2018).

The co-pyrolysis of CFW/PPW exhibited a significantly lower E of 55.06 kJ/mol, suggesting overall decomposition required less energy which indicates the synergistic interactions between the two feedstocks. The presence of free radicals and volatile fragments from CFW facilitated chain scission in PPW, thereby reducing the overall energy requirement (Huang et al., 2024). The similar finding is also reported in the kinetic study during co-pyrolysis of sewage sludge (SS) and LDPE, suggesting the radical interactions of SS during co-pyrolysis promote PPW chain cleavage. This interaction increases the concentration of reactive molecules in the reactor and lowers the energy required for the reaction (Zaker et al., 2021). Furthermore, in the process of CFW/PPW with catalyst, the E (47.25 kJ/mol) was lower than those of CFW/PPW, suggesting the catalyst lowering the energy barrier (Gupta & Mondal, 2021). The lower E possibly attributed to the higher surface area and pore volume which favor the distribution of active sites of the catalyst which possibly accelerates the degradation process of CFW/PPW (Zhang et al., 2019).

The value of A varied significantly among the samples. PPW showed the highest A (7.44×10^8 s^{-1}), followed by CFW (2.64×10^8 s^{-1}), CFW/PPW (4.81×10^3 s^{-1}), and CFW/PPW with catalyst (1.19×10^3 s^{-1}). This trend aligns with the values of E for the same samples. PPW, with its high E, required more energy for polymer decomposition

than CFW. In contrast, CFW/PPW exhibited a much lower A, indicating reduced molecular collision frequency due to radical interactions between the two feedstocks (Li et al., 2024). The addition of catalyst further lowered the activation energy, suggesting that the catalyst promoted selective conversion by enhancing cracking, ring-opening cyclization, and deoxygenation reactions (Alam et al., 2021). Similar trends have been supported in other studies. Zhang et al., (2016) observed that blending cellulose with LPPE reduced E and A and further reduced with the presence of catalyst. Likewise, Xiang et al., (2018) demonstrated that introducing catalyst further decreased E and A by providing active sites that redirected the reaction pathways toward cracking, cyclization, and deoxygenation. These findings support the present results, confirming that co-pyrolysis and catalytic not only reduce the energy demand but also enhance selective bio-oil formation.

The n ranged between 0.3 and 0.8 across the pyrolysis reactions. Individual CFW and PPW showed lower n values, which are 0.3 and 0.4, respectively. Thus, reflecting their independent decomposition complexity. The CFW/PPW exhibited a higher n of 0.8, indicating a more complex overall mechanism resulting from multiple simultaneous pathways. With catalyst, n decreased to 0.5, suggesting that the catalytic surface simplified the decomposition mechanism by enhancing specific reactions such as deoxygenation and aromatization (Xiang et al., 2018) . Therefore, it can be deduced that the kinetic expression of CFW, PPW, CFW/PPW and CFW/PPW with catalyst are expressed by equation 4.1–4.4.

CFW:

$$\frac{d\alpha}{dt} = 2.64 \times 10^{8}\ exp\left(-\frac{107.74}{8.314 \times 10^{-3} \cdot T(t)}\right) \cdot (1-\alpha)^{0.3} \quad (4.1)$$

PPW:

$$\frac{d\alpha}{dt} = 7.44 \times 10^{8}\ exp\left(-\frac{127.80}{8.314 \times 10^{-3} \cdot T(t)}\right) \cdot (1-\alpha)^{0.4} \quad (4.2)$$

CFW/PPW:

$$\frac{d\alpha}{dt} = 4.81 \times 10^{3}\ exp\left(-\frac{55.06}{8.314 \times 10^{-3} \cdot T(t)}\right) \cdot (1-\alpha)^{0.8} \quad (4.3)$$

CFW/PPW with catalyst:

$$\frac{d\alpha}{dt} = 1.19 \times 10^{3}\ \exp\left(-\frac{47.25}{8.314 \times 10^{-3} \cdot T(t)}\right) \cdot (1-\alpha)^{0.5} \quad (4.4)$$

CHAPTER 5
CONCLUSION

5.1 Conclusion

In the present work, the CE and CTE catalysts were synthesized via wet impregnation method in several catalyst preparation conditions which are metal loadings, calcination temperature, and calcination time. The metal loadings formulation contributed to their catalyst activity in co-pyrolysis of CFW and PPW. The calcination temperature during catalyst preparation was found to affect catalytic activity. The calcination temperature below and above 600 °C caused low activity for CE to be below 76.4 % bio-oil yield. While below and above 700 °C reduced catalyst activity for CTE21 catalyst. The calcination time of 5 h was also found to be adequate to promote the formation of active sites on 15CE-600 and CTE21-700 catalysts, whereas prolong to 6 h facing agglomeration and sintering effect that reduce catalyst activity. The best formulated catalysts for CE and CTE were found to be 15CE-600-5 and CTE21-700-5, respectively.

The physical and chemical properties of the CE and CTE catalyst gave further understanding of the catalytic behaviours. The Cr incorporation into EA enhanced the surface area and acidity compared to Cr alone. The best condition of 15CE-600-5 and CTE21-700-5 catalysts possessed suitable pore structures with the pore size of 4.3 nm and 14.3 nm, respectively which is characteristic of mesostructured material. The textural properties of the 15CE-600-5 and CTE21-700-5 catalysts exert positive influence on their catalytic performances with attributes include surface areas in the range of 50.4-71.2 m^2/g and pore volume within 0.0536–0.2539 cm^3/g that could adequately promote the reaction efficiency. The activity of the 15CE-600-5 and CTE21-700-5 are affected by the acidity that is crucial for the catalytic cracking and deoxygenation process. CTE21-700-5 showed greater acidity of 3.9 mmol/g compared to 15CE-600-5 catalyst (3.4 mmol/g) correlated with its better catalytic activity.

The catalyst activity of the best conditions CE and CTE catalysts were further investigated based on the effects of operating conditions. 15CE-600-5 maximum bio-oil yield of 74.6 % was obtained at best operating conditions of 500 °C, 50:50

CFW/PPW ratio, 1:1 F/C ratio and 60 min pyrolysis time. CTE21-700-5 best operating conditions are 550 °C, 50:50 CFW/PPW ratio, 1:1 F/C ratio and 60 min pyrolysis time that achieved maximum 87.6 % bio-oil yield. The variation in the catalyst activity is related to the characteristics of the catalysts such as the surface area, porosity, acidity, and morphology. At the best operating conditions, 15CE-600-5 and CTE21-700-5 catalyst produced high aliphatic hydrocarbons (HC) with comparable yield (40.3 % and 40.7 % for CE and CTE, respectively). Both enhanced reduction of acid and sugar compounds. CTE21-700-5 produced lower alcohol by 0.7 %, and reduced carbonyl to 7.1 %. Also, the CTE21-700-5 produced higher furans 12.5 % and ester 7.9 % compared to 15CE-600-5 (10.1 % furans and 3 % ester). Thus conclude the CTE21-700-5 catalyst is the best formulated catalyst to produced highest yield and higher aliphatic HC compound.

The reusability of 15CE-600-5 and CTE21-700-5 catalysts were investigated in the co-pyrolysis of CFW and PPW. The catalyst deactivation occurred for both CE and CTE for reusability test, but its activity was recovered after regeneration. The regeneration by calcination treatment at 600 °C for 5 h (CE) and 700 °C for 5 h (CTE) helps to recover blocked pore possibly due to the adsorbed species during reaction, which improved catalyst activity. The catalyst activity of CTE21-700-5 showed gradual decreased from 87.6 % in cycle 1 to 70.2 % in cycle 2 and 59.5 % in cycle 3. Compared to 15CE-600-5 catalyst, which the catalyst activity was reduced from 76.4 % in cycle 1 to 58.5 % in cycle 2 and 56.7 % in cycle 3 after regeneration. The study revealed that alterations in catalyst structure due to deactivation affected the active sites of the reused and regenerated metal oxides crucial for the heterogeneous system.

The kinetic study showed the co-pyrolysis of CFW and PPW catalysed by CTE21-700-5 could be described by 0.5 order reaction. The activation energy is 1.19 x 10^3 kJ/mol and the pre-frequency factor is 47.25 s^{-1}. From the activation energy and pre-exponential factor points of view, the addition of catalyst could further decrease the activation energy based on the result of the CFW/PPW ($E = 4.81 \times 10^3$ and $A = 55.06\ s^{-1}$).

5.2 Future Recommendations

The findings of this thesis are confined to a specific research scope, focusing on selected metal oxides, catalyst preparation conditions (metal loading, calcination temperature, and calcination time), process parameters (pyrolysis temperature, biomass-to-plastic ratio, feedstock-to-catalyst ratio, and pyrolysis time), catalyst reusability and regeneration, and kinetic modelling. Therefore, future research should broaden the scope by addressing the following directions:

1. This study employed acid leaching to extract aluminium from sludge. It is strongly recommended to explore alternative extraction methods and modify the extracted aluminium into zeolitic structures to enhance surface area, porosity, and acidity, thereby improving metal-support interactions.
2. Cotton fabric waste (CFW), a holocellulose material, was used as the biomass feedstock. However, the reaction mechanism remains complex. Employing model compounds such as cellulose and hemicellulose, co-fed with polypropylene waste (PPW), would provide deeper insights into the interactions occurring on the catalyst surface.
3. The catalyst in this study is in a form of powder. Thus, it is suggested to modify structure of catalyst such as in beads form that can be used in fluidised bed reactor for better performance.

REFERENCES

Abdullahi Shagali, A., Hu, S., Li, H., He, L., Han, H., Chi, H., Qing, H., Xu, J., Jiang, L., Wang, Y., Su, S., & Xiang, J. (2023). Synergistic interactions and co-pyrolysis characteristics of lignocellulosic biomass components and plastic using a fast heating concentrating photothermal TGA system. *Renewable Energy*, *215*, 118936.

Abnisa, F., & Wan Daud, W. M. A. (2014). A review on co-pyrolysis of biomass: An optional technique to obtain a high-grade pyrolysis oil. *Energy Conversion and Management*, *87*, 71–85.

Abtew, M. A., Atalie, D., & Dejene, B. K. (2025). Recycling of cotton textile waste: Technological process, applications, and sustainability within a circular economy. *Journal of Industrial Textiles*, *55*, 1–85.

Adrados, A., de Marco, I., Caballero, B. M., López, A., Laresgoiti, M. F., & Torres, A. (2012). Pyrolysis of plastic packaging waste: A comparison of plastic residuals from material recovery facilities with simulated plastic waste. *Waste Management*, *32*(5), 826–832.

Afolabi O, & Onwona A. (2023). Application of incipient wet impregnation (IWI) methodology in the synthesis of Ni/SiO2 catalysts for hydrodeoxygenation processes. *Journal of Sustainable Energy*, *14*(2), 77–85.

Aghamiri, A. R., & Lahijani, P. (2024). Catalytic conversion of biomass and plastic waste to alternative aviation fuels: A review. *Biomass and Bioenergy*, *183*, 107120.

Ahmad, N., Imtiaz, M., Hussain, M., Amjad, U.-S., Maafa, I. M., Ahmed, U., Gani Abdul Jameel, A., & Bafaqeer, A. (2024). Catalytic co-pyrolysis of Vachellia Farnesiana with polypropylene plastic to produce bio-oil: Parameter optimization study. *Fuel*, *367*, 131495.

Ahmed, M. H. M., Batalha, N., Mahmudul, H. M. D., Perkins, G., & Konarova, M. (2020). A review on advanced catalytic co-pyrolysis of biomass and hydrogen-rich feedstock: Insights into synergistic effect, catalyst development and reaction mechanism. *Bioresource Technology*, *310*, 123457.

Ahmed, M. H. M., Batalha, N., Qiu, T., Hasan, M. M., Atanda, L., Amiralian, N., Wang, L., Peng, H., & Konarova, M. (2020). Red-mud based porous nanocatalysts for valorisation of municipal solid waste. *Journal of Hazardous Materials*, *396*.

Akancha, Kumari, N., & Singh, R. K. (2019). Co-pyrolysis of waste polypropylene and rice bran wax– production of biofuel and its characterization. *Journal of the Energy Institute*, *92*(4), 933–946.

Al-Maari, M. A., Ahmad, M. A., Din, A. T. M., Hassan, H., & Alsobaai, A. M. (2021). Co-pyrolysis of oil palm empty fruit bunch and oil palm frond with low-density polyethylene and polypropylene for bio-oil production. *Arabian Journal of Chemistry*, *14*(8), 103282.

Al-Maari, M. A., Ahmad, M. A., Din, A. T. M., Hassan, H., & Alsobaai, A. M. (2025). Upgrading bio-oil production via catalytic co-pyrolysis of oil palm empty fruit bunch and low-density polyethylene using clinoptilolite catalyst. *Journal of Analytical and Applied Pyrolysis*, *186*, 106937.

Al-Salem, S. M., Antelava, A., Constantinou, A., Manos, G., & Dutta, A. (2017). A review on thermal and catalytic pyrolysis of plastic solid waste (PSW). *Journal of Environmental Management*, *197*, 177–198.

Alam, M., Bhavanam, A., Jana, A., Viroja, J. kumar S., & Peela, N. R. (2020). Co-pyrolysis of bamboo sawdust and plastic: Synergistic effects and kinetics. *Renewable Energy*, *149*, 1133–1145.

Alam, M., Rammohan, D., & Peela, N. R. (2021). Catalytic co-pyrolysis of wet-torrefied bamboo sawdust and plastic over the zeolite H-ZSM-5: Synergistic effects and kinetics. *Renewable Energy*, *178*, 608–619.

Alcazar-Ruiz, A., Sanchez-Silva, L., & Dorado, F. (2022). Enhancement of BTX production via catalytic fast pyrolysis of almond shell, olive pomace with polyvinyl chloride mixtures. *Process Safety and Environmental Protection*, *163*, 218–226.

Alcazar-Ruiz, A., Sanchez-Silva, L., & Dorado, F. (2023). Hydrocarbon selectivity enhancement through catalytic fast co-pyrolysis of almond shell and plastic blends. *Chemical and Biological Technologies in Agriculture*, *10*(1), 56.

Alfè, M., Gargiulo, V., Porto, M., Migliaccio, R., Le Pera, A., Sellaro, M., Pellegrino, C., Abe, A. A., Urciuolo, M., Caputo, P., Calandra, P., Loise, V., Rossi, C. O., & Ruoppolo, G. (2022). Pyrolysis and Gasification of a Real Refuse-Derived Fuel (RDF): The Potential Use of the Products under a Circular Economy Vision. *Molecules*, *27*(23), 8114.

Alhalili, Z., & Smiri, M. (2022). The Influence of the Calcination Time on Synthesis of Nanomaterials with Small Size, High Crystalline Nature and Photocatalytic

Activity in the TiO2 Nanoparticles Calcined at 500 °C. *Crystals*, *12*(11), 1629.

Alrozi, R., Zubir, N. A., Bakar, N. F. A., Ladewig, B. P., Motuzas, J., Bakar, N. H. H. A., Wang, D. K., & da Costa, J. C. D. (2023). Functional role of B-site substitution on the reactivity of CaMFeO3 (M = Cu, Mo, Co) perovskite catalysts in heterogeneous Fenton-like degradation of organic pollutant. *Journal of the Taiwan Institute of Chemical Engineers*, *143*, 104675.

Asadullah, M. (2014). Barriers of commercial power generation using biomass gasification gas: A review. *Renewable and Sustainable Energy Reviews*, *29*, 201–215.

Atanda, L., Batalha, N., Stark, T., Tabulo, B., Perkins, G., Wang, Z., Odedairo, T., Wang, L., & Konarova, M. (2020). Hybridization of ZSM-5 with Spinel Oxides for Biomass Vapour Upgrading. *ChemCatChem*, *12*(5), 1403–1412.

Atanda, L., Fraga, G. L. L., Ahmed, M. H. M., Alothman, Z. A., Na, J., Batalha, N., Aslam, W., & Konarova, M. (2021). Conversion of agricultural waste into stable biocrude using spinel oxide catalysts. *Journal of Hazardous Materials*, *402*, 123539.

Bagheri, M., Esfilar, R., Sina Golchi, M., & Kennedy, C. A. (2020). Towards a circular economy: A comprehensive study of higher heat values and emission potential of various municipal solid wastes. *Waste Management*, *101*, 210–221.

Baranitharan, P., Ramesh, K., & Sakthivel, R. (2019). Analytical characterization of the Aegle marmelos pyrolysis products and investigation on the suitability of bio-oil as a third generation bio-fuel for C.I engine. *Environmental Progress & Sustainable Energy*, *38*(4).

Barbosa, J. M., Rossi, R. A. S., Andrade, L. A., Barrozo, M. A. S., & Vieira, L. G. M. (2021). A study of optimization of solar pyrolysis and catalyst recovery and reuse. *Energy Conversion and Management*, *237*, 114094.

Berthold, E. E. S., Deng, W., Zhou, J., Bertrand, A. M. E., Xu, J., Jiang, L., Su, S., Hu, S., Hu, X., Wang, Y., & Xiang, J. (2023). Impact of plastic type on synergistic effects during co-pyrolysis of rice husk and plastics. *Energy*, *281*, 128270.

Bhaskar, T., & Pandey, A. (2015). Advances in Thermochemical Conversion of Biomass—Introduction. In *Recent Advances in Thermo-Chemical Conversion of Biomass* (pp. 3–30). Elsevier.

Bhushan, D., Hooda, S., Chitransh, S., & Mondal, P. (2024). Insights into catalytic co-pyrolysis of spent coffee grounds and high density polyethylene (HDPE) using

acid mine drainage (AMD) treated sludge based catalyst: Analysis of kinetics, mechanism and thermodynamic properties. *Sustainable Chemistry for Climate Action*, *5*, 100051.

Bhushan, D., Hooda, S., & Mondal, P. (2025). Co-pyrolysis of biomass and plastic wastes and application of machine learning for modelling of the process: A comprehensive review. *Journal of the Energy Institute*, *119*, 101973.

Bianasari, A. A., Khaled, M. S., Hoang, T.-D., Reza, M. S., Bakar, M. S. A., & Azad, A. K. (2024). Influence of combined catalysts on the catalytic pyrolysis process of biomass: A systematic literature review. *Energy Conversion and Management*, *309*, 118437.

Carriel Schmitt, C., Zimina, A., Fam, Y., Raffelt, K., Grunwaldt, J.-D., & Dahmen, N. (2019). Evaluation of High-Loaded Ni-Based Catalysts for Upgrading Fast Pyrolysis Bio-Oil. *Catalysts*, *9*(9), 784.

Cavelius, P., Engelhart-Straub, S., Mehlmer, N., Lercher, J., Awad, D., & Brück, T. (2023). The potential of biofuels from first to fourth generation. *PLOS Biology*, *21*(3), e3002063.

Chang, S. H. (2018). Bio-oil derived from palm empty fruit bunches: Fast pyrolysis, liquefaction and future prospects. *Biomass and Bioenergy*, *119*, 263–276.

Chang, S. H. (2023). Plastic waste as pyrolysis feedstock for plastic oil production: A review. *Science of The Total Environment*, *877*, 162719.

Charusiri, W., Phowan, N., Permpoonwiwat, A., & Vitidsant, T. (2023). Catalytic Copyrolysis of Used Waste Plastic and Lubricating Oil Using Cu-Modification of a Spent Fluid Catalytic Cracking Catalyst for Diesel-like Fuel Production. *ACS Omega*, *8*(43), 40785–40800.

Charusiri, W., Phowan, N., & Vitidsant, T. (2022). Catalytic Copyrolysis of Sugarcane Leaves and Low-Density Polyethylene Waste to Produce Bio-Oil and Chemicals Using Copper-Doped HZSM-35. *Energy & Fuels*, *36*(5), 2639–2655.

Chasioti, A., & Zabaniotou, A. (2024). An Industrial Perspective for Sustainable Polypropylene Plastic Waste Management via Catalytic Pyrolysis—A Technical Report. *Sustainability*, *16*(14), 5852.

Chava, R., Purbia, D., Roy, B., Janardhanan, V. M., Bahurudeen, A., & Appari, S. (2021). Effect of Calcination Time on the Catalytic Activity of Ni/γ-Al2O3 Cordierite Monolith for Dry Reforming of Biogas. *International Journal of Hydrogen Energy*, *46*(9), 6341–6357.

Chen, A., Tian, Z., Han, R., Wei, X., Hu, R., & Chen, Y. (2021). Preparation of Ni-based steel slag catalyst by impregnation method for sludge steam gasification. *Sustainable Energy Technologies and Assessments*, *47*, 101553.

Chen, D., Cen, K., Zhuang, X., Gan, Z., Zhou, J., Zhang, Y., & Zhang, H. (2022). Insight into biomass pyrolysis mechanism based on cellulose, hemicellulose, and lignin: Evolution of volatiles and kinetics, elucidation of reaction pathways, and characterization of gas, biochar and bio-oil. *Combustion and Flame*, *242*, 112142.

Chen, Weimin, Shi, S., Zhang, J., Chen, M., & Zhou, X. (2016). Co-pyrolysis of waste newspaper with high-density polyethylene: Synergistic effect and oil characterization. *Energy Conversion and Management*, *112*, 41–48.

Chen, Wenjun, Lu, J., Zhang, C., Xie, Y., Wang, Y., Wang, J., & Zhang, R. (2020). Aromatic hydrocarbons production and synergistic effect of plastics and biomass via one-pot catalytic co-hydropyrolysis on HZSM-5. *Journal of Analytical and Applied Pyrolysis*, *147*, 104800.

Chen, X., Che, Q., Li, S., Liu, Z., Yang, H., Chen, Y., Wang, X., Shao, J., & Chen, H. (2019). Recent developments in lignocellulosic biomass catalytic fast pyrolysis: Strategies for the optimization of bio-oil quality and yield. *Fuel Processing Technology*, *196*, 106180.

Chen, X., Chen, Y., Yang, H., Chen, W., Wang, X., & Chen, H. (2017). Fast pyrolysis of cotton stalk biomass using calcium oxide. *Bioresource Technology*, *233*, 15–20.

Chen, X., Li, S., Chen, W., Chen, Y., Chen, H., & Yang, H. (2022). Influence of calcination temperature on calcined carbide slag assisted biomass pyrolysis. *Fuel Processing Technology*, *234*, 107339.

Chen, Y., Wang, H., Wang, J., Hou, D., Lu, Y., Yang, F., Liu, C., Lin, X., Zheng, Z., & Zheng, Y. (2024). Efficient and stable Fe-Ce-Al catalyst for catalytic deoxygenation of lignin for phenol and hydrocarbon-rich fuel: Effect of the synthesis method. *Fuel Processing Technology*, *254*, 108034.

Cheng, S., Wei, L., Zhao, X., & Julson, J. (2016). Application, Deactivation, and Regeneration of Heterogeneous Catalysts in Bio-Oil Upgrading. *Catalysts*, *6*(12), 195.

Cheung, C. W., Porter, J. F., & Mckay, G. (2001). Sorption kinetic analysis for the removal of cadmium ions from effluents using bone char. *Water Research*,

35(3), 605–612.

Chi, Y., Xue, J., Zhuo, J., Zhang, D., Liu, M., & Yao, Q. (2018). Catalytic co-pyrolysis of cellulose and polypropylene over all-silica mesoporous catalyst MCM-41 and Al-MCM-41. *Science of the Total Environment*, *633*, 1105–1113.

Cho, D.-W., Tsang, D. C. W., Kim, S., Kwon, E. E., Kwon, G., & Song, H. (2018). Thermochemical conversion of cobalt-loaded spent coffee grounds for production of energy resource and environmental catalyst. *Bioresource Technology*, *270*, 346–351.

Chow, L. W., Tio, S. A., Teoh, J. Y., Lim, C. G., Chong, Y. Y., & Thangalazhy-Gopakumar, S. (2018). Sludge as a relinquishing catalyst in Co-Pyrolysis with palm Empty Fruit Bunch Fiber. *Journal of Analytical and Applied Pyrolysis*, *132*, 56–64.

Colelli, L., Grancini, A., Mattei, E., Bassano, C., & Vilardi, G. (2025). Preparation and Characterization of Ru-Based Catalyst for Power to Gas Applications. *Energies*, *18*(4), 827.

Cook, E., Ionkova, K., Bhada-Tata, P., Yadav, S., & van Woerden, F. (2026). *What a Waste 3.0: Global Snapshot of Solid Waste Management Toward Circularity until 2050*. Washington, DC: World Bank.

Czajczyńska, D., Anguilano, L., Ghazal, H., Krzyżyńska, R., Reynolds, A. J., Spencer, N., & Jouhara, H. (2017). Potential of pyrolysis processes in the waste management sector. *Thermal Science and Engineering Progress*, *3*, 171–197.

Dada, T. K., Islam, M. A., Duan, A. X., & Antunes, E. (2022). Catalytic co-pyrolysis of ironbark and waste cooking oil using X-strontium /Y-zeolite (X= Ni, Cu, Zn, Ag, and Fe). *Journal of the Energy Institute*, *104*, 89–97.

Daful, A. G., & R Chandraratne, M. (2020). Biochar Production From Biomass Waste-Derived Material. In S. Hashmi & I. A. B. T.-E. of R. and S. M. Choudhury (Eds.), *Encyclopedia of Renewable and Sustainable Materials* (pp. 370–378). Elsevier.

Dang, Z., Zhu, X., Wang, L., & Ji, G. (2021). Titanium dioxide catalytic hydrothermal liquefaction to treat oily sludge: As hydrogen production catalyst. *Chemical Engineering Journal Advances*, *8*, 100139.

Dawodu, F. A., Ayodele, O. O., Akintola, J. O., Obembe, O. A., Sanni, A. O., & Agbejinmi, B. D. (2019). Upgrading Bio-Oil Produced from Corn Cobs and Cedrela odorata via Catalytic Olefination and Esterification with 3,7-

Dimethyloct-1-ene and Butanol. *International Journal of Chemical Engineering*, *2019*(1), 1–6.

de Rezende Locatel, W., Laurenti, D., Schuurman, Y., & Guilhaume, N. (2021). Ex-situ catalytic upgrading of pyrolysis vapors using mixed metal oxides. *Journal of Analytical and Applied Pyrolysis*, *158*, 105241.

Devarajan, V. P., & Madhavan, V. R. (2023). Experimental analysis of CO2 reduction using low surface area carbon beads (CB) and Ca/CB catalyst by thermocatalytic gasification for fuel gas production. *Biomass Conversion and Biorefinery*, *13*(8), 7319–7331.

Dewangan, A., Pradhan, D., & Singh, R. K. (2016). Co-pyrolysis of sugarcane bagasse and low-density polyethylene: Influence of plastic on pyrolysis product yield. *Fuel*, *185*, 508–516. https://doi.org/10.1016/j.fuel.2016.08.011

Ding, J., Liu, H., Wang, M., Tian, H., Wu, J., Yu, G., & Wang, Y. (2020). Enhanced Ethylene Glycol Selectivity of CuO–La2O3 /ZrO2 Catalyst: The Role of Calcination Temperatures. *ACS Omega*, *5*(43), 28212–28223.

Ding, K., Zhong, Z., Wang, J., Zhang, B., Fan, L., Liu, S., Wang, Y., Liu, Y., Zhong, D., Chen, P., & Ruan, R. (2018). Improving hydrocarbon yield from catalytic fast co-pyrolysis of hemicellulose and plastic in the dual-catalyst bed of CaO and HZSM-5. *Bioresource Technology*, *261*(March), 86–92.

Dokl, M., Copot, A., Krajnc, D., Fan, Y. Van, Vujanović, A., Aviso, K. B., Tan, R. R., Kravanja, Z., & Čuček, L. (2024). Global projections of plastic use, end-of-life fate and potential changes in consumption, reduction, recycling and replacement with bioplastics to 2050. *Sustainable Production and Consumption*, *51*(September), 498–518.

Duan, D., Wang, Y., Dai, L., Ruan, R., Zhao, Y., Fan, L., Tayier, M., & Liu, Y. (2017). Ex-situ catalytic co-pyrolysis of lignin and polypropylene to upgrade bio-oil quality by microwave heating. *Bioresource Technology*, *241*, 207–213.

Dyer, A. C., Nahil, M. A., & Williams, P. T. (2021). Catalytic co-pyrolysis of biomass and waste plastics as a route to upgraded bio-oil. *Journal of the Energy Institute*, *97*, 27–36.

Dyer, A. C., Nahil, M. A., & Williams, P. T. (2022). Biomass:polystyrene co-pyrolysis coupled with metal-modified zeolite catalysis for liquid fuel and chemical production. *Journal of Material Cycles and Waste Management*, *24*(2), 477–490.

El-Desoky, M. M., Morad, I., Wasfy, M. H., & Mansour, A. F. (2020). Synthesis, structural and electrical properties of PVA/TiO2 nanocomposite films with different TiO_2 phases prepared by sol–gel technique. *Journal of Materials Science: Materials in Electronics*, *31*(20), 17574–17584.

Engamba Esso, S. B., Xiong, Z., Chaiwat, W., Kamara, M. F., Longfei, X., Xu, J., Ebako, J., Jiang, L., Su, S., Hu, S., Wang, Y., & Xiang, J. (2022). Review on synergistic effects during co-pyrolysis of biomass and plastic waste: Significance of operating conditions and interaction mechanism. *Biomass and Bioenergy*, *159*, 106415.

Engamba Esso, S. B., Yan, Q., Xiong, Z., Hu, X., Xu, J., Jiang, L., Su, S., Hu, S., Wang, Y., & Xiang, J. (2022). Importance of char-volatiles interactions during co-pyrolysis of polypropylene and biomass components. *Journal of Environmental Chemical Engineering*, *10*(5), 108202.

Escalante, J., Chen, W.-H., Tabatabaei, M., Hoang, A. T., Kwon, E. E., Andrew Lin, K.-Y., & Saravanakumar, A. (2022). Pyrolysis of lignocellulosic, algal, plastic, and other biomass wastes for biofuel production and circular bioeconomy: A review of thermogravimetric analysis (TGA) approach. *Renewable and Sustainable Energy Reviews*, *169*, 112914.

Esteve-Turrillas, F. A., & de la Guardia, M. (2017). Environmental impact of Recover cotton in textile industry. *Resources, Conservation and Recycling*, *116*, 107–115.

Fan, Y., Hou, G., Lu, D., Xiong, Y., & Zhu, J. (2022). A novel production of aromatic hydrocarbons via dielectric barrier discharge assisted one-stage pyrolysis-catalysis of biomass: Insights into modified HZSM-5 selectivity and stability. *Journal of Analytical and Applied Pyrolysis*, *161*, 105417.

Fan, Y., Zhu, M., Jin, L., Cui, E., Zhu, L., Cai, Y., & Zhao, W. (2020). Catalytic upgrading of biomass-derived vapors to bio-fuels via modified HZSM-5 coupled with DBD: Effects of different titanium sources. *Renewable Energy*, *157*, 100–115.

Fivga, A., & Dimitriou, I. (2018). Pyrolysis of plastic waste for production of heavy fuel substitute: A techno-economic assessment. *Energy*, *149*, 865–874.

Fu, P., Tang, B., Li, H., Liu, S., Wang, L., & Lin, X. (2024a). Chitosan-assisted reassembled hierarchical HZSM-5 for selective production of monocyclic aromatics in catalytic co-pyrolysis of biomass and plastic. *Renewable Energy*,

236(July), 121492.

Fu, P., Tang, B., Li, H., Liu, S., Wang, L., & Lin, X. (2024b). Chitosan-assisted reassembled hierarchical HZSM-5 for selective production of monocyclic aromatics in catalytic co-pyrolysis of biomass and plastic. *Renewable Energy*, *236*(July), 121492.

Garba, M. U., Inalegwu, A., Musa, U., Aboje, A. A., Kovo, A. S., & Adeniyi, D. O. (2018). Thermogravimetric characteristic and kinetic of catalytic co-pyrolysis of biomass with low- and high-density polyethylenes. *Biomass Conversion and Biorefinery*, *8*(1), 143–150.

Genuino, H. C., van Eijk, M. C. P., Kersten, S. R. A., & Ruiz, M. P. (2024). Pyrolysis of Real Packaging Plastic Waste Streams in a Fluidized-Bed Pilot Plant. *Energy & Fuels*, *38*(3), 2188–2199.

Geyer, R. (2020). *Chapter 2 - Production, use, and fate of synthetic polymers* (T. M. B. T.-P. W. and R. Letcher (ed.); (pp. 13–32). Academic Press.

Geyer, R., Jambeck, J. R., & Law, K. L. (2017). Production, use, and fate of all plastics ever made. *Science Advances*, *3*(7), e1700782.

Gholizadeh, M., & Hu, X. (2022). Progress in understanding the coking behavior of typical catalysts in the catalytic pyrolysis of biomass. *Sustainable Energy and Fuels*, *6*(9), 2113–2148.

Ghorbannezhad, P., Park, S., & Onwudili, J. A. (2020). Co-pyrolysis of biomass and plastic waste over zeolite- and sodium-based catalysts for enhanced yields of hydrocarbon products. *Waste Management*, *102*, 909–918.

Gin, A. W., Hassan, H., Ahmad, M. A., Hameed, B. H., & Din, A. T. M. (2024). Co-pyrolysis of polyolefin mixtures and oil palm fibre for the production of liquid fuel: kinetics and thermodynamic study. *Biomass Conversion and Biorefinery*, *14*(5), 6381–6395.

Gomes, V. A. do P., Bacelos, M. S., Xavier, T. P., & de Lira, T. S. (2025). Catalytic Copyrolysis of Lignocellulosic Biomass and Polyolefins: A Review on Catalysts for Enhancing Bio-Oil Production. *ACS Engineering Au*.

Gowda, A. S., Karadimas, D., & Seay, J. R. (2025). Analysis of Tar and Oil Derived from Pyrolysis and Copyrolysis of Waste Plastics and Biomass. *Industrial and Engineering Chemistry Research*, *64*(17), 8935–8942.

Greenpeace (2025). Malaysia's mounting plastic waste. Retrieved Aug 10, 2025, from the World Wide Web: www.greenpeace.org/malaysia/our-work/plastics

Gupta, S., Lanjewar, R., & Mondal, P. (2022). Enhancement of hydrocarbons and phenols in catalytic pyrolysis bio-oil by employing aluminum hydroxide nanoparticle based spent adsorbent derived catalysts. *Chemosphere*, *287*, 132220.

Gupta, S., & Mondal, P. (2021). Catalytic pyrolysis of pine needles with nickel doped gamma-alumina: Reaction kinetics, mechanism, thermodynamics and products analysis. *Journal of Cleaner Production*, *286*.

Hafriz, R. S. R. M., Nor Shafizah, I., Arifin, N. A., Maisarah, A. H., Salmiaton, A., & Shamsuddin, A. H. (2022). Comparative, reusability and regeneration study of potassium oxide-based catalyst in deoxygenation reaction of WCO. *Energy Conversion and Management: X*, *13*, 100173.

Han, B., Chen, Y., Wu, Y., Hua, D., Chen, Z., Feng, W., Yang, M., & Xie, Q. (2014). Co-pyrolysis behaviors and kinetics of plastics–biomass blends through thermogravimetric analysis. *Journal of Thermal Analysis and Calorimetry*, *115*(1), 227–235.

Han, R., Wang, Y., Xing, S., Pang, C., Hao, Y., Song, C., & Liu, Q. (2022). Progress in reducing calcination reaction temperature of Calcium-Looping CO2 capture technology: A critical review. *Chemical Engineering Journal*, *450*, 137952.

Hanoğlu, A., Çay, A., & Yanık, J. (2019). Production of biochars from textile fibres through torrefaction and their characterisation. *Energy*, *166*, 664–673.

Harith, N., Hafriz, R. S. R. M., Arifin, N. A., Tan, E. S., Salmiaton, A., & Shamsuddin, A. H. (2022). Catalytic co-pyrolysis of blended biomass – plastic mixture using synthesized metal oxide(MO)-dolomite based catalyst. *Journal of Analytical and Applied Pyrolysis*, *168*, 105776.

Hassan, H., & Hameed, B. H. (2023). Green hydroxyapatite-zeolite catalyst derived from steel waste as an effective catalyst for the hydrocarbon production via co-catalytic pyrolysis of sugarcane bagasse and high-density polyethylene. *Catalysis Communications*, *184*, 106795.

Hassan, H., Hameed, B. H., & Lim, J. K. (2020). Co-pyrolysis of sugarcane bagasse and waste high-density polyethylene: Synergistic effect and product distributions. *Energy*, *191*, 116545.

Hassan, H., Lim, J. K., & Hameed, B. H. (2019). Catalytic co-pyrolysis of sugarcane bagasse and waste high-density polyethylene over faujasite-type zeolite. *Bioresource Technology*, *284*, 406–414.

He, Y., Chen, J., Mo, Z., Hu, C., Li, D., Tu, J., Lin, C., Wang, Y., Liu, D., & Wang, T. (2023). Controlling Diels-Alder reactions in catalytic pyrolysis of sawdust and polypropylene by coupling CO2 atmosphere and Fe-modified zeolite for enhanced light aromatics production. *Journal of Hazardous Materials*, *455*, 131547.

He, Z., Jiao, Q., Fang, Z., Li, T., Feng, C., Li, H., & Zhao, Y. (2018). Light olefin production from catalytic pyrolysis of waste tires using nano-HZSM-5/γ-Al_2O_3 catalysts. *Journal of Analytical and Applied Pyrolysis*, *129*, 66–71.

HM Ahmed, M., Batalha, N., ALOthman, Z. A., Yamauchi, Y., Valentino Kaneti, Y., & Konarova, M. (2022). Transforming red mud into an efficient acid-base catalyst by hybridization with mesoporous ZSM-5 for co-pyrolysis of biomass and plastics. *Chemical Engineering Journal*, *430*, 132965.

Huang, X., Tan, Y., Huang, J., Zhu, G., Yin, R., Tao, X., & Tian, X. (2024). Industrialization of open and closed-loop waste textile recycling towards sustainability: A review. *Journal of Cleaner Production*, *436*, 140676.

Huang, Z., Wu, J., Yang, T., Wang, Z., Zhang, T., Gao, F., Yang, L., & Li, G. (2024). Synergistic effects and kinetic analysis in co-pyrolysis of Peanut Shells and Polypropylene. *Foods*, *13*(8), 1191.

Husain, H., Adi, W. A., Subaer, S., Taryana, Y., Setiawan, A., Putri, S. E., Klyusubun, W., & Wannapaiboon, S. (2024). Effect of calcination temperature on structure evolution of hematite nanoparticles. *Physica Scripta*, *99*(6), 065974.

Ida, H., Ohtani, H., & Karagöz, S. (2020). Online fast pyrolysis of cellulose over titanium dioxide using tandem micro-reactor-GC-MS. *Sustainable Chemistry and Pharmacy*, *16*, 100268.

Iliopoulou, E. F., Pachatouridou, E., Marianou, A. A., Michailof, C., Kalogiannis, K. K., & Lappas, A. A. (2023). Catalytic pyrolysis of olive mill wastes towards advanced bio-fuels and bio-chemicals using metal oxide catalysts. *Catalysis Today*, *420*, 114151.

IPCC. (2022). *Global Warming of 1.5°C*. Cambridge University Press.

IRENA. (2024). Renewable energy highlights: July 2024.

Isha, R., Wen, L. P., binti Mustafa, N., Ramli, H., & binti Ismail, R. (2022). Effect of calcination temperature on Ce/OPA catalyst in HDPE catalytic pyrolysis to fuel grade liquid product. *Materials Today: Proceedings*, *57*, 1269–1275.

Jaafar, Y., Ramirez, G. C. A., Abdelouahed, L., El Samrani, A., El Hage, R., & Taouk,

B. (2023). Upgrading Pyrolytic Oil via Catalytic Co-Pyrolysis of Beechwood and Polystyrene. *Molecules*, *28*(15), 5758.

Jamaluddin, N. S., Hassan, H., Ahmad, M. A., Kasim, N. N., Hameed, B. H., Idris, S. S., & Zahidi, M. M. (2026). Synergistic co-pyrolysis of spent coffee grounds and polypropylene into hydrocarbon-rich bio-oil and carbon-rich biochar. *Next Energy*, *11*, 100606.

Jeswani, H., Krüger, C., Russ, M., Horlacher, M., Antony, F., Hann, S., & Azapagic, A. (2021). Life cycle environmental impacts of chemical recycling via pyrolysis of mixed plastic waste in comparison with mechanical recycling and energy recovery. *Science of The Total Environment*, *769*, 144483.

Jia, Y., Chen, D., Wang, X., Li, E., Wang, P., & Guo, L. (2025). Simultaneous H_2 production and dechlorination in polyvinyl chloride (PVC) gloves pyrolysis process with catalysts derived from electroplating sludge. *International Journal of Hydrogen Energy*, *105*, 1425–1434.

Jin, X., Lee, J. H., & Choi, J. W. (2022). Catalytic co-pyrolysis of woody biomass with waste plastics: Effects of HZSM-5 and pyrolysis temperature on producing high-value pyrolytic products and reducing wax formation. *Energy*, *239*, 121739.

Johari, N. D., Yusof, N. L. N., Khit, K. Y., Kamarudin, M., Nosbi, N., & Wan Ali, W. F. F. (2025). Effect of calcination temperature and holding time on MCAS formation through the solid-state method: Structural and phase analysis. *Ceramics International*, *51*(12), 16396–16403.

Johnsson, F., Kjärstad, J., & Rootzén, J. (2019). The threat to climate change mitigation posed by the abundance of fossil fuels. *Climate Policy*, *19*(2), 258–274.

Kaewpengkrow, P., Atong, D., & Sricharoenchaikul, V. (2017). Effect of metal oxide/alumina on catalytic deoxygentation of biofuel from physic nut residues pyrolysis. *International Journal of Hydrogen Energy*, *42*(31), 19629–19640.

Kai, W., Xie, X., Lin, D., Isa, Y. M., Kozlov, A., Penzik, M., & Li, B. (2025). Catalytic pyrolysis of paper mill sludge over self-sourced CaO/biochar catalyst under different temperatures. *Fuel*, *398*(May), 135538.

Kalogiannis, K. G., Stefanidis, S. D., Karakoulia, S. A., Triantafyllidis, K. S., Yiannoulakis, H., Michailof, C., & Lappas, A. A. (2018). First pilot scale study of basic vs acidic catalysts in biomass pyrolysis: deoxygenation mechanisms

and catalyst deactivation. *Applied Catalysis B: Environmental*, *238*(July), 346–357.

Kamil, F. H., Salmiaton, A., Hafriz, R. S. R. M., Hussien, I. R., & Omar, R. (2020). Characterization and application of molten slag as catalyst in pyrolysis of waste cooking oil. *Bulletin of Chemical Reaction Engineering and Catalysis*, *15*(1), 119–127.

Kamil, F. H., Salmiaton, A., Raja Shahruzzaman, R. M. H., Omar, R., & Alsultsan, A. G. (2017). Characterization and Application of Aluminum Dross as Catalyst in Pyrolysis of Waste Cooking Oil. *Bulletin of Chemical Reaction Engineering & Catalysis*, *12*(1), 81–88.

Kanduri, P. K., & Seethamraju, S. (2023). In situ and ex situ catalytic co-pyrolysis of lignocellulosic biomass and plastics (low-density and high-density polyethylene) using spent fcc catalyst. *Waste and Biomass Valorization*, *14*(5), 1737–1751.

Kariim, I., Swai, H., & Kivevele, T. (2023). Bio-oil upgrading over ZSM-5 catalyst: a review of catalyst performance and deactivation. *International Journal of Energy Research*, *2023*, 1–33.

Kay Lup, A. N., Abnisa, F., Daud, W. M. A. W., & Aroua, M. K. (2017). A review on reaction mechanisms of metal-catalyzed deoxygenation process in bio-oil model compounds. *Applied Catalysis A: General*, *541*, 87–106.

Kay Lup, A. N., Abnisa, F., Wan Daud, W. M. A., & Aroua, M. K. (2017). A review on reactivity and stability of heterogeneous metal catalysts for deoxygenation of bio-oil model compounds. *Journal of Industrial and Engineering Chemistry*, *56*, 1–34.

Kaza, S., Yao, L. C., Bhada-Tata, P., & Van Woerden, F. (2018). What a Waste 2.0: A Global Snapshot of Solid Waste Management to 2050. Washington, DC: World Bank.

Kepp, K. P. (2016). A quantitative scale of oxophilicity and thiophilicity. *Inorganic Chemistry*, *55*(18), 9461–9470.

Kim, B.-S. S., Kim, Y.-M. M., Lee, H. W., Jae, J., Kim, D. H., Jung, S.-C. C., Watanabe, C., & Park, Y.-K. K. (2016). Catalytic copyrolysis of cellulose and thermoplastics over HZSM-5 and HY. *ACS Sustainable Chemistry & Engineering*, *4*(3), 1354–1363.

Kim, H., Park, J. H., Ha, J.-M., & Kim, D. H. (2024). Recent progress on the

hydrodeoxygenation of lignin-derived pyrolysis oil using Ru-based catalysts. *Korean Journal of Chemical Engineering*, *41*(4), 945–964.

Kloth Care. (2019). Keeping Fabric Out of Landfills. Retrieved August 10, 2022, from the world wide web:kloth.com.my

Kuchelar, P., & Sudarsan, J. S. (2022). Heavy Metal Assessment of Groundwater on the Periphery of a Semi-Urban Solid Waste Dumpsite and Mitigation Strategy. In *Climate Change Impact on Groundwater Resources* (pp. 241–255). Springer International Publishing.

Kumar, A., Kumar, N., Baredar, P., & Shukla, A. (2015). A review on biomass energy resources, potential, conversion and policy in India. *Renewable and Sustainable Energy Reviews*, *45*, 530–539.

Kusrini, E., Supramono, D., Degirmenci, V., Pranata, S., Bawono, A. A., & Ani, N. (2018). Improving the Quality of Pyrolysis Oil from Co-firing High-density Polyethylene Plastic Waste and Palm Empty Fruit Bunches. *International Journal of Technology*, *9*(7), 1498.

Kwon, D., Yi, S., Jung, S., & Kwon, E. E. (2021). Valorization of synthetic textile waste using CO_2 as a raw material in the catalytic pyrolysis process. *Environmental Pollution*, *268*, 115916.

Langa, C., Mathipa, M., Mabuba, N., & Hintsho-Mbita, N. C. (2025). Effect of calcination temperature on the structural and photocatalytic properties of nickel sulfide nanoparticles for dye degradation and antibacterial applications. *Chemical Physics Impact*, *11*, 100913.

Lani, N. S., Ngadi, N., Jusoh, M., Mohamad, Z., & Zakaria, Z. Y. (2019). Outstanding performance of waste chicken eggshell derived CaO as a green catalyst in biodiesel production: Optimization of calcination conditions. *Journal of Physics: Conference Series*, *1349*(1).

Leal Filho, W., Dinis, M. A. P., Liakh, O., Paço, A., Dennis, K., Shollo, F., & Sidsaph, H. (2024). Reducing the carbon footprint of the textile sector: an overview of impacts and solutions. *Textile Research Journal*, *94*(15–16), 1798–1814.

Lehto, J., Oasmaa, A., Solantausta, Y., Kytö, M., & Chiaramonti, D. (2014). Review of fuel oil quality and combustion of fast pyrolysis bio-oils from lignocellulosic biomass. *Applied Energy*, *116*, 178–190.

Leong, Y. K., Chew, K. W., Chen, W.-H., Chang, J.-S., & Show, P. L. (2021). Reuniting the biogeochemistry of algae for a low-carbon circular bioeconomy. *Trends in*

Plant Science, *26*(7), 729–740.

Li, H., Ma, H., Zhao, W., Li, X., & Long, J. (2019). Upgrading lignin bio-oil for oxygen-containing fuel production using Ni/MgO: Effect of the catalyst calcination temperature. *Applied Energy*, *253*(January), 113613.

Li, Jing, Dai, J., Liu, G., Zhang, H., Gao, Z., Fu, J., He, Y., & Huang, Y. (2016). Biochar from microwave pyrolysis of biomass: A review. *Biomass and Bioenergy*, *94*, 228–244.

Li, Jingbao, Wang, Y., Qi, J., Liu, H., Liu, X., Wang, M.-Y., Lv, J., Huang, S., & Ma, X. (2025). Effect of ordered mesoporous alumina on mass transfer to enhance dimethyl ether carbonylation of shaped mordenite catalysts. *Industrial & Engineering Chemistry Research*, *64*(24), 11826–11835.

Li, L., Shi, L., Zhang, Z., Sun, G., & Li, Z. (2024). Research on the mechanism of hydrogen production by catalytic fast co-pyrolysis of cotton stalks and polypropylene: An experimental and theoretical study. *Biomass and Bioenergy*, *191*, 107459.

Li, W., Lu, Y., Zhu, Y., Li, X., Wang, J., Li, S., Zheng, Y., & Zheng, Z. (2020). Catalytic pyrolysis vapor upgrading of corncob into furans over pyrolysis-comprehensive two-dimensional gas chromatography/mass spectrometry: significance of catalyst and temperature. *BioEnergy Research*, *13*(4), 1180–1193.

Li, X., Xie, H., Gao, X., Wu, Y., Wang, P., Tian, S., Zhang, T., & Tan, Y. (2018). Effects of calcination temperature on structure-activity of K-ZrO_2/Cu/Al_2O_3 catalysts for ethanol and isobutanol synthesis from CO hydrogenation. *Fuel*, *227*, 199–207.

Li, Yingna, Ahmad, M. S., Tahir, M. H., Bashir, M., Khan, A. M., Irfan, R. M., Malik, I. R., & Shen, B. (2024). Catalytic co-pyrolysis of cabbage waste and plastics with Ni/ZSM-5 catalysis to produce aromatic-rich oil. *Journal of Analytical and Applied Pyrolysis*, *179*, 106518.

Li, Yong, Kang, S., Han, W., & Yin, F. (2024). Synergistic effects between mixed plastics and their impact on pyrolysis behavior and pyrolysis products. *Molecules*, *29*(24), 1–15.

Li, Z., Shi, L., Liang, D., Li, F., Wei, L., Li, W., & Zha, X. (2025). Study on the hydrocarbon-rich bio-oil from catalytic fast co-pyrolysis cotton stalk and polypropylene over alkali-modified HZSM-5. *Industrial Crops and Products*, *224*, 120352.

Lin, X., Lei, H., Wang, C., Qian, M., Mateo, W., Chen, X., Guo, Y., & Huo, E. (2023). The effects of pore structures and functional groups on the catalytic performance of activated carbon catalysts for the co-pyrolysis of biomass and plastic into aromatics and hydrogen-rich syngas. *Renewable Energy*, *202*, 855–864.

Lin, X., Zhang, Z., Zhang, Z., Sun, J., Wang, Q., & Pittman, C. U. (2018). Catalytic fast pyrolysis of a wood-plastic composite with metal oxides as catalysts. *Waste Management*, *79*, 38–47.

Liu, Y., Lyu, Z., Wang, S., Zhang, Y., Wang, J., Chen, Z., & Wang, J. (2025). Activation and functionalization of biochar-based catalysts obtained from sewage sludge and cotton stalks to improve hydrogen-rich gas production. *Journal of Environmental Chemical Engineering*, *13*(5), 117665.

Lu, L.-C., Chen, Y.-W., & Chou, C.-C. (2005). Antibacterial activity of propolis against Staphylococcus Aureus. *International Journal of Food Microbiology*, *102*(2), 213–220.

Lu, M., Wang, S., Su, M., Weng, Z., Zheng, J., Gupta, N. K., Cai, K., Shou, Z., & Ke, Q. (2025). Insights into chemical recycling and upgrading strategies for polyolefin-based plastics. *Industrial & Engineering Chemistry Research*, *64*(11), 5765–5781.

Luo, L., Guo, X., Zhang, Z., Chai, M., Rahman, M. M., Zhang, X., & Cai, J. (2020). Insight into pyrolysis kinetics of lignocellulosic biomass: isoconversional kinetic analysis by the modified friedman method. *Energy & Fuels*, *34*(4), 4874–4881.

Luo, W., Dong, H., Wang, T., Zhang, S., Zhang, D., Li, B., Huang, S., Hu, J., Song, M., & Zhou, Z. (2022). Co-pyrolysis of chinese herb residue and polypropylene over Ni, Fe, Co and Cu/Ac: co-production and formation mechanism of carbon nanomaterials, liquid oil and pyrolysis gas. *Energy*, *244*, 122634.

Luo, W., Wang, T., Zhang, S., Zhang, D., Dong, H., Song, M., & Zhou, Z. (2022). Catalytic co-pyrolysis of herb residue and polypropylene for pyrolysis products upgrading and diversification using nickel-X/biochar and ZSM-5 (X = iron, cobalt, copper). *Bioresource Technology*, *349*.

Ma, M., Xu, D., Gong, X., Diao, Y., Feng, P., & Kapusta, K. (2023). Municipal sewage sludge product recirculation catalytic pyrolysis mechanism from a kinetic perspective. *Renewable Energy*, *215*, 118955.

Ma, Y., He, P., Lü, F., & Zhang, H. (2024). Greenhouse gas emissions and mitigation

strategies across the life cycle of municipal solid waste incineration plants in china. *ACS Sustainable Chemistry & Engineering*, *12*(24), 9268–9278.

Magalhães, E. R. B., Fonseca de Menezes, N. N., Silva, F. L., Alves Garrido, J. W., Angélica dos Santos Bezerra Sousa, M., & Santos, E. S. dos. (2021). Effect of oil extraction on the composition, structure, and coagulant effect of Moringa oleifera seeds. *Journal of Cleaner Production*, *279*, 123902.

Maneechakr, P., & Karnjanakom, S. (2021). Improving the bio-oil quality via effective pyrolysis/deoxygenation of palm kernel cake over a metal (Cu, Ni, or Fe)-Doped Carbon Catalyst. *ACS Omega*, *6*(30), 20006–20014.

Mat Aron, N. S., Khoo, K. S., Chew, K. W., Show, P. L., Chen, W.-H., & Nguyen, T. H. P. (2020). Sustainability of the four generations of biofuels – A review. *International Journal of Energy Research*, *44*(12), 9266–9282.

Mazibuko, M., Ndumo, J., Low, M., Ming, D., & Harding, K. (2019). Investigating the natural degradation of textiles under controllable and uncontrollable environmental conditions. *Procedia Manufacturing*, *35*, 719–724.

Miandad, R., Rehan, M., Barakat, M. A., Aburiazaiza, A. S., Khan, H., Ismail, I. M. I., Dhavamani, J., Gardy, J., Hassanpour, A., & Nizami, A.-S. (2019). Catalytic Pyrolysis of Plastic Waste: Moving Toward Pyrolysis Based Biorefineries. *Frontiers in Energy Research*, *7,* 27.

MIDF. (2024). Biomass energy, the pioneer of the circular economy revolution.

Mirzaei, R., Shirazvatan, M., & Tavakoli, O. (2026). Co-pyrolysis of microalgae Chlorella vulgaris and polyvinyl chloride: Synergistic effects, thermo-kinetic analysis, and thermal behaviour prediction via machine learning. *Biomass and Bioenergy*, *213*, 109158.

Mishra, R. K., Chistie, S. M., Naik, S. U., & Kumar, P. (2022). Thermocatalytic co-pyrolysis of waste biomass and plastics: Studies of physicochemical properties, kinetics behaviour, and characterization of liquid product. *Journal of the Energy Institute*, *105*, 192–202.

Mo, F., Ullah, H., Zada, N., & Shahab, A. (2023). A review on catalytic co-pyrolysis of biomass and plastics waste as a thermochemical conversion to produce valuable products. *Energies*, *16*(14), 5403.

Mohamed, A. R., Mohd Salleh, N. H., & Nordin, N. N. (2023). Kinetics analysis on isothermal torrefaction of sawdust in a fixed-bed reactor using the Coats-Redfern method and functional group analysis using FTIR spectroscopy.

Malaysian Journal of Chemical Engineering & Technology, *6*(1), 17–21.

Moonsrikaew, W., & Duangchan, A. (2022). Deoxygenation of pyrolysis vapor from palm fruit cake over NiMo/γ-Al_2O_3 catalyst: Effect of CeO_2, TiO_2, and ZrO_2 additives. *Molecular Catalysis*, *523*, 111712.

Mortensen, P. M., Grunwaldt, J.-D., Jensen, P. A., Knudsen, K. G., & Jensen, A. D. (2011). A review of catalytic upgrading of bio-oil to engine fuels. *Applied Catalysis A: General*, *407*(1–2), 1–19.

MSCI. (2023). Global primary energy consumption in 2023. Retrieved December 31, 2023, from the world wide web:www.msci-institute.com/charts/global-primary-energy-consumption-generation-in-2023

Muelas, Á., Aranda, D., Callén, M. S., Murillo, R., Veses, A., Asrardel, M., & Ballester, J. (2020). Properties and combustion characteristics of bio-oils from catalytic co-pyrolysis of grape seeds, polystyrene, and waste tires. *Energy and Fuels*, *34*(11), 14190–14203.

Muhammad, I., & Manos, G. (2021). Intensification of co-pyrolysis of plastic with biomass via pretreatment. *Process Safety and Environmental Protection*, *146*, 586–598.

Mullen, C. A., Dorado, C., & Boateng, A. A. (2018). Catalytic co-pyrolysis of switchgrass and polyethylene over HZSM-5: Catalyst deactivation and coke formation. *Journal of Analytical and Applied Pyrolysis*, *129*, 195–203.

Munnik, P., de Jongh, P. E., & de Jong, K. P. (2015). Recent developments in the synthesis of supported catalysts. *Chemical Reviews*, *115*(14), 6687–6718.

Nanda, S., & Berruti, F. (2021). Thermochemical conversion of plastic waste to fuels: a review. *Environmental Chemistry Letters*, *19*(1), 123–148.

Nandakumar, T., Dwivedi, U., Pant, K. K., Kumar, S., & Balaraman, E. (2023). Wheat straw/HDPE co-reaction synergy and enriched production of aromatics and light olefins via catalytic co-pyrolysis over Mn, Ni, and Zn metal modified HZSM-5. *Catalysis Today*, *408*, 111–126.

Nardella, F., Bellavia, S., Mattonai, M., & Ribechini, E. (2022). Co-pyrolysis of biomass and plastic: Synergistic effects and estimation of elemental composition of pyrolysis oil by analytical pyrolysis–gas chromatography/mass spectrometry. *Bioresource Technology*, *354*, 127170.

Ndou, V., & Rampedi, I. T. (2022). Bibliometric analysis of municipal solid waste management research: global and South African trends. *Sustainability*, *14*(16),

10229.

Niinimäki, K., Peters, G., Dahlbo, H., Perry, P., Rissanen, T., & Gwilt, A. (2020). The environmental price of fast fashion. *Nature Reviews Earth & Environment*, *1*(4), 189–200.

Nwankwor, P. E., Onuigbo, I. O., Chukwuneke, C. E., Yahaya, M. F., Agboola, B. O., & Jahng, W. J. (2021). Synthesis of gasoline range fuels by the catalytic cracking of waste plastics using titanium dioxide and zeolite. *International Journal of Energy and Environmental Engineering*, *12*(1), 77–86.

Ocreto, J. B., Chen, W.-H., Ubando, A. T., Park, Y.-K., Sharma, A. K., Ashokkumar, V., Ok, Y. S., Kwon, E. E., Rollon, A. P., & De Luna, M. D. G. (2021). A critical review on second and third generation bioethanol production using microwaved-assisted heating (MAH) pretreatment. *Renewable and Sustainable Energy Reviews*, *152*, 111679.

Ojha, D. K., & Vinu, R. (2015). Fast co-pyrolysis of cellulose and polypropylene using Py-GC/MS and Py-FT-IR. *RSC Advances*, *5*(82), 66861–66870.

Olutoye, M. A., & Hameed, B. H. (2010). Transesterification of palm oil on $K_yMg_{1-x}Zn_{1+x}O_3$ catalyst: Effect of Mg–Zn interaction. *Fuel Processing Technology*, *91*(6), 653–659.

Ooi, X. Y., Gao, W., Ong, H. C., Lee, H. V., Juan, J. C., Chen, W. H., & Lee, K. T. (2019). Overview on catalytic deoxygenation for biofuel synthesis using metal oxide supported catalysts. *Renewable and Sustainable Energy Reviews*, *112*, 834–852.

Ouedraogo, A. S., & Bhoi, P. R. (2020). Recent progress of metals supported catalysts for hydrodeoxygenation of biomass derived pyrolysis oil. *Journal of Cleaner Production*, *253*, 119957.

Özbay, N., Yargıç, A. Ş., Tatman, A., & Eroğlu, F. (2025). The impact of metal type on the pyrolysis product distribution of sugar beet pulp: An analytical Py-GC/MS study with alumina-based catalysts. *Sustainable Energy Technologies and Assessments*, *77*, 104323.

Padil, P., Sunarno, S., Mutamima, A., Purnama, I., Nurfatihayati, Utama, P. S., Noor, A. R., Sunariyo, S., & Aziz, M. (2025). Optimized liquid hydrocarbon production via co-pyrolysis of nypa fronds and polypropylene using fly ash catalyst. *Bioresource Technology Reports*, *31*, 102237.

Panicker, T. F., K, A., Tarkar, S. V., Mishra, R. K., Wang, X., & Mohanty, K. (2025).

Catalytic co-pyrolysis of waste coconut fibers and polystyrene using Py-GC-MS: Effect of temperatures and catalyst loading on pyrolytic hot vapours. *Industrial Crops and Products*, *236*, 121954.

Park, Y., Lee, H. W., Lee, J. Y., & Kim, Y. M. (2018). The use of high density polyethylene (HDPE) as a co-feeding feedstock on the catalytic pyrolysis of yellow poplar over Al-MCM-48 and Al-MSU-F. *Journal of Analytical and Applied Pyrolysis*, *135*, 390–396.

Parku, G. K., Collard, F.-X., & Görgens, J. F. (2020). Pyrolysis of waste polypropylene plastics for energy recovery: Influence of heating rate and vacuum conditions on composition of fuel product. *Fuel Processing Technology*, *209*, 106522.

Peng, X., Wang, Z., Huang, P., Chen, X., Fu, X., & Dai, W. (2016). Comparative study of two different TiO_2 film sensors on response to H_2 under uv light and room temperature. *Sensors*, *16*(8), 1249.

Phan, D.-P., Vo, T. K., Le, V. N., Kim, J., & Lee, E. Y. (2020). Spray pyrolysis synthesis of bimetallic NiMo/Al_2O_3–TiO_2 catalyst for hydrodeoxygenation of guaiacol: Effects of bimetallic composition and reduction temperature. *Journal of Industrial and Engineering Chemistry*, *83*, 351–358.

Praveen Kumar, K., & Srinivas, S. (2020). Catalytic co-pyrolysis of biomass and plastics (polypropylene and polystyrene) using spent FCC catalyst. *Energy and Fuels*, *34*(1), 460–473.

Prayitno, B., Musyarofah, M., Tajalla, G. U. N., Nafisah, A. R., Norhidayah, S., & Kartika, S. A. (2025). The effect of calcination temperature and holding time on structural properties of calcia powders derived from eggshell waste. *Indonesian Physical Review*, *8*(1), 281–299.

Qiu, B., Tao, X., Wang, J., Liu, Y., Li, S., & Chu, H. (2022). Research progress in the preparation of high-quality liquid fuels and chemicals by catalytic pyrolysis of biomass: A review. *Energy Conversion and Management*, *261*, 115647.

Qiu, B., Yang, C., Shao, Q., Liu, Y., & Chu, H. (2022). Recent advances on industrial solid waste catalysts for improving the quality of bio-oil from biomass catalytic cracking: A review. *Fuel*, *315*, 123218.

Rashidi, N. A., Chai, Y. H., & Yusup, S. (2022). Biomass energy in malaysia: Current scenario, policies, and implementation challenges. *Bioenergy Research*, *15(3)*,1371–1386.

Razzak, S. A., Haddad, H., Nawaz, A., & Hossain, M. M. (2025). Review for the

synergistic effects in catalytic co-pyrolysis of biomass and plastic waste: Pathways to sustainable energy. *Next Sustainability*, *6*, 100157.

Revilla, C., Challco, A., Tejada, K., Terán, R., Garcia, K., & Colina, G. (2025). Enhancing antibiotic degradation via photocatalysis and hydrodynamic cavitation using TiO_2 catalyst supported on aluminum sludge. *Environmental Technology and Innovation*, *37*.

Rezaei, P. S., Oh, D., Hong, Y., Kim, Y.-M., Jae, J., Jung, S.-C., Jeon, J.-K., & Park, Y.-K. (2017). In-situ catalytic co-pyrolysis of yellow poplar and high-density polyethylene over mesoporous catalysts. *Energy Conversion and Management*, *151*, 116–122.

Roslan, N. A., Abidin, S. Z., Nasir, N. S., Chin, S. Y., & Taufiq-Yap, Y. H. (2021). Extracted γ-Al_2O_3 from aluminum dross as a catalyst support for glycerol dry reforming reaction. *Materials Today: Proceedings*, *42*, 63–68.

Roy, Poritosh, & Dias, G. (2017). Prospects for pyrolysis technologies in the bioenergy sector: A review. *Renewable and Sustainable Energy Reviews*, *77*, 59–69.

Roy, Poulami, Jahromi, H., Adhikari, S., Zou Finfrock, Y., Rahman, T., Ahmadi, Z., Mahjouri-Samani, M., Feyzbar-Khalkhali-Nejad, F., & Oh, T.-S. (2022). Performance of biochar assisted catalysts during hydroprocessing of non-edible vegetable oil: Effect of transition metal source on catalytic activity. *Energy Conversion and Management*, *252*, 115131.

Ryu, S., Lee, H. W., Kim, Y.-M., Jae, J., Jung, S.-C., Ha, J.-M., & Park, Y.-K. (2020). Catalytic fast co-pyrolysis of organosolv lignin and polypropylene over in-situ red mud and ex-situ HZSM-5 in two-step catalytic micro reactor. *Applied Surface Science*, *511*, 145521.

Said, A. E. A., Goda, M. N., Abd El-Wahab, M. M. M., El-Gamal, N. O., & El-Aal, M. A. (2024). Promoted catalytic performance of sugarcane bagasse ash supported by γ-alumina as efficient, stable, and ecofriendly catalyst for dehydration of methanol to dimethyl ether. *Asia-Pacific Journal of Chemical Engineering*, *19*(3).

Sangpatch, T., Kanokkantapong, V., Puasuwon, P., Prasertsak, T., & Tuntiwiwattanapun, N. (2025). Development of a catalyst Co-pyrolysis process for producing pyrolysis oil and wax from cooking oil contaminated polypropylene plastic. *Scientific Reports*, *15*(1), 1–16.

Sardon, H., & Dove, A. P. (2018). Plastics recycling with a difference. *Science*,

360(6387), 380–381.

Sarker, M., Liu, R., Rahman, M. M., Li, C., Chai, M., Nishu, & He, Y. (2020). Impact of acid-modified ZSM-5 on hydrocarbon yield of catalytic co-pyrolysis of poplar wood sawdust and high-density polyethylene by Py-GC/MS analysis. *Journal of the Energy Institute*, *93*(6), 2435–2443.

Schmitt, C. C., Moreira, R., Neves, R. C., Richter, D., Funke, A., Raffelt, K., Grunwaldt, J.-D., & Dahmen, N. (2020). From agriculture residue to upgraded product: The thermochemical conversion of sugarcane bagasse for fuel and chemical products. *Fuel Processing Technology*, *197*, 106199.

Seah, C. C., Tan, C. H., Arifin, N. A., Hafriz, R. S. R. M., Salmiaton, A., Nomanbhay, S., & Shamsuddin, A. H. (2023). Co-pyrolysis of biomass and plastic: Circularity of wastes and comprehensive review of synergistic mechanism. *Results in Engineering*, *17*, 100989.

Sekyere, D. T., Zhang, J., Chen, Y., Huang, Y., Wang, M., Wang, J., Niwamanya, N., Barigye, A., & Tian, Y. (2023). Production of light olefins and aromatics via catalytic co-pyrolysis of biomass and plastic. *Fuel*, *333*.

Seo, D.-J., Lee, J. B., Kim, Y.-J., Cho, H.-R., Kim, S.-Y., Kim, G.-E., Park, Y.-D., Kim, G.-H., An, J.-C., Oh, K., & Park, J.-I. (2024). The characteristics of hydrodeoxygenation of biomass pyrolysis oil over alumina-supported nimo catalysts. *Catalysts*, *15*(1), 6.

Settle, A. E., Berstis, L., Rorrer, N. A., Roman-Leshkóv, Y., Beckham, G. T., Richards, R. M., & Vardon, D. R. (2017). Heterogeneous Diels–Alder catalysis for biomass-derived aromatic compounds. *Green Chemistry*, *19*(15), 3468–3492.

Shafaghat, H., Lee, H. W., Tsang, Y. F., Oh, D., Jae, J., Jung, S.-C., Ko, C. H., Lam, S. S., & Park, Y.-K. (2019). In-situ and ex-situ catalytic pyrolysis/co-pyrolysis of empty fruit bunches using mesostructured aluminosilicate catalysts. *Chemical Engineering Journal*, *366*, 330–338.

Shahdan, N. A., Balasundram, V., Ibrahim, N., Isha, R., & Manan, Z. A. (2022). Catalytic Co-pyrolysis of empty fruit bunch and high-density polyethylene mixtures over rice husk ash: Thermogravimetric, kinetic and thermodynamic analyses. *Cleaner Engineering and Technology*, *9*, 100538.

Shaib Aliwi, S. A., Ramli, M. Z., Wan Kamis, W. Z., Ali Bashah, N. A., & Olutoye, M. A. (2025). Synthesis of bio-oil via catalytic co-pyrolysis of cotton fabric waste and polypropylene plastic waste. *Journal of Advanced Reearch in Applied*

Scienced and Engineering Technology, *2*(2), 198–206.

Shao, S., Cao, Y., Ye, Z., Li, X., Zhang, H., & Xiao, R. (2024). Enhanced selective production of aldehydes and ketones by catalytic upgrading of pyrolysis vapor from holocellulose over red mud-based composite catalysts. *Fuel*, *355*, 129367.

Sharma, V., Tsai, M.-L., Chen, C.-W., Sun, P.-P., Nargotra, P., & Dong, C.-D. (2023). Advances in machine learning technology for sustainable biofuel production systems in lignocellulosic biorefineries. *Science of The Total Environment*, *886*, 163972.

Shi, Y., Liu, C., Zhuo, J., & Yao, Q. (2020). Investigation of a Ni-modified MCM-41 catalyst for the reduction of oxygenates and carbon deposits during the co-pyrolysis of cellulose and polypropylene. *ACS Omega*, *5*(32), 20299–20310.

Shirvanimoghaddam, K., Motamed, B., Ramakrishna, S., & Naebe, M. (2020). Death by waste: Fashion and textile circular economy case. *Science of The Total Environment*, *718*, 137317.

Shrivastava, P., Kumar, A., Tekasakul, P., Lam, S. S., & Palamanit, A. (2021). Comparative investigation of yield and quality of bio-oil and biochar from pyrolysis of woody and non-woody biomasses. *Energies*, *14*(4), 1092.

Singh, R., Chakinala, N., Mohanty, K., & Chakinala, A. G. (2023). Catalytic upgrading of biomass pyrolysis vapors for selective production of phenolic monomers over metal oxide modified alumina catalysts. *Journal of Environmental Chemical Engineering*, *11*(6), 111518.

Singh, S., Patil, T., Tekade, S. P., Gawande, M. B., & Sawarkar, A. N. (2021). Studies on individual pyrolysis and co-pyrolysis of corn cob and polyethylene: Thermal degradation behavior, possible synergism, kinetics, and thermodynamic analysis. *The Science of the Total Environment*, *783*, 147004.

Singhal, S., Agarwal, S., & Singhal, N. (2023). Chemical recycling of waste clothes: a smarter approach to sustainable development. *Environmental Science and Pollution Research*, *30*(19), 54448–54469.

Smirnov, A. A., Shilov, I. N., Bulavchenko, O. A., Saraev, A. A., & Yakovlev, V. A. (2019). Hydrotreatment of anisole and furfural as model compounds of bio-oil over chromium modified nickel-based catalysts. *ChemistrySelect*, *4*(24), 7317–7326.

Sophonrat, N., Sandström, L., Zaini, I. N., & Yang, W. (2018). Stepwise pyrolysis of mixed plastics and paper for separation of oxygenated and hydrocarbon

condensates. *Applied Energy*, *229*, 314–325.

Stefanidis, S. D., Karakoulia, S. A., Kalogiannis, K. G., Iliopoulou, E. F., Delimitis, A., Yiannoulakis, H., Zampetakis, T., Lappas, A. A., & Triantafyllidis, K. S. (2016). Natural magnesium oxide (MgO) catalysts: A cost-effective sustainable alternative to acid zeolites for the in situ upgrading of biomass fast pyrolysis oil. *Applied Catalysis B: Environmental*, *196*, 155–173.

Stuart, B. (2004). *Infrared Spectroscopy : Fundamentals and Applications*. J. Wiley.

Subhan Azeem, Muhammad Rizwan, & Sadiq Hussain. (2025). Calcination temperature effects on Ni/ZrO_2 catalysts for dry reforming of methane. *Frontiers in Chemical Sciences*, *6*(1), 1–13.

Sulaiman, S., & Rohana, S. (2016). Effect of calcination temperature and time on waste heterogeneous catalysts for biodiesel production. *Key Engineering Materials*, *707*, 161–165.

Sun, D., Sun, L., Han, D., Chen, L., Yang, S., Li, T., Dong, Z., Zhao, B., Xu, M., & Tian, S. (2025). Enhanced aromatics production via co-pyrolysis of biomass and plastic by Zn modified ZSM-5 catalysts. *Journal of Analytical and Applied Pyrolysis*, *189*, 107086.

Sun, K., Themelis, N. J., Bourtsalas, A. C. T., & Huang, Q. (2020). Selective production of aromatics from waste plastic pyrolysis by using sewage sludge derived char catalyst. *Journal of Cleaner Production*, *268*, 122038.

Sun, K., Wang, W., Themelis, N. J., Thanos Bourtsalas, A. C., & Huang, Q. (2021). Catalytic co-pyrolysis of polycarbonate and polyethylene/polypropylene mixtures: Promotion of oil deoxygenation and aromatic hydrocarbon formation. *Fuel*, *285*, 119143.

Sun, W., Yan, Y., Wei, Y., Ma, J., Niu, Z., & Hu, G. (2025). Catalytic pyrolysis of biomass: A review of zeolite, carbonaceous, and metal oxide catalysts. *Nanomaterials*, *15*(7), 1–22.

Supramono, D., Fadhlillah, A., & Nasikin, M. (2020). Formation of non-oxygenated phase of bio-oil produced by copyrolysis of corn cobs and polypropylene plastic using zeolite catalysts at low heating rate. *IOP Conference Series: Earth and Environmental Science*, *460*(1), 012021.

Suriapparao, D. V., Ojha, D. K., Ray, T., & Vinu, R. (2014). Kinetic analysis of co-pyrolysis of cellulose and polypropylene. *Journal of Thermal Analysis and Calorimetry*, *117*(3), 1441–1451.

Suriapparao, D. V., & Tejasvi, R. (2022). A review on role of process parameters on pyrolysis of biomass and plastics: Present scope and future opportunities in conventional and microwave-assisted pyrolysis technologies. *Process Safety and Environmental Protection*, *162*, 435–462.

Suriapparao, D. V., Vinu, R., Shukla, A., & Haldar, S. (2020). Effective deoxygenation for the production of liquid biofuels via microwave assisted co-pyrolysis of agro residues and waste plastics combined with catalytic upgradation. *Bioresource Technology*, *302*.

Tamilarasan, N., Sakthivel, R., & Balaji, K. (2024). Influence of metal oxide catalyst on co-pyrolysis of biomass and COVID-19 waste. *Environmental Technology*, *45*(9), 1721–1732.

Tan, K. B., Liu, Y., Wang, Y., Ali, S., Wang, W., Li, J., Shang, L., Yan, X., Zhang, X., & Zhan, G. (2024). Catalytic deoxygenation of stearic acid into olefins over Pt catalysts supported on MOF-derived metal oxides. *Catalysis Science & Technology*, *14*(12), 3436–3447.

Tang, K. H. D. (2023). State of the art in textile waste management: A review. *Textiles*, *3*(4), 454–467.

Tang, X., Yang, J. Y., Heluo, Y. Y., Li, X. Y., Dong, H., Zhou, Z., & Luo, W. (2025). Catalytic co-pyrolysis of tobacco stem and polypropylene over Ni/CaO-Al_2O_3: Synergistic production and distribution of pyrolysis oil, pyrolysis gas and carbon nanotubes. *Fuel*, *387*, 134354.

Tawalbeh, M., Al-Othman, A., Salamah, T., Alkasrawi, M., Martis, R., & El-Rub, Z. A. (2021). A critical review on metal-based catalysts used in the pyrolysis of lignocellulosic biomass materials. *Journal of Environmental Management*, *299*, 113597.

Taylor, C. J., Pomberger, A., Felton, K. C., Grainger, R., Barecka, M., Chamberlain, T. W., Bourne, R. A., Johnson, C. N., & Lapkin, A. A. (2023). A brief introduction to chemical reaction optimization. *Chemical Reviews*, *123*(6), 3089–3126.

Tedeeva, M. A., Mashkin, M. Y., Andresyuk, A. A., Pribytkov, P. V., Medvedev, A. A., Tkachenko, O. P., Kapustin, G. I., Dunaev, S. F., & Kustov, A. L. (2025). Effect of the textural characteristics of the support on the activity of chromium oxide catalysts in the propane dehydrogenation reaction in the presence of CO_2. *Russian Journal of Physical Chemistry A*, *99*(6), 1262–1269.

Terry, L. M., Li, C., Chew, J. J., Aqsha, A., How, B. S., Loy, A. C. M., Chin, B. L. F.,

Khaerudini, D. S., Hameed, N., Guan, G., & Sunarso, J. (2021). Bio-oil production from pyrolysis of oil palm biomass and the upgrading technologies: A review. *Carbon Resources Conversion*, *4*, 239–250.

Terry, L. M., Wee, M. X. J., Chew, J. J., Khaerudini, D. S., Darsono, N., Aqsha, A., Saptoro, A., & Sunarso, J. (2023). Catalytic co-pyrolysis of oil palm trunk and polypropylene with Ni–Mo/TiO_2 and Ni/Al_2O_3: Oil composition and mechanism. *Environmental Research*, *224*(August 2022), 115550.

Thommes, M., Kaneko, K., Neimark, A. V., Olivier, J. P., Rodriguez-Reinoso, F., Rouquerol, J., & Sing, K. S. W. (2015). Physisorption of gases, with special reference to the evaluation of surface area and pore size distribution (IUPAC Technical Report). *Pure and Applied Chemistry*, *87*(9–10), 1051–1069.

Thulluru, L. P., Dhanda, A., Ghangrekar, M. M., & Chowdhury, S. (2025). Alum and anaerobic sludge-derived high-performance electrocatalyst for enhanced oxygen reduction reaction in microbial fuel cell. *Fuel*, *397*.

Tian, H., Zhu, R., Zhu, G., Wang, J., & Cheng, Y. (2024). Hierarchical HZSM-5 catalysts enhancing monocyclic aromatics selectivity in co-pyrolysis of wheat straw and polyethylene mixture. *Renewable Energy*, *233*, 121150.

Tujjohra, F., Hoque, E., Kader, M. A., & Rahman, M. M. (2025). Sustainable valorization of textile industry cotton waste through pyrolysis for biochar production. *Cleaner Chemical Engineering*, *11*, 100161.

UNEP & ISWA. (2024). Global waste management outlook 2024 - Beyond an age of waste: Turning rubbish into a resource.

Uzi, A., Shen, Y., Kawi, S., Levy, A., & Wang, C.-H. (2019). Permittivity and chemical characterization of woody biomass during pyrolysis and gasification. *Chemical Engineering Journal*, *355*, 255–268.

Uzoejinwa, B. B., He, X., Wang, S., El-Fatah Abomohra, A., Hu, Y., & Wang, Q. (2018). Co-pyrolysis of biomass and waste plastics as a thermochemical conversion technology for high-grade biofuel production: Recent progress and future directions elsewhere worldwide. *Energy Conversion and Management*, *163*, 468–492.

Venegas-Vásconez, D., Orejuela-Escobar, L., Valarezo-Garcés, A., Guerrero, V. H., Tipanluisa-Sarchi, L., & Alejandro-Martín, S. (2024). Biomass valorization through catalytic pyrolysis using metal-impregnated natural zeolites: from waste to resources. *Polymers*, *16*(13), 1912.

Vilas-Boas, A. C. M., Tarelho, L. A. C., Moura, J. M. O., Gomes, H. G. M. F., Marques, C. C., Pio, D. T., Nunes, M. I. S., & Silvestre, A. J. D. (2025). Methodologies for bio-oil characterization from biomass pyrolysis: A review focused on GC-MS. *Journal of Analytical and Applied Pyrolysis*, *185*, 106850.

Vuppaladadiyam, A. K., Zhao, M., Memon, M. Z., Soomro, A. F., & Wei, W. (2019). Solid waste as a renewable source of energy: A comparative study on thermal and kinetic behavior of three organic solid wastes. *Energy & Fuels*, *33*(5), 4378–4388.

Wang, Jia, Jiang, J., Ding, J., Wang, X., Sun, Y., Ruan, R., Ragauskas, A. J., Ok, Y. S., & Tsang, D. C. W. (2021). Promoting Diels-Alder reactions to produce bio-BTX: Co-aromatization of textile waste and plastic waste over USY zeolite. *Journal of Cleaner Production*, *314*, 127966.

Wang, Jia, Jiang, J., Meng, X., Li, M., Wang, X., Pang, S., Wang, K., Sun, Y., Zhong, Z., Ruan, R., & Ragauskas, A. J. (2020). Promoting aromatic hydrocarbon formation via catalytic pyrolysis of polycarbonate wastes over fe- and ce-loaded aluminum oxide catalysts. *Environmental Science & Technology*, *54*(13), 8390–8400.

Wang, Jia, Zhong, Z., Ding, K., Li, M., Hao, N., Meng, X., Ruan, R., & Ragauskas, A. J. (2019). Catalytic fast co-pyrolysis of bamboo sawdust and waste tire using a tandem reactor with cascade bubbling fluidized bed and fixed bed system. *Energy Conversion and Management*, *180*(2), 60–71.

Wang, Jingyue, Wu, L., Huang, F., & Liang, J. (2025). Co-pyrolysis of neem sawdust and high-density polyethylene towards aromatic-rich bio-oil: Significance of zeolite mesopores. *Fuel*, *382*, 133724.

Wang, K., Khoo, K. S., Chew, K. W., Selvarajoo, A., Chen, W.-H., Chang, J.-S., & Show, P. L. (2021). Microalgae: The future supply house of biohydrogen and biogas. *Frontiers in Energy Research*, *9*.

Wang, Qi, Chen, J., Li, X., Yang, X., Wu, Y., Li, S., Ye, Y., Wang, D., Wang, D., & Zheng, Z. (2022). Calcination temperature induced structural change of red mud and its enhanced catalytic performance for hydrocarbon-based biofuels production. *Fuel Processing Technology*, *233*.

Wang, Qing, Zhang, X., Sun, S., Wang, Z., & Cui, D. (2020). Effect of CaO on pyrolysis products and reaction mechanisms of a corn stover. *ACS Omega*, *5*(18), 10276–10287.

Wang, W., Shi, Y., Cui, Y., & Li, X. (2018). Catalytic fast pyrolysis of cellulose for increasing contents of furans and aromatics in biofuel production. *Journal of Analytical and Applied Pyrolysis*, *131*, 93–100.

Wang, X., Li, F., Ali, A., Gu, H., Fu, H., Li, Z., & Lin, H. (2022). Preparation of sodium silicate/red mud-based ZSM-5 with glucose as a second template for catalytic cracking of waste plastics into useful chemicals. *RSC Advances*, *12*(34), 22161–22174.

Wang, Z., Liu, G., Shen, D., Wu, C., & Gu, S. (2020). Co-pyrolysis of lignin and polyethylene with the addition of transition metals - Part I: Thermal behavior and kinetics analysis. *Journal of the Energy Institute*, *93*(1), 281–291.

Weckhuysen, B. M., & Schoonheydt, R. A. (1999). Alkane dehydrogenation over supported chromium oxide catalysts. *Catalysis Today*, *51*(2), 223–232.

Wee, M. X. J., Chin, B. L. F., Saptoro, A., Chew, J. J., Sunarso, J., Yusup, S., & Sharma, A. (2024). Catalytic co-pyrolysis of oil palm empty fruit bunches (EFB) and surgical face mask (SFM) wastes: Thermo-kinetic study, ANN model fitting, and synergistic effect. *Journal of the Taiwan Institute of Chemical Engineers*, *165*, 105811.

Wee, M. X. J. J., Chin, B. L. F. F., Saptoro, A., Yiin, C. L., Chew, J. J., Sunarso, J., Yusup, S., & Sharma, A. (2023). A review on co-pyrolysis of agriculture biomass and disposable medical face mask waste for green fuel production: recent advances and thermo-kinetic models. *Frontiers of Chemical Science and Engineering*, *17*(9), 1141–1161.

Wen, Y., Zaini, I. N., Wang, S., Mu, W., Jönsson, P. G., & Yang, W. (2021). Synergistic effect of the co-pyrolysis of cardboard and polyethylene: A kinetic and thermodynamic study. *Energy*, *229*.

Waste Management Association of Malaysia. (2025). Transitioning to a circular fashion economy in Malaysia. Retrieved August, 10, 2025 from the world wide web:wmam.org/transitioning-to-a-circular-fashion-economy-in-malaysia

Xiang, Z., Liang, J., Morgan, H. M., Liu, Y., Mao, H., & Bu, Q. (2018). Thermal behavior and kinetic study for co-pyrolysis of lignocellulosic biomass with polyethylene over Cobalt modified ZSM-5 catalyst by thermogravimetric analysis. *Bioresource Technology*, *247*, 804–811.

Xing, B., Hu, Y., & Wang, S. (2025). Study of synergistic effects in co-pyrolysis of biomass and plastics from the perspective of phase reactions. *Journal of*

Analytical and Applied Pyrolysis, *186*, 106951.

Xu, D., Xiong, Y., Zhang, S., & Su, Y. (2021). The synergistic mechanism between coke depositions and gas for H_2 production from co-pyrolysis of biomass and plastic wastes via char supported catalyst. *Waste Management*, *121*, 23–32.

Xu, G., Li, P., Chen, P., Cui, L., Wang, Z., Ren, Z., Qin, X., Wang, N., & Liu, M. (2023). Flash pyrolysis of oil shale assisted by Zr-doped $TiOSO_4$ nanocomposites: Excellent selectivity for hydrocarbons and toluene. *Fuel*, *332*.

Xu, J., & Zhu, L. (2023). Molecular mechanism study of the kinetics and product yields during co-pyrolysis of biomass and solid wastes: reaxFF-MD method approach. *ACS Omega*, *8*(39), 36126–36135.

Xu, M., Shi, Z., Zhu, X., Lai, Y., Xia, A., Huang, Y., Jiang, X., He, J., Zhou, M., Zhu, X., & Liao, Q. (2024). Ex-situ catalytic upgrading of biomass pyrolysis volatiles over thermal-decomposition products of spent lithium-ion batteries for bio-oil deoxygenation and hydrogen-rich syngas production. *International Journal of Hydrogen Energy*, *52*, 83–96.

Xu, R., Yan, C., Liu, Q., Liu, E., Zhang, H., Zhang, X., Yuan, X., Han, L., Lei, H., Ruan, R., & Zhang, X. (2022). Development of metal-doping mesoporous biochar catalyst for co-valorizing biomass and plastic waste into valuable hydrocarbons, syngas, and carbons. *Fuel Processing Technology*, *227*, 107127.

Xu, S., Cao, B., Uzoejinwa, B. B., Odey, E. A., Wang, S., Shang, H., Li, C., Hu, Y., Wang, Q., & Nwakaire, J. N. (2020). Synergistic effects of catalytic co-pyrolysis of macroalgae with waste plastics. *Process Safety and Environmental Protection*, *137*, 34–48.

Xu, T., Xu, J., & Wu, Y. (2022). Hydrogen-rich gas production from two-stage catalytic pyrolysis of pine sawdust with calcined dolomite. *Catalysts*, *12*(2), 131.

Xu, Z., Zhao, W., Bai, L., & Fan, J. (2024). The effect of the calcination time on the microstructure and properties of MnZn ferrite powders. *Magnetochemistry*, *10*(10), 68.

Xue, J., Zhuo, J., Liu, M., Chi, Y., Zhang, D., & Yao, Q. (2017). Synergetic effect of co-pyrolysis of cellulose and polypropylene over an all-silica mesoporous catalyst MCM-41 using thermogravimetry-Fourier transform infrared spectroscopy and pyrolysis-gas chromatography-mass spectrometry. *Energy and Fuels*, *31*(9), 9576–9584.

Xue, X., Pan, Z., Zhang, C., Wang, D., Xie, Y., & Zhang, R. (2018). Segmented

catalytic co-pyrolysis of biomass and high-density polyethylene for aromatics production with $MgCl_2$ and HZSM-5. *Journal of Analytical and Applied Pyrolysis*, *134*, 209–217.

Yaman, E., Ulusal, A., & Uzun, B. B. (2021). Co-pyrolysis of lignite and rapeseed cake: a comparative study on the thermal decomposition behavior and pyrolysis kinetics. *SN Applied Sciences*, *3*(1), 97.

Yan, X., Ma, J., Wang, W., Zhao, Y., & Zhou, J. (2017). The effect of different catalysts and process parameters on the chemical content of bio-oils from hydrothermal liquefaction of sugarcane bagasse. *BioResources*, *13*(1), 997–1018.

Yang, Y., Luo, Z., Li, S., Lu, K., & Wang, W. (2019). Catalytic pyrolysis of hemicellulose to produce aromatic hydrocarbons. *BioResources*, *14*(3), 5816–5831.

Yipeng, W., Ge, N., Wenjia, W., Jinglai, Z., & Wei, H. (2017). Preparation and application of a new catalyst to produce bio-oil from microalgae liquefaction. *International Journal of Agricultural and Biological Engineering*, *10*(1), 169–175.

Yoon, J. S., Park, M. B., Kim, Y., Hwang, D. W., & Chae, H.-J. (2019). Effect of metal oxide–support interactions on ethylene oligomerization over nickel oxide/silica–alumina catalysts. *Catalysts*, *9*(11), 933.

Yu, D., Hui, H., Ding, G., Dong, N., & Li, S. (2021). Enhancement of aromatics production from catalytic co-pyrolysis of walnut shell and LDPE via a two-step approach. *Journal of Analytical and Applied Pyrolysis*, *157*, 105216.

Zaker, A., Chen, Z., Wang, X., & Zhang, Q. (2019). Microwave-assisted pyrolysis of sewage sludge: A review. *Fuel Processing Technology*, *187*, 84–104.

Zaker, A., Chen, Z., & Zaheer-Uddin, M. (2021). Catalytic pyrolysis of sewage sludge with HZSM5 and sludge-derived activated char: A comparative study using TGA-MS and artificial neural networks. *Journal of Environmental Chemical Engineering*, *9*(5), 105891.

Zaker, A., Chen, Z., Zaheer-Uddin, M., & Guo, J. (2021). Co-pyrolysis of sewage sludge and low-density polyethylene – A thermogravimetric study of thermo-kinetics and thermodynamic parameters. *Journal of Environmental Chemical Engineering*, *9*(1), 104554.

Zha, X., Li, F., Feng, B., Zhang, X., & He, R. (2024). Adsorption mechanism and regeneration performance of calcined zeolites for hydrogen sulfide and its

application. *ACS Omega*, *9*(17), 19493–19503.

Zhang, C., Chao, L., Zhang, Z., Zhang, L., Li, Q., Fan, H., Zhang, S., Liu, Q., Qiao, Y., Tian, Y., Wang, Y., & Hu, X. (2021). Pyrolysis of cellulose: Evolution of functionalities and structure of bio-char versus temperature. *Renewable and Sustainable Energy Reviews*, *135*, 110416.

Zhang, C., Hu, X., Guo, H., Wei, T., Dong, D., Hu, G., Hu, S., Xiang, J., Liu, Q., & Wang, Y. (2018). Pyrolysis of poplar, cellulose and lignin: Effects of acidity and alkalinity of the metal oxide catalysts. *Journal of Analytical and Applied Pyrolysis*, *134*, 590–605.

Zhang, C., Zhang, L., Li, Q., Wang, Y., Liu, Q., Wei, T., Dong, D., Salavati, S., Gholizadeh, M., & Hu, X. (2019). Catalytic pyrolysis of poplar wood over transition metal oxides: Correlation of catalytic behaviors with physiochemical properties of the oxides. *Biomass and Bioenergy*, *124*, 125–141.

Zhang, H., Nie, J., Xiao, R., Jin, B., Dong, C., & Xiao, G. (2014). Catalytic co-pyrolysis of biomass and different plastics (polyethylene, polypropylene, and polystyrene) to improve hydrocarbon yield in a fluidized-bed reactor. *Energy and Fuels*, *28*(3), 1940–1947.

Zhang, N., Li, R., Zhang, G., Dong, L., Zhang, D., Wang, G., & Li, T. (2020). Zn-Modified Hβ Zeolites Used in the Adsorptive Removal of Organic Chloride from Model Naphtha. *ACS Omega*, *5*(21), 11987–11997.

Zhang, Q., Zhang, S., Liu, J., Li, J., Liu, J., Zhou, J., & Wu, L. (2023). Catalytic upgrading of volatiles in co-pyrolysis of coal and biomass by Mo-MFI molecular sieves. *RSC Advances*, *13*(48), 33852–33862.

Zhang, Xikui, Yu, Z., Lu, X., & Ma, X. (2021). Catalytic co-pyrolysis of microwave pretreated chili straw and polypropylene to produce hydrocarbons-rich bio-oil. *Bioresource Technology*, *319*(September 2020), 124191.

Zhang, Xuesong, Lei, H., Chen, S., & Wu, J. (2016). Catalytic co-pyrolysis of lignocellulosic biomass with polymers: a critical review. *Green Chemistry*, *18*(15), 4145–4169.

Zhang, Xuesong, Lei, H., Zhu, L., Qian, M., Zhu, X., Wu, J., & Chen, S. (2016). Enhancement of jet fuel range alkanes from co-feeding of lignocellulosic biomass with plastics via tandem catalytic conversions. *Applied Energy*, *173*, 418–430.

Zhang, X., Lei, H., Zhu, L., Zhu, X., Qian, M., Yadavalli, G., Wu, J., & Chen, S. (2016).

Thermal behavior and kinetic study for catalytic co-pyrolysis of biomass with plastics. *Bioresource Technology*, *220*, 233–238.

Zhang, Y., Duan, D., Lei, H., Villota, E., & Ruan, R. (2019). Jet fuel production from waste plastics via catalytic pyrolysis with activated carbons. *Applied Energy*, *251*, 113337.

Zhang, Yongxun. (2020). Effect of calcination time on catalyst's activity and stability. *IOP Conference Series: Earth and Environmental Science*, *495*(1), 012075.

Zheng, A., Huang, Z., Wei, G., Zhao, K., Jiang, L., Zhao, Z., Tian, Y., & Li, H. (2020). Controlling deoxygenation pathways in catalytic fast pyrolysis of biomass and its components by using metal-oxide nanocomposites. *IScience*, *23*(1), 100814.

Zheng, Y., Li, D., Pei, T., Wang, J., Liu, C., Lu, Y., Lin, X., Li, J., & Zheng, Z. (2022). Mechanism of synergistic effects and kinetic analysis in bamboo-LDPE waste ex-situ catalytic co-pyrolysis for enhanced aromatic hydrocarbon production via CeZrAl and HZSM-5 dual catalyst. *Journal of Environmental Chemical Engineering*, *10*(3).

Zheng, Y., Tao, L., Yang, X., Huang, Y., Liu, C., Gu, J., & Zhang, Z. (2017). Effect of acidity and manner of addition of HZSM-5 catalyst on the aromatic products during catalytic upgrading of biomass pyrolysis. *BioResources*, *12*(4), 8286–8305.

Zheng, Y., Wang, J., Liu, C., Lin, X., Lu, Y., Li, W., & Zheng, Z. (2020). Enhancing the aromatic hydrocarbon yield from the catalytic copyrolysis of xylan and LDPE with a dual-catalytic-stage combined CaO/HZSM-5 catalyst. *Journal of the Energy Institute*, *93*(5), 1833–1847.

Zheng, Y., Wang, J., Liu, C., Lu, Y., Lin, X., Li, W., & Zheng, Z. (2020a). Catalytic copyrolysis of metal impregnated biomass and plastic with Ni-based HZSM-5 catalyst: Synergistic effects, kinetics and product distribution. *International Journal of Energy Research*, *44*(7), 5917–5935.

Zheng, Y., Wang, J., Wang, D., & Zheng, Z. (2022). Advanced catalytic upgrading of biomass pyrolysis vapor to bio-aromatics hydrocarbon: A review. *Applications in Energy and Combustion Science*, *10*, 100061.

Zhong, S., Zhang, B., Liu, C., Shujaa aldeen, A., Mwenya, S., & Zhang, H. (2022). A minireview on catalytic fast co-pyrolysis of lignocellulosic biomass for bio-oil upgrading via enhancing monocyclic aromatics. *Journal of Analytical and Applied Pyrolysis*, *164*, 105544.

Zou, X., Chen, T., Liu, H., Zhang, P., Ma, Z., Xie, J., & Chen, D. (2017). An insight into the effect of calcination conditions on catalytic cracking of toluene over 3Fe8Ni/palygorskite: Catalysts characterization and performance. *Fuel*, *190*, 47–57.

Zulkafli, A. H., Hassan, H., Ahmad, M. A., & Din, A. T. M. (2024). Co-pyrolysis of palm kernel shell and polypropylene for the production of high-quality bio-oil: product distribution and synergistic effect. *Biomass Conversion and Biorefinery*, *14*(12), 13391–13406.

Zulkafli, Aizatul Hikmah, Hassan, H., Ahmad, M. A., & Din, A. T. M. (2023). Catalytic co-pyrolysis of palm kernel shell and polypropylene to enhance pyrolysis yield and quality in a fixed-bed reactor. *AIP Conference Proceedings*, *2785*(1), 030020.

APPENDICES

APPENDIX 1

Sample Calculation of Normalising Raw Data and Dry-basis Weight Conversion

Ultimate and proximate of CFW (wt.% as received) are shown in Table A1

Table A1: Raw results of CFW samples

	Ultimate (wt.%)				Proximate (wt.%)			
Feedstock	C	H	N	S	VM	FC	Ash	Mo
CFW	42.6	5.9	0.5	0	88.7	3.7	2.9	4.8

VM (Volatile matter), FC (Fixed carbon), Mo (Moisture), C (Carbon), H (Hydrogen), N (Nitrogen), S (Sulfur)

Proximate analysis

Sample calculation for volatile matter of CFW

Total weight for proximate analysis = 100.1 wt.%

Weight % volatile matter (VM) = 88.7 wt.%

$$\text{Normalize VM (wt.\%)} = \frac{88.7\ \%}{100.1} \times 100 = 88.7\ \%$$

VM in dry basis (wt.% db)

Weight % normalize moisture = 4.8%

Total weight % without moisture = 95.2%

$$\text{VM(wt.\% db)} = \frac{(88.7\ \%)}{95.2\ \%} \times 100$$

$$= 93.1\ \%$$

Ultimate analysis

Sample calculation for carbon content

Carbon weight % = 42.6 %

Composition moisture content = 0.048 wt./wt.

$$\text{Carbon (wt.\% db)} = \frac{(42.6\ \%)}{(1\text{-}0.048)} \times 100$$

$$= 44.7\ \%$$

APPENDIX 2

Sample calculation of bio-oil yield

The formula uses to calculate bio-oil yield:

$$\text{Yield of oil (wt.\%)} = \frac{\text{Liquid (g)}}{\text{Total feedstock (g)}} \times 100$$

Where:

Liquid = Weight of bio-oil in wax trap + weight of bio-oil in condenser after pyrolysis

Total feedstock = Total weight of feedstock (biomass and plastic before pyrolysis)

$$\text{Yield of bio-oil (wt.\%)} = \frac{(0.1577+0.2195)}{1.0001} \times 100$$

$$= 37.7\ \%$$

APPENDIX 3

The Codes in Matlab Algorithms for Kinetic Study

```
% Load Data: time, Temperature, Conversion rate (TGA data)
% Assuming the data is in a matrix called TGA
data = TGA4; % Assume data is in columns: [time, temperature,
conversion_rate]
time = data(:, 1);  % Time (s)
temperature = data(:, 2);  % Temperature (K)
alpha_exp = data(:, 3);  % Experimental conversion rate (alpha)

% Constants
R = 0.008314;  % kJ/mol·K (universal gas constant)
beta = 40;     % Set Beta as a constant (heating rate)
n = 0.5;         % Fixed value of n

% Define the ODE system based on the rate equation
% dα/dt = A * exp(-E/(R*T)) * (1 - α)^n

odefun = @(t, alpha, A, E) A * exp(-E/(R * interp1(time, temperature, t,
'linear', 'extrap'))) * (1 - alpha)^n;

% Objective function to minimize the error between the model and
experimental data
objective = @(params) error_func(params, time, alpha_exp, odefun);

% Initial guess for A and E (n is fixed to 2)
initial_guess = [1e4, 80];  % [A, E] (n = 2 is fixed)

% Use fminsearch to minimize the error and estimate A and E
optimal_params = fminsearch(objective, initial_guess);

% Extract optimal parameters
A_est = optimal_params(1);
E_est = optimal_params(2);

% Display estimated parameters
disp(['Estimated Pre-exponential Factor (A): ', num2str(A_est)]);
disp(['Estimated Activation Energy (E): ', num2str(E_est), ' kJ/mol']);

% Solve ODE again with optimized parameters for plotting
[~, alpha_sim] = ode23s(@(t, alpha) odefun(t, alpha, A_est, E_est), time,
0);

% Plot Experimental vs Simulated Data
figure;
plot(time, alpha_exp, 'bo', 'DisplayName', 'Experimental Data');
hold on;
plot(time, alpha_sim, 'r-', 'DisplayName', 'Simulated Data');
xlabel('Time (s)');
ylabel('Conversion Rate (d\alpha/dt)');
legend;
grid on;
title('CFW/PPW with catalyst');

% Calculate R² (Coefficient of Determination)
R2 = calculate_R2(alpha_exp, alpha_sim);
```

```
% Display R² value
disp(['R² (Coefficient of Determination): ', num2str(R2)]);

% Function to calculate the error (sum of squared residuals)
function error = error_func(params, time, alpha_exp, odefun)
    A = params(1);
    E = params(2);

    % Solve the ODE for the given parameters
    [~, alpha_sim] = ode23s(@(t, alpha) odefun(t, alpha, A, E), time, 0);

    % Ensure alpha_sim is a column vector
    alpha_sim = alpha_sim(:);  % Convert to a column vector

    % Calculate the sum of squared residuals between experimental and
simulated alpha
    residuals = alpha_exp - alpha_sim;
    error = sum(residuals.^2);  % Sum of squared errors
end

% Function to calculate R² (Coefficient of Determination)
function R2 = calculate_R2(y_exp, y_sim)
    % Calculate the mean of experimental data
    mean_exp = mean(y_exp);

    % Calculate R² using the formula
    ss_tot = sum((y_exp - mean_exp).^2);  % Total sum of squares
    ss_res = sum((y_exp - y_sim).^2);    % Residual sum of squares

    % R² calculation
    R2 = 1 - (ss_res / ss_tot);
end
```

AUTHOR'S PROFILE

Nur Alwani Ali Bashah obtained Bachelor of Chemical Engineering (Hons.) in 2006 from Universiti Teknologi MARA, Shah Alam, MSc. in Chemical Engineering (2013) from Universiti Sains Malaysia, Pulau Pinang. Currently, she is pursuing a Ph.D. in Chemical Engineering at Universiti Teknologi MARA. Her research interests include renewable energy, heterogeneous catalysts, biofuel, pyrolysis, and neural network modelling. Her current research focus is on the synthesis of heterogeneous metal oxide catalysts that enhanced bio-oil production via co-pyrolysis of biomass and plastic.

LIST OF PUBLICATION

Nur Alwani AB, Muhammad ZR, Wan Zuraida WK, Siti SI, Mohamad AK, Ahmad SZ, Moses AO. Chromium-extracted aluminum catalyst for co-pyrolysis of cotton fabric waste and polypropylene plastic waste to bio-oil. Journal of Environmental Chemical Engineering, 12, 113757, 2024. (Q1 WOS, Impact Factor:7.4)

Nur Alwani AB, Muhammad ZR, Wan Zuraida WK, Siti SI, Mohamad AK. Bio-oil production from cotton fabric and plastic waste: Influence of pyrolysis time in catalytic co-pyrolysis. Esteem Academic Journal, vol 21, 36-45, 2025.

Nur Alwani AB, Muhammad ZR, Wan Zuraida WK, Siti SI, Mohamad AK, Ahmad SZ, Moses AO. Chromium/ Titanium-extracted aluminum catalyst for bio-oil production via co-pyrolysis of cotton fabric waste and polypropylene plastic

waste: Effects of metal loading. To be submitted to journal of biomass and bioenergy.

Nur Alwani AB, Muhammad ZR, Wan Zuraida WK, Siti SI, Mohamad AK, Ahmad SZ, Moses AO. Influence of calcination temperature and time in co-pyrolysis of cotton fabric waste and polypropylene plastic waste to produce bio-oil via chromium-extracted aluminum catalyt. To be submitted to Journal of Taiwan Institute of Chemical Engineers.

LAMPIRAN

JUDUL BAHAN: THE ROLE OF METAL OXIDES SUPPORTED ON EXTRACTED ALUMINIUM CATALYSTS IN THE CO-PYROLYSIS OF COTTON FABRIC AND POLYPROPYLENE WASTES FOR BIO-OIL PRODUCTION